Precision Spectroscopy and Quantum Information Processing with Trapped Calcium Ions

A thesis submitted to the
Faculty of Mathematics, Computer Science and Physics
of the University of Innsbruck
in partial fulfillment of the requirements
for the degree of

Doctor rerum naturalium

by

Jan Benhelm

Innsbruck, May 2008

Thesis advisor and referee	Prof. Dr. R. Blatt
External referees	Prof. I. L. Chuang (MIT, Cambridge, USA) Dr. D. M. Lucas (Clarendon Laboratory, Oxford, GB)
Rigorosum committee	Prof. Dr. P. Girtler (Chair) Prof. Dr. R. Blatt Prof. Dr. A. Hansel

The work described in this thesis was carried out at the

Universität Innsbruck
Institut für Experimentalphysik
Technikerstraße 25
6020 Innsbruck, Austria

and the

Institut für Quantenoptik und Quanteninformation
der Österreichischen Akademie der Wissenschaften
Otto Hittmair-Platz 1
6020 Innsbruck, Austria.

The experiment was funded by grants from the US funding agency IARPA, the European network SCALA, and the Austrian Academy of Sciences.

This document is available online at http://quantumoptics.at.

Abstract

Over the last decade quantum information processing (QIP) has exploded into a major field of physics, studied both experimentally and theoretically with a universal quantum computer as a long-term vision. Ions stored as strings in linear Paul traps are among the most promising systems for constructing a quantum device harnessing the computing power inherent in the laws of quantum physics.

The two most important challenges in trapped ion quantum computing today are to realize and control systems with large numbers of ions, and to improve and integrate the operations which serve as basic building blocks, in particular universal gate operations. Quite surprisingly, even after many years of intense research with different atom species, it is still not evident which ion is best suited for QIP.

This thesis describes the construction of a new experiment built to study a promising candidate qubit, namely the calcium isotope $^{43}Ca^+$. Due to its nuclear spin of $I = 7/2$, the isotope $^{43}Ca^+$ exhibits a relatively complicated level structure, compared to other ions used so far for QIP. This work develops various strategies to successfully control such a complex level scheme.

Initially we investigated the hyperfine structure of the $4s\,^2S_{1/2} \leftrightarrow 3d\,^2D_{5/2}$ quadrupole transition at a wavelength of 729 nm by laser spectroscopy using a single trapped $^{43}Ca^+$ ion. We determined the hyperfine structure constants of the metastable level as $A_{D_{5/2}} = -3.893\,12(3)$ MHz and $B_{D_{5/2}} = -4.239(1)$ MHz. The isotope shift of this transition with respect to $^{40}Ca^+$ was measured to be $\Delta_{\mathrm{iso}}^{43,40}/(2\pi) = 4\,134\,711\,720(390)$ Hz.

Armed with this knowledge, we were able to demonstrate ground-state cooling, robust state initialization and efficient readout of a qubit encoded in the ground-state hyperfine structure of a $^{43}Ca^+$ ion. A microwave and a Raman light field were used to drive qubit transitions, and the coherence times for both fields were compared. Phase errors due to interferometric instabilities in the Raman field generation were not limiting the experiments on a time scale of at least 100 ms. Even in the presence of magnetic field fluctuations we found a quantum information storage time exceeding one second.

We implemented a Mølmer-Sørensen type gate operation, entangling ions with a fidelity of 99.3(1)%. The gate was performed on a pair of qubits encoded in two trapped $^{40}Ca^+$ ions using an amplitude-modulated laser beam interacting with both ions at the same time. A robust gate operation, mapping separable states onto maximally entangled states was achieved by adiabatically switching the laser-ion coupling on and off. The performance of a single gate and concatenations of up to 21 gate operations were analyzed. Concerning the fidelity, this result sets a world record for creating two-qubit entanglement on-demand irrespective of the physical realization considered.

Zusammenfassung

Die Quanteninformationsverarbeitung (QIV) als experimentelles und theoretisches Teilgebiet der Physik mit dem universellen Quantencomputer als Fernziel entwickelte sich innerhalb der letzten Dekade geradezu explosionsartig. Für die technische Realisierung einer Maschine zur Ausnutzung der den Gesetzen der Quantenmechanik eigenen Rechenkraft gibt es eine Vielzahl an Möglichkeiten. Ionen, die sich in linearen Paul-Fallen wie auf einer Perlenschnur aufreihen, haben sich dabei mittlerweile als sehr vielversprechenden Ansatz etabliert.

Die beiden größten Herausforderungen der Ionenfallen-Experimente zur QIV bestehen gegenwärtig in der Skalierung zu einer Vielzahl kontrollierter Quantenbits und in der Verbesserung und Integration der bereits demonstrierten Grundbausteine, insbesondere universeller Gatteroperationen. Überraschenderweise ist auch nach vielen Jahren intensiver Forschung unklar, welche Ionen-Sorte zu diesem Zweck am besten geeignet ist.

Die vorliegende Arbeit beschreibt den Aufbau eines neuen Experiments zur Untersuchung des Calciumisotops $^{43}\mathrm{Ca}^+$ als attraktiven Kandidaten. Aufgrund des Kernspins von $I = 7/2$ hat das Isotop $^{43}\mathrm{Ca}^+$, verglichen mit Atomsorten, die bisher für die QIV verwandt wurden, ein komplizierteres Energieniveauschema. Diese Arbeit diskutiert die daraus resultierenden Möglichkeiten und beschreibt deren experimentelle Realisierung, so dass diese Komplexität erfolgreich genutzt werden kann.

Zunächst wurde die Hyperfein-Struktur des $4s\,^2S_{1/2} \leftrightarrow 3d\,^2D_{5/2}$ Quadrupol-Übergangs bei einer Wellenlänge von 729 nm mittels Laserspektroskopie an einem einzelnen $^{43}\mathrm{Ca}^+$-Ion untersucht. Die Hyperfein-Konstanten des metastabilen Energieniveaus wurden zu $A_{D_{5/2}} = -3.893\,12(3)\,\mathrm{MHz}$, $B_{D_{5/2}} = -4.239(1)\,\mathrm{MHz}$ bestimmt. Als Nebenprodukt ergab sich die Isotopieverschiebung auf diesem Übergang bezogen auf $^{40}\mathrm{Ca}^+$ zu $\Delta^{43,40}_{\mathrm{iso}}/(2\pi) = 4\,134\,711\,720(390)\,\mathrm{Hz}$.

Mit diesem Wissen gelang es einzelne $^{43}\mathrm{Ca}^+$-Ionen nahe an den Bewegungsgrundzustand einer Mode zu kühlen, sowie $^{43}\mathrm{Ca}^+$-Hyperfein-Qubits mit hoher Güte zu initialisieren und auszulesen. Die Kohärenzzeiten dieses Hyperfein-Qubits wurden mit einem Mikrowellenfeld und einem Raman-Lichtfeld gemessen. Trotz der Anwesenheit magnetischer Störfelder konnte Quanteninformation über eine Sekunde gespeichert werden. Außerdem ergaben Messungen, dass die interferometrischen Stabilitätsanforderungen der Raman-Lichtfelder, auf einer Zeitskala von 100 ms keine Limitierung darstellen.

Die Arbeit schließt mit der Beschreibung einer Mølmer-Sørensen Gatteroperation, die verschränkte Zustände mit einer Güte von 99.3(1)% erzeugte. Dieser Gattertyp wurde erstmals auf einem optischen Qubit mittels eines amplitudenmodulierten Lasers realisiert, der an zwei $^{40}\mathrm{Ca}^+$-Ionen gleichermaßen koppelte. Eine robuste Gatteroperation, die separable in verschränkte Zustände überführt, wurde durch adiabatisches An- und Ausschalten dieses Lasers erreicht. Zur Bestimmung möglicher Fehlerquellen wurden bis zu 21 aneinandergereihte Gatteroperationen analysiert. Bezüglich der erreichten Güte stellt das Ergebnis die momentan beste deterministische Zwei-Qubit-Verschränkungsoperation aller bekannter Systeme dar.

Contents

1 Introduction **1**

2 Trapped calcium ions as qubits **7**

2.1 Quantum bits 7

2.2 Atomic structure 12

2.3 Single ion coherent operation 19

2.4 Quadrupole transition 21

2.5 Raman interactions coupling hyperfine structure ground states 23

2.6 Microwave transitions 29

3 Experimental setup **31**

3.1 Linear ion trap and radiofrequency drive 31

3.2 Laser system and optics 34

3.3 Vacuum vessel 45

3.4 Magnetic field coils and current drivers 45

3.5 Optical access and individual ion addressing 46

3.6 Fluorescence detection 48

3.7 Experiment control and radiofrequency pulses 50

4 Experimental techniques **53**

4.1 Trap loading by photoionization 53

4.2 Pulsed mode 56

4.3 Compensation of excess micromotion 57

4.4 Referencing the laser at 729 nm to the ions and monitoring of the magnetic field 60

4.5 Heating rate, shuttling the ions and motional coherence 63

4.6 Individual ion detection, addressing and addressing error correction 66

5 Precision spectroscopy **69**

5.1 Measurement of the hyperfine constants of the $^{43}\mathrm{Ca}^+$ $D_{5/2}$ energy level . . . 69

5.2 Measurement of the isotope shift 76

5.3 Magnetic field independent transitions 80

6 Quantum information processing with a single $^{43}Ca^+$ ion **85**
6.1 Initialization of the hyperfine clock state qubit 85
6.2 State discrimination 91
6.3 Coherent state manipulation on the $^{43}Ca^+$ hyperfine qubit 92
6.4 Coherence properties of the $^{43}Ca^+$ hyperfine qubit 95

7 Entangled states with high fidelity **101**
7.1 Review of entanglement creation in ion traps 101
7.2 The Mølmer-Sørensen interaction on the optical qubit 103
7.3 Measurement results 105

8 Summary and outlook **115**

A Calcium physical and optical properties and hyperfine measurement data **119**

B Method of separated oscillatory fields **123**
B.1 Errors in frequency determination 123
B.2 Ramsey contrast and phase coherence 125

C Spin flip errors during the Mølmer-Sørensen interaction **127**

D Journal publications **129**

Bibliography **151**

Danksagung

Die vorliegende Arbeit ist das Ergebnis einer gemeinsamen Kraftanstrengung. Allen, die zu diesem Erfolg ihren Beitrag geleistet haben, möchte ich an dieser Stelle ganz herzlich danken.

Zu allererst richte ich ein großes Dankeschön an Rainer Blatt für die Herausforderung ein neues Experiment in einem neuen Labor praktisch ohne finanzielle Grenzen aufzubauen. Das hohe Maß an Entscheidungsfreiheit war für mich ein entscheidender Spaßfaktor und ließ mich ich in einem Schlaraffenland für Experimentalphysiker wähnen. Aber auch für die Gelegenheit fast alle "Big Shots" aus unserem Fachgebiet persönlich kennenzulernen möchte ich mich bedanken.

Ferdinand Schmidt-Kaler danke ich besonders dafür, dass er mich auf dieses faszinierende Teilgebiet der Physik aufmerksam gemacht hat. Sein mitreißender Enthusiasmus und die Teilhabe an seinem schier unerschöpflichen Erfahrungsschatz waren ein riesiger Gewinn für mich. Für die rasche Integration in das Experiment der "Linearen Falle" und die gemeinsam verbrachten Messnächte möchte ich außerdem Hartmut Häffner, Christian Roos, Wolfgang Hänsel und Mark Riebe danken.

Bei Umakant Rapol bedanke ich mich für die hervorragende Zusammenarbeit. Hervorzuheben ist seine große Unterstützung beim Aufbau des hier beschriebenen Experiments und unsere gemeinsamen Pioniertaten, wie z.B. das erstmalige Laden von $^{43}\mathrm{Ca}^+$-Ionen in die neue Falle. Timo Körber und Philipp Schindler gebührt mein Dank für die Entwicklung und die Implementierung der Experimentsteuerung.

Die meiste Zeit für diese Arbeit habe ich gemeinsam mit Gerhard Kirchmair bei den Messungen im Labor verbracht. Vielen Dank für Deinen hohen Einsatz und Deine fantastische Arbeit. Die Zusammenarbeit mit Dir war vom ersten Tag an eine große Bereicherung für mich. DANKE! Gerne möchte ich Christian Roos für die vielen Diskussionen danken, die mein Physikverständnis entscheidend voranbrachten. Er konnte mich letztlich doch davon überzeugen, dass das Mølmer-Sørensen Gatter auf optischen Qubits "einen Versuch wert ist". Seine Unterstützung bei der Vorbereitung und Auswertung der Messungen und beim Verfassen diese Arbeit war sehr wertvoll für mich. René Gerritsma und Florian Zähringer gilt mein Dank für die Unterstützung bei den Messungen von Gatteroperationen auf warmen Ionen.

Ein großer Dank ergeht auch an die Mitarbeiterinnen und Mitarbeiter in den Sekretariaten, der IT-Unterstützung sowie in den Elektronik- und Mechanikwerkstätten an der Uni sowie am IQOQI. Namentlich erwähnen möchte ich Markus Knabl, Elisabeth Huck, Doris Corona, Patricia Moser, Anneliese Werner, Thomas Wachtler, Valentin Staubmann, Andreas Knabl, Gerhard Hendl, Manuel Kluibenschädl, Arthur Wander, Stefan Haslwanter, Andreas Strasser, Anton Schönherr, Helmut Jordan und Josef Dummer. Immer stand man mir mit Rat und Tat - und auch einer großen Portion Humor - zur Seite.

Eine wahrhaft dankenswerte Abwechslung von der Arbeit waren die unzähligen gemeinsamen Mittagspausen mit Mike Chwalla. Selten war für wirklich gutes Essen gesorgt, dafür aber immer für gute Unterhaltung. Zusammen mit den Kollegen Thomas Deuschle, Herbert Crepaz, Philipp Schindler, Thomas Monz, Daniel Rotter und Mark Riebe haben wir uns den "schwarzen Mensagürtel" durch den Verzehr unzähliger Berner Würstel redlich verdient.
Nicht zu vergessen ist natürlich der Dank an alle Arbeitsgruppenmitglieder für die offene Diskussionskultur und ihre Geduld, wenn ich's beim Montag-Morgen-Treff mal wieder etwas genauer wissen wollte.

Ganz herzlich danken möchte ich auch Gabriele Wicker für ihre Gastfreundschaft sowie die Beratung beim Textsatz dieser Arbeit.

Ein großes Dankeschön geht auch an Renate Janssen und meine Eltern für die kontinuierliche Unterstützung und die Anteilnahme an meinem Studium und der Promotion - aber vor allem auch für den sensiblen Umgang mit der Frage, wann ich denn endlich fertig sei.

Jetzt!

Das größte Glück für mich bist Du, liebe Margit. Danke, dass Du mit mir den Weg nach Innsbruck und auf manch hohen Berg und durch manch tiefes Tal bis hierher gegangen bist. Dein großes Herz und Deine Liebe bedeuten eine ganze Welt für mich!

Vielen Dank!

1 Introduction

Two of the greatest advances in physics and technology of the twentieth century have been the discovery of quantum mechanics and the technological revolution based on classical computing. Quantum computation aims to marry both of these fields, an idea first conceived by Paul Benioff [1, 2] and Richard Feynman [3, 4] in the early 1980s.

Computations harnessing the laws of quantum physics were mainly considered as a curiosity rather than a high priority of experimental physics. This changed in 1994 when Peter Shor discovered an algorithm capable of factoring large numbers much faster than any method known for classical computers [5]. An experimental realization of Shor's factoring algorithm for large composite numbers would render public key encryption systems obsolete, and is therefore of importance to the intelligence agencies. Ironically, quantum mechanics does not only provide an option for eavesdropping but gives a solution for secure communication using *quantum key distribution* schemes [6, 7]. In contrast to the classical encryption techniques, quantum cryptography is not based on unproven assumptions but has shown to be unconditionally secure.

Another example where a universal quantum computer is more powerful than a classical computer is the search algorithm for unsorted databases found by Lov K. Grover [8] in 1996. However, the application that most physicists currently think will be first to surpass a classical computation is the simulation of one quantum system by another. In contrast to other possible applications, here the break-even point concerning the number of qubits needed and the complexity of operations is expected to be much relaxed; in particular if one concentrates on a certain quantum system omitting the high demands needed to achieve universality. For instance, the simulation of certain quantum systems consisting of 50 qubits is intractable with current computing technology. A quantum computer would need only 50 qubits to perform this task.

One of the most relevant findings for realizing a large scale universal quantum computer, was the discovery of *quantum error correction* protocols by Peter Shor [9] and Andrew Steane [10]. These protocols allow the implementation of arbitrary long quantum algorithms with finite errors in the presence of perturbations. Even better, Shor found that analogous to classical information processing there are methods to perform quantum calculations with arbitrarily small errors even if the operations used exhibit small unknown imperfections [11]. This technique called *fault-tolerant quantum computing* requires a significant amount of computational overhead though. To achieve fault-tolerance it is currently expected that the error rates should be smaller than 10^{-2} to 10^{-4} [12, 13, 14] per individual operation.

The harsh requirements for a physical system to realize a universal quantum computer can be summarized as five points, often referred to as the *DiVincenzo criteria* [15]:

1. A scalable physical system with well characterized qubits
2. The ability to initialize the state of the qubits to a simple fiducial state, such as $|0000...\rangle$
3. Long relevant decoherence times, much longer than the gate operation time
4. A "universal" set of quantum gates
5. Qubit-specific measurement capability

In order to create quantum networks and establish quantum communication with quantum computers, two additional demands need to be fulfilled:

6. Ability to interconvert stationary and flying qubits
7. Ability to faithfully transmit flying qubits between specified locations

Besides trapped ions, there have been a number of physical systems under investigation to meet these requirements, including: nuclear spins [16, 17], quantum dots [18, 19], superconducting Josephson junctions [20], photons [21], and neutral trapped atoms [22, 23, 24].

Quantum computing with nuclear spins is most advanced in a sense that the most complex algorithms involving the highest number of qubits were implemented with this technology [25]. However, it is clear that this technology cannot be scaled to several ten or hundreds of qubits without a technology to produce pure states. The implementations based on solid-state devices come with the appealing promise that once we are able to manufacture and control the basic building blocks, scaling up to many qubits seems to be straightforward akin to integrated circuits in classical computing. Great progress has been made in this field over the last decade. Most recently, Bell-states and a controlled-NOT gate were realized with pairs of Josephson junction qubits [26, 27]. But the biggest challenge in the solid-state systems remains to improve the coherence time which is at best on the order of a few microseconds today [28].

The idea to "imprison" charged particles with static electric fields goes back to K. H. Kingdon in 1923 [29]. Frans M. Penning pioneered a trap design based on static electric and magnetic fields in 1936 [30]. In the 1950s radiofrequency ion traps were invented by Wolfgang Paul [31, 32] and in 1980 a single atomic ion was trapped and observed by Neuhauser *et al.* [33] for the first time. Trapping of single ions had a huge impact on the development of atomic physics including laser cooling [34], atomic clocks [35], and mass spectrometry [36]. Today there are about 25 research groups working with single ions in radiofrequency traps.

Long before the application of ion traps for QIP was proposed, three out of the five DiVincenzo criteria had already been demonstrated with trapped ions in the laboratory: initialization [37], readout [38, 39, 40] and long coherence times [41]. Moreover, laser cooled Coulomb crystals with many ions that could serve as a quantum register had been observed [42, 43, 44, 45] and could be interpreted as the first step towards scaling the system with well characterized qubits.

The possibility of implementing QIP with trapped ions was first described in the seminal paper by Ignacio Cirac and Peter Zoller in 1995 [46]. They proposed coupling individual ions of an ion string by their collective motional degree of freedom with a series of laser pulses acting on each of the ions at the time. They also showed that scalability of this approach is possible because the required resources scale as a polynomial rather than an exponential with the number of qubits. In the same year the basic interaction of this two-qubit gate was demonstrated [47], setting the starting point of experimental quantum computing. Since then the field has been exploding and a host of theoretical proposals and experimental demonstrations has pushed to make trapped ions one of the most promising technical architectures for QIP [48].

Some of the most important experimental milestones in this field are the investigation of various universal gate operations [49, 50, 51, 52, 53, 54, 55], the first realization of quantum teleportation with massive particles [56, 57], a quantum error correction protocol [58], the creation of multi-particle entangled states of up to eight ions [59, 60, 61], entanglement purification [62] and the implementation of algorithms such as the Deutsch-Josza algorithm [63] and Grover's search algorithm [64]. Moreover, ions trapped in separate traps [65, 66] have been entangled using ion-photon interaction, a so-called decoherence free subspace [67] was realized. Finally, a nonlinear beam-splitter [68] has been simulated and partial readout of an entangled quantum register was demonstrated [69] as well as a quantum gate and a quantum process tomography [70, 71].

This list attests to the rapid progress that has been achieved to date; but the best prospect for technological applications in the near future is a small-scale quantum computer, designed to carry out a specific task. In contrast to quantum communication and quantum cryptography, where the applications are clear and first products are commercially available, the situation with quantum computing is quite different. Most importantly, even after many years of intense study and research the "killer application" for quantum information is not yet known, making it a field of fundamental research rather than a commercial application.

Today the two most challenging road blocks towards a “quantum computer-science test-bed regime” are: first, to realize an experimental setup that can handle tens or even hundreds of ions; and second, to improve all basic building blocks and operations to enter the regime of fault-tolerant QIP. The first task is pursued in a joint effort by all ion trapping groups, where miniaturization and integration of segmented ion traps is rapidly progressing. It is strongly supported by U.S. funding bodies coordinating different approaches and establishing contacts to microfabrication facilities, such as Lucent Technologies and Sandia National Laboratories.

The second task comes with two major challenges. State initialization, readout and single-qubit gates have been demonstrated with sufficiently high speed and errors of 10^{-2} or less, also coherence times of many seconds have been shown on various systems. Now, these building blocks have to be integrated into a single machine, run at the same time and under the same conditions. The most difficult operation in ion trap quantum computing remains the implementation of an entangling operation. Many schemes have been studied but only two of them were able to produce the desired state with an error rate of less than 10^{-1}. A major result of this thesis is the demonstration of a scheme that allows one to produce Bell states with an error of only 7×10^{-3}.

Quite remarkably, the ion trap community is still undecided on the question of which ion species to choose for QIP. It seems even possible that different ion species could serve different purposes. It is clear that the best storage of quantum information can be achieved with atoms exhibiting a hyperfine structure containing energy levels whose frequency splitting does not depend on small changes of the external magnetic field. Therefore, the best candidates today are $^{9}\mathrm{Be}^{+}$, $^{25}\mathrm{Mg}^{+}$, $^{43}\mathrm{Ca}^{+}$, $^{87}\mathrm{Sr}^{+}$, $^{111}\mathrm{Cd}^{+}$, $^{137}\mathrm{Ba}^{+}$, $^{171}\mathrm{Yb}^{+}$ and $^{199}\mathrm{Hg}^{+}$.

The ion $^{43}\mathrm{Ca}^{+}$ seemed to us particularly attractive for a number of reasons. The Innsbruck ion trapping group has great experience working with $^{40}\mathrm{Ca}^{+}$ for many years. So, the laser technology required to deal with $^{43}\mathrm{Ca}^{+}$ is well known. The wavelengths of calcium ions are such that all lasers and optical elements are commercially available. The hyperfine structure splitting of 3.2 GHz is still within the range that can be bridged by acousto-optical modulators and the ground-state Zeeman levels offer the ability of long quantum information storage times. The presence of lower lying D-states enables high fidelity initialization, readout and the option to also use the metastable states for quantum information processing as with $^{40}\mathrm{Ca}^{+}$ ions.

In this thesis a new experiment is described capable of trapping $^{40}\mathrm{Ca}^{+}$ and $^{43}\mathrm{Ca}^{+}$ ions, in order to explore the possibilities to improve on quantum information storage times and gate fidelities with calcium ions. The main findings are also published in the references [72, 73, 74].

This thesis is structured as follows: chapter 2 reviews the main ideas of quantum information and introduces the notation. It describes the atomic structure of the ^{43}Ca$^+$ and ^{40}Ca$^+$ ions and the relevant interaction of these ions with the applied electromagnetic fields. Chapter 3 describes the new setup that has been built consisting of a vacuum chamber housing the ion trap, nine solid-state laser systems and two PCs with software for control of the experiment. Chapter 4 explains a few basic experiments necessary to characterize the apparatus and the experimental steps required to perform QIP experiments with trapped ions. The chapters 5-7 present the main experimental results of this thesis. In chapter 5 high precision spectroscopy measurements on the $4s\,^2S_{1/2} \leftrightarrow 3d\,^2D_{5/2}$ quadrupole transition are described that were carried out at a wavelength of 729 nm by laser spectroscopy using a single trapped ^{43}Ca$^+$ ion. As a result we obtained the hyperfine structure constants of the $D_{5/2}$-states and the isotope shift of the $4s\,^2S_{1/2} \leftrightarrow 3d\,^2D_{5/2}$ transition with respect to ^{40}Ca$^+$ ions. Chapter 6 describes ground state cooling, robust state initialization and efficient readout of the ^{43}Ca$^+$ hyperfine clock states as qubits. A microwave field and a Raman light field are used to drive qubit transitions, and the coherence times for both fields are compared. Coherence times of more then 1 s have been observed. Chapter 7 details the first implementation of a Mølmer-Sørensen entangling gate on optical qubits. The quantum information is encoded in a $S_{1/2}$ and a metastable $D_{5/2}$-state of ^{40}Ca$^+$. Bell states were created and analyzed with an error as small as 7×10^{-3}. Moreover, we demonstrate the first creation of highly entangled ions in thermal motion with this method. Finally, chapter 8 gives a short summary and outlook to the next possible steps and opportunities.

2 Trapped calcium ions as qubits

This chapter quickly reviews the most basic ideas of quantum computing and introduces some mathematical notation. Further, the calcium energy level structure is described including shifts of the energy levels caused by external magnetic fields. Then a number of options for encoding quantum information in calcium ions are discussed. In case of trapped ions, quantum information is encoded, processed and read out by applying electromagnetic fields to the quantum system. Two energy splittings are of importance: the optical domain with a wavelength of 729 nm and the microwave domain with a frequency of 3.2 GHz. For both cases the possible electromagnetic field interactions with the ions are detailed.

2.1 Quantum bits

In this section a brief summary of quantum computing and its mathematical description is given. It is strongly inspired by reference [75] which gives an excellent introduction to the field and points the reader to numerous references for further reading.

Single qubits

Quantum computing requires quantum information to be stored and manipulated in real physical systems. To get an idea how this can be achieved, let us have a quick look on the classical case: In classical computing information is often stored in the magnetization (up or down) of a certain material. Processing is done with highly integrated electrical circuit elements like transistors that can be either conducting or non-conducting depending on the state of other circuit elements. Typically, each element is in either of only two states, logically expressed as 0 and 1. Similar, to store quantum information, one needs at least two quantum states, here labeled $|0\rangle$ and $|1\rangle$. The main difference from the classical case is that the system can take on not only either of the states but also all linear combinations

$$|\psi\rangle = \alpha|0\rangle + \beta|1\rangle, \tag{2.1}$$

where α and β are complex numbers. In analogy to the classical case, such two-level quantum systems capable of storing quantum information are termed *quantum bits* or

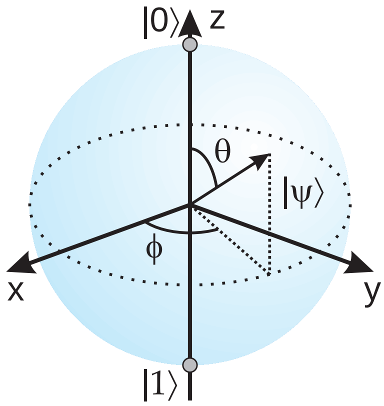

Figure 2.1: Bloch sphere representation of a qubit state.

qubits. However, we cannot directly measure α and β with a single shot. Instead, each measurement finds $|0\rangle$ with a probability $|\alpha|^2$ or the state $|1\rangle$ with a probability $|\beta|^2$. As the probabilities have to sum up to 1 ($|\alpha|^2 + |\beta|^2 = 1$), it is convenient to rewrite Eq. (2.1) as

$$|\psi\rangle = e^{i\gamma}\left(\cos\frac{\theta}{2}|0\rangle + e^{i\phi}\sin\frac{\theta}{2}|1\rangle\right), \tag{2.2}$$

where θ, ϕ and γ are real numbers and the latter can be set to zero, since it has no observable effect. Equation 2.2 allows us to visualize the qubit state $|\psi\rangle$ by interpreting θ and ϕ as polar coordinates of the so called *Bloch vector*. The available space for this unit vector is the surface of a sphere usually referred to as *Bloch sphere*. An example is depicted in Fig. 2.1. Unfortunately, this intuition is limited because there is no simple generalization of the Bloch sphere known for multiple qubits.

Multiple qubits

For N qubits, one possible set of basis states is given by the 2^N product states of the individual qubit states $|0\rangle$ and $|1\rangle$. Basis states are labeled

$$|n\rangle = |i_N\rangle \otimes .. \otimes |i_2\rangle \otimes |i_1\rangle,$$

where $i_k \in \{0,1\}$ and $n = \sum_{k=1}^{N} i_k\, 2^{k-1}$. The vectors $|n\rangle$ form the *computational basis* in which every N qubit quantum state can be represented as

$$|\psi\rangle = \sum_{k=0}^{2^{N-1}} \alpha_k |k\rangle$$

with state amplitudes α_k, satisfying the normalization condition $\sum_{k=0}^{2^{N-1}} |\alpha_k|^2$. Already for a few hundred qubits we end up with such a huge number of state amplitudes α_k, that no classical computer will be able to store, let alone process, them.

To give an example, any arbitrary two-qubit state can be described by

$$|\psi\rangle = \alpha_0|00\rangle + \alpha_1|01\rangle + \alpha_2|10\rangle + \alpha_3|11\rangle,$$

where the coefficients α_k again fulfill the condition $\sum_{k=0}^{3} |\alpha_k|^2$.

Measurements

An important prerequisite for quantum computation is the ability to make measurements on the system. For trapped ions we conveniently make use of an auxiliary state that is strongly coupled by a dipole transition to one of the qubit levels. By scattering light on this transition the ions' internal state is projected (i.e. von Neumann measurements) into a particular internal energy state where it either scatters light or not[1]. As a consequence, to obtain an observable M every measurement process causes an irreversible collapse of the quantum system onto one of the eigenstates of the measurement operator $\hat{M}$ with eigenvalues m. With the corresponding projector P_m this reads

$$\hat{M} = \sum_m m\, P_m.$$

The probability to obtain a certain output m is given by

$$p(m) = \langle\psi|P_m\,|\psi\rangle,$$

where after the projection the system is left in the well defined state

$$|\check{\psi}\rangle = \frac{P_m|\psi\rangle}{\sqrt{p(m)}}.$$

Typically, a natural measurement basis is given by the structure of the physical system in which the qubits are encoded. For trapped ions this is strongly related to the energy level structure of the ions used. A change of the measurement basis can be achieved though by changing the reference frame with appropriate single and two-qubit rotations prior to the actual projection. One example where this was realized is the measurement with respect to a basis of entangled states in the quantum teleportation experiment described in reference [56].

[1] This can be also understood as a quantum non-demolition measurement since a large number of photons can be scattered without further perturbing the measurement result.

Entanglement

An important example for a two-qubit state is the *Bell state*[2] or *EPR pair*[3],

$$|\Psi\rangle = \frac{|00\rangle + |11\rangle}{\sqrt{2}}.$$

Measuring the first qubit state results in two possible outcomes: in fifty percent of the cases we measure 0 leaving the post measurement state in $|00\rangle$ in the other half of the cases we obtain 1 leaving $|11\rangle$. So, a measurement of the second qubit gives always the same result as the measurement of the first. We say the measurement outcomes are *correlated*. Furthermore, it is not possible to decompose $|\Psi\rangle$ into a product of any two states $|a\rangle$ and $|b\rangle$. To generalize this property:

> Any multi-qubit state that cannot be written as a product of states of its component systems is called an *entangled state*, all others are termed *separable* or *product states*.

Many experiments have shown that it is not possible to explain entanglement by a classical model and is a purely quantum mechanical phenomenon. The peculiar behavior resulting from the existence of entanglement is nicely described by N. D. Mermin in reference [77], which is addressed to the general reader. Today, entanglement is considered as a physical resource, like energy, that can be measured, transformed and purified. The entanglement of two remote quantum systems can be utilized as a quantum channel in order to exchange quantum information between two sites that are connected only by a classical channel. This is the basic idea of quantum teleportation and other computational and cryptographic tasks. An open question in this context still is how strongly the few quantum algorithms known today that are in principle able to outperform classical computing (i.e. Shor's factorization algorithm [5] and Grover's database search algorithm [8]) rely on quantum entanglement.

Quantum gates

The quantum circuit model is a bottom up approach to describe changes of a multi-qubit system. In analogy to classical computers, quantum circuits consist of wires (where quantum and classical information is carried around in the system), a set of elementary quantum gates to manipulate the quantum information and measurements with classical information as outcomes that can be further processed and fed back. A sketch of a simple quantum circuit is given in Fig. 8.1 (b).

[2]named after John Stewart Bell
[3]named after Einstein, Podolsky and Rosen [76]

In theory, the simplest operation is the identity, where the state of the system is left unchanged; this implies that the quantum system neither interacts with the environment, nor that unwanted interactions within the system occur. This sets already high demands for physical realizations where the suppression of *decoherence* is a major task. A prominent example for unwanted interactions within the system is NMR quantum computing where considerable efforts (still polynomial though) are spent on the cancelation of permanent interactions between the nuclear spins and so achieve the identity operation.

Interactions with the quantum system that affect only one of the qubits are called *single-qubit operations*. They have to act linearly and preserve the normalization condition. As a consequence, in the Bloch-sphere representation any single-qubit operation corresponds to a rotation by certain angle around a real unit vector. Mathematically this is conveniently described in terms of unitary matrices as for example the Pauli spin matrices

$$\hat{I} = \begin{bmatrix} 1 & 0 \\ 0 & 1 \end{bmatrix}, \ \sigma_x = \begin{bmatrix} 0 & 1 \\ 1 & 0 \end{bmatrix}, \ \sigma_y = \begin{bmatrix} 0 & -i \\ i & 0 \end{bmatrix} \text{and } \sigma_z = \begin{bmatrix} 1 & 0 \\ 0 & -1 \end{bmatrix}. \tag{2.3}$$

Euler's rotation theorem implies that any arbitrary single-qubit operation can be achieved by a concatenation of at most three rotations around two linear independent axis. The general rotations around x- and the y-axis represented in matrix notation as

$$R_x(\gamma) = e^{-i\frac{\gamma}{2}\sigma_x} = \begin{bmatrix} \cos\frac{\gamma}{2} & -i\sin\frac{\gamma}{2} \\ -i\sin\frac{\gamma}{2} & \cos\frac{\gamma}{2} \end{bmatrix}, \tag{2.4}$$

$$R_y(\beta) = e^{-i\frac{\beta}{2}\sigma_y} = \begin{bmatrix} \cos\frac{\beta}{2} & -\sin\frac{\beta}{2} \\ \sin\frac{\beta}{2} & \cos\frac{\beta}{2} \end{bmatrix}, \tag{2.5}$$

shall serve as an example. If we have an arbitrary single-qubit operation available for each individual qubit, we require only one type of multi-qubit gate in order to construct all arbitrary operations, in particular all other multi-qubit gates. Multi-qubit gates with this property are termed *universal gates*. A prominent example for a universal two-qubit gate is the *controlled-NOT* or *CNOT* gate. One of the two input qubits is known as the *control qubit* and is left unchanged by the operation. The other qubit is called *target qubit* and is flipped depending on the state of the control qubit. The matrix representation of a CNOT gate is

$$U_{\text{CNOT}} = \begin{bmatrix} 1 & 0 & 0 & 0 \\ 0 & 1 & 0 & 0 \\ 0 & 0 & 0 & 1 \\ 0 & 0 & 1 & 0 \end{bmatrix}, \tag{2.6}$$

where the matrix is notated with respect to the basis order $\{|00\rangle, |01\rangle, |10\rangle, |11\rangle\}$. As for single-qubit gates, multi-qubit gates have to preserve a total measurement probability of one, formally expressed by the fact that they are described by unitary matrices with $U_{gate}^{\dagger} U_{gate} = \hat{I}$.

There are many other types of universal quantum gates available. An example is the Mølmer-Sørensen-gate [78, 79], which was experimentally implemented in the framework of this thesis to create entangled states. Its matrix representation is

$$U_{\mathrm{MS}} = \frac{1-i}{2} \begin{bmatrix} 1 & 0 & 0 & i \\ 0 & 1 & -i & 0 \\ 0 & -i & 1 & 0 \\ i & 0 & 0 & 1 \end{bmatrix} \tag{2.7}$$

and introduces population changes of both qubit states simultaneously. The details of the experimental implementation and the underlying theory are given in chapter 7.

With a certain universal set of quantum gates and projective measurements available, all other complex computations are constructed by concatenation of these basic building blocks.

2.2 Atomic structure

Two different calcium isotopes were used for quantum information processing in this thesis: $^{40}\mathrm{Ca}^{+}$ and $^{43}\mathrm{Ca}^{+}$. This section describes the level structure of both isotopes and their energy level shifts in external magnetic fields. Various ways to encode quantum information are discussed. Since $^{43}\mathrm{Ca}^{+}$ is very similar to neutral cesium atoms, large parts of this section are directly taken from reference [80] and adapted to calcium.

Gross structure and wavelengths

Single charged alkali earth ions like Ca^{+} have a single valence electron and therefore an energy level structure similar to neutral alkali atoms, in particular the hydrogen atom. The energy level scheme showing the three lowest orbitals available to the valence electron of a single $^{40}\mathrm{Ca}^{+}$ ion is given by Fig. 2.2.

Calcium ions have a gross structure with a ground-state S-orbital. The lowest excited state is the D-orbital, which is metastable with a radiative live time of 1.17 s [81] corresponding to a line width of 0.14 Hz. The $S_{1/2} \leftrightarrow D_{5/2}$ transition is accessible via an electric quadrupole radiation at 729 nm.

The second lowest excited state is a P-orbital with a radiative lifetime of 7 ns [82]. $P_{1/2}$ is accessible from the ground-state by electric dipole radiation at 397 nm. This transition

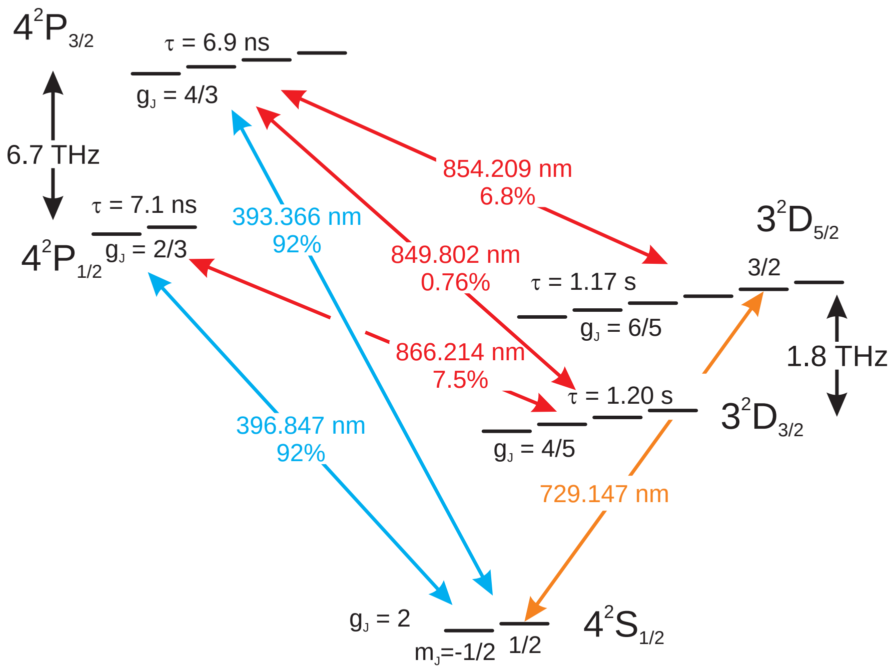

Figure 2.2: Detailed energy level scheme showing all Zeeman sublevels of the three lowest orbitals of a $^{40}Ca^+$ ion. Laser light at 397 nm is used for Doppler-cooling, optical pumping and detection, the lasers at 866 nm and 854 nm pump out the D-states. An ultra-stable laser at 729 nm is used for spectroscopy on the quadrupole transition, state preparation, optical shelving and ground-state cooling. For the experiments described in chapter 7 the states $S_{1/2}(\mathrm{m}_J{=}1/2)$ and $D_{5/2}(\mathrm{m}_J{=}3/2)$ are chosen to form an optical qubit. The wavelengths in air, natural lifetimes τ and the branching ratios given are taken from references [82, 83, 81], the Landé factors g_J result from Eq. (2.9).

has a line width of 21 MHz. The P-levels exhibit a *branching ratio* such that one out of 13 decays populates the D-levels. Therefore, the dipole transitions connecting the P and the D-levels at wavelengths of 866 nm and 854 nm are of importance to clear out the D-states.

Fine and hyperfine structure splitting

Due to coupling between the orbital angular momentum $\boldsymbol{L}$ of the outer electron and its spin angular momentum $\boldsymbol{S}$ calcium ions exhibit a fine structure splitting with a total angular momentum $\boldsymbol{J} = \boldsymbol{L} + \boldsymbol{S}$. The corresponding quantum number J lies in the range $|L - S| \leq J \leq L + S$ where the magnitude of $\boldsymbol{J}$ is $\sqrt{J(J+1)}\hbar$ and the eigenvalue of J_z is $m_J\hbar$.

For the calcium ground-state ($4^2S_{1/2}$), $L = 0$ and $S = 1/2$, so $J = 1/2$ and for the lowest excited state ($3^2\mathrm{D}_{3/2}$ and $3^2\mathrm{D}_{5/2}$) $L = 2$ and $S = 1/2$, so $J = 3/2$ or $J = 5/2$; similar for the second lowest excited state ($4^2P_{1/2}$ and $4^2P_{3/2}$) we have $L = 1$ and $S = 1/2$, so $J = 1/2$ or $J = 3/2$. The meaning of the spectroscopic notation is as follows: the

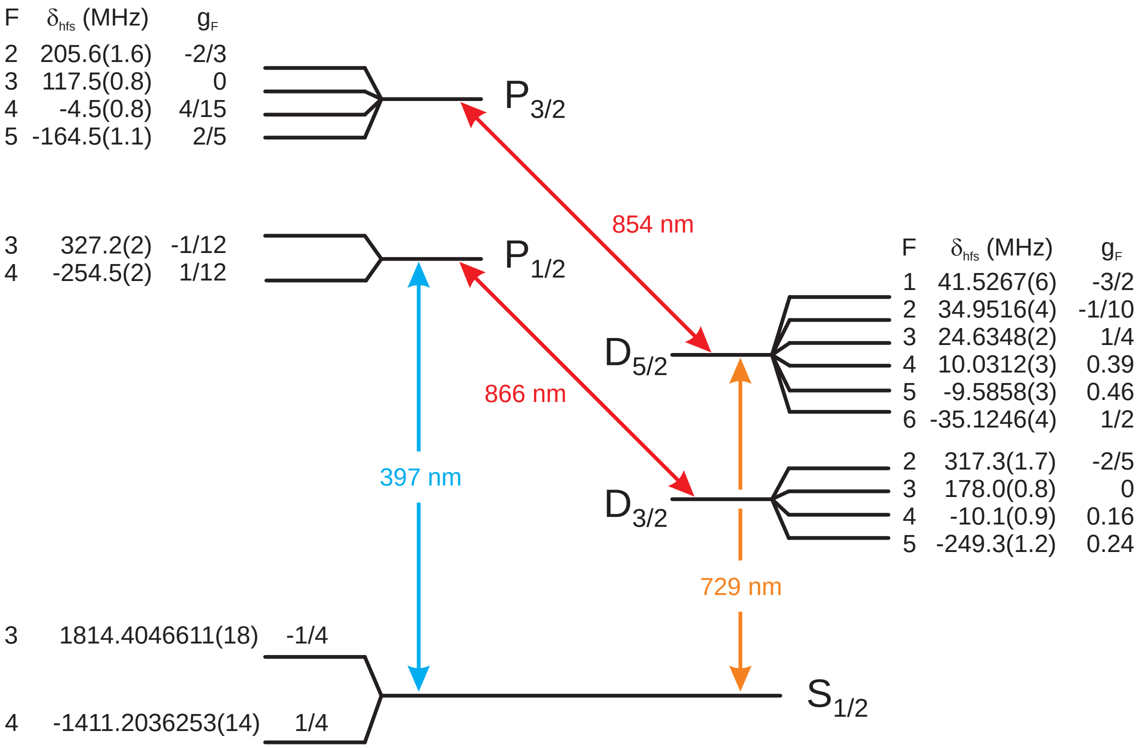

Figure 2.3: ^{43}Ca$^+$ level scheme showing the hyperfine splitting of the lowest energy levels. Hyperfine shifts δ_{hfs} of the levels are quoted in MHz (the splittings are taken from [84, 85] and section 5.1). Laser light at 397 nm is used for Doppler-cooling, optical pumping and detection, the lasers at 866 nm and 854 nm pump out the D-states. An ultra-stable laser at 729 nm is used for spectroscopy on the quadrupole transition, state preparation, optical shelving and ground-state cooling. The Landé factors g_F follow from Eq. (2.10).

first number gives the principal quantum number of the outer electron, the superscript is $2S+1$, the letter refers to L (i.e., $S \leftrightarrow L=0, P \leftrightarrow L=1, D \leftrightarrow L=2$, etc.) and the last subscript gives the value of J.

In case of ^{40}Ca$^+$, the total nuclear angular momentum $\boldsymbol{I}$ is zero such that each fine structure level splits into $2J+1$ Zeeman substates labeled by the magnetic quantum number $-J \leq m_J \leq J$ (see Fig. 2.2). When no external fields are present, these Zeeman states are degenerate (i.e. they have the same energy).

The isotope ^{43}Ca$^+$ is the only stable calcium isotope with non-zero nuclear spin (see Tab. A.2). It has a total nuclear angular momentum $I = 7/2\,\hbar$. The coupling between total electronic angular momentum $\boldsymbol{J}$ and $\boldsymbol{I}$, to give a total atomic angular momentum $\boldsymbol{F}=\boldsymbol{J}+\boldsymbol{I}$, results in a hyperfine structure. The corresponding quantum number F can take on the values $|J-I| \leq F \leq J+I$. For the ground-state of ^{43}Ca$^+$ ($J=1/2$ and $I=7/2$) this gives rise to two hyperfine states with $F=3$ and $F=4$. The relevant energy levels are shown in Fig. 2.3.

Compared to the energy shift due to the fine structure splitting which is as large as 6.7 THz for the P-states and 1.8 THz for the D-states, the hyperfine energy splittings are much smaller and it is useful to have a formalism describing these shifts.

The Hamiltonian describing the relevant spin-spin interactions is

$$H_{\text{hfs}} = A_{\text{hfs}}\mathbf{I}\cdot\mathbf{J} + B_{\text{hfs}}\frac{3(\mathbf{I}\cdot\mathbf{J})^2 + \frac{3}{2}(\mathbf{I}\cdot\mathbf{J}) - I(I+1)J(J+1)}{2I(2I-1)J(2J-1)},$$

leading to a hyperfine energy shift of

$$\Delta E_{\text{hfs}} = \frac{1}{2}A_{\text{hfs}}K + B_{\text{hfs}}\frac{\frac{3}{2}K(K+1) - 2I(I+1)2J(J+1)}{2I(2I-1)J(2J-1)},$$

where

$$K = F(F+1) - I(I+1) - J(J+1),$$

A_{hfs} is the magnetic dipole constant, and B_{hfs} is the electric quadrupole constant (the latter term does not apply to levels with $J = 1/2$). The hyperfine splitting of the $S_{1/2}$ ground-state was measured to a high precision by Arbes *et al.* [84] with a laser microwave double resonance experiment in which $^{43}Ca^+$ ions were stored in a Paul trap. They found the value for the hyperfine splitting of the ground states to be

$$\omega_{S_{1/2}}/(2\pi) = 3\,225\,608\,286.4(3)\,\text{Hz}$$

corresponding to magnetic dipole constant $A_{S_{1/2}} = -806.402\,071\,60(8)\,\text{MHz}$. The values for the other energy levels are given in Tab. A.5 and Fig. 2.3.

Interaction with static magnetic fields

Each of the hyperfine energy levels (F) contains $2F+1$ magnetic sublevels that determine the angular distribution of the electronic wavefunction and are labeled m_F. In the absence of external magnetic fields, these sublevels are degenerate. The Hamiltonian describing the lifting of this degeneracy due to the interaction with an external magnetic field $\boldsymbol{B} = B\boldsymbol{e}_z$ (assumed to be in z-direction) is given by

$$\begin{aligned} H_B &= \frac{\mu_B}{\hbar}\left(g_S\boldsymbol{S} + g_L\boldsymbol{L} + g_I\boldsymbol{I}\right)\cdot\boldsymbol{B} \\ &= \frac{\mu_B}{\hbar}\left(g_S S_z + g_L L_z + g_I I_z\right)B_z, \end{aligned}$$

where g_S, g_L and g_I are the electron spin, electron orbital and the nuclear *g-factors* that account for various modifications to the corresponding magnetic dipole moments. The value for g_S has been measured very precisely by Tommaseo *et al.* [86] to be $g_S = 2.002\,256\,64(9)$. The value of g_L can be approximated as $g_L = 1 - \frac{m_e}{m_{nuc}} \simeq 1$, which is correct to lowest order in m_e/m_{nuc}, where m_e is the electron mass and m_{nuc} the mass of the atomic nucleus. The nuclear factor g_I accounts for the entire complex structure of the nucleus, and has been measured to be $2.050\,32(1) \times 10^{-4}$ [87]. If the energy shift due to the magnetic field is small compared to the fine structure splitting, then J is a good quantum number and the interaction Hamiltonian can be written as

$$H_B = \frac{\mu_B}{\hbar}\left(g_J J_z + g_I I_z\right) B_z. \tag{2.8}$$

Here, the *Landé factor* g_J is given by

$$\begin{aligned} g_J &= g_L \frac{J(J+1) - S(S+1) + L(L+1)}{2J(J+1)} + g_S \frac{J(J+1) + S(S+1) - L(L+1)}{2J(J+1)} \\ &\simeq 1 + \frac{J(J+1) + S(S+1) - L(L+1)}{2J(J+1)}, \end{aligned} \tag{2.9}$$

where the second term is an approximation assuming $g_S \simeq 2$ and $g_L \simeq 1$. This expression does not include corrections due to the complicated multielectron structure of Ca^+ and QED effects.

If the energy shift due to magnetic field is small compared to the hyperfine splittings, then similarly F is a good quantum number and the interaction Hamiltonian becomes

$$H_B = \mu_B g_F F_z B_z,$$

where the hyperfine Landé g-factor g_F is given by

$$\begin{aligned} g_F &= g_J \frac{F(F+1) - I(I+1) + J(J+1)}{2F(F+1)} + g_I \frac{F(F+1) + I(I+1) - J(J+1)}{2F(F+1)} \\ &\simeq g_J \frac{F(F+1) - I(I+1) + J(J+1)}{2F(F+1)}. \end{aligned} \tag{2.10}$$

The approximate expression neglects the nuclear term which leads to errors at the level of 0.1%, because g_I is much smaller than g_J.

For weak magnetic fields, the interaction Hamiltonian H_B perturbs the zero-field eigenstates of H_{hfs}. To lowest order, the energy of the levels shifts linearly according to

$$E_{|F,m_F\rangle} = \mu_B g_F m_F B_z. \tag{2.11}$$

The splitting in this regime is called the *anomalous Zeeman effect*. For stronger magnetic fields the interaction term dominates the hyperfine energy and Eq. (2.8) gives the appropriate description. The resulting energies are then given to lowest order by

$$\begin{aligned}E_{|J,m_J,I,m_I\rangle} = & A_{\text{hfs}} m_J m_I + \\ & + B_{\text{hfs}} \frac{3(m_J m_I)^2 + \frac{3}{2} m_J m_I - I(I+1)J(J+1)}{2J(2J-1)I(2I-1)} + \\ & + \mu_B (g_J m_J + g_I m_I) B_z.\end{aligned}$$

The energy splitting in this regime is called the *Paschen-Back effect*.

For most cases there exists no handy approximation for intermediate fields, so one must numerically diagonalize

$$H_{\text{tot}} = H_{\text{hfs}} + H_B. \tag{2.12}$$

One exception are the *stretched states*, defined by $m_F = \pm(I+J)$ which are eigenstates of the Hamiltonian (2.12). Their energy changes linearly with the magnetic field as

$$E_{|J=1/2,m_J,I,m_I\rangle} = \Delta E_{\text{hfs}} \frac{I}{2I+1} \pm \frac{1}{2}(g_J + 2g_I I)\mu_B B. \tag{2.13}$$

Another notable exception is the *Breit-Rabi formula* [88], which applies to the $S_{1/2}$ ground-state manifold:

$$E_{|J=1/2,m_J,I,m_I\rangle} = -\frac{\Delta E_{\text{hfs}}}{2(2I+1)} + g_I \mu_B (m_I \pm \frac{1}{2}) B \pm \frac{\Delta E_{\text{hfs}}}{2} \left(1 + \frac{4(m_I \pm \frac{1}{2})x}{2I+1} + x^2 \right)^{1/2} \tag{2.14}$$

with the hyperfine splitting $\Delta E_{\text{hfs}} = A_{\text{hfs}}(I + 1/2)$ and $x = (g_J - g_I)\mu_B B / \Delta E_{\text{hfs}}$. Equation 2.13 can help to avoid sign ambiguity in evaluating Eq. (2.14). Figure 2.4 shows the resulting energy dependence of the $^{43}Ca^+$ $4S_{1/2}$ ground level hyperfine structure for magnetic fields up to 200 G.

When it comes to choosing two of the energy levels as a qubit, the sensitivity to external magnetic field fluctuations is of major importance. In previous experiments with $^{40}Ca^+$ ions the quantum information was stored in one of the ground-state levels $S_{1/2}(m_J = \pm 1/2)$ and one of the metastable $D_{5/2}(m_J = \pm 1/2, \pm 3/2, \pm 5/2)$ states. Since the energy difference between the qubit states lies in the optical domain, this type of encoding is also termed *optical qubit*. Similar to Eq. (2.11) we obtain a differential splitting of the qubit states

$$\Delta E_{S \leftrightarrow D} = \mu_B (m_S g_{S_{1/2}} - m_D g_{D_{5/2}}) B_z.$$

with a Landé g-factor $g_{D_{5/2}} \simeq 1.2$. In the best case the lowest sensitivity one could get with respect to changes of the magnetic field is 560 kHz/G. A fundamental limitation of this optical qubit is of course the finite lifetime of the metastable state. If we choose two ground-state Zeeman levels instead, the spontaneous decay problems are avoided at the price that sensitivity to external magnetic field fluctuations worsens to 2.8 MHz/G.

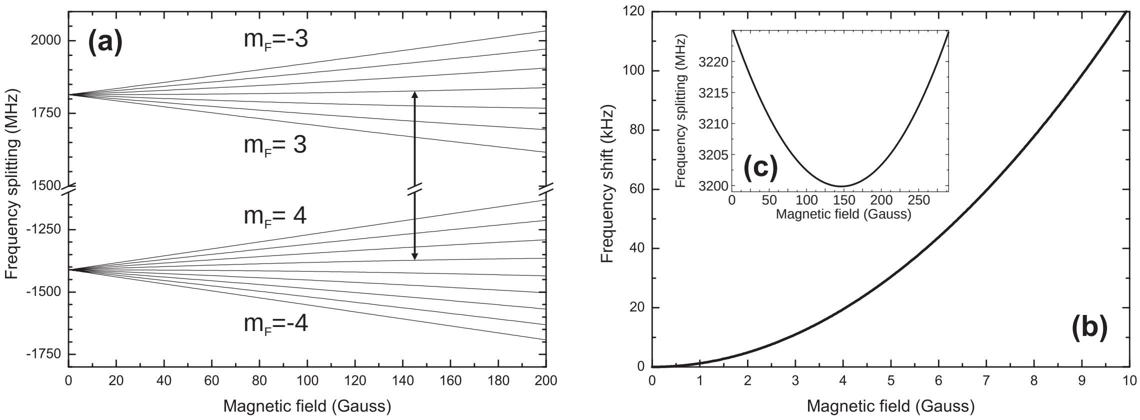

Figure 2.4: **(a)** $^{43}\mathrm{Ca}^+$ $4S_{1/2}$ ground level hyperfine structure in a low external magnetic field (anomalous Zeeman regime). **(b)** The two microwave clock states $S_{1/2}(F=4, m_F=0)$ and $S_{1/2}(F=3, m_F=0)$ exhibit only a second order Zeeman shift. The sensitivity to external magnetic field fluctuations is given by the parabola's slope of $2.4\,\mathrm{kHz/G}^2 \times B$. For a magnetic field of 150 G the transition between the states $S_{1/2}(F=4, m_F=1)$ and $S_{1/2}(F=3, m_F=0)$ gets also field independent to the first order. The inset **(c)** shows the energy splitting for this transition as a function of the magnetic field. The slope of the parabola is the same as for the clock states.

For stability under magnetic field fluctuations, $^{43}\mathrm{Ca}^+$ offers an important advantage. From the Breit-Rabi formula (2.14) we directly obtain that the two $m_F = 0$ sublevels of the two hyperfine ground states exhibit no first-order Zeeman shift. This property is also useful when building a clock, hence they are often called *clock states*. The differential shift of these two states is given by

$$\Delta\omega_{0\leftrightarrow 0} = \frac{(g_J - g_I)^2 \mu_B^2}{2\hbar\Delta E_{\mathrm{hfs}}} B^2 \simeq 2\pi \times 1.2\,\mathrm{kHz/G}^2 \times B^2$$

in a second order approximation of the magnetic field strength. The linear dependence vanishes completely only for zero fields and increases then linearly with 2.4 kHz/G. Due to the degeneracy of the magnetic sub-levels at zero field they cannot be resolved spectrally. Still, for a magnetic field of 1 G the sensitivity is suppressed by more than a factor 230 compared to the optical qubit in $^{40}\mathrm{Ca}^+$.

It is also possible to find field-independent transitions in the ground-state manifold for a non-zero field. The one occurring for the lowest magnetic field is at 150 G between the states $S_{1/2}(F=4, m_F=1)$ and $S_{1/2}(F=3, m_F=0)$. The second order approximation for the frequency change around this point is the same as for the clock states. For both cases the change in transition frequency is plotted over the magnetic field in Fig. 2.4 (b).

2.3 Single ion coherent operation

The standard circuit model of quantum computing requires a set of universal quantum logic gates for the implementation of arbitrary quantum operations. An example is a two-qubit entangling operation in combination with arbitrary single-qubit gates. This section details atom-field interactions in order to perform single-qubit operations on optical and hyperfine encoded qubits in $^{43}Ca^{+}$ ions by means of microwave and laser radiation. A two-qubit entangling operation is discussed in chapter 7.

2.3.1 Single-qubit rotation

Any two-level quantum system can be considered as a qubit. For the mathematical treatment it is convenient to exploit the analogy to a particle with a spin of 1/2. We assign the label $|\downarrow\rangle(|\uparrow\rangle)$ to the lower (upper) energy level describing a pseudo-spin. For trapped ion based quantum bits the frequency difference between the two qubit levels can range from a couple of kHz (i.e. for two neighboring Zeeman levels) to the optical frequency domain which is hundreds of THz. The further discussion is restricted to the interaction of a single ion with these two internal energy levels plus one harmonic oscillator mode that models the external motion of the ion in the trapping potential. The Hamiltonian in the absence of interaction with further electromagnetic fields is then given by

$$H_0 = \frac{1}{2}\hbar\omega_0\sigma_z + \hbar\omega_z\left(a^\dagger a + \frac{1}{2}\right)$$

where $\hbar\omega_0$ denotes for the energy splitting of the qubit levels. Moreover, σ_z is the Pauli spin matrix, the energy splitting of the harmonic oscillator level is $\hbar\omega_z$ and the creation (annihilation) operators for this mode is denoted $a^\dagger$ (a). The state vector of the system can be expressed as

$$|\Psi(t)\rangle = \sum_{n=1}^{\infty}\left(a_{\uparrow,n}(t)|\uparrow\rangle + a_{\downarrow,n}(t)|\downarrow\rangle\right)|n\rangle$$

with the harmonic oscillators eigenstates $|n\rangle$ of energy $n\hbar\omega_z$. For the moment we assume that single photon transitions between the two qubit levels can be achieved through an electric dipole coupling. The interaction between the applied electromagnetic field $\boldsymbol{E}$ and the qubit levels is described by the Hamiltonian

$$H_I(t) = -\boldsymbol{d}\cdot\boldsymbol{E} = -\boldsymbol{d}\cdot\boldsymbol{\varepsilon}\,E_0\cos(-\omega_l\,t + k\,\tilde{z} + \phi), \tag{2.15}$$

where $\boldsymbol{d}$ denotes the dipole operator. The field has a frequency ω_l, an amplitude E_0 at the ion's position and a polarization $\boldsymbol{\varepsilon}$. The propagation direction of the field, represented by the vector $\boldsymbol{k}$, is assumed along the trap axis in z-direction parallel to the harmonic oscillator mode. $\tilde{z}$ is the ions displacement from the equilibrium position and ϕ denotes an offset phase of the field. The dipole operator is proportional to $\sigma^+ + \sigma^-$ where $\sigma^+ \equiv |{\uparrow}\rangle\langle{\downarrow}|$ and $\sigma^- \equiv |{\downarrow}\rangle\langle{\uparrow}|$. With the creation and annihilation operators, Eq. (2.15) becomes after a rotating wave approximation

$$H_I = \hbar\Omega \left(e^{i\eta(a+a^\dagger)}\sigma^+ e^{-i(\omega_l t+\phi)} + e^{-i\eta(a+a^\dagger)}\sigma^- e^{i(\omega_l t+\phi)} \right), \tag{2.16}$$

where the coupling strength is given by Ω, also referred to as *Rabi frequency*. Equation (2.16) contains all details about the exact interaction of the applied field and the ion. Moreover, the *Lamb-Dicke parameter* is defined as $\eta \equiv kz_0 = \boldsymbol{k}\cdot\boldsymbol{e}_z\sqrt{\frac{\hbar}{2M\omega_z}}$ and describes the ability of the field to couple to the harmonic oscillator mode along z-direction where M denotes the mass of the ion. It relates the spread z_0 of the ion's wave function to the wave vector k of the applied field. In the Lamb-Dicke limit defined by $\eta^2(2n+1) \ll 1$ the extension of the ion's wave function z_0 is much smaller than the applied wavelength. From Eq. (2.16) we then obtain in the interaction frame

$$H_I = \hbar(\Omega e^{i\phi})\sigma^+ e^{-i(\omega_l-\omega_0)t} \left(1 + i\eta(ae^{-i\omega_z t} + a^\dagger e^{i\omega_z t})\right) + h.c. \tag{2.17}$$

where higher order sidebands were omitted.

2.3.2 Coupling internal and external degrees of freedom

A coupling of the external field to the motion is required for laser cooling and conditional two-qubit operations. For $\eta > 0$ the evaluation of Hamiltonian (2.17) is considered in the resolved sideband limit with $\Omega \ll \omega_0$. Regarding the frequency ω_l of the applied field, H_I exhibits three spectral components where the coupling strength $\Omega_{n,n'}$ of the transition $|{\downarrow}\rangle|n\rangle \leftrightarrow |{\uparrow}\rangle|n'\rangle$ depends on the population of the harmonic oscillator mode n (n') of the involved states:

1. For $\omega_l = \omega_0$ no coupling to the motion is achieved and $\Delta n = 0$. The coupling strength for these *carrier transitions* is approximately given by $\Omega_{n,n} = \Omega(1-\eta^2 n)$ and the interaction Hamiltonian is given by $H_I^{(c)} = \hbar\Omega e^{i\phi}\sigma^+ + h.c.$
2. For $\omega_l = \omega_0 - \omega_z$ each transition $|{\downarrow}\rangle \rightarrow |{\uparrow}\rangle$ is accompanied by a decrease in the population of the harmonic oscillator ($|n\rangle \rightarrow |n-1\rangle$). The coupling strength for these *red sideband transitions* is approximately given by $\Omega_{n,n-1} = \eta\sqrt{n}\Omega$ and the interaction Hamiltonian is given by $H_I^{(rsb)} = \hbar\Omega_{n,n-1}\, a\, e^{i\phi}\sigma^+ + h.c.$
3. For $\omega_l = \omega_0 + \omega_z$ each transition $|{\downarrow}\rangle \rightarrow |{\uparrow}\rangle$ is accompanied by an increase in the population of the harmonic oscillator ($|n\rangle \rightarrow |n+1\rangle$). The coupling strength for these *blue sideband transitions* is approximately given by $\Omega_{n,n+1} = \eta\sqrt{n+1}\Omega$ and the interaction Hamiltonian is given by $H_I^{(bsb)} = \hbar\Omega_{n,n+1}\, a^\dagger\, e^{i\phi}\sigma^+ + h.c.$

Red sideband transitions can be exploited in order to cool the ions by reducing the population of the harmonic oscillator. Carrier transitions are of particular importance since they are used for single-qubit spin rotations and state transfers. For the further discussion we neglect the coupling to the motion by setting the Lamb-Dicke parameter to zero (e.g. $\boldsymbol{k} \perp \boldsymbol{e}_z$). Then the Hamiltonian (2.17) further simplifies to

$$H_I = \hbar\Omega \left(\sigma^+ e^{-i(\delta\omega\, t+\phi)} + \sigma^- e^{i(\delta\omega\, t+\phi)} \right),$$

with the detuning $\delta\omega = \omega_l - \omega_0$ of the field from the qubit resonance. The solution to this problem is given by

$$\begin{aligned} \dot{c}_\uparrow &= -i\Omega e^{-i(\delta\omega\, t+\phi)} c_\downarrow \\ \dot{c}_\downarrow &= -i\Omega e^{i(\delta\omega\, t+\phi)} c_\uparrow, \end{aligned}$$

where $c_m(t)$ are the amplitudes of the spin states $|\uparrow\rangle$ and $|\downarrow\rangle$. In case of a resonant interaction ($\delta\omega = 0$) the time evolution of the quantum state can be expressed in the energy basis by $|\psi(t)\rangle = \hat{U}(t)|\psi(0)\rangle$, where

$$\hat{U}(t) = \begin{pmatrix} \cos(\Omega t) & -ie^{-i\phi}\sin\Omega t \\ -ie^{i\phi}\sin\Omega t & \cos\Omega t \end{pmatrix} = R(\theta,\phi).$$

With this interaction at hand, arbitrary single-qubit rotations can be carried out as visualized in the Bloch sphere picture in Fig. 2.1. The direction of the rotation axis is given by $\cos(\phi)\boldsymbol{e}_x + \sin(\phi)\boldsymbol{e}_y$ and lies within the equatorial plane. When the field is applied for the first time, ϕ can be set to zero. For all subsequent pulses the axis of rotation is then referenced to the first pulse by means of the relative phase of the external field. If we set for instance $\phi = \pi$ we directly realize the single-qubit rotations around the y-axis as described by Eq. (2.5). The rotation angle θ is then given by the interaction strength Ω and the duration t of the interaction.

The next three sections discuss the coupling strengths Ω and the corresponding coupling to the harmonic oscillator mode η for the three different fields that were experimentally studied.

2.4 Quadrupole transition

In the experiments extensive use is made of the laser at a wavelength of 729 nm. It can be used to coherently drive transitions between the $S_{1/2}$ and $D_{5/2}$-state manifold, for instance to initialize the hyperfine qubit. Moreover, quantum information can be encoded in a metastable $D_{5/2}$-state and one of the $S_{1/2}$-states as has been done with $^{40}\mathrm{Ca}^+$ for many years now. The laser-ion interaction for this optical qubit in $^{40}\mathrm{Ca}^+$ has been discussed in detail in the references [83, 89]. Here the results are briefly summarized including particularities concerning $^{43}Ca^{+}$.

2.4.1 Rabi frequency

The transition under consideration is dipole forbidden. Instead the gradient of the laser field applied couples to the induced electric-quadrupole moment $\hat{\mathrm{Q}}$

$$H_I = -\hat{\mathrm{Q}}\,\nabla E(t).$$

The coupling of the laser to the ion can be expressed in terms of the Rabi frequency as

$$\Omega = \left| \frac{eE_0}{4\hbar} \langle S_{1/2}, F, m_F | (\boldsymbol{\varepsilon} \cdot \boldsymbol{r})(\boldsymbol{k} \cdot \boldsymbol{r}) | D_{5/2}, F', m_F' \rangle \right|, \tag{2.18}$$

where E_0 is the electric field amplitude, $\boldsymbol{r}$ is the position operator of the valence electron relative to the atomic nucleus. For quadrupole transitions the selection rules allow $\Delta m = m_F - m_F' = 0, \pm 1, \pm 2$. In the case of $^{43}Ca^{+}$ also $\Delta F = F_S - F_D = 0, \pm 1, \pm 2$ has to be fulfilled. The effective coupling strength Ω for a certain transition depends on the atomic transition properties and the geometry of the magnetic field, the polarization vector $\boldsymbol{\varepsilon}$ and the laser beam direction $\boldsymbol{n} = \boldsymbol{k}/|\boldsymbol{k}|$. These can be combined into an effective coupling constant

$$\tilde{g} \equiv \left| \sqrt{(2J'+1)(2F+1)(2F'+1)} \begin{Bmatrix} J & J' & 2 \\ F' & F & I \end{Bmatrix} \sum_{q=-2}^{2} \begin{pmatrix} F' & 2 & F \\ m' & q & -m \end{pmatrix} c_{ij}^{(q)} \varepsilon_i n_j \right| \tag{2.19}$$

where the term in round (curly) brackets represents Wigner 3(6)-j symbols. The sum over q is only non-zero for $q = m - m'$. The second rank tensor[4] $c_{ij}^{(q)}$ takes into account both the radiative pattern and the quantization axis defined by the direction of a small magnetic field. Equation 2.18 turns then into

$$\Omega = \frac{eE_0}{4\hbar} \sqrt{\frac{15}{c\alpha} \frac{\Gamma_{D_{5/2}}}{k^3}}\; \tilde{g}$$

with the fine structure constant α, the speed of light c, the electron charge e and the spontaneous decay rate $\Gamma_{D_{5/2}}$. Neglecting the geometry and polarization dependence by

[4]defined as:

$$c^{(1)} = -\frac{1}{\sqrt{2}}(1, -i, 0), c^{(0)} = (0, 0, 1), c^{(-1)} = \frac{1}{\sqrt{2}}(1, i, 0)$$

$$c_{ij}^{(q)} = \sqrt{\frac{10}{3}}(-1)^q \sum_{m_1, m_2 = -1}^{1} \begin{pmatrix} 1 & 1 & 2 \\ m_1 & m_2 & -q \end{pmatrix} c_i^{(m_1)} c_j^{(m_2)}$$

omitting the factor $c_{ij}^{(q)}\varepsilon_i n_j$, the values of the coupling strengths $\tilde{g}$ for $^{43}Ca^+$ are listed in Fig. A.1.

Assuming an axial center of mass (COM) mode trapping frequency $\omega_z/(2\pi) = 1.2\,\mathrm{MHz}$ and an angle between trap axis and laser beam of 45° we attain a single ion Lamb-Dicke parameter of $\eta = 0.06$.

2.5 Raman interactions coupling hyperfine structure ground states

The following section discusses quantitatively the aspects of the light-atom interaction on the hyperfine structure of the $^{43}Ca^+$ ground-state with a Raman-type laser setup. Parameters like laser power, detuning and geometry have to be set to find a good compromise between a number of, often contradictory, requirements. The choice of the laser detuning from the P-levels, for example, is guided by at least three considerations: The spontaneous emission rate due to non-resonant excitations should be minimal, the light shifts caused by the Raman beams have to be controlled, and the Raman transition rate has to be sufficiently large. This has been detailed in the references [90, 91] for a number of different ion species. In the following three sections their results are summarized regarding coupling strength, light shifts and spontaneous emission that are relevant to the experiments done with $^{43}Ca^+$. Parts of the text of this section are taken from reference [92].

2.5.1 Resonant Raman transitions: Rabi frequencies and geometries

The goal of this section is to calculate the properties of Raman transitions in the ground-state of $^{43}Ca^+$, i.e. the Rabi frequencies and their dependence on laser frequencies and polarizations. In preparation, we first consider a generic two-state system $|0\rangle \equiv |j_0, m_0\rangle$ and $|1\rangle \equiv |j_1, m_1\rangle$ with intermediate state $|i\rangle \equiv |j_i, m_i\rangle$ to which dipole amplitudes exist. The light fields are described as plane waves of the form

$$\boldsymbol{E}(\boldsymbol{r}, t) = E\boldsymbol{\varepsilon}\cos(-F\omega_l t + \boldsymbol{k}\cdot\boldsymbol{r} + \phi),$$

evaluated at the position of the ion $\boldsymbol{r}$. We make the rotating wave approximation, and set the phase $\phi = 0$ for now. Two such light fields E_1 and E_2 are assumed in the resonant case where the detuning $\delta_R \equiv \omega_0 + \omega_1 - \omega_2$ of the lasers is equal to the energy separation ω_0 of $|0\rangle$ and $|1\rangle$. In the regime where $\Omega \ll \omega_0$, with Ω being the largest Rabi frequency due to coupling to the intermediate level, the Hamiltonian of this three-level system can be written in terms of an approximate, "effective Hamiltonian" that captures the dynamics of the system but only acts on the subspace $\{|0\rangle, |1\rangle\}$. The resulting effective Rabi frequency is given in terms of the individual Rabi frequencies

$$\Omega_1 = \frac{1}{2\hbar} E_1 \langle 0|\boldsymbol{d}\cdot\boldsymbol{\varepsilon}^{(1)}|i\rangle$$
$$\Omega_2 = \frac{1}{2\hbar} E_2 \langle 1|\boldsymbol{d}\cdot\boldsymbol{\varepsilon}^{(2)}|i\rangle$$

as

$$\Omega = \frac{\Omega_1\Omega_2^*}{\Delta} = \frac{E_1E_2}{4\hbar^2\Delta}\langle 0|\boldsymbol{d}\cdot\boldsymbol{\varepsilon}^{(1)}|i\rangle\langle i|\boldsymbol{d}\cdot\boldsymbol{\varepsilon}^{(2)}|1\rangle,$$

or, with the inclusion of magnetic sublevels,

$$\Omega = \frac{E_1E_2}{4\hbar^2\Delta}\sum_{m_i}\langle 0, m_0|\boldsymbol{d}\cdot\boldsymbol{\varepsilon}^{(1)}|i, m_i\rangle\langle i, m_i|\boldsymbol{d}\cdot\boldsymbol{\varepsilon}^{(2)}|1, m_1\rangle$$

To calculate the Raman coupling strength for $^{43}Ca^+$ regarding the involved frequencies we refer to the conventions of Fig. 2.5 (a). In general the two levels are of the two $4S_{1/2}$ hyperfine manifolds ($F = 3$ and $F = 4$). But in the end we are mostly interested in the clock states with $m_F = 0$ because of their insensitivity to magnetic field fluctuations. The Raman Rabi frequency is given by the coherent sum of the couplings via all available intermediate states. In the case of $^{43}Ca^+$ ions these are the $P_{1/2}$ and $P_{3/2}$ levels including their hyperfine structure and Zeeman levels. We therefore have to calculate the sum

$$\Omega = \frac{1}{4\hbar^2}\sum_{J=\frac{1}{2},\frac{3}{2}}\sum_{F=|I-J|}^{I+J}\sum_{m=-F}^{F}\left(\frac{E_1E_2}{(\Delta_J + \omega_{\mathrm{hfs}}(J,F))}\langle 0|\boldsymbol{d}\cdot\boldsymbol{\varepsilon}^{(1)}|J,F,m\rangle\langle J,F,m|\boldsymbol{d}\cdot\boldsymbol{\varepsilon}^{(2)}|1\rangle\right) \tag{2.20}$$

where again only resonant transitions ($\delta_R = 0$) are considered.

The scalar product can be written as

$$\boldsymbol{d}\cdot\boldsymbol{\varepsilon} = \sum_{s=-1}^{+1}(-1)^s d_s \varepsilon_{-s},$$

where d_s (and ε_s) are the spherical components given by

$$d_{\pm 1} = \frac{1}{\sqrt{2}}(\mp d_x - i d_y)$$
$$d_0 = d_z$$

The conjugated spherical components can be rewritten according

$$d_q^* = (-1)^q d_{-q}$$

ε_0 refers to a π-polarized laser field, whereas $\varepsilon_\pm$ indicate $\sigma^\pm$-polarized fields, respectively.

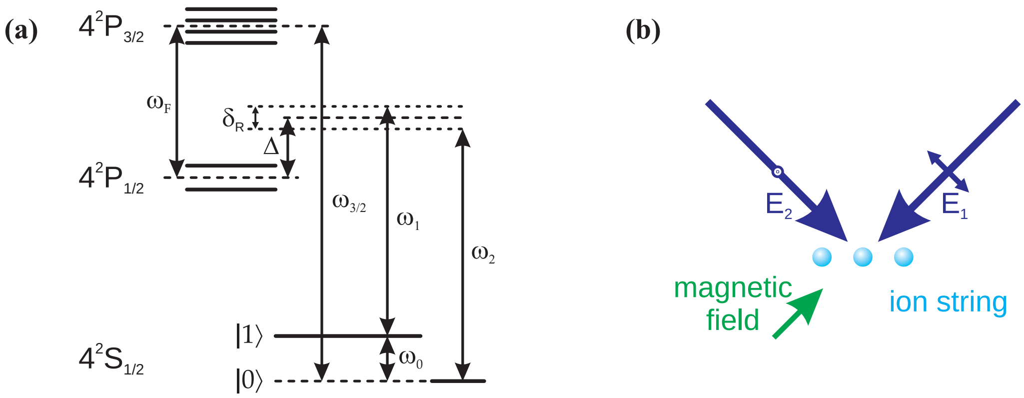

Figure 2.5: **(a)** Sketch of the energy levels relevant for the calculations for stimulated Raman transitions. Eventually, we are mostly interested in the case where the quantum information is encoded in two states of the $S_{1/2}$ ground-state manifold labeled $|\downarrow\rangle \equiv |F=4, m_F=0\rangle$ and $|\uparrow\rangle \equiv |F=3, m_F=0\rangle$. The hyperfine splitting of the excited states is not considered in the calculation. **(b)** Schematic of a possible beam geometry and polarizations for which the coupling between laser field and qubit transition is maximized. In this configuration the Lamb-Dicke parameter is 0.2 for an axial COM mode trapping frequency of $\omega/(2\pi) = 1.2\,\mathrm{MHz}$.

Now we can factor out the angular dependence and write the matrix element of Eq. (2.20) using the Wigner-Eckart theorem as

$$\langle 0|\boldsymbol{d}\cdot\boldsymbol{\varepsilon}^{(1)}|J,F,m\rangle\langle J,F,m|\boldsymbol{d}\cdot\boldsymbol{\varepsilon}^{(2)}|1\rangle = \langle 0||d||J,F,m\rangle\langle 1||d||J,F,m\rangle(2F+1)\times$$
$$\sum_{q=-1}^{1}(-1)^{q+F-1+m_0}\begin{pmatrix} F & 1 & F_0 \\ m & q & -m_0 \end{pmatrix}\varepsilon_{-q}^{(1)}\sum_{s=-1}^{1}(-1)^{s+F-1+m_1}\begin{pmatrix} F & 1 & F_1 \\ m & s & -m_1 \end{pmatrix}\varepsilon_{-s}^{(2)}$$

where the doubled bars indicate that the matrix element is reduced. This expression is only non-zero if $q = m_i - m_0$ and $s = m_1 - m_i$.

To obtain a concise expression for the Rabi frequency, we make some additional approximations and substitutions. First, we neglect $\omega_{\mathrm{hfs}}(J,F)$ because it is much smaller than the detunings Δ used in the experiment. Also, we express the reduced hyperfine matrix elements that show up in Eq. (2.20) by their corresponding fine structure matrix elements [80]

$$\langle F||d||F'\rangle = (-1)^{J+I+F'+1}\langle J||d||J'\rangle\sqrt{(2F+1)(2F'+1)}\begin{Bmatrix} J & F & I \\ F' & J' & 1 \end{Bmatrix}.$$

Finally, we introduce the coupling constant g_i

$$g_i = \frac{E_i}{2\hbar}\langle P_{3/2}, F=5, m_F=5|\boldsymbol{d}\cdot\sigma^{+}|S_{1/2}, F=4, m_F=4\rangle \tag{2.21}$$

with a right circular component of the dipole operator $\boldsymbol{d} \cdot \sigma^{+}$. Plugging all of this into Eq. (2.20), we get the following equation for a resonant carrier Rabi frequency in $^{43}\mathrm{Ca}^{+}$ between the hyperfine clock states

$$\Omega_{0\leftrightarrow 0} = \frac{1}{2} \left|\Lambda_{0,0}\right| g_1 g_2 \left(\varepsilon_{-1}^{(1)}\varepsilon_{-1}^{(2)} - \varepsilon_{1}^{(1)}\varepsilon_{1}^{(2)}\right) \frac{\omega_{\mathrm{F}}}{\Delta(\Delta - \omega_{\mathrm{F}})}, \tag{2.22}$$

where $\omega_{\mathrm{F}}/(2\pi) = 6.7\,\mathrm{THz}$ denotes the fine structure splitting of the P-states and $\Lambda_{m_F,m_{F'}}$ is the corresponding Clebsch-Gordan coefficient representing the relative coupling strength of the possible transition. The explicit values for $|\Lambda_{m_F,m_{F'}}|$ are given in Tab. 2.1.

The polarization dependence tells us important facts about the geometry of the experiment: First of all, π-polarized light ($\varepsilon_0^{(1)}$, $\varepsilon_0^{(2)}$) does not contribute to the Rabi frequency as given in Eq. (2.22). This makes sense because for such light, one of the two matrix elements of each coupling in sum Eq. (2.20) has to be of the form $\langle F, m_F = 0|z|F, m_F = 0\rangle$, which vanishes because the corresponding 3-j symbol

$$\begin{pmatrix} F & 1 & F \\ 0 & 0 & 0 \end{pmatrix} = 0.$$

Therefore, both beam polarizations must have a component perpendicular to the quantization axis.

Furthermore, the two beam polarizations must have components which are mutually orthogonal because otherwise the two terms in $\varepsilon_{-1}^{(1)}\varepsilon_{-1}^{(2)} - \varepsilon_{1}^{(1)}\varepsilon_{1}^{(1)}$ cancel. A possible geometry for beams with perpendicular k-vectors is given in Fig. 2.5 (b).

We can classify the possible Raman transitions between $F = 4$ and $F = 3$ by the change in the magnetic quantum number Δm. We find that the following polarizations are required:

Δm	polarizations
0	$\varepsilon_{-1}^{(1)}\varepsilon_{-1}^{(2)} - \varepsilon_{1}^{(1)}\varepsilon_{1}^{(2)}$
$+1$	$\varepsilon_{0}^{(1)}\varepsilon_{-1}^{(2)} - \varepsilon_{1}^{(1)}\varepsilon_{0}^{(2)}$
-1	$\varepsilon_{-1}^{(1)}\varepsilon_{0}^{(2)} - \varepsilon_{0}^{(1)}\varepsilon_{1}^{(2)}$
± 2	— forbidden —

In case the Raman beam difference frequency δ_R is set to plus (minus) the harmonic oscillator mode frequency the interaction Hamiltonian (2.17) is valid and oscillations on the blue (red) sideband can be driven. In the experiment, we use two different geometries for the Raman beams. For two copropagating laser fields the Lamb-Dicke parameter is negligible and no coupling to the motional sidebands is obtained. In the other configuration (see Fig. 2.5 (b) the laser beams' k-vectors enclose an angle of 90° and the resulting k-

hyperfine ground-state transition $(F=4, m_F) \leftrightarrow (F'=3, m_{F'})$										
0↔0	0↔1	1↔0	1↔1	1↔2	2↔1	2↔2	2↔3	3↔2	3↔3	4↔3
$\frac{2}{3}$	$\frac{1}{\sqrt{6}}$	$\sqrt{\frac{5}{18}}$	$\sqrt{\frac{5}{12}}$	$\sqrt{\frac{1}{12}}$	$\sqrt{\frac{5}{12}}$	$\sqrt{\frac{1}{3}}$	$\frac{1}{6}$	$\sqrt{\frac{7}{12}}$	$\frac{\sqrt{7}}{6}$	$\frac{\sqrt{7}}{3}$

Table 2.1: Clebsch-Gordan coefficients $|\Lambda_{m_F,m_{F'}}|$ representing the relative coupling strength for the possible Raman and microwave transitions in the $^{43}\mathrm{Ca}^+$ ground state manifold $(F = 4, m_F) \leftrightarrow (F' = 3, m_{F'})$. Coefficients other than the ones listed directly follow from the relation $|\Lambda_{m_F,m_{F'}}| = |\Lambda_{-m_F,-m_{F'}}|$

vector of both beams added is parallel to the trap axis. That results in a Lamb-Dicke parameter η of 0.2 for an axial COM mode trapping frequency of $\omega_z/(2\pi) = 1.2\,\mathrm{MHz}$.

2.5.2 Numerical evaluation

For now we assume that the two laser fields are equally strong ($E_1 = E_2 \equiv E$). Then the coupling constants $g_1 = g_2 \equiv g$ can be linked to atomic constants and the field amplitudes by

$$\frac{\Gamma_P}{g^2} = \frac{4\hbar\omega_{3/2}^3}{3\pi\epsilon_0 c^3 E^2}$$

where $\omega_{3/2}$ is the frequency of the transition $S_{1/2} \leftrightarrow P_{3/2}$. Here we assumed an equal decay rate Γ_P which leads to a few percent error as the rates are slightly different ($\Gamma(P_{1/2} \rightarrow S_{1/2}) = 1/(7.7\,\mathrm{ns})$ and $\Gamma(P_{3/2} \rightarrow S_{1/2}) = 1/(7.4\,\mathrm{ns})$ [83]).

The electric field strength E is linked to the laser power $\mathcal{P}$ in the center of a Gaussian beam with waist size w_0 by

$$E^2 = \frac{4\mathcal{P}}{\pi w_0^2 \epsilon_0 c}$$

If we choose a detuning $\Delta = (\sqrt{2}-1)\omega_\mathrm{F}$ where detrimental scattering is largely suppressed (see below), and assume polarizations such that $\varepsilon_{-1}^{(1)}\varepsilon_{-1}^{(2)} - \varepsilon_{1}^{(1)}\varepsilon_{1}^{(2)} = 1$, we find for the resonant carrier Rabi frequency on the clocks states

$$\Omega_{0\leftrightarrow 0} = \frac{9}{2}\frac{c^2\,\Gamma_P}{\hbar\omega_{3/2}^3\omega_\mathrm{F}}\frac{\mathcal{P}}{w_0^2} = 2\pi \times 0.16\,\mathrm{MHz} \times \frac{\mathcal{P}}{w_0^2} \times \left[\frac{10\,\mu\mathrm{m}^2}{1\,\mathrm{mW}}\right].$$

The time it takes for a full population transfer is usually referred to as the corresponding π-time and given by $\tau_\pi = \pi/(2\Omega)$.

2.5.3 Light shifts

The off-resonant light shift of a level $|m\rangle$ - also termed *AC-Stark shift* - due to coupling with a laser of field strength E to level $|j\rangle$ is given by

$$\delta(m) = \frac{|E|^2}{4\hbar^2\Delta}|\langle m|\boldsymbol{d}\cdot\boldsymbol{\varepsilon}|i\rangle|^2.$$

Here the detuning of the laser Δ is assumed large compared to the intermediate level's decay rate Γ_P.

In case of $^{43}Ca^+$, we have to sum over all the intermediate levels and get for the AC-Stark shift of the level $|m\rangle$ of each of the laser beams i

$$\delta(m)^{(i)} = \frac{1}{4\hbar^2}\sum_j\left(\frac{E_i^2}{\Delta_j}|\langle m|\boldsymbol{d}\cdot\boldsymbol{\varepsilon}^{(i)}|j\rangle|^2\right).$$

As with calculating the Rabi frequency, we neglect the hyperfine splitting in the excited state as an approximation which holds for larger laser detunings Δ. When using the coupling constants of Eq. (2.21) we obtain for the differential light shift of the clock state qubit due to both Raman beams

$$\begin{aligned}\delta_{0\leftrightarrow 0} =& \frac{g_2}{3}\left(\frac{1}{\Delta+\omega_0} - \frac{2}{\Delta-\omega_F} + \frac{2}{\Delta+\omega_0-\omega_F} - \frac{1}{\Delta}\right) + \\ &+ \frac{g_1}{3}\left(\frac{1}{\omega_0-\Delta} + \frac{2}{\Delta-\omega_F} - \frac{2}{\Delta-\omega_0-\omega_F} + \frac{1}{\Delta}\right) \\ \approx& -\frac{(g_1^2+g_2^2)}{3}\omega_0\left(\frac{1}{\Delta^2} + \frac{2}{(\Delta-\omega_F)^2}\right),\end{aligned}$$

where the approximation holds for $\omega_0 \ll \Delta, \omega_F$. The differential shift is independent from the polarization of the Raman beams.

2.5.4 Spontaneous photon scattering

While the ion is in either one of the two qubit states, spontaneous decay can be neglected completely. However, during Raman transitions the ion is off-resonantly excited to the P-levels, which decay rather quickly. In a two-level system, the average probability for the ion to be found in the excited state is given by the ratio of the light shift δ and the laser detuning Δ. A multiplication with the decay rate Γ_P of the excited state gives an estimate of the decoherence rate R_{SE} due to spontaneous decay. This spontaneous decay limits the coherent operations in a fundamental way since both decay rate and coherent transition rate scale with g_i^2.

With the approximation $\omega_0, \Gamma_P \ll \omega_F, |\Delta|$ the average spontaneous decay rate during the Raman interaction is

$$R_{\mathrm{SE}} = \frac{\Gamma_P}{3}(g_1^2 + g_2^2)\left(\frac{1}{\Delta^2} + \frac{2}{(\Delta - \omega_{\mathrm{F}})^2}\right)$$

In order to avoid scattering during the coherent operation the ratio

$$R_{\mathrm{SE}}/|\Omega| = \frac{\left(g_1^2 + g_2^2\right)\Gamma_P}{g_1 g_2(\varepsilon_{-1}^{(1)}\varepsilon_{-1}^{(2)} - \varepsilon_1^{(1)}\varepsilon_1^{(2)})}\left(\frac{2}{\Delta - \omega_F} - \frac{1}{\Delta} + \frac{3}{\omega_F}\right)$$

has to be minimized. This can be achieved by choosing equal intensities in both Raman beams and proper polarizations (e.g. $\varepsilon_{-1}^{(1)} = \varepsilon_{-1}^{(2)} = -\varepsilon_1^{(1)} = \varepsilon_1^{(2)} = 1/\sqrt{2}$). If we set the Raman detuning to $\Delta_{\mathrm{opt}} = (1-\sqrt{2})\omega_{\mathrm{F}}$ the probability of spontaneous emission P_{SE} during a carrier π-pulse is

$$P_{\mathrm{SE}} = \frac{2\sqrt{2}\,\pi\,\Gamma_P}{\omega_F} = 3 \times 10^{-5}.$$

In order to achieve a π-time of $1\,\mu$s Raman beams with a waist of $10\,\mu$m would require 1.6 mW of laser power for this detuning. The differential AC-Stark shift would then be $\delta_{0\leftrightarrow 0} = -4\sqrt{2}\,|\Omega|\,\omega_0/\omega_F = -2\pi \times 680\,\mathrm{Hz}$.

In addition to this inelastic scattering also elastic scattering events can occur. It has been shown though that these will not lead to decoherence [93].

2.6 Microwave transitions

The spontaneous scattering problem is not present when driving microwave transitions on the $^{43}\mathrm{Ca}^+$ hyperfine ground-state. The magnetic dipole coupling of the ion to electromagnetic radiation in the microwave domain can be expressed in terms of a Rabi frequency as

$$\Omega_{\mathrm{MW}} = \left|\frac{1}{2\hbar}\langle S_{1/2}, F = 4, m_F|(\boldsymbol{\mu}\cdot\boldsymbol{B}_{\mathrm{MW}})|S_{1/2}, F' = 3, m'_F\rangle\right|$$

with the ion's magnetic dipole moment $\boldsymbol{\mu}$ and the magnetic field amplitude $\boldsymbol{B}_{\mathrm{MW}}$ of the microwave radiation.

Transitions where the magnetic quantum number is not changed ($\Delta m = 0$) are driven by a π-polarized AC magnetic field, whereas for transitions with a change in magnetic quantum number by one ($\Delta m = \pm 1$) a $\sigma^{\pm}$ polarized field is needed. The relative strengths of the transitions are given by the corresponding Clebsch-Gordan coefficients and are the same as for the Raman transitions given in Tab. 2.1.

For typical axial COM mode trapping frequencies of $\omega/(2\pi) = 1.2\,\mathrm{MHz}$ and the hyperfine splitting of the ground-state $\omega_0/(2\pi) = 3.2\,\mathrm{GHz}$, the Lamb-Dicke parameter is $\eta_{\mathrm{MW}} \simeq 10^{-6}$. The coupling to the first motional sideband relative to the carrier is suppressed by that amount, unless large magnetic field gradients are applied [94]. This makes the use of this coupling impractical. Another drawback concerning the usage of microwave radiation for QIP is that addressing of single ions cannot be achieved by focusing the radiation since the wavelength is orders of magnitude bigger than typical ion distances. Despite the fact that this could be circumvented by applying large magnetic field gradients, such that transitions of ions at different sites can be spectrally resolved, we discard this as a impractical solution because at least some of the ions would experience fields where the transitions become rather sensitive to external magnetic field fluctuations. In addition, when moving the ions within the trap, phase tracking would be challenging, too.

Although, microwave driven qubit transitions are a valuable tool for example to study mechanisms of decoherence present for Raman lasers (see section 6.4).

3 Experimental setup

For the experiments reported below a new setup has been constructed consisting of three major building blocks: the ion trap, the lasers and the computer control. The experiment was set up on two optical tables, one accommodating the photoionization lasers, the cooling laser and the repumping lasers as well as their frequency references. The other optical table carries the trap setup and ion detection, the laser source for the Raman beams and a titanium-sapphire laser for the quadrupole transition, including its frequency reference. All laser sources - except the Raman beams - are linked to the ion trap part of the experiment by single-mode glass fibers. The experiment resides at the Institut für Quantenoptik und Quanteninformation in Innsbruck, Austria.

3.1 Linear ion trap and radiofrequency drive

One of the big advantages of trapped ions as a physical implementation of QIP is the high amount of control for initialization, readout and manipulation of internal and external degrees of freedom by using focused laser beams and microwave radiation. At the same time these interactions can be switched off almost completely and also environmental perturbations are strongly suppressed. The latter is usually achieved by suspending the ions in a trap, which is mounted in an ultra high vacuum environment. Our experiments are performed either with a single or a pair of calcium ions held in a linear Paul trap consisting of two tips and four blade-shaped stainless steel electrodes [95, 96]. A picture and schematic drawings of the trap can be seen in Fig. 3.1. A trap of the same type has been intensively investigated over the past years in another experiment of the group and is quite well understood. It has reasonably high trapping frequencies in the radial and axial direction. This design was chosen because such a structure can be machined with higher precision than rod-like electrodes which were used in earlier experiments. One advantage over more modern micro-machined segmented traps is the low heating rate (see section 4.5) and ease of optical access.

In order to attain large secular frequencies, two of the trap blades are held at ground while the two others are fed a radiofrequency high voltage $V_{\mathrm{rf}}(t)$. Voltage enhancement is achieved by the use of a helical resonator with a silver plated helix exhibiting a quality

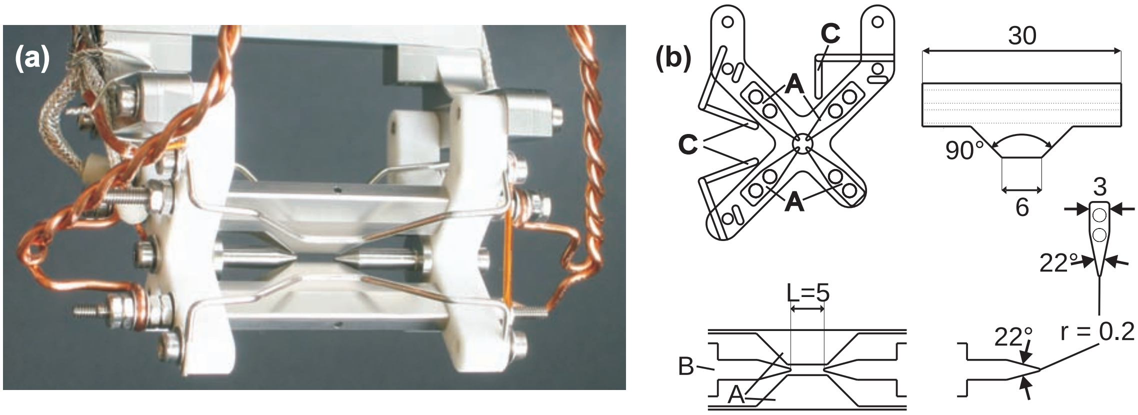

Figure 3.1: **(a)** Picture of the linear Paul trap used for the experiments. The four blade-electrodes are connected with twisted OFHC copper wires and the DC-electrodes by a Kapton insulated wire. **(b)** Schematics of the trap construction. Two of the blade-shaped electrodes (A) are connected to ground, the other two are supplied with radiofrequency high voltage. The minimal distance between the radial electrodes and the ions is $r_0 = 0.8\,\mathrm{mm}$. The two tip electrodes (B) are connected to high positive voltages of up to 1.5 kV. Moreover, compensation electrodes (C) are placed close to the trap center such that electric stray fields in radial directions can be compensated. The minimal distance from these electrodes to the ions is for the one(s) on the top (side) 7.3 mm (7.7 mm). The top one is also used to guide microwave and radiofrequency signals close to the ions. All measures of distances and radii are given in mm.

factor of $Q = 300$. An input signal with a trap drive frequency of $\Omega_{\mathrm{rf}}/(2\pi) \simeq 25.5\,\mathrm{MHz}$ is produced by a frequency synthesizer[1]and then amplified[2] to 5-13 W radiofrequency power which is resonantly coupled into the helical resonator attached to the trap electrodes. By this means a two-dimensional electric quadrupole field is generated which provides radial confinement for a charged particle. In case of hyperbolic trap surfaces the time varying quadrupole potential Φ_{rf} in the $x, y-$ or radial plane is given by

$$\Phi_{\mathrm{rf}}(x, y, t) = \Phi_0 \frac{x^2 - y^2}{2r_0^2} \cos(\Omega_{\mathrm{rf}}\, t), \tag{3.1}$$

where $r_0 = 0.8\,\mathrm{mm}$ is the minimal distance from the trap center to the blade-electrodes. Even though the radial electrodes are rather shaped like blades than having a hyperbolic form, Eq. (3.1) can serve as a good approximation in particular for small excursions.

In order to confine the ions in axial direction (along $\boldsymbol{e}_z$), two stainless steel tips are placed $L = 5\,\mathrm{mm}$ apart in the trap's symmetry axis and are held at a positive voltage $U_{\mathrm{tip}} = 500 - 1500\,\mathrm{V}$. The electrodes are electrically isolated by Macor ceramics spacers which assure a 20 μm tolerance in the positioning of the four blades and the tip electrodes. Each tip is separately connected such that the ions can be shuttled along the trap axis by applying different voltages to each of the tips (see section 3.5). Assuming a perfect

[1]Rohde & Schwarz, SML01
[2]Mini Circuits ZHL-5W-1 or LZY-1

quadrupole field and equal tip voltages, the potential imposed by the two tips is given by

$$\Phi_{\text{tip}}(x,y,z) = \frac{U_{\text{tip}}}{L}[z^2 - \frac{1}{2}(x^2+y^2)].$$

In the resulting potential $\Phi = \Phi_{\text{rf}} + \Phi_{\text{tip}}$ an ion with charge e experiences the force $F = -e \cdot \Delta\Phi$. This leads to equations of motion for the trapped particles of mass M in three dimensions that take the form of a *Mathieu equation* [97]

$$\ddot{u}_i + [b_i + 2q_i \cos(\Omega_{\text{rf}}\, t)]\frac{\Omega_{\text{rf}}^2}{4} u_i = 0, \tag{3.2}$$

where $\boldsymbol{u} = u_x \boldsymbol{e}_x + u_y \boldsymbol{e}_y + u_z \boldsymbol{e}_z$ is the position of the ion. The stability parameter q is defined for ions with mass M as

$$q \equiv \frac{2eV_{\text{rf}}}{M r_0^2 \Omega_{\text{rf}}^2}$$

and stable solutions occur for $0 < q < 0.908$ [98]. The components of $\boldsymbol{q}$ are then defined by $q_x = -q_y = q$ and $q_z = 0$.

The components of $\boldsymbol{b}$ are given by

$$b_x = b_y = -\frac{1}{2} b_z = -\frac{e\,\tilde{\alpha}\, U_{\text{tip}}}{M L^2 \Omega_{\text{rf}}^2},$$

where $\tilde{\alpha}$ is a factor taking into account the actual trap geometry.

In case $q, |\boldsymbol{b}| \ll 1$, a first-order solution to Eq. (3.2) is given by

$$u_i(t) \approx \breve{u} \cos(\omega_i t) \left[1 + \frac{q_i}{2}\cos(\Omega_{\text{rf}} t)\right]. \tag{3.3}$$

with the amplitude $\breve{u}$ of the ion motion and a frequency

$$\omega_i = \frac{\Omega_{\text{rf}}}{2}\sqrt{b_i + q_i^2/2}. \tag{3.4}$$

The solution in the axial direction describes a harmonic motion with a frequency of

$$\omega_{\text{ax}} = \omega_z = \sqrt{\frac{e\,\tilde{\alpha}\, U_{\text{tip}}}{2\, M L^2}}.$$

For a tip voltage of $U_{\text{tip}} = 1000\,\text{V}$ $^{43}\text{Ca}^+$ ions are confined in a harmonic potential with an axial COM mode frequency of $\omega_{\text{ax}}/(2\pi) = 1.2\,\text{MHz}$.

In the radial directions the motion exhibits two frequency components. One is given by the radial components of Eq. (3.4) which can also be written as

$$\omega_r = \omega_x = \omega_y = \sqrt{\frac{(\Omega_{\text{rf}} q)^2}{8} - \frac{1}{2}\omega_z^2}.$$

Thus it is evident that the frequency, characterizing the *secular motion* is lowered when the potential along the trap axis is increased.

The second frequency component of the motion along the radial direction is at the trap drive frequency Ω_{rf} and is termed *micromotion*. The amplitude of this micromotion is by a factor of $q/2$ smaller than the secular motion and usually not of importance for the experiments.

For our trap parameters we typically obtain secular frequencies of the radial motion between $\omega_r/(2\pi) = 2\,\mathrm{MHz}$ and $4\,\mathrm{MHz}$ for calcium ions. From spectroscopic measurements we infer that the degeneracy of the two radial directions is lifted, so we can resolve two radial sideband components which are separated by $\Delta\omega_r/(2\pi) \simeq 40\,\mathrm{kHz}$, with a small dependence on the tip voltage. This asymmetry is introduced by the fact that only two of the radial trap electrodes are powered with radiofrequency where the two others are attached to ground.

In the presence of external electric stray fields, the ions' equilibrium position is shifted out of the radiofrequency potential's node. This leads to an increased amplitude of the motional component at the trap drive frequency Ω_{rf} termed *excess micromotion*. The amplitude of this excess micromotion can be largely suppressed by applying voltages to compensation electrodes such that the ions are shifted back to the radiofrequency potential's node (see section 4.3).

In the experiment we are mostly interested in the regime where multiple ions are aligned in a linear crystal when sufficiently cold. This is the case for $\omega_r \gg \omega_z$. The equilibrium position in the case of multiple ions is then determined by the trapping potential and the Coulomb repulsion of the ions. For two ions the distances from the center of the trapping potential in axial direction is given by [83]

$$\Delta z = \left(\frac{e^2}{16\pi\epsilon_0 M\omega_z^2}\right)^{1/3}. \tag{3.5}$$

For an axial COM mode frequency of $\omega_{\mathrm{ax}}/(2\pi) = 1.2\,\mathrm{MHz}$, two $^{40}\mathrm{Ca}^+$ ions exhibit an inter ion spacing of $4.9\,\mu\mathrm{m}$. Since the trap frequencies can be measured precisely we use the knowledge of the associated ion spacing to calibrate the magnification of the imaging system.

3.2 Laser system and optics

One big advantage of calcium is the fact that today all laser light sources needed can be derived from commercially available diode lasers. Except for the laser at 729 nm, which

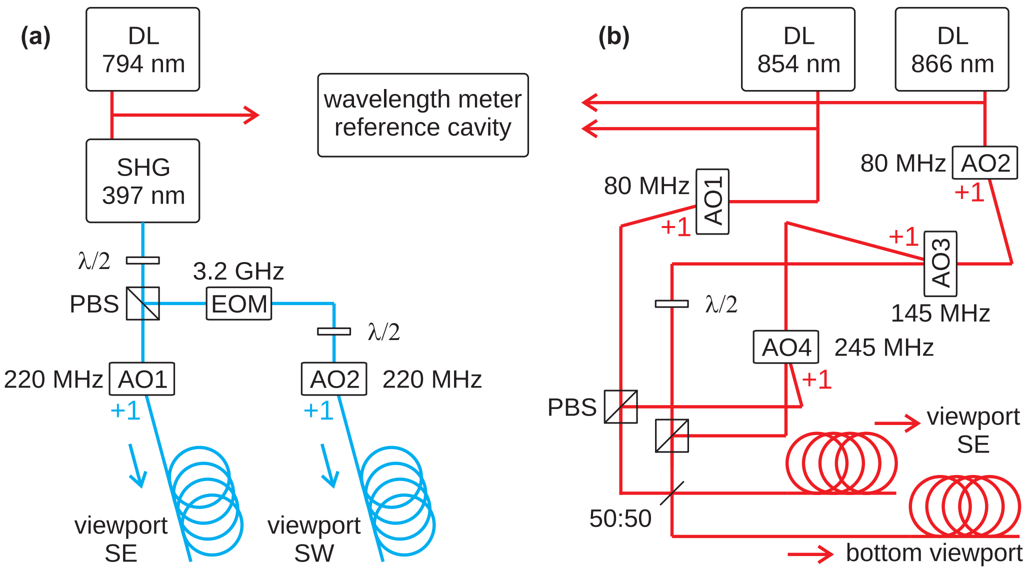

Figure 3.2: **(a)** Laser beamline providing light for Doppler-cooling, state detection and optical pumping at a wavelength of 397 nm. The EOM at 3.2 GHz is used to address both hyperfine ground states of $^{43}Ca^+$. **(b)** In order to pump out the D-states, light at wavelengths 866 nm and 854 nm is needed. Both wavelengths are superimposed on a 50:50 beam splitter before sending them through polarization-maintaining single-mode glass fibers to the experiment. In case of $^{43}Ca^+$, multiple frequencies of the repumper at 866 nm can help to increase the fluorescence rate. Two additional frequencies are modulated onto the beam with two extra AOM's operated at 145 MHz and 245 MHz as sketched.

is a titanium-sapphire laser[3] and was already available, all other coherent light sources are Toptica diode lasers, partially with second harmonic generation. Furthermore, all lenses, waveplates, glass fibers, electro-optical devices, filters, polarizers, coatings, etc. are commercially available components.

3.2.1 Lasers for Doppler-cooling and optical pumping and repumping

Laser at 397 nm

For Doppler-cooling, state detection and optical pumping the ions are excited on the $S_{1/2} \leftrightarrow P_{1/2}$ dipole transition (see Fig. 2.3) at a wavelength of 397 nm. At the time when the experiment was set up, there were no laser diodes available at this particular wavelength with sufficiently low amplified spontaneous emission. Therefore, the light is produced by second harmonic generation (SHG) from a diode laser at 794 nm[4]. Approximately 100 μW of the red light is used for frequency stabilization to a reference cavity (see below). At the output of the doubling cavity we have about 10 mW of blue light, which is

[3] Coherent, 899 modified by L. Windholz (Graz University) in company with Radiant Dyes; Pump laser: Coherent, Verdi V-10

[4] Toptica DL-SHG

then split into a σ-beam and a π-beam as depicted in Fig. 3.2 (a). Each of the beamlines has an acousto-optical modulator (AOM) at 220 MHz[5] for switching the beams on and off. Additionally, the σ-beam has an electro-optic phase modulator (EOM)[6] in order to generate sidebands at 3.2 GHz, needed to address both hyperfine ground-state manifolds of $^{43}\mathrm{Ca}^+$. The beams are then sent through single-mode polarization-maintaining fibers[7] to the experiment. Similarly, a second laser system of this type is available where the wavelength can be tuned between 393 nm and 397 nm. This laser is used to improve on the $^{43}\mathrm{Ca}^+$ fluorescence rate.

Lasers at 866 nm and 854 nm

For repumping from the $3D_{3/2}$ and $3D_{5/2}$-states two diode lasers (DL)[8] provide light at 866 nm and 854 nm. As sketched in Fig. 3.2 (b) both beams are switched on and off with AOM's operating at 80 MHz[9]. In case of $^{40}\mathrm{Ca}^+$ it is sufficient to work with a single laser frequency for efficient repumping. For $^{43}\mathrm{Ca}^+$ though it turns out that the fluorescence that is observed during Doppler-cooling and detection can be increased by adding two more frequencies with AOM's to the light at 866 nm. Therefore, the two AOM's at 145 MHz and 245 MHz[10] (see Fig. 3.2 (b)) are turned on only when $^{43}\mathrm{Ca}^+$ is used. All light fields of 866 nm and 854 nm are collected and sent to the experiments with two single-mode polarization-maintaining fibers[11] to one of the equatorial ports (SE) and one on the bottom flange. For $^{40}\mathrm{Ca}^+$ one of these ports is sufficient, whereas for $^{43}\mathrm{Ca}^+$ an increase in fluorescence was observed while Doppler-cooling and state detection when both ports were used. In addition a diode laser 850 nm is available to investigate alternative shelving techniques and potentially improve on the $^{43}\mathrm{Ca}^+$ fluorescence rate.

Laser frequency references

Unlike in neutral atom experiments, for the wavelengths needed for ions usually there are no vapor cells that can be used as laser frequency reference by certain spectroscopy techniques. Therefore, all the lasers described earlier in this chapter are referenced to Fabry-Pérot cavities. The design of such a resonator is always a trade-off between a number of different needs, that partly lead to conflicts. For instance it is hard to obtain high stability and tunability at the same time. The frequencies of lasers acting on dipole

[5] Crystal Technology, 3230-120
[6] New Focus, 4431
[7] Schäfter + Kirchhoff, PMC-400-4.2-NA010-APC
[8] Toptica, DL-100
[9] Brimrose, EF-80-20-866 and Crystal Technology, 3080-120
[10] Brimrose, EF-145-30-866 and EF-250-30-866
[11] Schäfter + Kirchhoff, PMC-850-5.2-NA012-3-APC

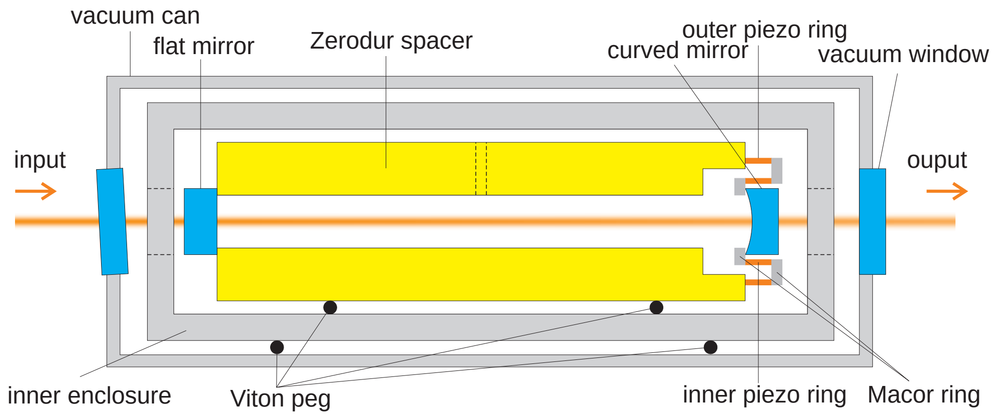

Figure 3.3: Cavity setup that is used as a variable, passively stable frequency reference for the lasers at wavelengths of 866 nm, 854 nm and 794 nm. One curved and one flat mirror are kept at distance of 100 mm by a Zerodur spacer whose length is hardly sensitive to temperature changes. In order to gain tunability without compromising the stability too much, the curved mirror is mounted onto two concentric piezo transducers of equal height, interconnected by ceramic rings. The cavity assembly is kept in vacuum to get a better thermal insulation from the environment and to prevent changes in air pressure to change the optical path length between the mirrors. Both vacuum windows are anti-reflection coated and the input port is slightly tilted to avoid spurious reflections perturbing the error signal.

transitions with a line width on the order of 20 MHz should be defined to better than 1 MHz. Therefore, the resonator stability can be slightly compromised by gaining in the flexibility of frequency tuning. A cavity setup was designed with one flat and one concave mirror[12] with a reflectivity of 99.1% (finesse $\mathcal{F} \approx 300$). The flat mirror is directly glued[13] to a 100 mm spacer made of the glass ceramic Zerodur[14] and used as input port. The thermal expansion coefficient of the Zerodur used is specified to be $0 \pm 0.02 \times 10^{-6}$ /K at room temperature. As sketched in Fig. 3.3 the curved mirror is mounted to the spacer with two concentric piezo transducers[15] of the same height (5 mm). The ceramics of the piezos has a rather high temperature expansion coefficient of 2×10^{-6} /K. By this assembly thermal drifts can by largely suppressed while having the flexibility to tune the cavity over several free spectral ranges (FSR = 1.5 GHz) by applying voltages up to 300 V to the piezos' electrodes. After scanning over large ranges, the piezos have to settle. This takes typically a few minutes. For daily operation this is a minor problem. The 397 nm cooling laser is the only laser that needs to be tuned over several GHz during operation. In order to cope with the slow frequency drift while settling, we monitor the amount of fluorescence during Doppler-cooling and feed this signal back to the cavity piezo voltage. Thus, on a time scale of minutes, the cooling laser is directly stabilized to the ions' $S_{1/2} \leftrightarrow P_{1/2}$ dipole transition.

[12]Laseroptik Garbsen, radius of curvature 250 mm
[13]Norland Products Inc., UV-glue
[14]Helma Optics, Dehnungsklasse 0
[15]Ferroperm, Pz27

In order to suppress perturbations caused by acoustic noise and changes of the air pressure and to improve the thermal decoupling of the environment, the whole setup is contained in a vacuum can. After pumping with a turbo pump for a day the setup was detached from this pump by means of an all-metal valve, and is pumped using an ion getter pump[16]. A steady state pressure of 10^{-8} mbar was reached after one day. The vacuum in combination with the Viton-pegs (see Fig. 3.3) provide a good thermal isolation from the environment and the heat exchange with the environment is dominated by radiation. To avoid gradients that could change over time, an additional metal enclosure inside the vacuum was installed. Thermalization within this inner aluminum shield is expected to occur on much shorter time scales than the radiative heat exchange of this shield with the vacuum can. The whole setup is enclosed in a metal housing and the temperature is stabilized by resistive heating. Servo independent temperature measurements reveal that the averaged temperature inside the box varies by less then ± 2 mK within 24 h.

Direct beat note measurements with a referenced laser (see subsection 3.2.2) have shown that for relaxed piezos the drift rates are well below 100 Hz/s, which accumulates to less than half the line width of the transitions of interest within a day. The resulting line width of the lasers referenced to these cavities is mainly limited by acoustic vibrations of the optical setup to about 100 kHz.

The distance and the curvature of one of the mirrors were chosen such that the frequencies of the higher order transversal modes are far off from the TEM_{00}-mode. As a result, small changes in the coupling efficiency of the laser to the cavity have a minor effect to the error signal and hence to the lock performance. All lasers are locked to the cavities with a Pound-Drever-Hall technique [99]. The necessary sidebands are directly modulated onto the light by means of a bias-T that alters the current of the laser diode slightly at a frequency of 20 MHz. Photodiodes with a bandwidth of 125 MHz[17] are used for error signal detection.

[16]Varian, Star Cell 201
[17]New Focus, 1801

3.2.2 Ultra-stable titanium-sapphire laser at 729 nm

With a laser at a wavelength of 729 nm we have the opportunity to excite calcium ions on the $S_{1/2} \leftrightarrow D_{5/2}$ quadrupole transition. This offers a large number of possible applications, including:

- precision spectroscopy on the quadrupole transition
- coherent manipulation of optical qubits
- sideband cooling to the motional ground-state
- state transfer and initialization
- optical shelving for state detection
- frequency resolved optical pumping

The tasks listed here are very demanding with regard to the laser's line width, its frequency and output power stability. Furthermore, the ability is needed to tune the laser frequency over 100 MHz within a microsecond and to switch between different transitions of $^{43}Ca^+$and $^{40}Ca^+$differing by several GHz within minutes. The setup of the laser was part of Gerhard Kirchmair's Diplomarbeit. A detailed technical description of the laser system and the frequency stabilization scheme can be found in his thesis [100], here only the idea is given and the performance is described.

The requirements discussed above are met by stabilizing the laser to a high finesse cavity[18] ($\mathcal{F} = 410\,000$, line width = 5 kHz, FSR = 2 GHz) which is vertically mounted [101] in a temperature stabilized (±1 mK) vacuum (10^{-8} mbar) enclosure. Ideally the expansion coefficient is zero at a certain temperature T_c and the relative length change is then described by $\Delta l/l \sim 10^{-9}(T - T_c)^2$. For cavities from the same batch but operated at a different wavelength the quadratic expansion coefficient was measured by Janis Alnis *et al.* [102]. They also determined T_c for two different cavities to be $7°C$ and $12°C$, respectively. We assume similar values for our system. The temperature of our cavity setup was stabilized though by resistive heating to about 30 °C. The sensitivity to temperature changes at this point was measured to be 20 MHz/K. In case we could stabilize the temperature to T_c, a further suppression in sensitivity of two orders of magnitude can be expected where drifts induced by the heating of the mirror coatings start becoming important. The typical drift rates of the Fabry-Pérot cavity we obtained with the ions as reference (see section 4.4) are 3 Hz/s or below. It is quite remarkable that a 1 Hz/s drift is equivalent with a change in the cavity mirror distance of less than 6 nm per year for this setup.

This stability comes of course at the price that this reference cavity cannot be tuned since it consists of fixed mirrors optically contacted to a spacer. In order to get the

[18]Advanced Thin Films, CO, USA

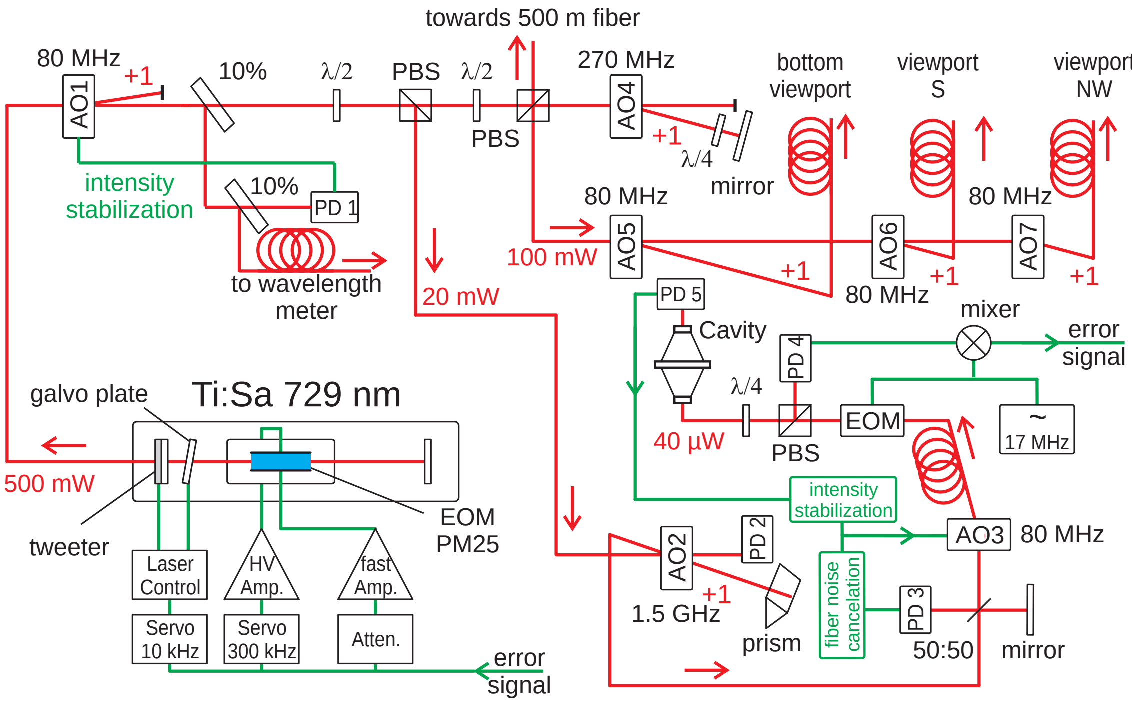

Figure 3.4: Schematic of the laser setup to provide light at 729 nm. The light intensity of the laser is stabilized by feeding back the signal of PD1 to the radiofrequency amplitude of AO1. A high finesse cavity serves as a frequency reference. The feedback to the titanium-sapphire laser is threefold. A slow feedback is applied to the tweeter and the Brewster plate. A mid and a high frequency feedback is applied to an intracavity EOM. In total three different beams can be used on the ions. Each of them is switched on and of by either of AO5-7 and then guided to the experiment with a short single-mode polarization-maintaining glass fiber.

laser output to any desired frequency a 1.5 GHz AOM[19] in double-pass configuration is used. It has a tuning bandwidth of more than 900 MHz and a diffraction efficiency to the first order of 14% (single-pass) so that enough light can be provided for the frequency stabilization. The drive frequency of the AOM is provided by frequency-doubling[20] the output of a synthesizer to which a signal derived from measurements on the ions can be phase-continuously fed back, such that the cavity drift is compensated on a time scale of minutes to hours (see section 4.4).

The frequency of the laser is actively locked by means of the Pound-Drever-Hall locking technique. The necessary sidebands for the locking are phase-modulated onto the light with an EOM[21] operated at 17 MHz and the obtained error signal describes the phase deviation between the light stored in the cavity and the light send to it. The servo loop consist of three branches and is sketched in Fig. 3.4. For a servo loop bandwidth of 300 kHz and above, the error signal is sent through a proportional amplifier[22], whose

[19] Brimrose GPF-1500-1000
[20] Mini-Circuits, FK-3000
[21] Linos/Gsänger, PM25
[22] Femto HVA-10M-60-F

output is connected to one of the intracavity EOM's[21] electrodes. The other electrode of this EOM receives a feedback signal which is modified by a loop filter (proportional part and shunted integrator) and amplified by a home-made high voltage amplifier[23]. With an amplification of 30 the bandwidth of this branch is about 300 kHz. Slow fluctuations are corrected by modifying the error signal with a loop filter and feeding back onto the tweeter (piezo transducer to which one of the laser's cavity mirrors is mounted to). This part of the feedback loop is limited by the mechanical resonance of the piezo-mirror assembly to 10 kHz. In addition, an extra servo loop stabilizes the intensity that is transmitted through the reference cavity to prevent small variations in laser polarization, fiber coupling efficiency, etc. from changing the error signal.

The laser output and the reference cavity setup are linked with a single-mode polarization-maintaining fiber. To prevent acoustical noise coupling into the fiber from compromising the frequency stability, we introduced an active fiber-noise cancelation [103]. Before sending the laser light through the fiber it is split into two branches by a 50:50 beam splitter (see Fig. 3.4). The reference arm is directly reflected from a planar mirror to the beam splitter whereas the other part is frequency shifted by AO3 (80 MHz) and then guided to the cavity by a single-mode polarization-maintaining glass fiber. The end facet of this fiber is polished at a right angle such that about 4% of the light is back reflected through the fiber where it gets frequency shifted again. A photodiode (PD3) with a bandwidth of 1 GHz[24] measures the beat frequency of the reference beam and the laser sent to the cavity which is then compared with the signal of a highly stable frequency reference[25] at 160 MHz. Implementing a phase-locked loop, the frequency of the beat signal is kept in phase by feeding back to the voltage-controlled oscillator providing for AO3's input frequency signal. The laser's frequency spectrum was characterized by recording an optical beat note with a similar laser, that is situated in a university building. Two 500 m long single-mode polarization-maintaining glass fibers[26] are used to sent the light between the sites, one for each direction. Similar as in the frequency stabilization setup fiber noise cancelations are installed for both fibers. In order to measure the laser line width, a beat signal at 10.8 MHz was recorded with a spectrum analyzer[27]. The relative drift of the two lasers was compensated for the measurement by implementing a phase-continuous linear frequency chirp to AO2 (see Fig. 3.4). Figure 3.5 (a) shows the resulting power spectral density over the frequency for a 4 s integration time and a resolution bandwidth of 1 Hz. A Lorentzian fit yields a full width at half maximum (FWHM) line width of 1.8 Hz. Assuming both lasers having the same frequency spectrum, we infer a line width for each of the lasers of 0.9 Hz.

[23]based on Apex, PA98
[24]New Focus, 1601
[25]Rohde & Schwarz, SML01
[26]Laser 2000, custom-made fiber cord
[27]Rohde & Schwarz, FSP 9 kHz...13.6 GHz

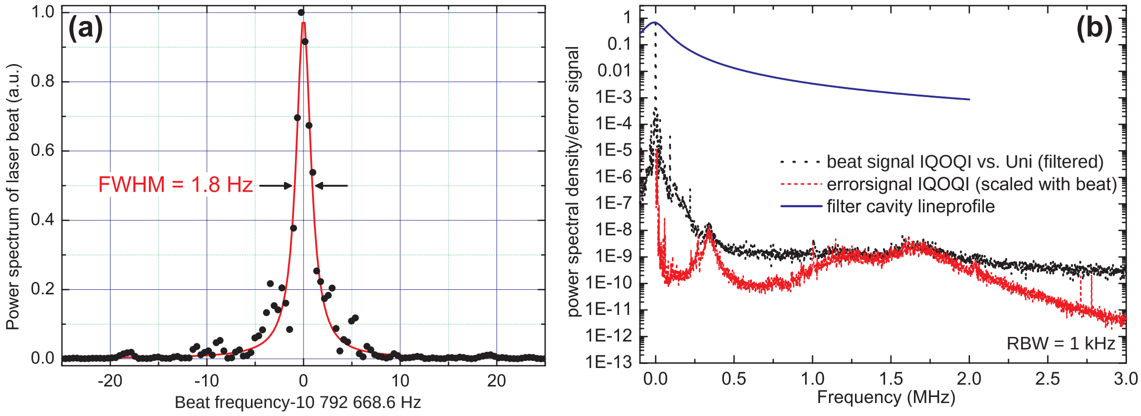

Figure 3.5: **(a)** Beat measurement of two remote lasers linked over a 500 m glass fiber with the fiber noise compensated. A Lorentzian fit yields a FWHM of 1.8 Hz, indicating a sub-Hertz line width for each laser within the measurement interval of 4 s. **(b)** Power spectral density of the laser beat where the reference laser is spectrally cleaned by sending it through a filter cavity. The transmission function of the filter cavity is given as the upper trace. By referencing the normalized spectrum of the error signal to the beat signal we can conclude that the measurement is largely limited by the reference laser and measurement sensitivity. From an integration of the power spectral density we obtain that a fraction of less than 10^{-4} of laser light power is outside a ±250 Hz interval of the laser's carrier frequency.

For the experiments described in chapter 7 the spectral purity of the light is of importance. This quantity is also accessible from the beat measurement. Since the control electronics of the two lasers are fairly different (e.g. servo oscillation frequencies), we do not expect them to have the same spectrum. In order to characterize our laser, we spectrally filtered the reference laser with a clean-up cavity. The transmission function of this clean-up cavity is given as upper line in Fig. 3.5 (b) and the normalized power spectral density of the laser beat measurement is plotted as middle trace for a resolution bandwidth of 1 kHz. The characteristics of the locking electronics is clearly visible as “servo bumps”. By referencing the normalized spectrum of the error signal to the beat signal we can conclude that the measurement is largely limited by the other laser and the sensitivity of the spectrum analyzer. From an integration of the power spectral density we obtain that a fraction of less than 10^{-4} of laser light power is outside an ±250 Hz interval of the laser's carrier frequency.

The output power of the laser is stabilized by diffracting a small amount of the light power to the first order of AO1. The error signal is derived with photodiode PD1[28], sent through a loop filter[29], and than fed back to a variable attenuator[30] to adjust the radiofrequency amplitude of AO1. The relative power stability was measured to be about 1%.

[28]Thorlabs, PDA100A-EC
[29]SRS, SIM960
[30]Mini Circuits, ZX73-2500

3.2.3 Raman beam setup

The purpose of the Raman beams is to manipulate quantum information encoded in the hyperfine splitting of the ground-state in $^{43}Ca^+$ by a bichromatic electromagnetic field. For this, two coherent light fields with a frequency separation of the hyperfine qubit's frequency of about 3.2 GHz are needed. In a configuration where the k-vectors of these two laser fields differ in angle, momentum can be transferred to and from the ions. For collinear lasers this is largely suppressed. By focusing the laser beams tightly, we have the ability to address individual ions in a string. Driving qubit transitions demands a fixed phase relation between the driving field and the qubit transition frequency. Assuming a fixed qubit frequency for the Raman interaction, this requires the two Raman light fields to be stable with respect to each other on the optical wavelength scale for the time of each experiment.

Decoherence by spontaneous scattering can be suppressed by larger detunings from the atomic level mediating the Raman transition while elastic scattering doesn't lead to decoherence (see subsection 2.5.4). High-speed operations while having large detunings requires a high amount of laser power. Furthermore, it is important that the output power has low amplitude noise and is stable over time. Demands regarding frequency stability are quite relaxed since variations of the absolute frequency of the laser give little effects for large detunings.

To meet these requirements light at 794 nm of an external cavity diode laser is amplified by a master-oscillator power-amplifier (MOPA)[31]. This light is frequency doubled by second harmonic generation using a LBO crystal in an enhancement cavity. The total output power is about 50 mW. The frequency of the laser can be set between 393 nm and 398 nm. For mode cleaning the light is then sent through a short single-mode polarization-maintaining fiber[32].

As discussed in section 2.5 there are four different ways to drive the transitions in the microwave domain, depending on whether the change in the magnetic field quantum number is zero or ± 1 and whether a coupling to the ion motion is needed. Full flexibility is obtained by the generation of two red detuned and two blue detuned light fields that are sent to the ions from different directions.

The frequency splitting of 3.2 GHz is achieved by sending the laser through a cascade of AOM's (see Fig. 3.6). AO1 operating at 1 GHz[33] splits the laser beam into two beamlines. The minus first diffraction order starts the red beamline and the zeroth diffraction order the blue beamline. In the red beamline three AOM's at frequencies of 300 MHz[34] follow, such

[31] Toptica, TA-SHG
[32] Schäfter + Kirchhoff, PMC
[33] Brimrose, QZF-995-20, maximum diffraction efficiency to the first order is 15%
[34] Brimrose, QZF-300-50, maximum diffraction efficiency to the first order is 70%

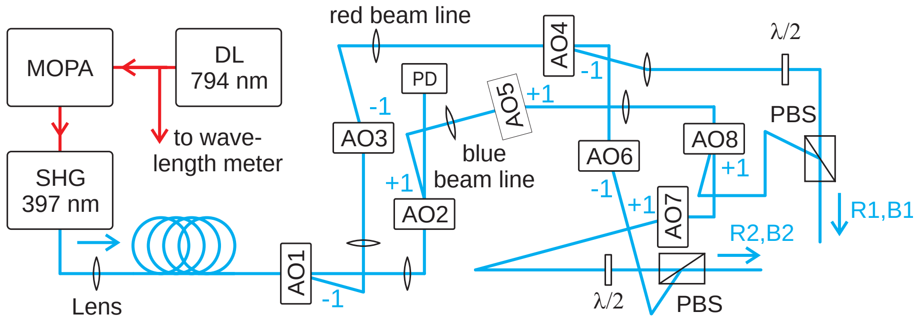

Figure 3.6: Schematics of the Raman beam setup and the generation of the 3.2 GHz frequency separation. AO1 and AO2 run at a fixed frequency of 1 GHz. The drive frequencies and radiofrequency amplitudes powering AO3 to AO8 are derived from the versatile frequency source (see section 3.7) in combination with a network of radiofrequency switches. All diffraction orders of the AOM's are given in the figure. The signal of the photo diode (PD) monitoring the light intensity of the fundamental beam of AO2 is fed back to the current powering the MOPA in order to stabilize the light intensity.

that two beams with a detuning of -1.6 GHz from the incoming light can be individually frequency controlled and switched. The blue beamline consists of another 1 GHz AOM which is then followed by three AOM's at 300 MHz. The input of the two 1 GHz AOM's is provided by a signal generator[35] with an amplifier[36] and kept constant during the experiments. The 300 MHz AOM's are all connected by a network of radiofrequency switches and amplifiers to the radiofrequency output of the versatile frequency source (see section 3.7). So any pair of light fields can be accurately switched, amplitude-shaped and their relative frequencies can be set within an experimental cycle. The output of the setup consists of two laser beamlines each containing a blue and a red detuned light component which are then sent through a beam expander and a focusing lens to the ions. Typically, about 10% of the light intensity sent into AO1 is effectively used as Raman light field.

In order to cope with the high demand of interferometric stability, the whole setup was put as close to the trap as possible. Additionally, all parts were assembled as near to the optical table as possible and enclosed to prevent disturbances from air turbulence. To suppress the sensitivity to acoustical and mechanical noise further, it was built such that it encloses a possibly small area ($\sim 0.04\,\mathrm{m}^2$). In case momentum has to be exchanged between the Raman light fields and the ions, a non copropagating pair of lasers is needed. These are split such that they can be sent to the ions under an angle of 90° with the differential k-vector pointing along the trap axis. From the point of splitting (AO1) to the ions these two beams enclose an area of about $0.15\,\mathrm{m}^2$.

Due to the finite diffraction efficiencies of the AOM's a large fraction of the light sent into the frequency separation setup remains in the zeroth order of AO2 (see Fig. 3.6).

[35]Rohde & Schwarz, SML-01
[36]Mini Circuits, ZHL-1000 3W

This light is monitored with a photodiode (PD) and the signal is fed back to the current powering the MOPA, in order to stabilize the Raman beams' power.

3.3 Vacuum vessel

The vacuum system housing the ion trap is all made of stainless steel and consists of an octagon with two conflate flanges (CF200) on top and bottom and eight CF63 flanges in the equatorial plane. A schematic drawing is given in Fig. 3.7 (c). A six-way cross is attached to the western CF63 flange and carries an ion pump[37], a titanium sublimation pump[38] (TSP), a Bayard-Alpert-Gauge[39] and an all-metal valve[40]. Three of the eight CF63 octagon flanges are equipped with inverted viewports[41]. This enables us to bring lenses close enough to the ions in order to have a good imaging resolution, photon collection efficiency and the ability to narrowly focus lasers to individual ions while having the ability to steer or replace the lenses without opening the vacuum can. The other flanges have regular viewports[42] attached. The CF200 flange mounted on the bottom side carries two CF40 windows and two CF16 electrical feedthroughs to which the calcium ovens are connected. The CF200 flange atop the octagon provides support for the ion trap. Furthermore, it has two CF40 viewports and also a CF16 flange with four electrical feedthroughs for the DC-electrodes (trap tips and compensation electrodes).

After baking the system at a temperature of 350 °C for one week the turbopump was detached by closing the all-metal valve. At this time a pressure of 10^{-10} mbar was measured. Since then the ion pump runs permanently whereas the TSP is used irregularly about once per week. The measurement limit of the Bayard-Alpert-Gauge is 2×10^{-11} mbar. When the TSP is used every three days, the pressure drops below this limit. Lifetimes of a single trapped ion of up to 13 days (with all lasers off) have been observed.

3.4 Magnetic field coils and current drivers

To control the magnetic field at the trap center two coil pairs are placed symmetrically with an angle of 90° in the equatorial plane (see Fig. 3.7 (c)). Though the ratio of their distance (300 mm) and their inner diameter (115 mm) doesn't fulfill the Helmholtz criterium exactly, we expect low gradients at the position of the ions. The coil pair[43]

[37] Varian Star Cell, 20 l
[38] Varian
[39] Varian, UHV-24 Gauge
[40] VAT
[41] Ukaea, fused silica, anti reflection coating (Tafelmaier, 397 nm and 720-870 nm) on vacuum side only
[42] Caburn, fused silica, anti reflection coating (Tafelmaier, 397 nm and 720-870 nm)
[43] Oswald Elektromotoren, copper wire with cross section $2.0 \times 1.25\,\mathrm{mm}^2$

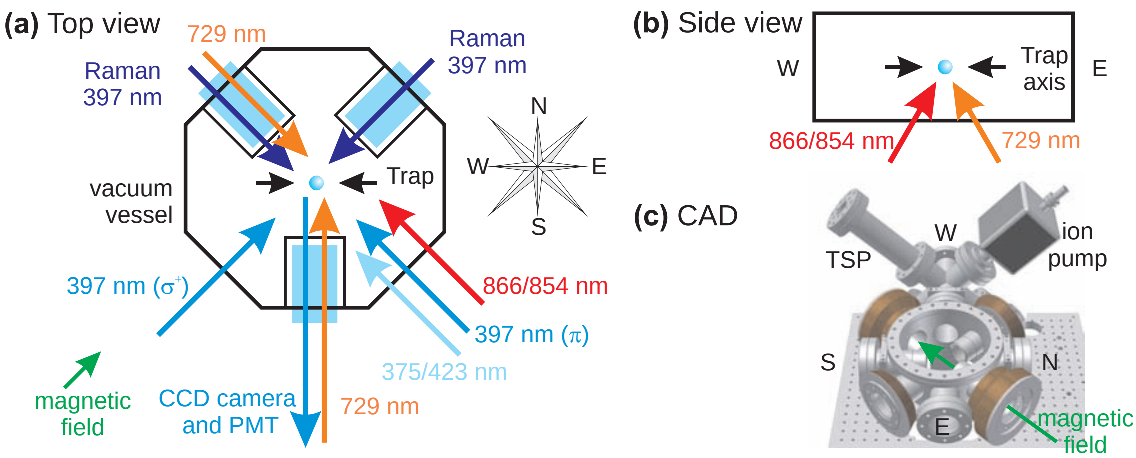

Figure 3.7: **(a)** Schematic top view onto the trap setup. The quantization axis is provided by a small magnetic field along SW-NE and most of the laser beams sent to the ions lay within the equatorial plane. Custom made lenses are placed close to the ions by means of three inverted viewports (NW, NE, S). This allows us to focus laser beams tightly, and to achieve a high efficiency collecting the ions' fluorescence. **(b)** The side view onto the setup shows the two beams sent in through the viewports of the bottom flange in a 60° angle with respect to the trap's symmetry axis. It is a second repumper beam and a laser beam at 729 nm, which typically is used for sideband cooling. **(c)** Computer aided drawing of the vacuum setup. The TSP and the ion getter pump are mounted to the six-way cross as seen in the back. Two large coils (SW, NE) provide for the magnetic field defining the quantization axis. The other coil pair compensates for external magnetic fields along SE-NW.

defining the quantization axis has 350 windings of copper wire. Sending 1 A through both coils results in a magnetic field of 3.4 G. Perpendicular to these a coil pair of 100 windings of copper wire each is used to compensate for external magnetic fields. In addition, a single large coil (diameter 200 mm) is used to compensate for stray fields along the direction of gravity.

To set the magnitude and orientation of the magnetic field, a single $^{40}Ca^+$ ion was loaded into the trap. The ambient magnetic field was nulled by applying currents to all coils so as to minimize the ion's fluorescence by varying the current through the five coils around the trap. After that, the amplitude and the direction of magnetic field can be set by changing the current through the pair of coils defining the quantization axis. All coils are powered by home-made current drivers having a relative current drift of less than 2×10^{-5} in 24 h. This is achieved by a servo loop with a highly stable resistor[44] as reference.

3.5 Optical access and individual ion addressing

Laser light is guided to the ions through seven different viewports (see Fig. 3.7). The light for Doppler-cooling, repumping, photoionization and sideband cooling is sent to the ions

[44]Vishay, VCS 302

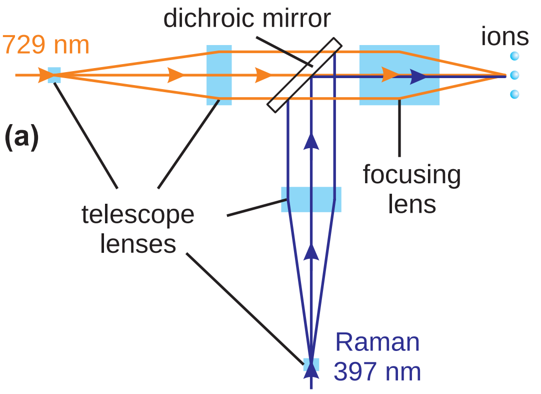

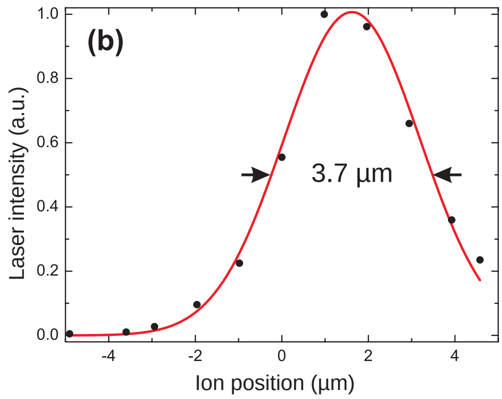

Figure 3.8: **(a)** Arrangement of the lenses in order to focus light at wavelengths 729 nm and 397 nm through the same focusing lens. A similar setup using a dichroic mirror is used for the imaging port (S) which is simultaneously used for focusing light at a wavelength of 729 nm. **(b)** Measurement of the intensity profile of the laser beam at 729 nm entering from the southern viewport. For the measurement a single ion was moved witch respect to the position of the laser by changing the tip voltages. At each point Rabi oscillations on a quadrupole transition were recorded with the same laser power. From the π-time we derived the relative laser intensity for eleven different tip voltage settings. The ion's position was measured by observing the shift on the CCD image.

directly by adjusting the output couplers of the optical fibers such that the light is focused at the ions' position. Typical beams waist are about 100-200 μm, which is a good trade-off between high enough intensities for the given laser powers, alignment stability and equal illumination of ions for multiple ion crystals.

For the four Raman beams and the light at a wavelength of 729 nm that is sent in within the equatorial plane individual ion addressing should be possible. It is a basic requirement for quantum state tomography and also needed for certain two-qubit gates. Typically, we have to deal with ion distances of 4-5 μm which requires a laser spot size significantly smaller, if a Gaussian beam is assumed. For this purpose a lens system was designed that consists of two telescope lenses in order to expand the beam. This large and almost collimated beam is then sent through one of the three focusing lenses inside the inverted viewports (see Fig. 3.8 (a)). Ideally the light is focused down to a diffraction limited spot size of 1.7 μm (2.9 μm) for light at 397 nm (729 nm). The focusing lens is also used for imaging (see section 3.6). In practice it is quite challenging to adjust the optics properly such that the diffraction limit is obtained. So far, only the beam at 729 nm entering from the southern viewport has been tightly focused. A single ion was used as a probe and revealed a FWHM resolution of 3.6 μm (see Fig. 3.8 (b)). The ability of single ion addressing for a two ion crystal is demonstrated in section 4.6.

In order to address different individual ions lined up in a linear chain, we can either steer the laser beams accordingly or move the ions. In another experiment of the group, the concept of deflecting a laser was thoroughly investigated. A number of major disadvantages became evident. First, only electro-optic deflectors have proven to be fast and precise enough for the technical implementation. However, these need fast high voltage supply electronics and one deflector is needed for each beam. Moreover, the maximum deflection angle is rather small whereas at the same time adjustment and focusing gets more involved since these deflectors alter the Gaussian modes notably. Last, though the deflectors can switch within a few microseconds, experiments have shown that it takes a settling time of more than 200 μs until the optical phase is in a steady state. These issues let us conclude that for an experiment, where in the long run more than a single laser beam shall be addressed, a shuttling of the ions by quickly adjusting the two tip voltages while having fixed laser foci seems more attractive. In order to avoid a change of the population in the harmonic oscillator mode, the relative potential of the two tips preferably stays constant during this process such that its curvature of the potential doesn't change. In a first attempt only an adiabatic movement was considered, where the ion was accelerated slowly compared to the inverse of the lowest trap frequency such that a transfer of energy to the ions' motional mode is expected to be negligible. Technically this was realized by referencing the electronics providing the differential tip voltages to a high voltage power supply that provides the axial trapping potential. Analog inputs for setting certain different axial trapping positions and the logical inputs, to switch among them during a sequence, are interconnected to the analog and logical output of the experiment control by means of analog and fast logical optocouplers[45]. The two high voltage outputs are connected to the trap tips with low-pass filters in between. These have a time constant such that full settling is observed after 40 μs (see section 4.5), which corresponds to roughly 50 axial oscillations of the ions. On one hand the low-pass filters screen the trap electrodes from high frequency noise heating up the ions. On the other hand they shield the high voltage electronics from radiofrequency pick-up by the trap's tip electrodes.

3.6 Fluorescence detection

Light emitted by the ions at a wavelength of 397 nm is collected by a custom-made objective[46]. Consisting of five lenses (see Fig. 3.9 (a)), this objective is corrected and antireflection coated for the wavelengths 397 nm and 729 nm. Three of the lenses are mounted outside the vacuum in inverted viewports with a distance of $r = 58$ mm (first lens surface on optical axis) to the ions. The spherical abberation induced by the 6 mm fused silica window corrected by the lens design. The entrance diameter towards the ions is $d = 38$ mm. With these parameters we can calculate the collection efficiency of the light emitted by the ions

$$\frac{d\Omega}{4\pi} = \frac{1}{2}\left(1 - \sqrt{1 - \frac{1}{1 + (\frac{2r}{d})^2}}\right) \approx \frac{1}{40}.$$

[45] Todd P. Meyrath, University of Texas at Austin

[46] Silloptics, Germany

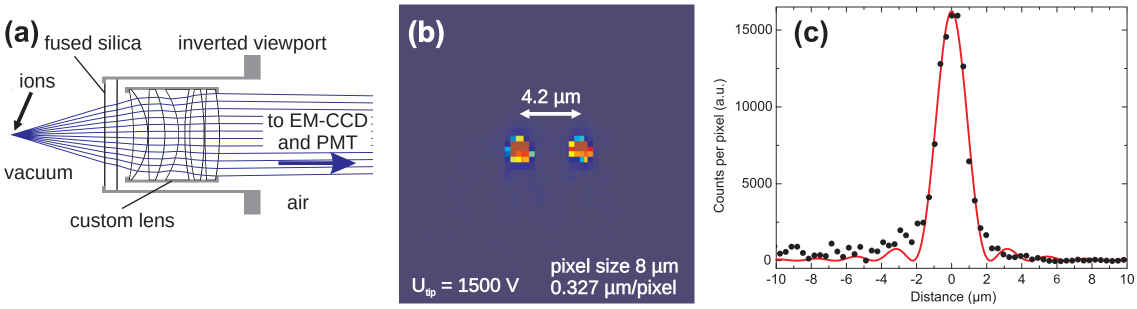

Figure 3.9: **(a)** Schematics of the custom-made lens used to collect fluorescence light for the ion detection with the EM-CCD camera and a PMT. The same type of objective is used to focus light of the wavelengths 729 nm and 397 nm tightly. **(b)** Ion crystal of two $^{43}Ca^{+}$ ions recorded with the EM-CCD camera. The tip voltage was set to $U_{tip} = 1500\,\mathrm{V}$ which corresponds to an axial trap frequency of about $\omega_{\mathrm{ax}}/(2\pi) = 1.46\,\mathrm{MHz}$ and an ion separation of $4.2\,\mu\mathrm{m}$ **(c)** After defining a region of interest around a single ion the pixel counts from a CCD-image were summed up in vertical direction. Small imperfections can be seen on the left side of the peak. These are attributed to imperfect alignment. A least square fit with a sinc-function (solid line) to the data points yields a distance of $2.2\,\mu\mathrm{m}$ from the first minimum to the center.

Measurements have shown a $2.2\,\mu\mathrm{m}$ imaging resolution (see Fig. 3.9 (c)) at a wavelength of 397 nm. This enables us to discriminate light emitted from neighboring ions easily (see Fig. 3.9 (b)). The absorptive loss is 4% by the objective and another 6% by a narrow bandpass filter[47] used to suppress stray light leaking to the detection system. As discussed in section 3.5 the same lens is used to achieve small laser spot sizes at the position of the ions for individual addressing.

With a switching box, containing a coated window, a 90 : 10 beam-splitter and a mirror, we can send the light collected by the objective either to a camera or to a photo-multiplier tube[48] (PMT) or both of them at the time. In the branch of the PMT, at the place of the image, a variable slit aperture is installed[49] to choose a small field of view in order to suppress stray light detection. The image plane is about 1.5 m behind the lens which results in a magnification of 24.5. Unless mentioned otherwise in the text, all experiments were performed with PMT detection. This has foremost the advantage that for state discrimination the data can be directly read out and processed by acquiring a histogram and setting a proper threshold. An example is given in Fig. 3.10. From the observed count-rate, we can distinguish between events, when the ion is projected into the $S_{1/2}$-state where it emits light, and events where the $D_{5/2}$-state is populated and no fluorescence is observed. By counting the number of events for a total number of measurements N, we determine the probabilities p_0 and p_1 corresponding to $|\alpha|^2$ and $|\beta|^2$ of Eq. (2.1). The statistical error in the determination of the state's population probabilities is also termed

[47]Semrock, FF01-377/50-23.7-D
[48]Electron tubes, P25PC, Quantum efficiency = 28% at 400 nm
[49]Owis, Spalt 40

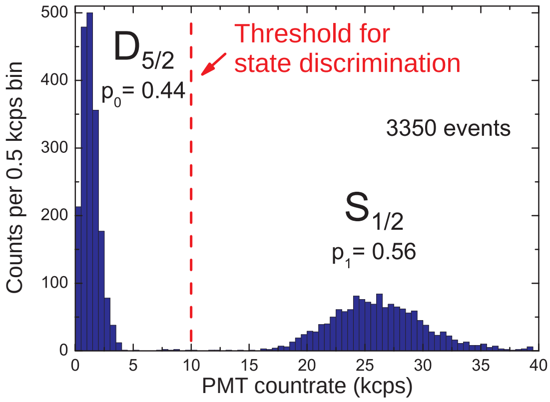

Figure 3.10: The histogram illustrates the dicrimination of the two electronic states $S_{1/2}$ and $D_{5/2}$ of a single $^{40}Ca^+$ ion by means of a PMT. The ion was prepared in a superposition of the $S_{1/2}(m_J = 1/2)$ and $D_{5/2}(m_J = 5/2)$-states. For each data point the average fluorescence rate was determined over an interval of 5 ms. The plot shows a total of 3350 measurement results. By setting a threshold at for example 10 kcps, we can distinguish between events, when the ion is projected into the $S_{1/2}$-state where it emits light, and events where the $D_{5/2}$-state is populated and no fluorescence is observed. By comparing the quantities for each of the cases, we determine the probabilities p_0 and p_1 corresponding to $|\alpha|^2$ and $|\beta|^2$ of Eq. (2.1).

quantum projection noise Δp_{QPN}. It depends on the number of measurement repetitions as

$$\Delta p_{\mathrm{QPN}} = \sqrt{\frac{p_k\,(1 - p_k)}{N}}. \tag{3.6}$$

This state discrimination scheme works also for multiple ions, where for each set of measurement the probabilities p_k to observe k fluorescing ions are estimated.

For experiments with more than one ion the camera brings in the advantage of individual ion detection. The camera used is a Electron Multiplying Charge Coupled Device (EMCCD) camera[50]. By making use of an extra amplification register this technology offers single photon detection sensitivity and sufficiently short exposure times (~5 ms). This comes at the overhead of additional complexity since the camera is controlled by an additional computer which takes care of the communication with the camera and the image evaluation. This action has to be synchronized with the experiment control computer.

At this stage, the camera was mainly used to determine the number of ions loaded and to see that they are properly cooled and form a Coulomb crystal.

3.7 Experiment control and radiofrequency pulses

Most of the systems proposed for QIP need modulated electromagnetic waves. In the case of trapped ions this necessitates the control of the frequency and phase of certain laser

[50] Andor , Ixon DV885JCs-VP, Pixel size 8 × 8 μm, Quantum efficiency at 397 nm is 37%

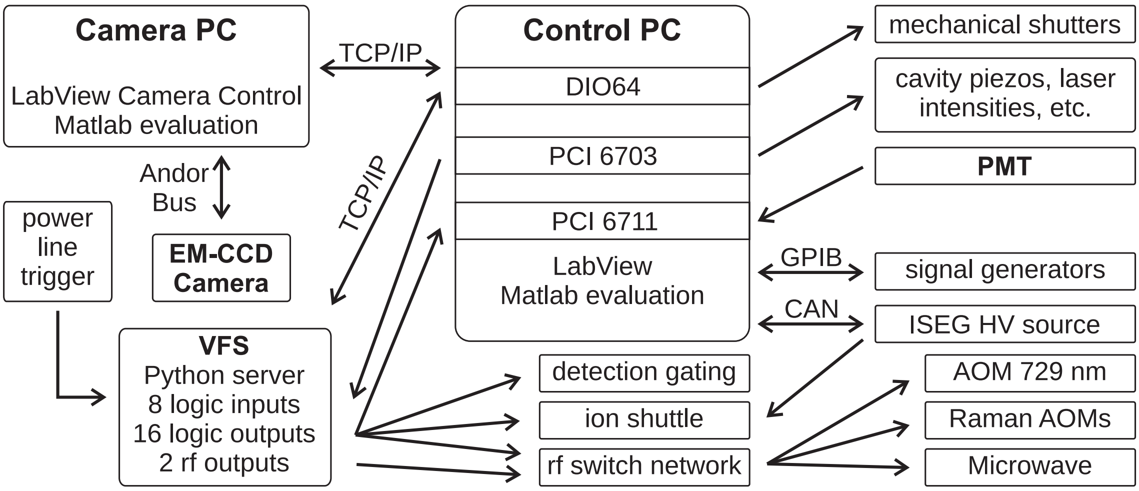

Figure 3.11: The experiment is controlled by a software written in LabView running on two Windows PCs. One controls the EM-CCD camera (Camera PC) including data acquisition and evaluation. The other one controls the remaining hardware of the experiment, collects data from the Camera PC and the PMT and programs the versatile frequency source (VFS) which is triggered by the AC power line and autonomously provides all radiofrequency and digital signals in the pulsed mode (see section 4.2) . The sketch shows the different hardware components and their interconnections with different bus systems.

light fields. This is achieved by the use of AOM's, which directly transfer frequency and phase information from the radiofrequency to the optical domain, with a high bandwidth. In this way, the problem is reduced to the generation of precisely timed digital signals (e.g. switching of lasers, trap potentials, etc.) and the generation of various phase-coherent and amplitude-shaped radiofrequency pulses. For this purpose a versatile frequency source [104, 105] was developed. Its working principle is based on a direct digital synthesis microchip controlled by a field-programable gate array (FPGA). It has two separate radiofrequency outputs that can deliver up to 16 different frequencies in each experimental cycle and allows for phase coherent switching between those frequencies. Amplitude shaping of the radiofrequency pulses is achieved by means of a variable-gain amplifier that is also controlled by the FPGA. Typically, the radiofrequency pulse lengths are in a range from 1 μs up to 100 ms. In addition, the versatile frequency source has 16 logic channels (TTL) with a timing resolution of 10 ns. These are used in combination with a network of radiofrequency switches, amplifiers, attenuators and mixers to send the radiofrequency pulses individually or combined to the double pass AOM controlling the frequency of the laser at 729 nm, to the AOM's controlling the frequency difference of the Raman light fields or as direct microwave source at 3.2 GHz. The frequency output is limited to values below 310 MHz. Higher frequencies are achieved by proper mixing and filtering. The frequency resolution is about 0.1 Hz. The versatile frequency source runs a Python[51]-server and is connected to the experiment control computer by ethernet network cable. It is

[51] High-level programming language

programmed before each experimental sequence. The box is armed by a trigger signal of the experiment computer. Each experiment is then started through a trigger pulse coming from the power line trigger and so every experiment is synchronized to the AC power line's phase. Both of these trigger signals are connected to one of the eight logical inputs of the versatile frequency source that can also be used to branch sequences depending on an input acquired during each experiment.

The versatile frequency source and the other hardware of the experiment is controlled by a computer using software written in Labview[52]. There are a number of different interfaces to the experimental hardware. Readout of PMT data is performed with a fast counter input card[53]. Analog outputs are mainly controlled by a 16 channel analog interface PCI card[54] and digital outputs that have not to be switched within a sequence are connected to a fast digital input and output card[55]. Some of the signal generators are computer-controlled via a GPIB-bus[56]. The high voltage source providing the tip voltage[57] is connected by CAN-bus[58] to the control PC. Figure 3.11 shows the different hardware components and their interconnections.

[52]Programming language by National Instruments
[53]National Instruments, PCI 6711
[54]National Instruments, PCI 6703
[55]United Electronic Industries, DIO 64
[56]IEEE-488, short-range, digital communications bus
[57]ISEG, EHQ F020p, up to 2 kV with ripples $< 10^{-5}$
[58]Controller Area Network, serial bus standard

4 Experimental techniques

This chapter explains the fundamental techniques and concepts applied in our experiments with trapped calcium ions. Some of them such as the compensation of excess micromotion and the measurement of heating rates are used to further characterize the new experimental setup. Most others are part of a daily experimental routine or hint at future options. The topics are arranged in a natural order reflecting their temporal order in the stage of setting up the experiment.

4.1 Trap loading by photoionization

Loading ions into the trap is one of the most basic experimental requirements. Most ion trapping experiments have in common that the traps are loaded from a flux of neutral atoms, which are ionized within the trap volume. Ideally, the atom flux is confined to a small region, such that the trap electrodes are not contaminated, which could lead to small changes in the patch potentials. Moreover, an efficient ionization process helps to reduce the neutral atom flux and associated contaminations. For this particular experiment we want to choose between loading $^{43}\mathrm{Ca}^+$ and $^{40}\mathrm{Ca}^+$ ions.

These requirements are met by an isotope-selective two-step photoionization [95, 106]. The first transition from the ground-state 4s $^1\mathrm{S}_0$ to the excited state 4p $^1\mathrm{P}_1$ in neutral calcium (line width $2\pi\times 35$ MHz) is driven by an external cavity diode laser in Littrow configuration at 423 nm[1]. Its frequency is monitored by saturation spectroscopy (see Fig. 4.1 (a)+(b)) on a calcium vapor cell held at a temperature of 300 °C. The cell was filled once, evacuated with a roughing pump while heated to about 400 °C; then the valve was closed and the pump was detached. The cell has been in continuous operation for more than two years now. In order to adjust the frequency for the different isotopes, we use a wavelength meter[2] with a resolution of 10 MHz. The second excitation step connecting the 4p $^1\mathrm{P}_1$-state to continuum states requires light with a wavelength below 389.8 nm (see Fig. 4.1 (c)). In our experiment this is accomplished by a free-running laser diode at 375 nm[3]. The two beams

[1] Toptica DL-100, Nichia laser diode, 30 mW
[2] Toptica WS-7
[3] Nichia, 5 mW

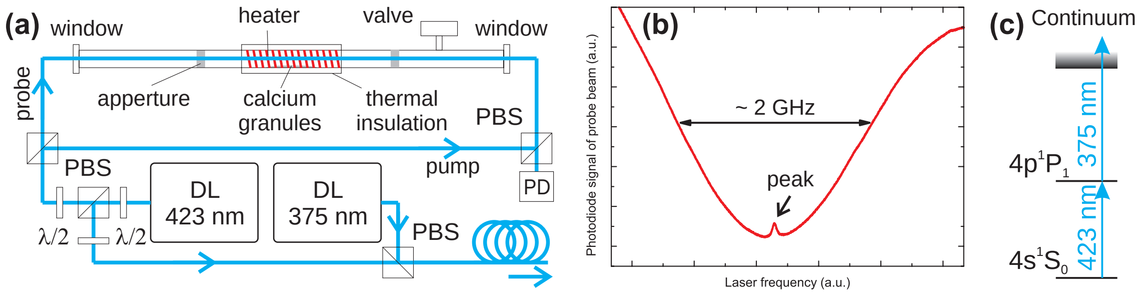

Figure 4.1: **(a)** Setup of the photoionization lasers and the Doppler-free saturation spectroscopy. The calcium vapor cell is kept at 300 °C. Two cold apertures prevent the vacuum windows from being coated with calcium atoms. **(b)** Typical photodiode signal derived from the saturation spectroscopy on neutral calcium atoms. The peak in the middle has a width of about 35 MHz. The FWHM of the whole profile is given by the Doppler-broadening of about 2 GHz at 300 °C. **(c)** Energy level scheme for the two step photoionization of neutral calcium as used in the experiment. The first stage at a wavelength of 423 nm can be used for isotope selection. The shift for the various isotopes on this transition is given in Tab. 4.1.

are superimposed on a polarizing beam splitting cube[4] and then sent through a single-mode glass fiber[5] to the experiment, where the light is focused at the trap center by the output coupler of the glass fiber. 50 μW light power at a wavelength of 423 nm is sufficient to achieve saturation on the first stage (beam waist $\sim$100 μm). Higher intensities do not increase the loading rate but instead decrease isotope selectivity due to power broadening. Thus, the bottle neck of the process is the light power available for the second stage. Typically, we use 500 μW of light power at 375 nm. To demonstrate that a coherent light source is not required we have also tested a light emitting diode (LED)[6] for the second stage. The LED was emitting about 2 mW light power in a spectrum of 370-390 nm and provided good loading rates for slightly higher currents as for the laser. Since the emitting surface and angle are rather large the major challenge with the LED is to get enough light intensity inside the small trap volume.

The flux of neutral calcium atoms is provided by a home-build oven construction. It consists of an 8 cm stainless steel tube that is connected to the end of an electric feedthrough of the bottom flange. A tantalum square is spot-welded to the middle of the tube, which is then connected to another electrical feedthrough. The lower part of the tube contains metallic calcium granules. By adjusting the electric current over this lower part of the stainless steel tube, calcium can be easily heated to several hundred degrees Celsius. At temperatures slightly below 300 °C the neutral atom flux through the trap volume is high enough to achieve loading rates of about one ion per second.

Two of these ovens are built into the vacuum vessel, one of them being filled with natural metallic calcium granules. It is used to efficiently load $^{40}Ca^{+}$ ions. Another oven contains

[4]Lens Optics
[5]Oz Optics, QSMJ-A3A-400-3/125
[6]Roithner Lasertechnik, UVLED380-10, directivity 10°

Mass number	Natural abundance	Enriched source	Isotope shift
40	96.9%	12.8%	0 MHz
42	0.647%	0.7%	393.5(2) MHz
43	0.135%	81.1%	611.8(3) MHz
44	2.09%	5.4%	773.8(3) MHz
46	0.004%	<0.1%	1159.8(7) MHz
48	0.187%	<0.1%	1513.0(4) MHz

Table 4.1: The table shows the fraction of different isotopes for a natural source of calcium and a ^{43}Ca enriched sample that is used in a second oven. In addition, the isotope shifts occurring in the first stage of the photoionization scheme are given relative to the transition of ^{40}Ca [107].

approximately 5 mg of metallic ^{43}Ca$^+$ isotope-enriched metal granules[7]. Table 4.1 shows the fractions of different isotopes in each of the ovens and the isotope shift on the first stage of the photoionization scheme.

At the time when the experiment was set up it was unclear whether the isotope-selectivity due to the transition frequency differences of the photoionization's first stage was high enough to reliably load ^{43}Ca$^+$, which is of higher importance the larger the ion crystals get. From the relative occurrence of ^{40}Ca and ^{43}Ca in a natural source it was concluded, assuming a Lorentzian line shape, that the relative loading rate for ^{43}Ca$^+$ ions compared to other isotopes is only about 50%. Meanwhile it has been shown though, that by the proper choice of cooling laser frequencies the selectivity from a natural source can be largely enhanced [106, 108]. A problem that then still remains is isotope replacement by bombardment with neutral atoms due to charge-exchanging collisions. Therefore, in particular when larger ion crystals of a rare isotope are needed, it still makes sense to use an enriched source.

The appearance of ions in the trap is usually monitored by means of the EM-CCD camera with the experiment operated in a *continuous mode* where all lasers powers, frequencies, etc. can be adjusted manually. In case of ^{40}Ca$^+$ ions, only the laser fields at 866 nm and 397 nm are required to observe a fluorescence signal. We usually set the loading rate to about one per 20 s. Larger crystals are obtained by waiting for the right number of ions to appear. It happens often that instead of a single ion two or even three are loaded simultaneously. Unfortunately, we can only eject all of them at the same time by switching off the radiofrequency confinement and have to start loading again if we need a smaller number. After loading the continuous mode is used to optimize the fluorescence signal and to set proper conditions for Doppler-cooling, detection, etc.

In order to load ions for the first time and to improve on the signal-to-noise ratio of the

[7] Oak Ridge National Laboratory

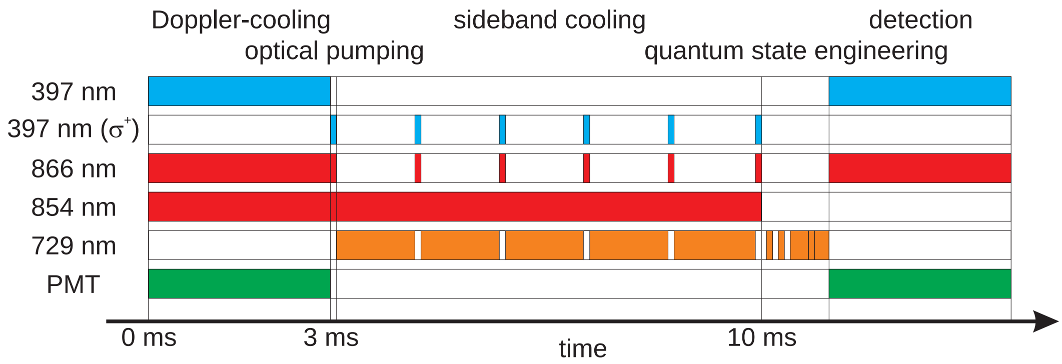

Figure 4.2: Typical sequence of laser pulses for experiments performed in the pulsed mode. The five building blocks of the pulsed mode are indicated on top. Usually these sequences are repeated 50, 1000 or 200 times for each setting.

imaging system it is helpful to operate the experiment in a *differential mode*. Here the cooling laser at a wavelength of 397 nm illuminates the ions continuously whereas the laser at 866 nm is switched on and off at a rate of 20 Hz. In the absence of this laser the ions are immediately pumped into a dark state and stop to fluoresce. By subtracting the fluorescence signal for the time the laser at 866 nm is off from the signal when it is on, we are able to get rid of a possible stray light offset caused by the cooling laser at a wavelength of 397 nm. Light at 866 nm is efficiently filtered and cannot leak towards the PMT and camera. Ion signals as small as 1000 counts per second have been observed on a background which was 400 times higher. Moreover, with this method we can directly optimize the signal-to-noise ratio of the detection by adjusting laser powers, polarizations and the slit aperture in front of the PMT. For $^{40}Ca^+$ ions, the signal-to-noise ratio is typically between 100 and 200. In case of $^{43}Ca^+$ ions it is ranging between 30 and 70 due to the higher laser powers required and smaller fluorescence count rate (see subsection 6.1.1).

4.2 Pulsed mode

After the laser frequencies and powers are set properly in the continuous mode, we switch to a *pulsed mode* which consist of five basic building blocks. These shall be briefly discussed for $^{40}Ca^+$ ions as an example:

1. *Doppler-cooling*: A slightly red detuned laser on the $S_{1/2} \leftrightarrow P_{1/2}$ transition (397 nm) causes the ions to fluoresce and leads to Doppler-cooling. A laser on the transition $D_{3/2} \leftrightarrow P_{1/2}$ (866 nm) prevents pumping into a dark state. After 3 ms the ions have a mean vibrational quantum number between about 5 and 20.
2. *Optical pumping*: A short pulse with a σ^+-polarized laser on the $S_{1/2} \leftrightarrow P_{1/2}$ transition in combination with light at 866 nm and 854 nm transfers the population into $S_{1/2}(m_J = 1/2)$.

3. *Ground-state cooling*: A certain motional mode can be cooled to the ground-state by tuning a narrow bandwidth laser to the red sideband of the transition $S_{1/2}(m_J = 1/2) \leftrightarrow D_{5/2}(m_J = 5/2)$ (729 nm). For every state transfer from $S_{1/2}$ to $D_{5/2}$ one motional quantum can be taken away from the ions. By simultaneously exciting the transition $D_{5/2}(m_J = 5/2) \leftrightarrow P_{3/2}(m_J = 3/2)$ (854 nm) the population is pumped to the $P_{3/2}(m_J = 3/2)$-state from where a decay back to $S_{1/2}(m_J = 1/2)$ takes the entropy away. After 7 ms enough photons are scattered and the ion is cooled to the ground state. The small leak of this cooling cycle due to the finite decay probability from the $P_{3/2}$-state to the $D_{3/2}$-state is closed by introducing a few steps of optical pumping.
4. *Laser spectroscopy/quantum state engineering*: With the ions prepared in the motional ground-state and initialized to a distinct electronic state we can start probing the $S_{1/2} \leftrightarrow D_{5/2}$ quadrupole transition or implement a pulse sequence to realize a certain protocol for QIP.
5. *State discrimination:* Finally, the lasers at 397 nm and 866 nm are switched on for a few milliseconds and the fluorescence is detected either by a PMT or an EM-CCD camera. We can discriminate only between the $S_{1/2}$ and the $D_{5/2}$ levels in this step. Population of other levels can be measured by including appropriate transfer pulses into the step prior to the detection.

The temporal switching of the different lasers involved is sketched in Fig. 4.2. Typically, such an experimental cycle is repeated between 50 and 200 times with the same setting to acquire enough statistical significance for the measured probability values. This is what we refer to as a single measurement or data point. For the observation of Rabi oscillations on a certain transition, the quantum state engineering would consist of a single laser pulse whose length is increased for every subsequent data point. An example is given in Fig. 6.4 (a).

For $^{40}Ca^+$ ions, a more detailed description of the pulsed scheme can be found in the references [89, 96]. For $^{43}Ca^+$ ions, the same five building blocks apply but the laser scheme used on each of them is quite different and a detailed discussion is given in chapter 6.

4.3 Compensation of excess micromotion

External forces due to electric fields from the environment but also from geometric imperfections of the trap construction can shift the ions away from the radiofrequency zero line. As a result the ions experience an oscillating electric field of the trap drive and start moving with amplitudes that can easily exceed a wavelength of the cooling laser. This gives rise to Doppler-shifts leading to a number of negative consequences, among which

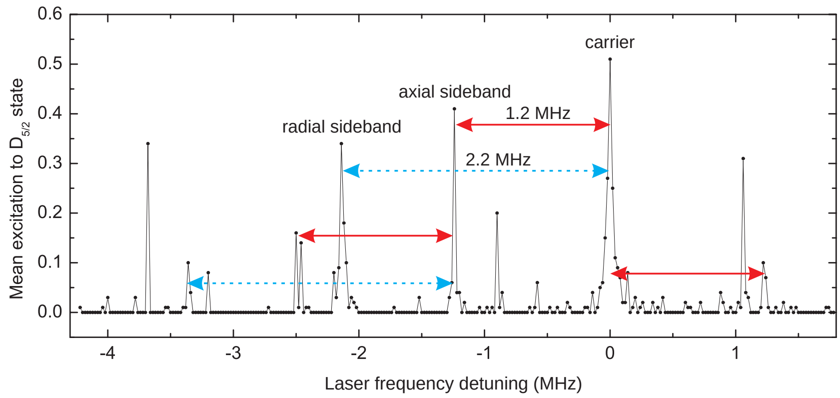

Figure 4.3: Spectrum around the carrier transition $S_{1/2}(m_J = -1/2) \leftrightarrow D_{5/2}(m_J = -3/2)$ with a 6 MHz span and a resolution of 10 kHz recorded at a magnetic field of about 3.5 G. Axial sidebands occur at relative frequencies of $\omega_{\mathrm{ax}}/(2\pi) = 1.2\,\mathrm{MHz}$ from the carrier. The radial sidebands are separated by $\omega_r/(2\pi) = 2.2\,\mathrm{MHz}$ from the carrier. The arrows indicate these frequency separations. Some of the lines in the spectrum can be identified as higher order sidebands.

are a decrease in Doppler-cooling efficiency, shortening of the life time of ions in the trap, second order Doppler-shifts as well as AC-Stark shifts leading to errors in high accuracy studies, etc. As a driven motion it cannot be cooled.

A steady state solution to the optical Bloch equations taking into account the Doppler-effect caused by micromotion [97] results in a probability of the upper level populations of

$$P \propto \Omega^2 \sum_{n=-\infty}^{\infty} \frac{J_n^2(\beta)}{(\Delta\omega + n\Omega_{\mathrm{rf}})^2 + (\Gamma/2)^2}, \tag{4.1}$$

where Ω is the carrier Rabi frequency for the ion at rest, Γ is the line width of the transition and $\Delta\omega$ is the detuning between the laser frequency ω_{L} and the atomic transition frequency. For the $S_{1/2} \leftrightarrow P_{1/2}$ cooling transition we are typically in a regime where $\Omega_{SP} \leq \Gamma_{SP}$. An increasing modulation index β effectively broadens the transition line width and leads to a rise of the Doppler-temperature

$$T_D = \frac{\hbar\Gamma_{SP}}{2k_B\omega_{\mathrm{L}}}$$

where k_B is the Boltzmann constant. Particular values of β can even lead to changes of the line structure such that heating of the ions occurs in situations where cooling is expected.

For the quadrupole transition we have $\Omega_{SD} \gg \Gamma_{SD}$. Therefore, with an increase in β the spectrum develops sidebands at multiples n of the trap drive frequency Ω_{rf}. By probing the coupling strength of these micromotion sidebands, we have a very sensitive method to measure the modulation index β.

When spectroscopy on the quadrupole transition was performed in this new experiment for the first time, neither the magnetic field inside the trap was known well nor was the laser

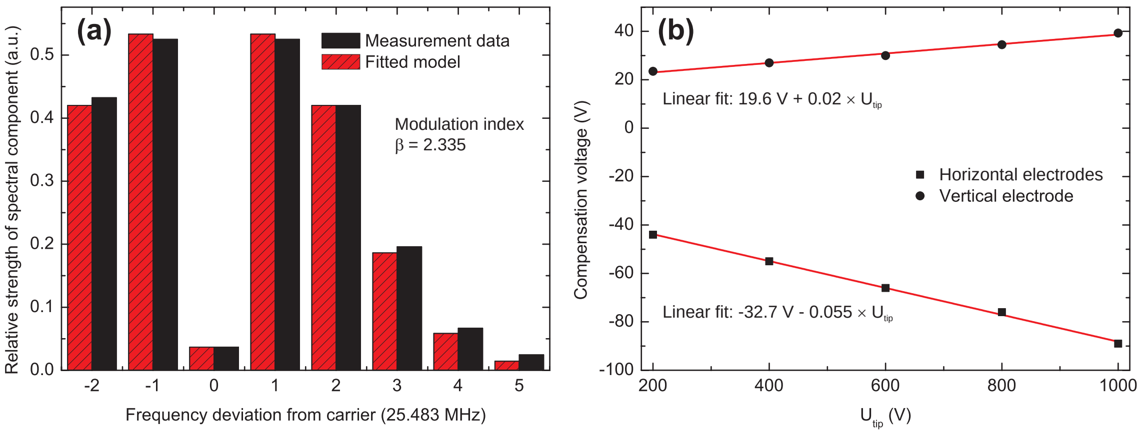

Figure 4.4: **(a)** Measurement of the micromotion modulation index β using a single $^{40}Ca^+$ ion with a beam entering from the southern viewport. The relative coupling strengths $\Omega^{(n)}$ of spectral components separated by exactly the trap drive frequency $\Omega_{\mathrm{rf}} = 25.483\,\mathrm{MHz}$ are mapped out by driving Rabi oscillations on these transitions with the same laser power. The result can be understood in a picture of phase modulation caused by the Doppler-effect. Then the strength of the n$^{\mathrm{th}}$ sideband component is described by the Bessel function $J_n(\beta)$ and a modulation depth β. A fit with this model given by the striped bars matches the measurement data and yields a modulations depth of $\beta = 2.335$. **(b)** Measurement of the compensation voltages in horizontal and vertical direction for different tip voltages U_{tip}. The non-zero y-intercept of the linear fits are attributed to electric stray fields present at the trap center. The dependence on the tip voltages is attributed to small geometrical imperfections in the trap electrode alignment.

frequency exciting the quadrupole transition known precisely enough to address a certain transition. Even for a single $^{40}Ca^+$ ion there is a huge number of spectral components, including the ten carrier transitions and their axial, radial and micromotional sidebands, and the sidebands thereof (see Fig. 4.3). Since the secular trapping frequencies could only roughly be estimated at that time the only frequency known exactly was the trap drive frequency Ω_{rf}, which determines the frequency separation of the micromotion sidebands. Therefore, in a first set of measurements we recorded excitation spectra of a single $^{40}Ca^+$ ion over tens of MHz (similar to the one shown in Fig. 4.3) with the beam entering from the southern viewport (see Fig. 3.7). Driving Rabi oscillations on the strongest spectral component found and the ones separated by multiples n of Ω_{rf}, we mapped out the coupling strengths $\Omega^{(n)}$. The result is depicted in Fig. 4.4 (a). It turned out that the strongest spectral component wasn't actually the carrier but the first micromotion sideband with $n = 1$. According to Eq. (4.1) the coupling strength of the n$^{\mathrm{th}}$ micromotion sideband is proportional to the Bessel functions $J_n(\beta)$, analogous to the modulation implied by an electric phase modulator to a monochromatic laser beam. A fit for this set of data yields a modulation index of $\beta = 2.335$. In order to reduce β to possibly small values we first increased the coupling strength on the carrier and then maximized the ratio between the coupling strength on the carrier with respect to the first sidebands by changing the voltage applied to the vertical compensation electrode. As a typical result we obtain ratios of $\Omega^{(0)}/\Omega^{(1)} = 100$, which corresponds to a modulation index of $\beta = 0.02$. This procedure was repeated in order to compensate for the other direction with a beam entering from the bottom viewport. As a result the amplitude of the ion's micromotion is reduced to $\check{u}_{\mathrm{mm}} = \lambda\,\beta/(2\pi) < 2.3\,\mathrm{nm}$. This compares to a $\sqrt{\hbar/(2M\omega_r)} \simeq 6.1\,\mathrm{nm}$ radial spread of the calcium ion's wave function when cooled to the motional ground state, assuming a radial COM mode trapping frequency of $\omega_r/(2\pi) = 3.4\,\mathrm{MHz}$. A possible limitation set to the compensation of excess micromotion in the radial direction is caused by slightly different radiofrequency phases on the two blade electrodes. Then the node of the radiofrequency field shifts as a function of time. As a consequence, there is no point in space where the radiofrequency field completely vanishes. Along the axial direction, the fact that the blades have a finite width comes into play and makes the radiofrequency field not truly two-dimensional but exhibiting a small curvature along the symmetry axis of the linear trap. A single ion can then still be shifted to the ideal position by unbalancing the tip voltages, but strings of ions will exhibit micromotion along the trap axis.

Finally, we repeated the compensation at different settings for the tip voltages and found a slight change of the compensation voltages (see Fig. 4.4 (b)). This dependence can be understood when a small displacement of the tip electrodes from the trap axis is assumed. The fact that both fits have a non-zero y-intercept is attributed to electric stray fields that can change over time for instance by calcium depositions on the electrodes and ceramic pieces nearby the trap center.

4.4 Referencing the laser at 729 nm to the ions and monitoring of the magnetic field

The setup of the laser emitting at a wavelength of 729 nm and its spectral properties are described in subsection 3.2.2. In order to make use of the laser in the context of quantum computation but also for precision spectroscopy it is necessary to know the laser's frequency relative to the atomic transitions involved and compensate for the drift of the laser's reference cavity. This has been achieved by taking either $^{43}Ca^+$ or $^{40}Ca^+$ ions as a reference. For this purpose we single out two of the many different possible $S_{1/2}$ to $D_{5/2}$ quadrupole transitions. By measuring the two transition frequencies and from the knowledge of the frequency splitting of the involved levels at certain magnetic fields, we can infer the relative laser frequency and the magnetic field. With this knowledge the feedback to the laser frequency can be made independent of small variations of the energy levels caused by the Zeeman effect. In case of $^{43}Ca^+$ though, the nonlinear behavior of the energy splitting of the $D_{5/2}$-states with respect to the magnetic field (see chapter 5) can lead to ambiguities and poor discrimination. These problems can be easily avoided by the right choice of transitions probed for a specific magnetic field.

The frequency measurements are realized in the pulsed mode of operation as described in section 4.2. Usually sideband cooling is omitted and two transitions are probed from the stretched state which is initialized by optical pumping. The actual frequency measurement is then achieved by applying a Ramsey scheme. A $\pi/2$-pulse creates a superposition of the two levels that are probed, then a waiting time τ_{R} and last another $(\pi/2)_\phi$-pulse are applied. In a first measurement the last pulse is applied with a phase $\phi_1 = \pi/2$ and then in a second one with $\phi_2 = 3\pi/2$. After each Ramsey experiment, we determine the population of the involved Zeeman states by the state discrimination technique described in section 3.6 and obtain two probability values p_{ϕ_1} and p_{ϕ_2} of the $D_{5/2}$-state population. Each of these sequences is typically repeated a hundred times.

The frequency difference between laser and the probed transitions of the ion follows from the measured probability values as

$$\Delta\nu/(2\pi) = \frac{1}{2\pi(\tau_{\mathrm{R}} + 2\,\tau_\pi/\pi)} \arcsin\left(\frac{p_{\phi_1} - p_{\phi_2}}{p_{\phi_1} + p_{\phi_2}}\right),$$

where we make use of an effective Ramsey time (see Appendix B) and τ_π is the time it takes to drive a π-pulse with the chosen laser power. Typically τ_π is set to values by a factor 10 smaller than τ_{R}. From the frequency difference $\nu_1 - \nu_2$ we first calculate the magnitude of the magnetic field inside the trap. With the knowledge of the magnetic field and one transition frequency we then determine the transition frequency at zero magnetic field as a reference for other transitions.

This measurement procedure including the evaluation is fully automated and the measurement of the two transitions takes about 25 s. Typically, a complete set of measurements is repeated every one to two minutes using Ramsey times τ_{R} between 0.2 and 1 ms, depending on the magnetic field sensitivity of the transitions involved and the accuracy required.

The squares in Fig. 4.5 (a) represent 378 of these measurements taken over an interval of more than four hours. Here, a single $^{43}\mathrm{Ca}^+$ ion was initialized to the Zeeman state $S_{1/2}(F = 4, m_F = 4)$ from which the two transitions to the states $D_{5/2}(F = 4, m_F = 2)$ and $D_{5/2}(F = 4, m_F = 4)$ were probed with a Ramsey time of $\tau_{\mathrm{R}} = 0.2$ ms. The times τ_π for performing a π-pulse were set to 19 μs and 10.6 μs, respectively. A linear fit to the measurement data reveals an average reference cavity drift rate of 0.6 Hz/s. In order to keep the laser frequency output stable over time we estimated the reference cavity's drift between the measurements from a polynomial fit to the last couple of data points. We use this extrapolation as a feedback to the signal generator that controls the high frequency AOM (AO2 in Fig. 3.4). The circles in Fig. 4.5 (a) represent these predictions. Their difference to the actual measurements is depicted as histogram in Fig. 4.5 (b). Of the 52 Hz standard deviation of the Gaussian fit shown as solid line 19 Hz are attributed to quantum projection noise (see Eq. (3.6)) which could be further reduced by increasing the

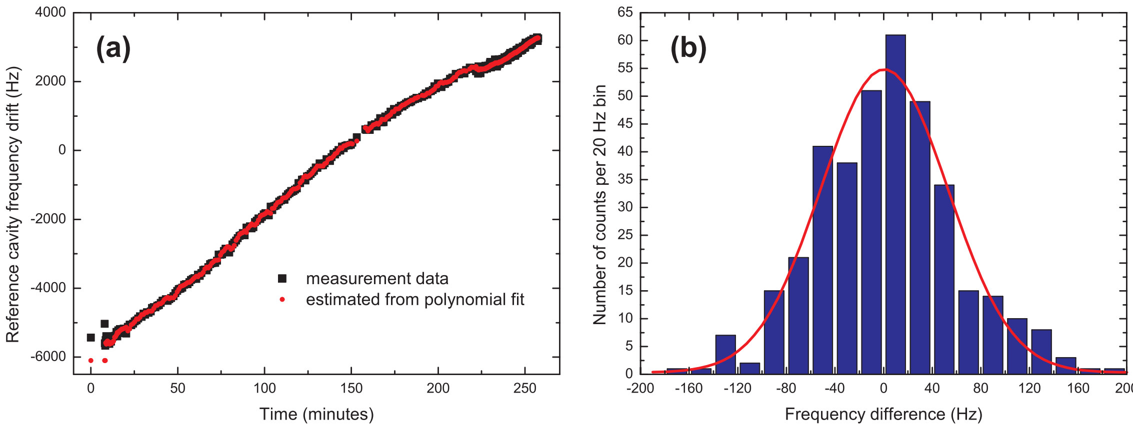

Figure 4.5: Measurement of the frequency drift of the 729 nm laser's reference cavity relative to a single ^{43}Ca^{+} ion. **(a)** The squares represent 378 measurements taken over more than 4 h measurement time with Ramsey experiments where the waiting time was set to $\tau_R = 0.2$ ms. The circles are our best guess during the experiment for the next measurement outcome derived from a polynomial fit before each measurement. The difference between the two is plotted in **(b)** as a histogram. The Gaussian fit given as solid line exhibits a standard deviation of 52 Hz.

number of the measurements and their accuracy by an increase of the Ramsey times τ_R. Here the coherence time of a few milliseconds sets an upper boundary for robust operation. A further limitation is the actual drift of the laser's reference cavity. As soon as the cavity drift becomes nonlinear the predictions start getting poorer.

The measurement outcome for the magnetic field is shown in Fig. 4.6 (a). A linear fit to the measurement results reveals an average magnetic field drift rate of 64 μG/h. Similar to what is done for the frequency of the reference cavity, we also make a prediction for the magnetic field expected for the next measurement by a linear extrapolation of the last couple of data points. These predictions are plotted as circles in the graph. The inset of Fig. 4.6 (a) shows the difference between the measurements and the predictions as a histogram. A Gaussian fit with a standard deviation of 53 μG describes the distribution well. Here, quantum projection noise contributes with 16 μG to the deviation. At the moment we do not use the prediction for the magnetic field in order to actively feed back to the current driver supplying the magnetic field coils. Instead we recalculate all relevant transition frequencies that are used accordingly.

All Ramsey measurements were carried out with a fixed phase relation ϕ_{ac} relative to the 50 Hz AC power line, i.e. each experiment is started by a line trigger pulse. Figure 4.6 (b) shows the change of the magnetic field at the trap center with the phase ϕ_{ac}. Magnetic field components at 50 Hz that have a fixed phase relation to the AC power line exhibit an amplitude of 1.6 mG. Additional tests with a fluxgate magnetometer[8] and measurements of the coils' current spectrum strongly support the hypothesis that the 50 Hz magnetic

[8]Stefan Mayer Instruments, Fluxmaster

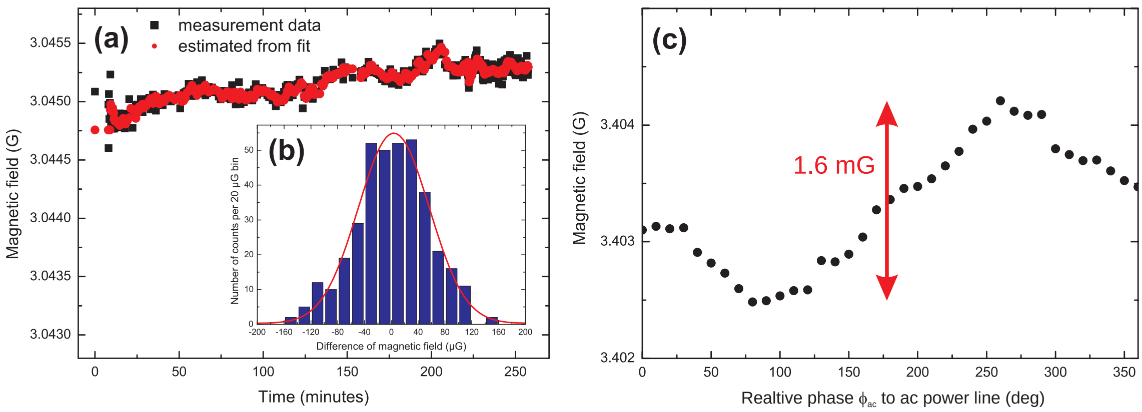

Figure 4.6: Measurement of the magnetic field at the trap center by probing two quadrupole transitions of a single $^{43}Ca^+$ ion. **(a)** The squares represent 378 measurements recorded over more than 4 h. A linear fit results an average drift of 64 μG/h. The circles are our best guess during the experiment for the next measurement outcome derived from a linear fit to the last few data points before the measurement. The inset **(b)** plots the difference between the two as a histogram. The Gaussian fit is characterized by a standard deviation of 53 μG. **(c)** All experiments are carried out at a fixed phase ϕ_{ac} with respect to the 50 Hz AC power line. Changing the phase ϕ_{ac} reveals the magnetic field noise components at 50 Hz that have a fixed phase relation to the AC power line. These are most likely caused by transformers and other parts of the apparatus.

field components are mainly caused by transformers and other lab equipment part of the apparatus. The results shown in panels (a) and (b) of Fig. 4.6 were taken at a different magnetic fields. However, both graphs are scaled to have the same spread along the y-axis. Thus, it becomes immediately obvious, that the magnetic field variations within 20 ms are much larger than changes over hours when the phase ϕ_{ac} is kept constant. As a result all experiments reported in this thesis are performed with ϕ_{ac} being fixed. Since some of the transitions used exhibit a magnetic field sensitivity as high as 2.8 MHz/G, transition frequency changes of more than 4.5 kHz have to be taken into account over the course of a pulse sequence. An active compensation or a passive shielding could help to get rid of this problem.

4.5 Heating rate, shuttling the ions and motional coherence

A critical parameter of an ion trap is the heating rate of the ions' motional degrees of freedom due to electric field noise from the trap electrodes. As most current quantum gates rely on the coupled motion of two or more ions, the motional quantum state needs to be controlled to a degree dependent on the actual scheme. Noise in the motion can degrade this control and lead to a decrease in gate fidelities.

One method to access the heating rate is to cool a single ion close to the motional ground-state of the axial mode. Assuming a thermal state, the mean population of the axial mode

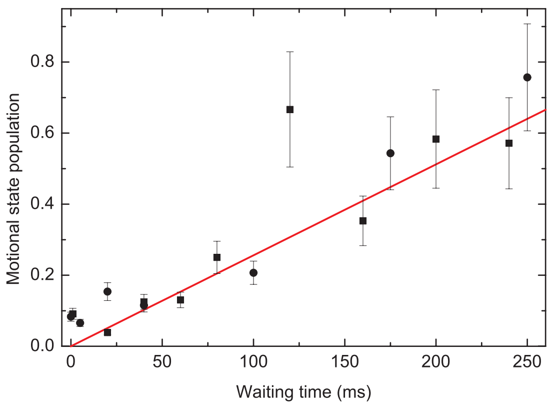

Figure 4.7: The heating rate of the axial COM mode at a trapping frequency of $\omega_{\mathrm{ax}}/(2\pi) = 1.2\,\mathrm{MHz}$ was measured using a single $^{40}\mathrm{Ca}^{+}$ ion cooled close to the motional ground-state. Probing the excitation on the red and the blue axial sideband we infer the population of the motional mode by the ratio given in Eq. (4.2). By introducing and varying a waiting time before the probe pulses we can measure a slow increase of the population. The plot shows two sets of data taken with an 11 month pause in between. A linear fit to both data sets with a zero y-intercept reveals a heating rate of about one motional quantum in 390(20) ms.

$\bar{n}_{\mathrm{ax}}$ can be measured by comparing the excitation of a red sideband p_{rsb} with excitation on the blue sideband component p_{bsb} (see Fig. 6.3 (a)) of the same transition [109]

$$\bar{n}_{\mathrm{ax}} = \frac{p_{\mathrm{rsb}}}{p_{\mathrm{bsb}} - p_{\mathrm{rsb}}}. \tag{4.2}$$

By introducing and varying a waiting time between ground-state cooling and the measurement of motional state population we have mapped out the increase of $\bar{n}_{\mathrm{ax}}$ as a function of this time (see Fig. 4.7). From a linear fit to the data, we obtain a heating rate of one motional quantum in 390(20) ms at an axial trapping frequency of $\omega_{\mathrm{ax}}/(2\pi) = 1.2\,\mathrm{MHz}$ which is one of the lowest values ever reported.

In section 3.5 we have discussed the advantages of addressing different individual ions with various lasers by moving the linear ion crystal along the trap axis. We can quickly imbalance the tip voltages such that the ions move along the symmetry axis of the trap without changing the actual axial trapping frequency. As described in section 3.5, our tip voltage control electronics allows us to add an input voltage signal to one of the tip voltages and subtract it from the other. By using a signal generator with a rectangular output pattern of an amplitude of $\pm 10\,\mathrm{V}$ we can shift the ions over a distance of $10\,\mu\mathrm{m}$ for an average tip voltage of 1000 V. The shuttling distance was measured by observing the movement on the EM-CCD camera image. The imaging magnification was calibrated using the known inter-ion distance of a two-ion crystal where the axial COM mode trapping frequency was known (see Eq. (3.5)). Camera pictures of the ions were taken with an acquisition time of 20 ms, which is about three orders of magnitudes larger than the time the shuttling is expected to take. Setting the signal generator to a frequency of 1 kHz the single ion occurs at two sites on the EM-CCD image and no fluorescence is observed

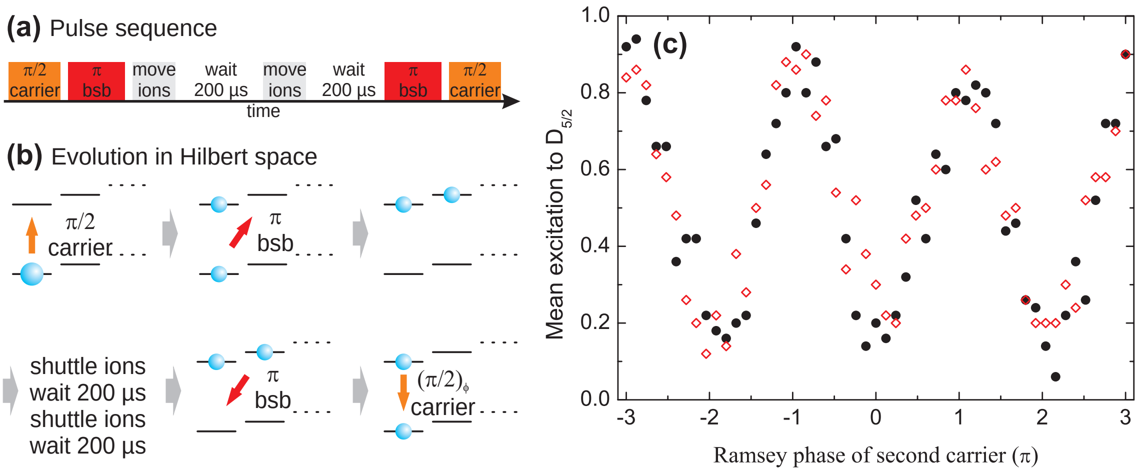

Figure 4.8: **(a)** Pulse sequence that describes a Ramsey phase experiment where the coherence of the two lowest motional quantum states is probed. **(b)** A superposition of those is prepared by a $\pi/2$-pulse on the carrier followed by a π-pulse on the blue sideband. Then the ion is moved over a distance of $10\,\mu$m and a waiting time of $200\,\mu$s is introduced. Then the ion is shuttled back and after another waiting time of $200\,\mu$s the superposition is analyzed by applying another π-pulse on the blue sideband and a $(\pi/2)_\phi$-pulse on the carrier. Below is a step-wise illustration of the evolution in the Hilbert space. **(c)** Measurement results (●) of the Ramsey phase experiment where the phase ϕ of the last laser pulse is scanned. Also shown are the results from a reference experiment (◇) were the movement of the ion was omitted. From the data we can conclude that neither amplitude nor the phase of the fringe pattern is affected by the shuttling.

from in between. Only if we increased the frequency to above 30 kHz fluorescence was also observed between the two extremal ion sites. Here, the two low-pass filters prevented the two tip voltages being interchanged fast enough such that the amplitude of the movement decreased. Measurements with two $^{40}Ca^+$ ions have shown that full settling was achieved after $40\,\mu$s. This value corresponds to about 50 oscillations of the ions along the axial direction.

To see if the population of the axial COM mode is affected by this shuttling we performed a Ramsey phase experiment on the two lowest motional states. A single $^{40}Ca^+$ ion was initialized to the motional ground-state of the axial mode by sideband cooling. A $\pi/2$-pulse on the transition from $S \equiv S_{1/2}(m_J = 1/2)$ to the $D \equiv D_{5/2}(m_J = 1/2)$-state creates a superposition state of the form $(|S0\rangle + |D0\rangle)/\sqrt{2}$. With an additional π-pulse on the blue sideband of this transition we mapped the superposition of the electronic state to the motion and created $(|D0\rangle + |D1\rangle)/\sqrt{2}$. Then we moved the ion over a distance of $10\,\mu$m along the trap axis. After a waiting time of $200\,\mu$s we shuttled the ion back and waited another $200\,\mu$s. In order to probe the coherence we repeated the first two pulses in reverse order and scanned the phase ϕ of the last carrier pulse to observe a fringe pattern. In addition we recorded a reference measurement where the ion was not moved. The pulse sequence, a sketch of the Hilbert space and the measurement results are shown in Fig. 4.8. Within the accuracy of the measurements both data sets reveal the same fringe amplitude and no phase shift in the Ramsey pattern is observed. This lets us conclude that the motional coherence is not affected by the movement and that the population of the motional quantum state is unperturbed by the shuttling.

4.6 Individual ion detection, addressing and addressing error correction

To get the maximum information out of each measurement when working with more than one ion, it is necessary to discriminate fluorescing ions from the dark ones. Individual ion detection can be achieved using the EM-CCD camera by defining a region of interest around each of the ions' images. Two reference pictures are taken, one with all ions dark (omitting 866 nm laser during detection) and another one with all ions fluorescing. For the actual measurement we collect photons for 5 ms to 20 ms, then an evaluation software on the camera PC compares each ion's region of interest with the reference pictures and decides whether it is considered to be bright or dark and sends this information to the experiment control PC. The whole process is technically quite a bit more demanding than the PMT detection. Thus, the measurements presented here are more about proving the basic working principles for the new setup than demonstrating the ultimate performance.

Arbitrary quantum operations with many qubits require that interactions on individual qubits can be implemented to make the particles distinguishable. In ion trap quantum computing this is equivalent to limiting the laser ion interaction to one ion at the time which can be achieved in various ways. One approach is to use micro-fabricated segmented traps and to shuttle the ions around through different trapping zones. In this scheme larger ion crystals can be split up into smaller ones and brought to zones where they can interact with a laser [110]. This requires a very high amount of control concerning the trapping potentials and only a few experiments have demonstrated the fundamental principles of these techniques so far [111, 112]. In particular, the splitting of an ion crystal seems to be a costly operation. If ρ denotes the distance from the ions to the nearest electrodes the time to split a two ion crystal scales with $\rho^{9/10}$ [113] for a given trap structure. This gets compromised by the fact that the heating rate scales approximately as ρ^{-4} [109, 114]. Another way to talk to individual ions when using larger ion crystals is to focus light so strongly, that only one of the ions is illuminated. Assuming a Gaussian beam shape, this requires a beam waist at the ions' position ideally much smaller than the inter-ion distances of a few micrometer. However, even for perfect optical components we expect residual coupling Ω_{res} on the neighboring ions caused by the tail of the Gaussian beam profile and diffraction due to finite apertures. The ratio $\varepsilon_{ae} \equiv \Omega/\Omega_{\text{res}}$ defines the *relative addressing error*. In reality it turns out to be quite challenging to adjust the optics properly and reduce this addressing error to a few percent level.

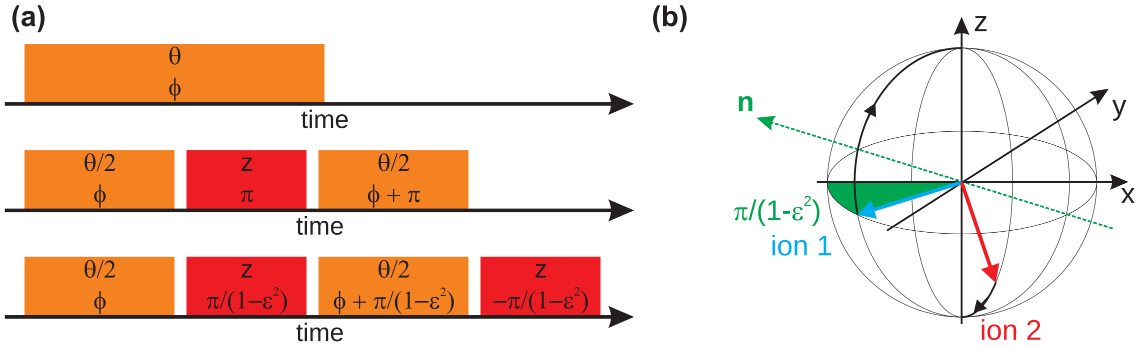

Figure 4.9: **(a)** To induce a qubit rotation on a single ion of a two-ion crystal we strongly focus a laser beam. For a single pulse we expect an error on the neighboring ion that scales with the square root of residual laser intensity on this ion. By splitting the single pulse into two an introducing a π-rotation around the z-axis by AC-Stark shift the error is reduced to $\leq \pi\varepsilon^2$ and scales linear with the residual laser intensity on the second ion. In case the relative addressing error is known a further reduction of the error is obtained by adapting the phases of the second an the third pulse accordingly. Optionally the residual phase acquired on each ion can be taking into account for the following pulses or a fourth pulse can be used to revert this phase back. For this scheme panel **(b)** shows a Bloch sphere representation of the two ions after the second pulse. The normal vector $\boldsymbol{n}$ of the plane spanned by the two Bloch vectors lies within the equatorial plane and serves as rotation axis for the third pulse.

Fortunately it is possible to relax the demands concerning the optics quite a bit by a technique termed *addressing error correction*. Let us consider a simple scenario with two calcium ions trapped and both initialized to the south pole of the Bloch sphere. We want to implement a single-qubit rotation $R^{(1)}(\theta = \pi, \phi = 0)$ on the first ion and leave the second ion unaffected with $R^{(2)}(0, 0)$. Since the coupling strength Ω is proportional to the square root of the laser intensity, a residual laser intensity of only 2% on the second ion leads already to a relative addressing error Ω_1/Ω_2 as high as 14%. Instead of a single pulse we can use three pulses (see Fig. 4.9 (a)) where the first is equivalent to a rotation $R^{(1)}(\pi/2, \pi)$ on ion 1. This excites also ion two to about 7%. Also the second pulse acts primarily on the first ion but now we detune the laser frequency so far from the transition frequency, that populations do not get exchanged and only a phase shift is introduced due to the AC-Stark effect. In the Bloch sphere representation this is equivalent to a rotation around the z-axis, noted $R_z(\psi)$, where the rotation angle ψ is proportional to the pulse duration and laser intensity of the pulse. For $\psi = \pi$ on ion 1, we expect a rotation of only $\pi/50$ for ion 2. The third pulse again is similar to the first with $R^{(1)}(\pi/2, 0)$. It flips ion 1 completely up to the north pole of the Bloch sphere, where the second ions is almost completely rotated back towards the south pole. For this simple example the addressing error is reduced from $\pi\varepsilon_{ae}$ to about $\pi\varepsilon_{ae}^3$. A measurement result for this scheme is given in Fig. 4.10.

In general with this scheme the actually acquired addressing error is dependent on the state of the neighboring second ion. In the worst case, when the second ion's state is near the equatorial plane of the Bloch sphere, the error can get as large as $\pi\varepsilon_{ae}^2$ such that the

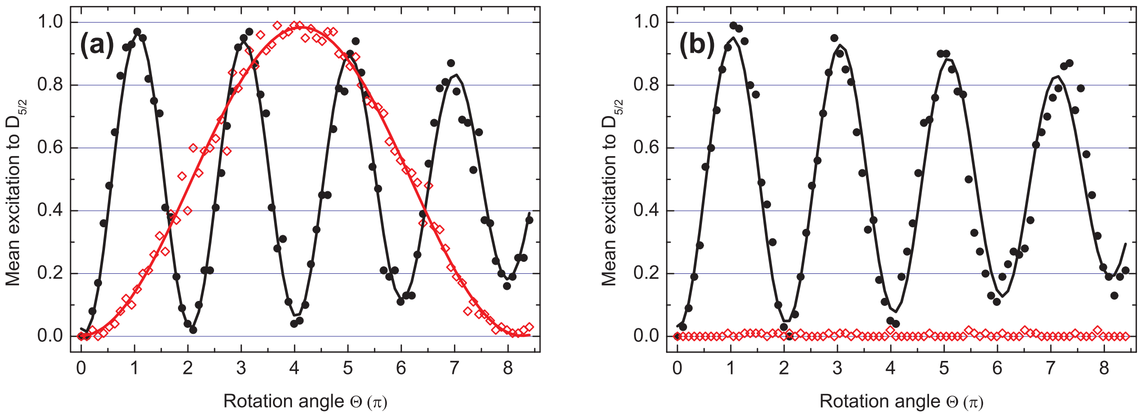

Figure 4.10: **(a)** Exciting mainly one ion of a two ion crystal with the laser at a wavelength at 729 nm. The camera detection was used to discriminate between the states $|SD\rangle$ and $|DS\rangle$ such that individual ion excitations of ion 1 (•) and ion 2 (◇) were measured. The ratio between the wanted coupling strength on ion 1 and the erroneous coupling strength on ion 2 is about 7. **(b)** In case the individual pulse was replaced by a composite pulse the excitation on the second ion can be largely suppressed.

maximum error is given by the ratio of the laser intensities on the neighboring ions. One major advantage of this scheme is that it works irrespective of whether ε_{ae} is a known quantity or not.

In the experiment ε_{ae} is usually a known quantity on the order of 5% for the nearest neighbors. Moreover, we can tune the laser beam such that both neighboring ions exhibit the same addressing error. Armed with this knowledge the effective addressing error is further reduced by modifying the previous scheme. Now the length of the second pulse is adjusted such that the Bloch vectors of ion 1 and ion 2 span a plane with a normal vector $\boldsymbol{n}$ being in the equatorial plane after the z-rotation (see Fig. 4.9 (b)). This is the case for a rotation angle of $\psi = \pi/(1-\varepsilon_{ae}^2)$. Then a rotation $R^{(1)}(\pi/2, \pi/(1-\varepsilon_{ae}^2))$ brings ion 2 exactly back to the south pole and ion 1 up to the north pole. Finally, the single-qubit phases can be either taken into account for the subsequent pulses or one additional rotation around the z-axis $R_z^{(1)}(-\pi/(1-\varepsilon^2))$ on ion 1 can make them vanish. Furthermore, this scheme works for arbitrary input states and angles θ and ϕ. Here, the residual error is no longer given as a function of ε_{ae} but instead by the balancing of this residual light intensity on the neighboring ions and by the precision of the relative coupling strengths. Thus, addressing error correction relaxes the demands on laser spot sizes by at least an order of magnitude.

5 Precision spectroscopy

This chapter describes the hyperfine structure investigation of the $4s\,^2S_{1/2} \leftrightarrow 3d\,^2D_{5/2}$ quadrupole transition at 729 nm by laser spectroscopy using a single trapped ^{43}Ca$^+$ ion. We determine the hyperfine structure constants $A_{D_{5/2}}$ and $B_{D_{5/2}}$ of the metastable level and the isotope shift $\Delta_{\mathrm{iso}}^{43,40}$ of this transition with respect to ^{40}Ca$^+$. Moreover, the existence of transitions that become independent of the first-order Zeeman shift at nonzero low magnetic fields is demonstrated. These transition's abilities to serve as an optical frequency standard or qubit are briefly discussed and one of them is used as a probe for the spectroscopy laser's line width and phase stability. The main findings of this chapter were also published in reference [72].

5.1 Measurement of the hyperfine constants of the ^{43}Ca$^+$ D$_{5/2}$ energy level

In recent years, optical frequency standards based on single trapped ions and neutral atoms held in optical lattices have made remarkable progress [115, 116, 117] towards achieving the elusive goal of a fractional frequency stability of 10^{-18} [35]. In ^{199}Hg$^+$, ^{27}Al$^+$, ^{171}Yb$^+$, ^{115}In$^+$, and ^{88}Sr$^+$, optical frequencies of dipole-forbidden transitions have been measured [115, 118, 119, 120, 121]. Among the singly-charged alkali-earth ions, the odd isotope ^{43}Ca$^+$ has been discussed as a possible optical frequency standard [122, 123] because of its nuclear spin $I = 7/2$ giving rise to transitions $4s\,^2S_{1/2}(F, m_F = 0) \leftrightarrow 3d\,^2D_{5/2}(F, m_F = 0)$ that are independent of the first-order Zeeman effect. Our major motivation for precision spectroscopy comes from the fact that our scheme to utilize the ^{43}Ca$^+$ hyperfine clock states for QIP requires the a precise knowledge of the quadrupole transition frequencies.

From earlier measurements and calculations of the isotope shift [124] and the hyperfine splitting of the $S_{1/2}$ [84] and the $D_{5/2}$ [85, 125, 126] states, the transition frequencies on the quadrupole transition in ^{43}Ca$^+$ are known to within 20 MHz with respect to the transitions in ^{40}Ca$^+$. This enabled us to unambiguously identify the lines observed in spectra of the $S_{1/2} \leftrightarrow D_{5/2}$ transition as a starting point.

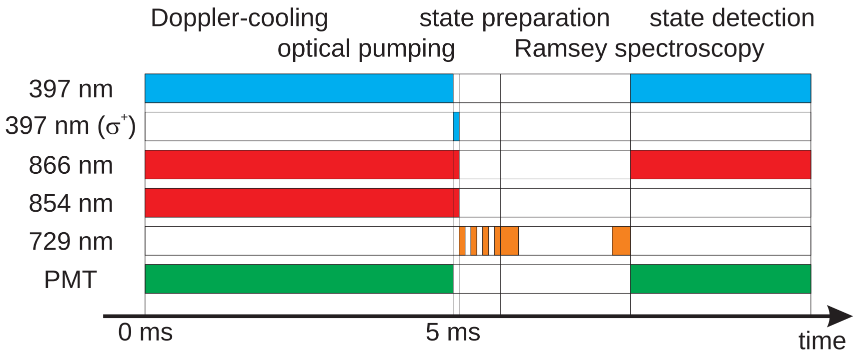

Figure 5.1: Pulse sequence used to measure the different frequencies of the quadrupole transition of $^{43}\mathrm{Ca}^{+}$and $^{40}\mathrm{Ca}^{+}$. Each start of a sequence is triggered to the AC power line. Doppler-cooling and optical pumping to a designated Zeeman state is followed by state preparation which can have a different number of pulses and vary in length. To start the Ramsey experiment always at the same phase with respect to the AC power line phase a pause was introduced accounting for variations of the state preparation time.

5.1.1 Measurement scheme and results

In order to set the magnetic field precisely, we used a single $^{40}\mathrm{Ca}^{+}$ ion to determine the field strength by measuring the frequency splitting of the two transitions $S_{1/2}(m_J = +1/2) \leftrightarrow D_{5/2}(m_J = +5/2)$ and $S_{1/2}(m_J = +1/2) \leftrightarrow D_{5/2}(m_J = -3/2)$. Stray magnetic fields oscillating at multiples of 50 Hz changed the magnitude of the field by less than 2 mG over one period of the power line frequency (see section 4.4). Spectroscopy on the quadrupole transition was implemented in the pulsed mode of operation (see section 4.2). By synchronizing the experiments with the phase of the power line, magnetic field fluctuations at multiples of 50 Hz were largely eliminated as a source of measurement error. The duration of a single experimental cycle (see Fig. 5.1) was on the order of 10 ms, such that this procedure slightly slowed down the repetition rate of the experiments.

In a first series of measurements after Doppler-cooling the ion was prepared in the state $S_{1/2}(F = 4, m_F = +4)$ by optical pumping with σ^+-polarized light (see subsection 6.1.1). There are fifteen transitions to the $D_{5/2}$ levels allowed by the selection rules for quadrupole transitions. Spectra were recorded on all of them with an excitation time of 500 μs in a magnetic field of about 3.40 G. In a second measurement series, after pumping the ion into $S_{1/2}(F = 4, m_F = -4)$ another fifteen transitions were measured. To obtain the hyperfine constants of the $D_{5/2}$-state, we fitted the set of 30 transition frequencies by diagonalizing the Hamiltonian (2.12) taking the hyperfine constants $A_{D_{5/2}}$, $B_{D_{5/2}}$, the magnetic field and a frequency offset as free parameters. The hyperfine constant $A_{S_{1/2}}$, the g-factors g_I and $g_{S_{1/2}}$ were taken from other references (see Tab. A.5), $g_{D_{5/2}} = 1.2003(1)$ was measured by us in an experiment with a single $^{40}\mathrm{Ca}^{+}$ ion. For this set of data (see Fig. 5.2 (a)) a fit yields $A_{D_{5/2}} = -3.8931(2)$ MHz and $B_{D_{5/2}} = -4.241(4)$ MHz, where the standard deviation of the determination is added in parentheses. The average deviation between

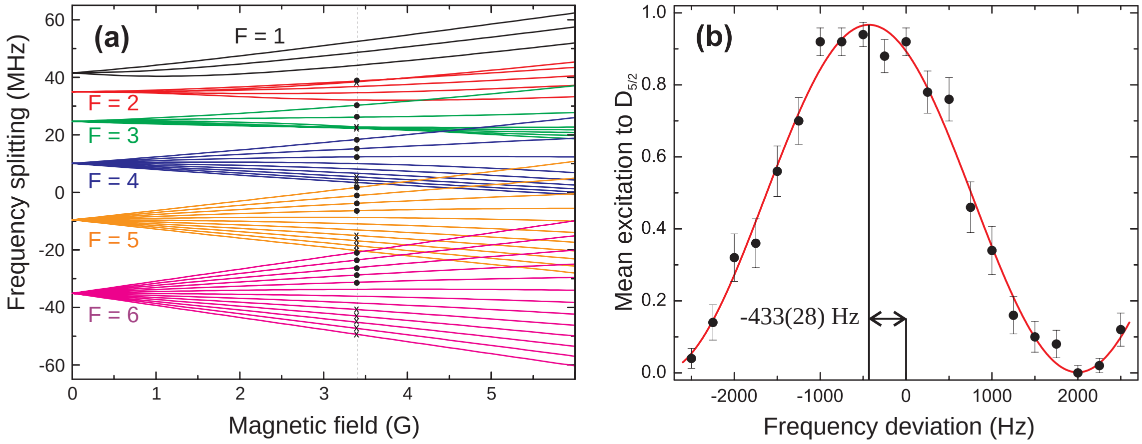

Figure 5.2: **(a)** Hyperfine and Zeeman splitting of the $^{43}Ca^{+}$ $D_{5/2}$-state manifold calculated for hyperfine constants measured in our experiment. Filled circles (•) and crosses (**x**) mark states that were probed starting from the $S_{1/2}(F=4, m_F=\pm 4)$-states. The vertical dashed line indicates the magnetic field used for measuring the frequency shifts in the experiment. **(b)** Result of a Ramsey frequency scan over 5 kHz with $\tau_R = 200\,\mu$s on the transition $S_{1/2}(F=4, m_F=4) \leftrightarrow D_{5/2}(F=5, m_F=4)$. The solid line is a sinusoidal fit with the maximum indicating a deviation of $-433(28)$ Hz from what was expected during the experiment from theoretical calculations based on previous measurements of $A_{D_{5/2}}$ and $B_{D_{5/2}}$.

the measured and the fitted frequencies is about 1 kHz. If $g_{D_{5/2}}$ is used as a free parameter, we obtain $g_{D_{5/2}} = 1.2002(2)$ and the fitted values of the hyperfine constants do not change. Also, adding a magnetic octupole interaction [127] to the hyperfine Hamiltonian does not change the fit values of the hyperfine constants.

In a second attempt we probed all $D_{5/2}$ levels that are accessible from the $S_{1/2}(F=4)$ manifold. The single $^{43}Ca^{+}$ ion was first initialized in the $S_{1/2}(F=4, m_F=4)$-state by optical pumping. Then the ion is prepared by a series of π-pulses on the quadrupole transition into the desired starting level of the ground-state manifold. Subsequent to the state preparation the frequency measurement was performed by a Ramsey frequency experiment. For this purpose a first light pulse created a superposition between the two states probed. Then a waiting time τ_R is introduced before a second light pulse. For each transition two sets of measurements were taken, one with a Ramsey time of $\tau_R = 50\,\mu$s to avoid ambiguities and another one with $\tau_R = 200\,\mu$s, limited by the magnetic field sensitivity of the most sensitive transition probed. At the end of the experimental cycle, the ion's quantum state is detected. This measurement cycle is repeated fifty times before setting the probe laser to a different frequency and repeating the experiments all over again. The laser power was set such that the time for a $\pi/2$-pulse was between 5 and 20 μs. A sine-curve was fitted to the resulting fringe pattern. The location of maximum determines the frequency difference between the expected transition frequency and the one measured. A typical result is shown in Fig. 5.2 (b). Before each of these experiments, the two transition frequencies of $S_{1/2}(F=4, m_F=4) \leftrightarrow D_{5/2}(F=4, m_F=2)$ and $S_{1/2}(F=4, m_F=0) \leftrightarrow D_{5/2}(F=4, m_F=2)$ were measured also with $\tau_R = 200\,\mu$s. From these the

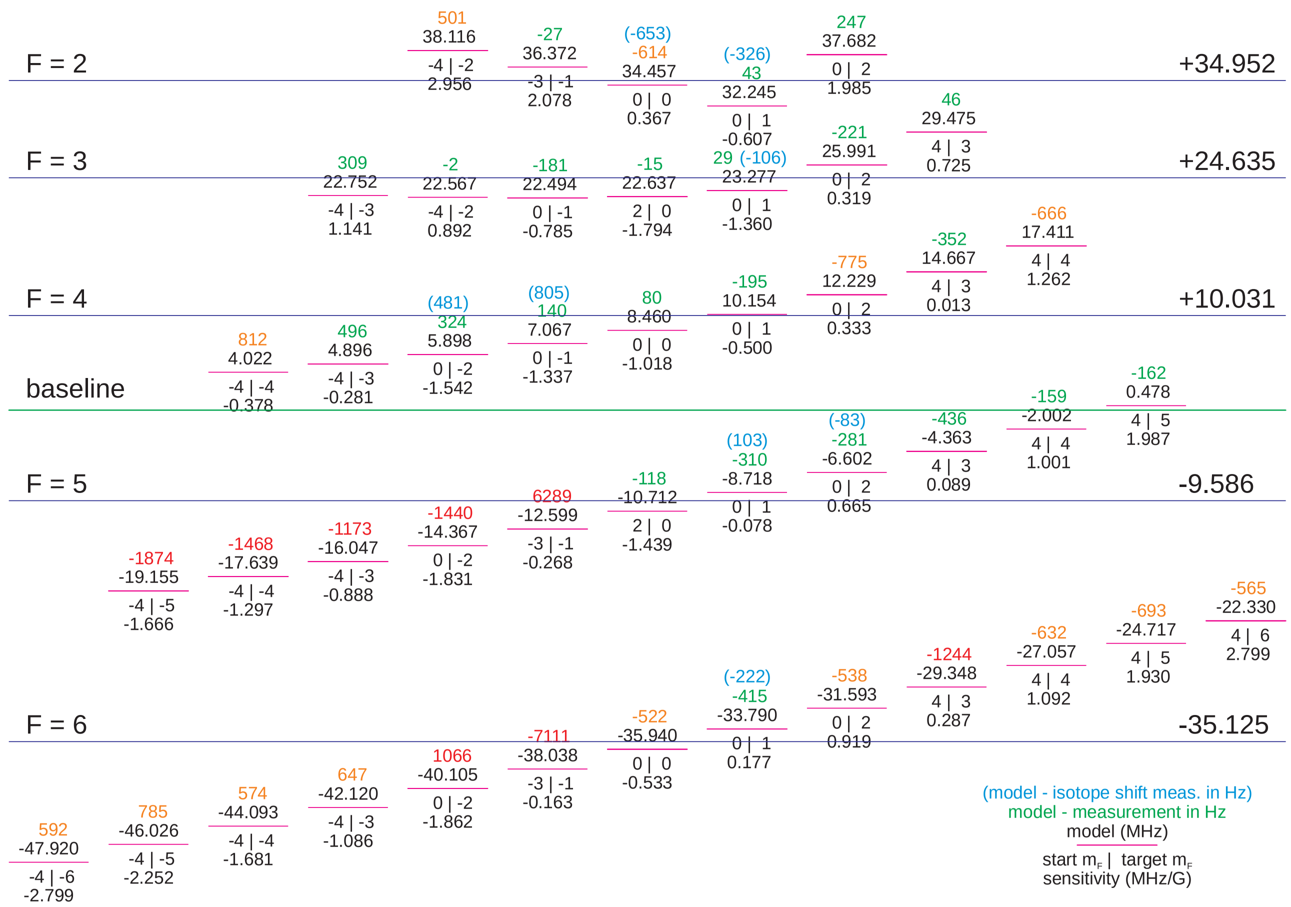

Figure 5.3: In order to determine the hyperfine constants of the ^{43}Ca$^+$ $D_{5/2}$-state we probed all 45 available levels from the $S_{1/2}(F = 4)$ manifold. The results are given as numbers in Hertz as deviation from the model which is stated below as difference from the $D_{5/2}$ baseline in MHz. Moreover, the sensitivity for each of the probed transitions is given in MHz/G and was used to apply small correction so that all frequencies given correspond to the same magnetic field of 3.045 524 G. In a later measurement we probed again 8 of these transitions in order to determine the isotope shift on this transition with respect to ^{40}Ca$^+$. The resulting frequency differences from the model are the values given in brackets above the other measurements. Alternatively the values are given in Tab. A.6.

magnetic field during the measurement of the transition could be determined from the Zeeman splitting of the $S_{1/2}$-state manifold solely using the g-factor and the hyperfine constant $A_{S_{1/2}}$, which are known with high precision. By introducing small waiting times dependent on the duration of the transfer pulses for state initialization we assured that all frequency measurements occurred at the same phase with respect to the AC power line.

The result of these measurements for the 45 different levels probed is given in Fig. 5.3 and Tab. A.6. With the knowledge of the magnetic field for each data point, the level shifts were recalculated with respect to the mean magnetic field of all measurements which was 3.045 524 G. All of these corrections were below 1 kHz.

We obtain the hyperfine constants of the $D_{5/2}$-state from fitting 41 transition frequencies by diagonalizing the Hamiltonian (2.12) and using the hyperfine constants $A_{D_{5/2}}$, $B_{D_{5/2}}$ and a frequency offset as free parameters. In the meantime another experiment in the group revealed a more accurate measurement of metastable state's g-factor $g_{D_{5/2}} = 1.200\,334\,0(3)$ by probing a single ^{40}Ca$^+$ ion [128]. As a result of the fit we obtain the values

$$\mathbf{A_{D_{5/2}}} = -\mathbf{3.893\,12(3)\,MHz},$$
$$\mathbf{B_{D_{5/2}}} = -\mathbf{4.239(1)\,MHz},$$

where the statistical error (1σ) of the determination is added in parentheses. The average deviation between the measured and the fitted frequencies is below 600 Hz now and the results are consistent with the ones obtained earlier. If $g_{D_{5/2}}$ is used as a free parameter, we obtain $g_{D_{5/2}} = 1.200\,36(4)$ and the fitted values of the hyperfine constants do not change.

5.1.2 Limitations of the measurement

There is a number of effects that can systematically disturb the precise determination of the transition frequencies. First of all the whole measurement is limited by the ability to stabilize the spectroscopy laser relative to the ion. For the second set of measurements the laser was referenced to the two transitions $S_{1/2}(F=4, m_F=4) \leftrightarrow D_{5/2}(F=4, m_F=4)$ and $S_{1/2}(F=4, m_F=4) \leftrightarrow D_{5/2}(F=4, m_F=2)$ with a scheme described in section 4.4. The Ramsey time was set for both transitions to $\tau_{\mathrm{R}} = 200\,\mu$s and the times τ_π were set to $\sim 15\,\mu$s. The whole measurement took about 500 min during which a total of 664 service measurements were taken. The difference between these service measurements and the predictions is given in Fig. 5.4 (a) as a histogram together with a Gaussian fit. We obtain a standard deviation of 60 Hz. This sets a boundary to the accuracy of all transition frequency measurements. The evaluation of the magnetic field measurement is given in Fig. 5.4 (b). The standard deviation describing the Gaussian fit to the histogram is 54 μG.

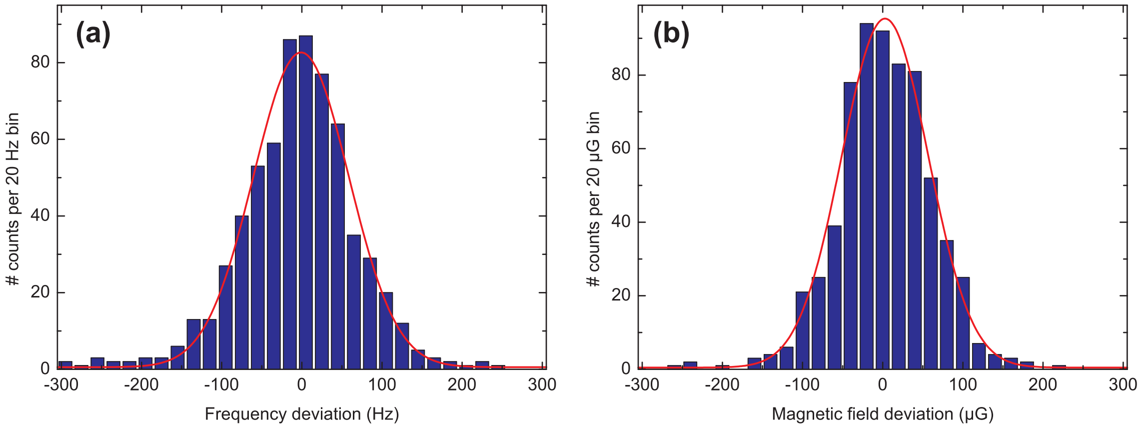

Figure 5.4: Automated service measurements as described in section 4.4 referenced the spectroscopy laser to the $^{43}Ca^{+}$ ion during the spectroscopic measurements. In total 664 of these service measurements were taken over a measurement time of 500 min. **(a)** The histogram shows the frequency deviation between the measurements and our predictions. A Gaussian fits well to the data which exhibit a standard deviation of 60 Hz. **(b)** From the same set of measurement we also obtain values for the magnetic field. The histogram shows the deviation from the extrapolation together with a Gaussian fit with a standard deviation of 54 μG.

Transitions to the stretched states come with the highest sensitivity of 2.8 MHz/G which would then lead to an error in frequency estimation of 150 Hz.

Another error source are the radiofrequency currents that supply two of the four trap blades with high voltage $V_{\mathrm{rf}}(t)$. The trap drive frequency Ω_{rf} is determined by the helical resonator and the capacity of the trap structure. During these measurements the frequency was set to $\Omega_{\mathrm{rf}}/(2\pi) = 25.466$ MHz. This comes fairly close to the hyperfine splitting of the $D_{5/2}(F=6)$ and $D_{5/2}(F=5)$-states. In particular, for the given magnetic field the difference between the transition frequency $D_{5/2}(F=6, m_F=-1) \leftrightarrow D_{5/2}(F=5, m_F=-1)$ and the trap drive frequency $V_{\mathrm{rf}}(t)$ is as small as $\Delta_{td}/(2\pi) = 14.6$ kHz and a magnetic dipole coupling exists. Comparing the model with the measurements of these levels shows for each of them a shift of approximately $\delta_{acB}/(2\pi) \approx 6.7$ kHz in opposite direction. If we neglect the coupling to other levels for the moment we can calculate the coupling strength Ω_{DD} by

$$\Omega_{DD} \approx \sqrt{\delta_{acB}(\delta_{acB} + \Delta_{td})} = 2\pi \times 12\,\mathrm{kHz}.$$

Similarly, we have $\Delta_{td} = -270$ kHz for the level pair $D_{5/2}(F=6, m_F=-2)$, $D_{5/2}(F=5, m_F=-2)$ and observe a shift of about 1.3 kHz in the opposite direction. For this reason these levels were not taken into account for the determination of the hyperfine coefficients $A_{D_{5/2}}$ and $B_{D_{5/2}}$. Other inter-level frequency differences deviate more from Ω_{rf} and we expect these shifts to be less than 1 kHz. In principle we could investigate the polarization and the exact coupling strength of these AC magnetic fields by varying the static magnetic field such that certain of these transitions become resonant. This has not been done so far.

As discussed in Appendix B for the method of separated oscillatory fields, AC-Stark shifts from other transitions can lead to an additional phase in the observed fringe pattern and hence lead to an error in the frequency determination. For the coupling strength used here the contribution of neighboring dipole transitions is estimated to be less than a few Hertz. Coupling to other levels in the $D_{5/2}$ and $S_{1/2}$ manifold strongly depends on the Zeeman splitting of the neighboring levels and can lead to much larger shifts. At a magnetic field of 3 G, the Zeeman splitting is larger than 1 MHz for most of the levels and so the error is also on the order of a few Hertz. One exception is the level $D_{5/2}(F=3, m_F=-2)$ which is separated by only 73 kHz from the level $D_{5/2}(F=3, m_F=-1)$. Probing the level from the ground-state $S_{1/2}(F=4, m_F=0)$ led to an error of 4 kHz in frequency determination due to the AC-Stark shift. When instead the $D_{5/2}(F=3, m_F=-2)$-state was probed from the $S_{1/2}(F=4, m_F=-4)$ ground-state a coupling to the close by $D_{5/2}(F=3, m_F=-1)$-level is forbidden by the selection rules and the obtained value deviates only by -2 Hz from the model. An exact analysis would require the summation over all possible couplings to neighboring transitions including sidebands due to the motion of the ion.

An AC-Stark shift can also be caused by spurious light fields that couple to the levels under investigation. Already small amounts of light at the dipole transitions from $S_{1/2} \leftrightarrow P_{1/2}$, $P_{3/2}$ and $P_{3/2} \leftrightarrow D_{5/2}$ can cause large shifts. The light fields at wavelengths of 397 nm and 854 nm are needed though within the experimental cycle for detection and repumping. Usually these lasers are switched off by single pass AOM's in front of a single-mode glass fiber which typically gives an extinction ratio on the order of 10^{-5}. In order to investigate possible light shifts caused by imperfect laser switching additional mechanical shutters were installed to shut these lasers completely off. The largest shift due to residual laser light observed in a series of measurements using different transitions in ^{43}Ca^{+} and ^{40}Ca^{+} by a direct comparison was about 10 Hz (see next section).

The $D_{5/2}$-state's atomic electric quadrupole moment interacting with residual electric quadrupole fields gives rise to frequency shifts of a few Hertz [129]. Several series of measurements were performed for different voltages on the tip electrodes of the trap. No effect was observed within the accuracy of the measurements which was about 10 Hz.

Other deteriorating effects due to residual micromotion, black body radiation, higher order AC-Stark shifts, etc. are all expected to contribute less than a few Hertz and are also not considered for the evaluation.

Taking all the above error sources into account, deviations from the model of a few hundred Hertz are expected. The measurement results shows a mean deviation of 600 Hz with maximum deviations of up to 1.5 kHz. In order to make use of these transitions for QIP this level of accuracy is sufficient. Due to variations of the magnetic field of up to 2 mG within 20 ms we determine each transition frequency depending at which particular point of the sequence we use it anyway.

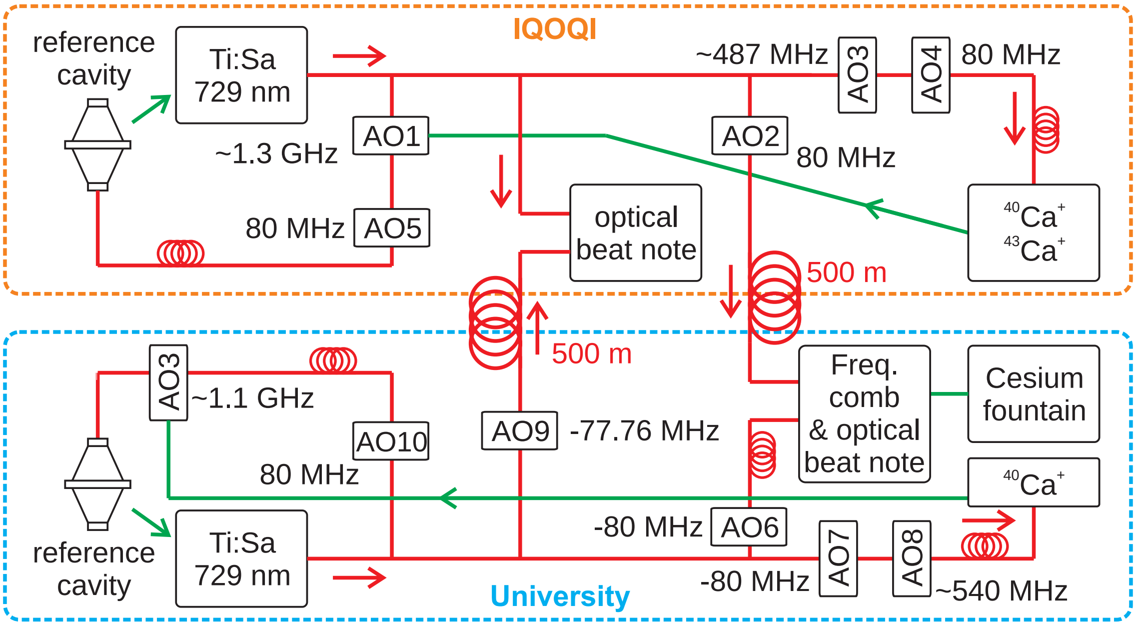

Figure 5.5: For the measurement of the isotope shift on the $S_{1/2} \leftrightarrow D_{5/2}$ quadrupole transition between the ion species ^{40}Ca$^+$ and ^{43}Ca$^+$ we make use of two independent ion trap experiments. One of them is located at the IQOQI and described in chapter 3. The other experiment and a frequency comb referenced to a cesium fountain is located at the university [130]. We transfer light of our spectroscopy lasers between the two sites over 500 m long single-mode polarization-maintaining glass fibers. Both experiments continually measure the frequency deviation between their spectroscopy laser and the atomic transition and feed the signal back onto AOM's in order to stabilize the output frequency of the lasers relative to the ion. Fiber-noise cancelations are installed on all fibers except the ones leading to the ions since here we have to switch the laser on and off quickly.

5.2 Measurement of the isotope shift

One goal pursued by our group is the precise determination of the absolute frequency of the ^{40}Ca$^+$ $S_{1/2} \leftrightarrow D_{5/2}$ transition [128]. The frequency of our spectroscopy laser was measured by means of an optical frequency comb referenced to a mobile cesium fountain as absolute frequency standard. As a result we obtained for the transition frequency a value of

$$\omega^{40}_{S\leftrightarrow D}/(2\pi) = 411\,042\,129\,776\,393.2(1.0)\,\mathrm{Hz}.$$

By an intensive study of the apparatus and the systematic effects we were able to achieve an inaccuracy as low as ± 1 Hz. A detailed description of the apparatus located at a university building, the measurements and its limitations is given in Michael Chwalla's thesis [130]. The new experimental setup described in chapter 3 assisted these measurements. As a byproduct we were able to determine the isotope shift $\Delta^{43,40}_{\mathrm{iso}}$ on this quadrupole transition between ^{40}Ca$^+$ and ^{43}Ca$^+$ ions.

5.2.1 Measurement scheme and results

A sketch of the different components of the measurement setup and their location is given in Fig. 5.5. Similar to what was described in section 4.4 a laser system at 729 nm is referenced to calcium ions at the experiment in the university building. The lasers of both experiments are sent to a frequency comb[1] which can simultaneously measure the absolute frequencies of both light fields referenced to a mobile cesium fountain[2]. In addition, light of the spectroscopy laser is sent from the university building to the IQOQI where an optical beat measurement was recorded to determine the frequency difference between both lasers. When both lasers are referenced to $^{40}\mathrm{Ca}^+$ ions this beat signal was about 30 MHz. In case a $^{43}\mathrm{Ca}^+$ ion was used at the IQOQI a beat frequency of typically 5.4 GHz was recorded with a fast photo detector[3]. In both cases the optical beat frequency was mixed down[4] to around 10.7 MHz where it was counted with a frequency counter[5]. The beat measurement typically takes data over many hours (see Fig. 5.6 (a)) which was not the case for the frequency comb. A comparison between the two measurements has shown though that the transfer of the lasers over the 500 m glass fiber does not impose changes to the laser frequency on a Hertz level when the fiber-noise cancelation (see subsection 3.2.2) is used. On the IQOQI side all relevant radiofrequency sources, the frequency counter and spectrum analyzer were referenced to an ultra-stable quartz which is locked to the global positioning system signal on a long time scale[6]. All computers recording measurement data are synchronized to within 10 ms by having a common internet time basis.

In a first set of measurements we had both experiments running automated frequency measurements on a single $^{40}\mathrm{Ca}^+$ ion. On both experiments we repeatedly probed the two transitions $S_{1/2}(m_J = +1/2) \leftrightarrow D_{5/2}(m_J = +1/2)$ and $S_{1/2}(m_J = -1/2) \leftrightarrow D_{5/2}(m_J = -1/2)$ with a Ramsey time of $\tau_\mathrm{R} = 1\,\mathrm{ms}$ and feeding back the signal to acousto-optic elements as described in section 4.4. The magnetic field in the university experiment was set to 3.4 G and the excitation times were $\tau_\pi = 400\,\mu\mathrm{s}$ at the experiment located at the IQOQI the values were 0.55 G and $\tau_\pi = 12\,\mu\mathrm{s}$ respectively. Simultaneously we measured the beat note of the two spectroscopy lasers at a frequency of about 29 MHz as seen in Fig. 5.6 (a). With a gate time of 1 s we acquired in total 8605 frequency measurements. After subtracting the mean value these data are displayed in a histogram (Fig. 5.6 (b)) where a Gaussian fit with a standard deviation of 21.1 Hz describes the distribution of the data well. The center is determined to better than 1 Hz. Since both lasers were independently referenced to an atomic transition of known transition frequency

[1] Menlo Systems, FC 8003
[2] The cesium fountain was provided and operated by Michel Abgrall, Daniele Rovera, Philippe Laurent and Giorgio Santarelli (LNE-SYRTE, Observatoire de Paris)
[3] photodiode: Hamamatsu, G4176; bias-tee: Miteq, 40 GHz BT 4000; amplifier: Miteq, AFS42-00101200
[4] Rohde & Schwarz, SMA 100 A; Miteq, D80118LA2
[5] Stanford Research Systems, SR-620
[6] Menlo Systems, GPS 6-12

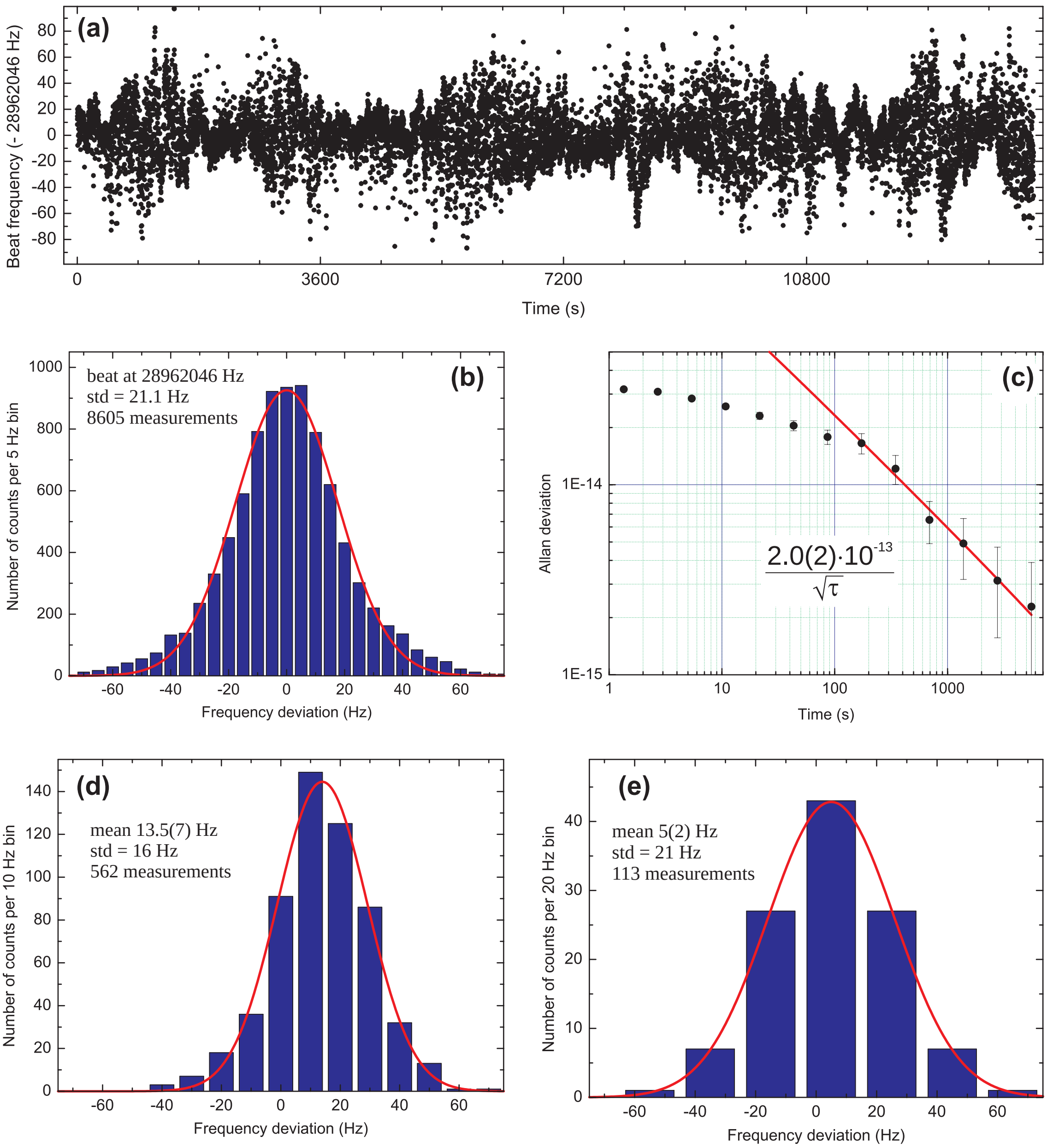

Figure 5.6: **(a)** Optical beat note at about 29 MHz between the two spectroscopy lasers at a wavelength of 729 nm recorded with a frequency counter. The gate time was set to 1 s and we had a dead time of about 0.3 s between the measurements. Both lasers were referenced to a single $^{40}Ca^+$ ion in different experiments. **(b)** The standard deviation of the beat frequency from the mean value is 21 Hz and a Gaussian fits well to the histogram. **(c)** By plotting the Allan deviation we see the expected drop with $\tau^{-1/2}$ after 120 s, indicating the time constant of our feedback loops. **(d)** In total 562 measurements were taken on the IQOQI site over an interval of 4 h. Comparing these with the beat data reveals 13(2) Hz offset of the transition base line compared to the experiment located at the university. **(e)** A large fraction of this difference can be attributed to AC-Stark shifts caused by residual light intensity at wavelengths of 397 and 854 nm. These were eliminated in a set of 113 measurements were mechanical shutters were used in addition. Here a standard deviation of 21 Hz and a relative shift between the two experiments of 5(2) Hz was found.

this measurement can also be seen as the comparison of two atomic clocks. An estimate of the statistical measurement uncertainty versus the measurement duration is given by the Allan deviation

$$\sigma(\tau) \equiv \sqrt{\frac{1}{2} < (y_{n+1} - y_n)^2 >}$$

as shown in Fig. 5.6 (c). Here y_n denote the normalized frequency departure, averaged over sample period n, and τ is the time per sample period. To be exact, the data have to be collected without a dead time in between which was not the case for this particular measurement. Nevertheless, we can obtain from the graph an important time constant of about 120 s after which the expected drop of the Allan deviation with $\tau^{-1/2}$ occurs. This time constant is caused by the accuracy and the rate at which our measurements for the feedback occur. The value could be significantly reduced if a cavity of lower drift was used.

About every one to two minutes on the experiment located at the IQOQI we took data on the same transitions where the lasers at wavelengths of 397 nm and 854 nm were closed with a mechanical shutter[7] for the time of the Ramsey experiment. The mechanical shutters have a closeing/opening time of about 5 ms with a maximum rate of 10 Hz such that their use slows down experiments significantly. Over a total measurement time of three hours we recorded 562 sets of measurements without use of mechanical shutters and only 113 measurements where shutters were used. Only the measurements without shutters were taken to reference the laser to the ion. In order to compare the measurement results we interpolated the data of the beat measurements to the ones taken on the ion. Both measurement results are displayed as histograms in Fig. 5.6 (d)+(e). Gaussians fit well to both distributions and we find standard deviations of 16 Hz and 21 Hz respectively. The mean value of the measurements taken without shutter is shifted by 13.5(7) Hz from the line center determined from the university setup. With the shutter we still find a difference of 5(2) Hz. This difference cannot be explained yet and further investigations on the experiment located at the IQOQI would be required.

With the confidence that our measurement technique is accurate to a few Hertz, we repeated these measurements with the spectroscopy laser at the IQOQI referenced to a single $^{43}Ca^+$ ion. All experimental conditions were chosen to be equal as for the hyperfine structure measurement described earlier in this chapter. For the determination of the isotope shift we probed only 8 of the 45 available $D_{5/2}$-states, all of them starting from $S_{1/2}(F = 4, m_F = 0)$. These measurements allow us to determine the line center of the $D_{5/2}$-state with an 1σ statistical error of ± 390 Hz. The individual measurement results are given as difference to what was expected from the model by values in brackets depicted in Fig. 5.3. Parallel to the measurements we recorded a beat note of the spectroscopy laser with the laser coming from the university which again was referenced to a single $^{40}Ca^+$

[7] Densitron

ion. The optical beat note had a frequency of 5 464 355 931 Hz. From these results we infer an isotope shift on the $S_{1/2} \leftrightarrow D_{5/2}$ transition between the species $^{40}\mathrm{Ca}^+$ and $^{43}\mathrm{Ca}^+$ of

$$\boldsymbol{\Delta_{\mathrm{iso}}^{43,40}/(2\pi) = 4\,134\,711\,720(390)\,\mathrm{Hz}}.$$

with a relative error of 9.4×10^{-8}. This value is in good agreement with a previous measurement that determined the value to $\Delta_{\mathrm{iso}}^{43,40}/(2\pi) = 4129(18)\,\mathrm{MHz}$ [84]) and our own previous result of $\Delta_{\mathrm{iso}}^{43,40}/(2\pi) = 4134.713(5)\,\mathrm{MHz}$ [72] which was obtained without the use of a second experiment and derived by the precise knowledge of the free spectral range of our reference cavity.

5.2.2 Limitations of the measurement

The major limitation to the accuracy of this measurement is given by the precise determination of the $^{43}\mathrm{Ca}^+$ $D_{5/2}$-state's line center. The uncertainty of the hyperfine constants $A_{D_{5/2}}$ and $B_{D_{5/2}}$ contribute with an error of at least 62 Hz and 26 Hz to the determination of the line center. In addition the same errors as described earlier for the determination of the hyperfine constants contribute to these measurements. In order to get a better confidence in our result we took a few more data using other sets of transitions. The values obtained for the isotope shift $\Delta_{\mathrm{iso}}^{43,40}$ all lay in a range of -268 Hz and $+301$ Hz of the above given value. In these measurements we again investigated the effects of mechanical shutters for the lasers at 397 nm and 854 nm with about the same result as for $^{40}\mathrm{Ca}^+$. Moreover, we made series of measurements where the magnetic field was changed between 0.5 G and 5 G, the tip voltage of the trap set to values between 500 and 1500 V and the radial trapping frequency between 2.4 MHz and 4.2 MHz. For none of these measurements we have observed a significant shift caused by the change of these parameters.

5.3 Magnetic field independent transitions

With a precise knowledge of the hyperfine structure constants at hand, the magnetic field dependence of the $D_{5/2}$ Zeeman states is calculated by diagonalizing the Breit-Rabi Hamiltonian (see Fig. 5.2 (a)). It turns out that several transitions starting from one of the stretched states $S_{1/2}(F = 4, m_F = \pm 4)$ become independent of the first-order Zeeman shift at field values of a few Gauss (see Fig. 5.7 (b)). Transitions with vanishing differential Zeeman shifts at non-zero fields have been investigated in experiments with cold atomic gases [131] to achieve long coherence times and with trapped ions [132] for the purpose of processing quantum information. These transitions are also potentially interesting for building an optical frequency standard.

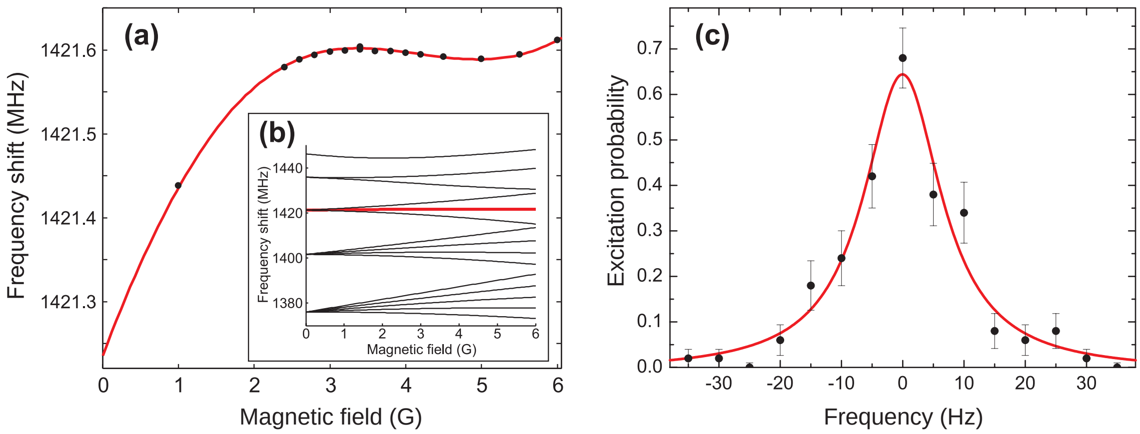

Figure 5.7: **(a)** Frequency dependence of the $S_{1/2}(F=4, m_F=4) \leftrightarrow D_{5/2}(F=4, m_F=3)$ transition frequency for low magnetic fields. The transition frequency becomes field-independent at magnetic fields of 3.38 G and 4.96 G with a second-order Zeeman shift of $\mp 16\mathrm{kHz/G}^2$. The measured data are not corrected for the drift of the reference cavity which may lead to errors in the shift of less than 2 kHz. To match the data with the theoretical curve based on the previously measured values of $A_{D_{5/2}}$, $B_{D_{5/2}}$, an overall frequency offset was adjusted. **(b)** Calculated shift of the fifteen allowed transitions starting from $S_{1/2}(F=4, m_F=4)$. The thick line shows the transition to the state $D_{5/2}(F=4, m_F=3)$. **(c)** Frequency scan over the transition $S_{1/2}(F=4, m_F=-4) \leftrightarrow D_{5/2}(F=4, m_F=3)$ with an interrogation time of 100 ms. A Lorentzian fit (solid line) reveals a width of 16 Hz which is dominated by the line width of the spectroscopy laser at 729 nm.

To experimentally confirm our calculations we mapped out the field-dependence of the transition $S_{1/2}(F=4, m_F=4) \leftrightarrow D_{5/2}(F=4, m_F=3)$, which experiences the lowest second-order dependence on changes in the magnetic field. We measured the change in transition frequency for magnetic fields ranging from one to six Gauss as shown in Fig. 5.7 (a). The solid line is a theoretical calculation based on the measurement of the hyperfine constants described earlier in this chapter. For the data, the frequency offset is the only parameter that was adjusted to fit the calculated curve. Both, the experimental data and the model show that the transition frequency changes by less than 400 kHz when the field is varied from one to six Gauss. The transition frequency becomes field-independent at magnetic fields of 3.38 G and 4.96 G with a second order magnetic field dependence of $\mp 16\,\mathrm{kHz/G}^2$, which is six times less than the smallest coefficient for a clock transition based on $m_F=0 \leftrightarrow m_F=0$ transitions at zero field. Another advantage over the transitions with $m_F=0$ is that state initialization into the stretched states can be easily achieved by optical pumping (see subsection 6.1.1). Moreover, the clock states ideally have to be probed at zero magnetic field which makes state initialization and detection even more challenging since the Zeeman states are then degenerate. In addition, to serve as an optical frequency standard, the hyperfine structure of the $D_{5/2}$ energy levels and possible systematics of measurement errors have to be studied in more detail as it was done here. The fact that the hyperfine frequency splitting of the $D_{5/2}$-states is close to the typical frequencies used to drive Paul traps might be a major disadvantage for this ion species to serve as an absolute frequency reference since systematic errors can be large. The benchmark here is currently set by the frequency ratio measurement of two optical atomic clocks (single $^{27}\mathrm{Al}^+$ and $^{199}\mathrm{Hg}^+$) with a fractional uncertainty of 5.2×10^{-17} [117].

As an application we used the field-independence of this transition for investigating the line width of our spectroscopy laser. We set the magnetic field to 3.39 G and recorded an excitation spectrum of the transition by scanning the laser over the line with an interrogation time of 100 ms. Each data point consists of 50 measurements. The result is depicted in Fig. 5.7 (c) where the solid line is a Lorentzian least square fit revealing a line width of 16 Hz. The observed line width is neither limited by the $D_{5/2}$-state's life time ($\tau = 1.17\,\mathrm{s}$) nor by the chosen interrogation time. Line broadening caused by magnetic field fluctuations can be also excluded on this transition. For the small laser powers AC-Stark shifts are expected to play only a minor role. During the measurement the drift of the spectroscopy laser's reference cavity was measured to be 1.5 Hz/s and fully compensated. Therefore, the observed line width is attributed to the emission spectrum of the spectroscopy laser.

The levels comprising these transitions are certainly attractive candidates to serve as an optical qubit leaving the remaining limitation of these to laser stability and spontaneous decay from the metastable state. From the different measurements of the laser line width we obtained the following results:

measurement method	acquisition time	line width $\Delta\nu_{\mathrm{FWHM}}/(2\pi)$
power spectral density of beat note (see Fig. 3.5 (a))	4 s	~ 1 Hz
field independent transition (see Fig. 5.7 (c))	150 s	< 16 Hz
beat note frequency measurement (see section 5.2)	> 4 h	< 50 Hz

Assuming a simple noise model where the laser frequency is constant over each experimental cycle but varies from shot-to-shot according to a Gaussian distribution (see Appendix B) we expect a coherence time on the order of 10 ms. We tested the phase coherence with a Ramsey phase experiment at a magnetic field of 4.99 G on the transition $S_{1/2}(F{=}4, m_F{=}4) \leftrightarrow D_{5/2}(F{=}4, m_F{=}3)$. For two different Ramsey waiting times τ_R of 3 ms and 5 ms the results are given in Fig. 5.8 (a)+(b). Each data point consists of 100 measurement repetitions with the statistical errors indicated. The weighted least square fits with the function $A/2\sin(\phi+\phi_0)$ reveal fringe amplitudes $A = 0.99(1)$ and $0.81(2)$. In the simple noise model these results correspond to laser line width $\Delta\nu^*_{\mathrm{FWHM}}/(2\pi)$ of 18 Hz and 49 Hz and are consistent with our previous measurements listed in the table above. For longer Ramsey times a rather wide scatter of data points is observed which cannot be explained with the simple noise model. Measurements taken using a single $^{40}\mathrm{Ca}^+$ ion with the apparatus at the university building which has a magnetic field shielding and active magnetic field noise compensation give a similar reduction of Ramsey fringe contrast after a few milliseconds.

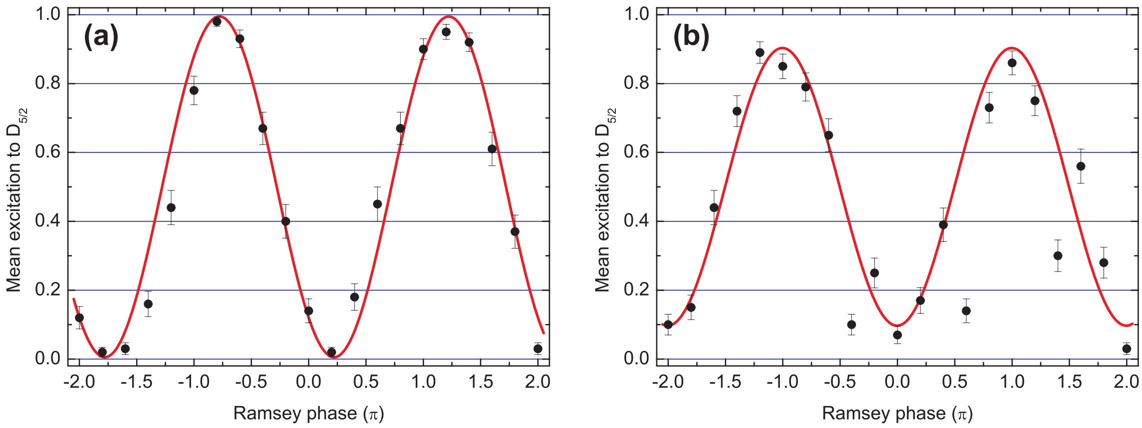

Figure 5.8: The optical qubit's phase coherence was measured by probing the transition $S_{1/2}(F=4, m_F=4) \leftrightarrow D_{5/2}(F=4, m_F=3)$ with Ramsey phase experiments using waiting times of $\tau_{\mathrm{R}} = 3\,\mathrm{ms}$ **(a)** and $5\,\mathrm{ms}$ **(b)**. The magnetic field was set to $4.98\,\mathrm{G}$. Each data point consists of 100 measurements with the statistical errors indicated. The sinusoidal least square fits give as solid lines reveal amplitudes of $A = 0.99(1)$ and $0.81(2)$.

We conclude that even with the considerable resources of a narrow bandwidth laser and the use of a magnetic field insensitive transition (or alternatively a magnetic field noise shielding and active compensation) it seems challenging to further increase the coherence time of the optical qubit significantly. Since an entangling gate on the optical qubit takes only $50\,\mu$s in our setup it makes sense though to consider the optical qubit as processing qubit and the hyperfine clock states as quantum memory. Here $^{43}Ca^{+}$ ions offer the advantage that we can benefit from the best of both worlds.

6 Quantum information processing with a single $^{43}Ca^+$ ion

There are many ways to encode quantum information in the $^{43}Ca^+$ level structure. An optical qubit with vanishing first-order dependence on magnetic field fluctuations was proposed in chapter 5. Here, we consider the hyperfine ground-state manifold depicted in Fig. 2.4 where the energy splitting between the $F=3$ and $F=4$ manifold is 3.2 GHz. For low magnetic fields, the two states $|\downarrow\rangle \equiv S_{1/2}(F=4, m_F=0)$ and $|\uparrow\rangle \equiv S_{1/2}(F=3, m_F=0)$ (hyperfine clock state qubit) exhibit only a weak linear Zeeman effect and are therefore attractive as a robust quantum information carrier. Doppler-cooling, the initialization of external and internal degrees of freedom, state discrimination and the measurement of the qubit's phase coherence are demonstrated on a single $^{43}Ca^+$ ion in this chapter. The main findings of this chapter were also published in reference [74].

6.1 Initialization of the hyperfine clock state qubit

Similar to classical computing, also QIP devices need to be initialized. For our experiments using $^{43}Ca^+$ ions the initialization step comprises Doppler-cooling, optical pumping, cooling to the motional ground-state and state transfer to $|\downarrow\rangle$.

6.1.1 Doppler-cooling and optical pumping

For Doppler-cooling and fluorescence detection, the ion is excited on the $S_{1/2} \leftrightarrow P_{1/2}$ dipole transition with two laser beams. The beam entering from SE (see Fig. 3.7) is π-polarized and slightly red detuned from the transition $S_{1/2}(F=4) \leftrightarrow P_{1/2}(F=4)$. The second beam is σ^+-polarized and sent through an electro-optic phase modulator producing sidebands at 3.2 GHz containing about 20% of the carrier intensity. With this beam the ions are excited from the $S_{1/2}(F=3)$ and $S_{1/2}(F=4)$ to the $P_{1/2}(F=4)$ manifold. Coherent population trapping is avoided by lifting the degeneracy of the Zeeman sub-levels with a magnetic field. To avoid population trapping in the $D_{3/2}$ manifold, repumping laser light at 866 nm is applied. The repumping efficiency was improved by tuning the laser close to the $D_{3/2}(F=3) \leftrightarrow P_{1/2}(F=3)$ transition frequency and providing two additional

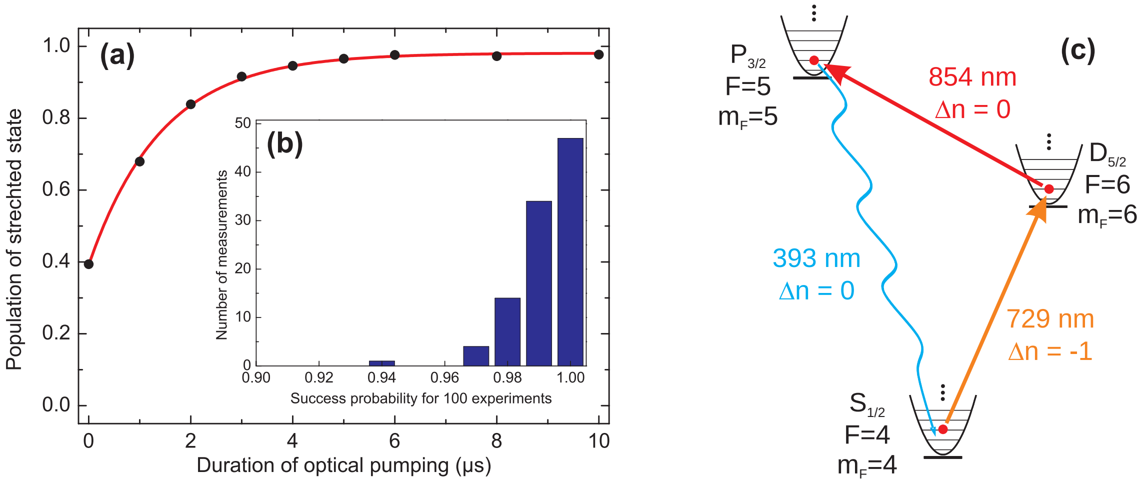

Figure 6.1: **(a)** The population in the stretched state $S_{1/2}(F = 4, m_F = 4)$ is plotted as a function of the duration of optical pumping. An exponential fit (solid line) reveals a time constant of $1.4\,\mu$s. After $10\,\mu$s, the population is in the desired state in 98% of the measurements. **(b)** The inset shows a histogram of the success rate of 100 measurements each containing 100 experiments when two π-pulses on the quadrupole transition are applied and an additional intermediated optical pumping interval is used. This enhances the fidelity of the process to above 99.2%. **(c)** Sideband cooling on the quadrupole transition involves using the stretched states. For each cooling cycle one phonon can be taken away from the ions and the entropy is carried away by the photon emitted at 393 nm. The same states are also used to enhance the quality of optical pumping.

frequencies shifted by -150 MHz and -395 MHz such that all hyperfine $D_{3/2}$ levels are resonantly coupled to one of the $P_{1/2}(F=3,4)$ levels. We observed a maximum fluorescence count-rate of 24 kcps per $^{43}Ca^+$ ion on the PMT for magnetic fields ranging from 0.2 to 5 G. This is about 45% of the count-rate we observe for $^{40}Ca^+$ ions. We tried various other laser polarizations and the use of additional lasers at wavelengths of 393 nm, 397 nm and 850 nm in order to further increase the fluorescence rate. Only when we replace the EOM sideband by an independent laser at 397 nm we see a small improvement on the order of 5%. It is not yet clear what the bottleneck for the produced photon flux is. Moreover, for loading $^{43}Ca^+$ ions into the trap we found that the configuration where the laser at 397 nm is tuned to the $S_{1/2}(F=3) \leftrightarrow P_{1/2}(F=4)$ transition and the polarization of the blue laser beam entering from SW is switched to linear works much more efficiently. However, the maximum net count-rate in this configuration is only about 14 kcps per $^{43}Ca^+$ ion.

After switching off the π-polarized laser beam, a single $^{43}Ca^+$ ion is optically pumped into the state $S_{1/2}(F=4, m_F=4)$. This state's population is then measured with two consecutive π-pulses exciting the population to different Zeeman states of the $D_{5/2}$ manifold and subsequent fluorescence detection (see section 6.2). Figure 6.1 (a) shows the dynamics of optical pumping and illustrates that the stretched Zeeman state of the ground-state manifold is already strongly populated during Doppler-cooling. A least-square exponen-

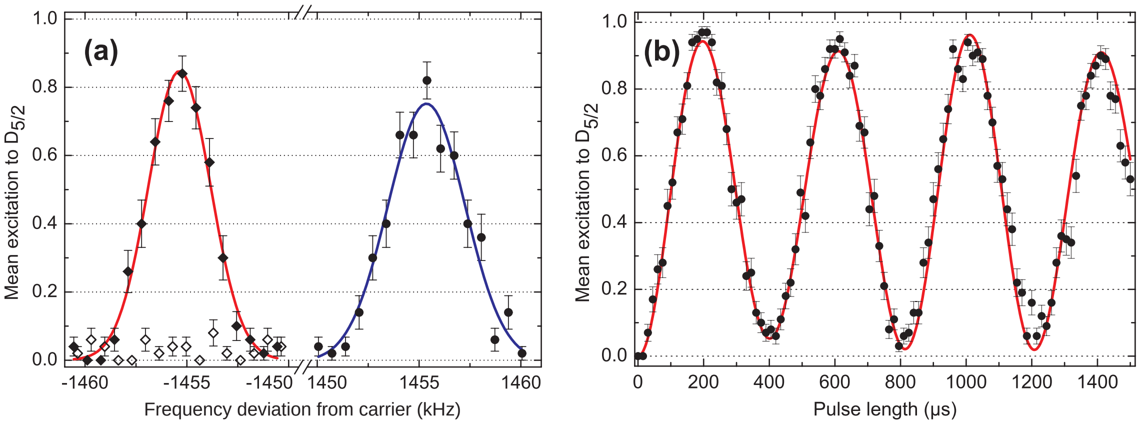

Figure 6.2: (a) Excitation spectrum of the red and blue axial sideband of the quadrupole transition $S_{1/2}(F=4, m_F=4) \leftrightarrow D_{5/2}(F=6, m_F=6)$. The excitation on the red sideband is strongly suppressed when sideband cooling is on ($\diamond$) compared to when it is omitted ($\blacklozenge$). By comparison with the excitation after sideband cooling on the blue sideband ($\bullet$) we obtain a mean population of the axial mode of $\bar{n}_{\mathrm{ax}} = 0.06$. **(b)** Rabi oscillations on the blue sideband ($\omega_{\mathrm{ax}}/(2\pi) = 1.18\,\mathrm{MHz}$) of the transition $S_{1/2}(F=4, m_F=4) \leftrightarrow D_{5/2}(F=6, m_F=6)$ after ground-state cooling. The solid line is a least square fit assuming a thermal state. It yields a mean occupation of the axial mode of $\bar{n}_{\mathrm{ax}} = 0.06$.

tial fit to the data points yields a time constant of $1.4\,\mu$s. After $10\,\mu$s, the desired state is populated in 98% of the cases.

The pumping efficiency can be improved by transferring the population after this first step with a π-pulse to the $D_{5/2}(F=6, m_F=6)$-state and repeating the optical pumping. By applying another π-pulse on the same transition, the populations in $S_{1/2}(F=4, m_F=4)$ and $D_{5/2}(F=6, m_F=6)$ are exchanged. On average 98% should now be in $S_{1/2}(F=4, m_F=4)$ and the rest in the $D_{5/2}$-state. Finally the two populations are combined by switching on the 854 nm laser for a short time to clear out the $D_{5/2}$-state via the $P_{3/2}(F=5, m_F=5)$-state from where it can decay only into the desired stretched state. For this scheme the same states are involved as for sideband cooling (see Fig. 6.1 (c)). The inset Fig. 6.1 (b) shows a histogram built from 100 measurements each comprising 100 experiments indicating a lower bound of the pumping efficiency of 99.2%.

After Doppler-cooling and optical pumping, an average population $\bar{n}_{\mathrm{ax}} = 10(5)$ of the axial mode is inferred from measuring the decay of Rabi oscillations on an axial sideband. The average number of quanta is heavily dependent on the laser detunings and powers.

6.1.2 Sideband cooling on the quadrupole transition

Cooling the ions to the motional ground-state is mandatory in order to maximize quantum gate fidelities. In our experiment, it has been implemented with a scheme analogous to the one demonstrated with $^{40}Ca^+$ ions about ten years ago [133]. In order to obtain a

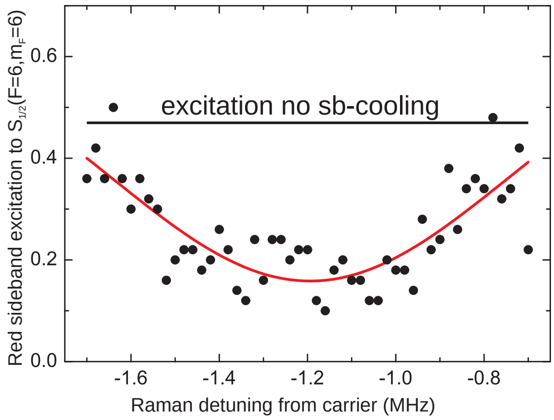

Figure 6.3: Mean excitation on the red sideband of the quadrupole transition $S_{1/2}(F=4, m_F=4) \leftrightarrow D_{5/2}(F=6, m_F=6)$ after Raman sideband cooling where the relative frequency of the Raman light fields is scanned over the red sideband. Close to the red sideband resonance we observe a drop of excitation indicating a reduction of the mean phonon number of the axial mode.

closed cooling cycle (see Fig. 6.1 (c)), the frequency of the laser at 729 nm is tuned to the red sideband of the transition $S_{1/2}(F = 4, m_F = 4) \leftrightarrow D_{5/2}(F = 6, m_F = 6)$. An additional quenching laser at 854 nm is required to increase the spontaneous decay rate to the energy level $S_{1/2}$ by coupling the $D_{5/2}(F=6, m_F=6)$ to the $P_{3/2}(F=5, m_F=5)$-state. Spontaneous decay to the stretched state takes the entropy away from the ion. In each cycle, one motional quantum can be removed.

The residual occupation of the motional mode was inferred from the ratio of the red and the blue sideband excitation (see Fig. 6.3 (a)) using Eq. (4.2). Alternatively, Rabi oscillations on the blue motional sideband of the transition $S_{1/2}(F=4, m_F=4) \leftrightarrow D_{5/2}(F=6, m_F=6)$ can be observed to measure the average population of the axial mode (see Fig. 6.3 (b)). The solid line is a fitted model function [89] with the average population of the axial mode $\bar{n}_{\mathrm{ax}}$ as a free parameter. From both methods, we consistently obtain $\bar{n}_{\mathrm{ax}} = 0.06$.

6.1.3 Raman sideband cooling

A second option for ground-state cooling that has been only briefly studied so far is to use a Raman laser detuned from the $S_{1/2} \leftrightarrow P_{1/2}$ dipole transition to implement cooling in a similar fashion as demonstrated for beryllium ions [134]. This technique is expected to have a number of advantages over the method exploiting the quadrupole transition. First, since the Lamb-Dicke parameter is larger by about a factor of four, the Raman method should be faster. Moreover, no narrow bandwidth laser stabilized to the ion transitions is required but the relevant frequency is directly determined by setting a microwave signal generator appropriately. In a first attempt we tested a continuous scheme where the phonons are taken out by transferring population on the red sideband of the transition

$S_{1/2}(F=4, m_F=4) \leftrightarrow S_{1/2}(F=3, m_F=3)$ with a non-copropagating Raman light field. Spontaneous scattering, induced by the light fields as set for optical pumping, transfers entropy away from the ions. In Fig. 6.3 a first shot result is given where subsequently to the Raman sideband cooling the red sideband of the quadrupole transition $S_{1/2}(F=4, m_F=4) \leftrightarrow D_{5/2}(F=6, m_F=6)$ was probed while the detuning of the two Raman light fields was varied. Close to the resonance of the red sideband the excitation drops to a lower value indicating a significant reduction of the harmonic oscillator mode population. Since the excitation does not vanish completely we have to improve the scheme by a more careful analysis of the used laser detunings and powers. In addition, a pulsed scheme can be tested where optical pumping and driving the red sideband with the Raman field are applied alternately.

6.1.4 Transfer to the hyperfine clock states

Ground-state cooling on quadrupole transitions requires a closed cooling cycle which can only be achieved efficiently when working with the stretched hyperfine ground states $S_{1/2}(F=4, m_F=\pm 4)$. For this reason, methods are needed that allow for a transfer from these to the qubit state $|{\downarrow}\rangle$. Ideally, this process should be easy to implement, robust to its input parameters, fast, should not cause heating, and should be applicable to one or many ions at the time. Four different techniques were under consideration:

Optical pumping on the $\mathsf{S_{1/2}} \leftrightarrow \mathsf{P_{1/2}}$ transition

The state $|{\downarrow}\rangle$ could be populated by optical pumping with π-polarized light fields exciting the transitions $S_{1/2}(F=4) \leftrightarrow P_{1/2}(F=4)$ and $S_{1/2}(F=3) \leftrightarrow P_{1/2}(F=4)$ within a few microseconds. However, the many scattering events required to pump the population to the desired state are likely to heat up the ion from the motional ground-state. Moreover, the efficiency of the optical pumping would probably be fairly poor as small polarization imperfections of the beams and repumping via the $S_{1/2}(F=4) \leftrightarrow P_{1/2}(F=3)$ transition are likely to occur.

Raman light field

Transferring the population can also be achieved with a Raman light field detuned from the $S_{1/2} \leftrightarrow P_{1/2}$ dipole transition at 397 nm. In the simplest scenario, a sequence of four π-pulses would be used to populate the state $|{\downarrow}\rangle$ starting from $S_{1/2}(F=4, m_F=\pm 4)$ by changing the magnetic quantum number in units of $\Delta m = \mp 1$. Use of copropagating beams with properly set beam polarizations can help to suppress unwanted excitations of motional sidebands and transitions to other Zeeman states.

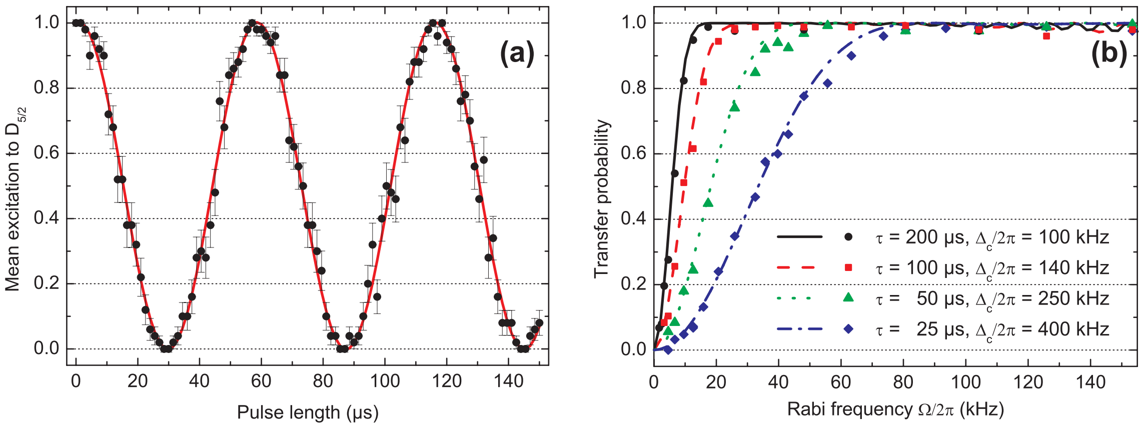

Figure 6.4: **(a)** Pulse length scan of the second transfer pulse on the transition $D_{5/2}(F=6, m_F=2) \leftrightarrow |\downarrow\rangle$ to initialize the hyperfine qubit. A weighted least square fit with Eq. (6.1) reveals a fringe amplitude of 1.004(5) consistent with one. **(b)** Transfer probability measurement of an amplitude-shaped laser pulse on the transition $S_{1/2}(m_F=1/2) \leftrightarrow D_{5/2}(m_F=3/2)$ of a single $^{40}Ca^{+}$ ion as a function of the coupling strength Ω. Data were taken for four different pulse lengths τ and frequency chirp spans Δ_c as given in the plot legend. The lines indicate our theoretical predictions. With enough laser power available, the transfer probability hardly changes over a wide range of Rabi frequencies.

Microwave

Instead of a Raman light field, also a microwave field can be used to transfer the ions in a four-step process to $|\downarrow\rangle$. An additional advantage here is that the field's wavelength is huge compared to the distance of the ions and therefore an equal coupling of all ions to the field is guaranteed.

A limitation for the methods based on Raman light fields and microwave radiation, is the small Clebsch-Gordan coefficient (see Tab. 2.1) on the transitions $S_{1/2}(F=3, m_F=\pm 3) \leftrightarrow S_{1/2}(F=4, m_F=\pm 2)$. That makes the whole process either slow or necessitates a larger frequency separation of the Zeeman levels in order to suppress non-resonant excitation of neighboring transitions.

Transfer via quadrupole transition

State transfer based on a laser operating on the quadrupole transition $S_{1/2} \leftrightarrow D_{5/2}$ reduces the transfer process to two steps since the selection rules allow for $\Delta m = \pm 2$. The duration of a π-pulse can be as short as a few microseconds, and only a single laser beam is needed that can be either focused to a small region or illuminate the whole trap volume. If the $D_{5/2}(F=4)$ is chosen as intermediate state, a good compromise is achieved between the quadrupole coupling strength of the involved transitions and the frequency separation of the neighboring $D_{5/2}$-state Zeeman levels. The latter is by a factor 1.6 larger as for the ground states. In particular for low magnetic fields this method is expected to work

better than a transfer with Raman or microwave fields.
With the precision laser for the quadrupole transition acting on a single $^{43}\mathrm{Ca}^+$ ion, the implementation of state transfer is straightforward. With two consecutive π-pulses we achieved a transfer success probability of more than 99% for a single ion. Rabi oscillations on the second transfer transition (here $D_{5/2}(F=6, m_F=2) \leftrightarrow |\downarrow\rangle$) are depicted in Fig. 6.4 (a). A weighted least square fit with the function

$$f(t) = \frac{A}{2}\cos(\pi\, t/\tau_\pi) + y_0 \tag{6.1}$$

reveals a fringe amplitude $A = 1.004(5)$ consistent with one.

However, assuming Gaussian laser beams, we cannot expect equal light intensities on all ions for larger ion crystals, unless one is willing to waste most of the laser power by making the beam size very large. As variations of the coupling strengths may also arise from other technical imperfections, a more robust scheme seems to be desirable. Inspired by reference [135], we introduce amplitude-shaping and a linear frequency sweep of the transfer pulses to demonstrate a transfer technique less sensitive to changes in the laser intensity. Figure 6.4 (b) shows the demonstration of this technique using a single $^{40}\mathrm{Ca}^+$ ion. The transfer probability from the $S_{1/2}(m_J = 1/2)$ to the $D_{5/2}(m_J = 3/2)$-state is plotted as a function of the Rabi frequency Ω for four different pulse durations τ. The intensity of the laser pulses had a $\cos^2$-shape over the pulse duration. The frequency of the laser was linearly swept over a range Δ_c centered on the transition frequency. The measurement data coincide well with the predicted evolution given as lines and demonstrate that the transfer probability is hardly affected over a broad range of Rabi frequencies for the different parameters. Of course, this technique can also be used with microwave and Raman fields.

6.2 State discrimination

For efficient state detection of the $^{43}\mathrm{Ca}^+$ hyperfine qubit states we make use of the electron shelving technique first introduced by Hans G. Dehmelt in 1975 [136]. The discrimination between the $|\downarrow\rangle$ and $|\uparrow\rangle$ states is achieved by scattering light on the $S_{1/2} \leftrightarrow P_{1/2}$ transition after having shelved the $|\downarrow\rangle$ state to the $D_{5/2}$ metastable state. In our experiment, the same light fields are used as for Doppler-cooling but with slightly more power. With this method, not only $|\uparrow\rangle$ and $|\downarrow\rangle$ can be discriminated but the other Zeeman levels in the $S_{1/2}$ and $D_{5/2}$-state manifolds, too. The quality of the transfer pulses sets a limitation to the state discrimination. Again, pulse shaping and frequency sweeping can help to increase the robustness with respect to intensity variations of the shelving laser. In addition, instead of using a single π-pulse excitation to a certain Zeeman state in the $D_{5/2}$-state manifold, the first π-pulse can be followed by a second one, exciting any population still remaining in $|\downarrow\rangle$ to a different $D_{5/2}$-Zeeman state. Assuming an error smaller than 1% for each of the pulses, one expects a shelving error of less then 10^{-4}. The final detection fidelity will then be limited by spontaneous decay from the $D_{5/2}$-state during the detection which depends on the signal-to-noise ratio and signal strength. For the experiments reported here, the detection time was set to 5 ms. The error due to spontaneous decay is estimated to be 0.5% on average for the $|\downarrow\rangle$-state.

6.3 Coherent state manipulation on the ^{43}Ca$^+$ hyperfine qubit

Once external and internal degrees of freedom are initialized, quantum information needs to be encoded into the ions, stored and manipulated. This is achieved with a driving field tuned to the qubit's transition frequency. Two different driving fields were investigated.

6.3.1 Microwave

From an experimental point of view, quantum state manipulation by microwave radiation is simple and robust. There is no alignment required and stable frequency sources are readily available with computer-controlled power, frequency and phase.

At first we determined the polarization of the microwave photons. After initializing a single ^{43}Ca$^+$ ion in $|\downarrow\rangle$ we recorded Rabi oscillations on the three allowed transitions to the $S_{1/2}(F=3)$ manifold using the same microwave power. As a result we obtained the times to perform a π-pulse:

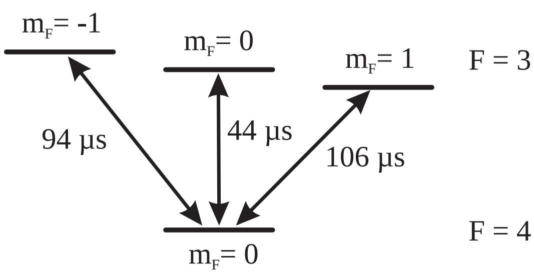

Taking into account the transitions' relative coupling strengths (see Tab. 2.1) we see the radiation is almost linear polarized where the part of the π-polarization is slightly dominating the $\sigma^{\pm}$-component. With this type of field all possible transitions can be efficiently driven. To further characterize the microwave properties on the ion we induced Rabi oscillations on the transition $S_{1/2}(F=4, m_F=4) \leftrightarrow S_{1/2}(F=3, m_F=3)$. For each experiment the ion is initialized into $S_{1/2}(F=4, m_F=4)$ by means of optical pumping on the $S_{1/2} \leftrightarrow P_{1/2}$ transition. The microwave is then turned on with a power of about 24 dBm for a variable amount of time. The two states are then discriminated by transferring

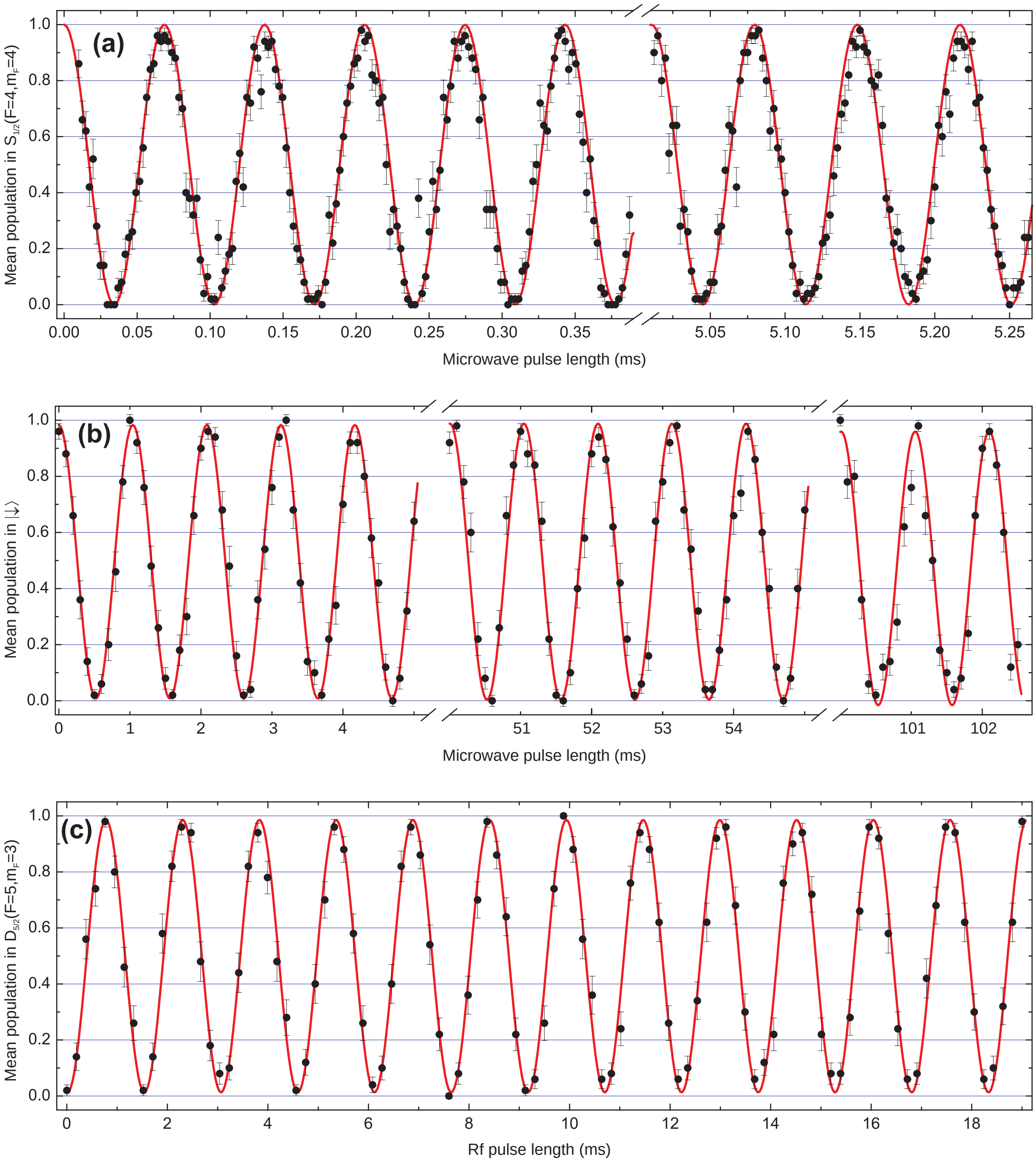

Figure 6.5: **(a)** Rabi oscillations on the transition $S_{1/2}(F=4, m_F=4) \leftrightarrow S_{1/2}(F=3, m_F=3)$ mediated by direct microwave application where the dots represent the measurements (à 50 cycles) and the solid line is a sine with full contrast and a π-time set to $\tau_\pi = 34.3\,\mu$s. Thus, even after more than 150 state transfers the fringe amplitude is still close to unity. **(b)** Rabi oscillations on the ^{43}Ca^{+} hyperfine qubit ($|\downarrow\rangle \leftrightarrow |\uparrow\rangle$) mediated by a microwave field after 0, 50 and 100 ms. Each data point represent 50 individual measurements. The solid line is a weighted least square fit with Eq. (6.1) which results $y_0 = 0.490(3)$, $\tau_\pi = 520.83(3)\,\mu$s and $A = 0.974(11)$. Since the amplitude of the Rabi oscillation is still close to unity after 200 state transfers the microwave can serve as a reference to the Raman light field regarding power and phase stability. **(c)** Rabi oscillations on the transition $D_{5/2}(F=4, m_F=3) \leftrightarrow D_{5/2}(F=5, m_F=3)$ mediated by direct radiofrequency application where the dots represent the measurements (à 50 cycles) and the solid line is least square fit using the same function as above. Here we obtain $y_0 = 0.499(3)$, $\tau_\pi = 763.3(5)\,\mu$s and $A = 0.973(8)$.

the population remaining in $S_{1/2}(F=4, m_F=4)$ with a π-pulse to $D_{5/2}(F=6, m_F=6)$. A typical result is given in Fig. 6.5 (a). Each data point represents 50 individual measurements. The solid line is given by Eq. (6.1) with $A=1$, $y_0=0.5$ and τ_π set to $34.3\,\mu$s. We see that even after about 150 state transfers the fringe amplitude is close to unity.

An example for Rabi oscillations on the clock state qubit $|\downarrow\rangle \leftrightarrow |\uparrow\rangle$ is given in Fig. 6.5 (b) recorded at a magnetic field of 3.4 G. After initializing the ion into $|\downarrow\rangle$, a microwave signal of 3.226 GHz is turned on for a variable amount of time followed by state detection. The resulting Rabi oscillations are depicted at instances of 0, 50 and 100 ms. The solid line represents a weighted least square fit based on Eq. (6.1) where $y_0 = 0.490(3)$, $\tau_\pi = 520.83(3)\,\mu$s and $A = 0.974(11)$. About 200 state transfers are observed over a time of 100 ms with hardly any decrease in fringe amplitude A. In both cases the subsequent decay of the fringe amplitude for more oscillations indicates a limitation due to small fluctuations of the microwave power.

Today, there are a number of different ideas to implement two-qubit gates with ^{43}Ca^{+}. One of them working on the ground-state hyperfine qubits [137] relies on a Raman-light field that is slightly detuned from the quadrupole transition. It is technically quite demanding to create such a laser field and therefore it can be helpful to study the situation differently by encoding the quantum information in two of the $D_{5/2}$-states. By proper choice of states and magnetic field, this qubit is insensitive to magnetic field fluctuations and in contrast to the ground-state encoding the frequency difference is only a couple of MHz. Using AOM's it is technically easy to create a phase-coherent Raman light field to drive this qubit. In this context a direct radiofrequency drive can also be an attractive reference to characterize the phase coherence of the light field and may also be used for spin echos. To test this idea a single ^{43}Ca^{+} ion was optically pumped into $S_{1/2}(F=4, m_F=4)$ and initialized into $D_{5/2}(F=4, m_F=3)$ with a π-pulse. Then a radiofrequency pulse (~19 MHz, 2 W) was applied for a variable amount of time to drive the transition $D_{5/2}(F=4, m_F=3) \leftrightarrow D_{5/2}(F=5, m_F=3)$. State discrimination was achieved by transferring the population in $D_{5/2}(F=4, m_F=3)$ back to $S_{1/2}(F=4, m_F=4)$ and subsequent fluorescence detection. The resulting Rabi oscillations are depicted in Fig. 6.5 (c). The dots are the measurement results and the solid line represents a weighted least square fit with Eq. (6.1) resulting in a fringe amplitude of $A = 0.973(8)$. Coherence is preserved for tens of milliseconds making $D_{5/2}$-encoded qubits an attractive test bed for new gate schemes.

Unfortunately, microwave and radiofrequency fields do not couple motional and electronic states unless strong magnetic field gradients are applied [94] and they cannot be focussed to a single qubit location. Nevertheless, microwave excitation turns out to be a useful reference for investigating the phase stability of Raman excitation schemes to be discussed in the next paragraph.

6.3.2 Raman light field

In contrast to the microwave excitations the interaction region of the Raman field detuned from the dipole transition $S_{1/2} \leftrightarrow P_{1/2}$ is as small as the diameter of the involved laser beams. The coupling to the motional mode along the trap axis is described by the Lamb-Dicke parameter (see section 2.5). For copropagating lasers the Lamb-Dicke factor is negligible whereas it is maximized for lasers counter-propagating along the motional mode axis.

We characterize the Raman interaction on a single ion by driving Rabi oscillations on the hyperfine qubit with copropagating beams from NW that are detuned from the $S_{1/2} \leftrightarrow P_{1/2}$ transition frequency by -10 GHz. Figure 6.6 (a) shows Rabi oscillations for excitation times of up to 4 ms with a π-time set to $\tau_\pi = 65.3(1)\,\mu$s. The first few oscillations have a fringe amplitude of $A = 0.97(1)$ which is reduced to 0.80(2) after more than 50 state transfers. Shot-to-shot variations in Raman light intensity contribute to a loss symmetrically to the average excitation. In addition, the fringe center dropped from $y_0 = 0.479(5)$ to $y_0 = 0.428(7)$ due to non-resonant scattering introduced by the Raman light field.

The ability to couple electronic and motional states by the Raman excitation was tested by comparing Rabi frequencies on the carrier and on the first blue axial sideband with non-copropagating beams (from NW and NE) illuminating an ion initially prepared in the motional ground-state. The two Raman beams enclose a 90° angle such that the differential k-vector is collinear with the trap axis to optimize for the momentum transfer with the motional mode in axial direction. From the ratio of the Rabi frequencies Fig. 6.6 (b)+(c), we directly infer the Lamb-Dicke parameter to be $\eta = 0.216(2)$ in good agreement with the theory.

Finally we measured the dependence of the π-pulse duration to the Raman detuning Δ and the coupling strength to the Raman light power. Both measurement results are depicted in Fig. 6.6 (d)+(e). As expected for Raman detunings much smaller than the fine structure splitting of the P-states, both data sets are well reproduced by the linear fits given as solid lines.

6.4 Coherence properties of the ^{43}Ca$^+$ hyperfine qubit

Applying the methods described before, we investigated quantum information storage capabilities of the ^{43}Ca$^+$ hyperfine qubit. Limitations to the coherence time arise from both, scattering events and dephasing. For the hyperfine qubit, spontaneous decay is negligible since the lifetime of the involved states can be considered as infinite for all

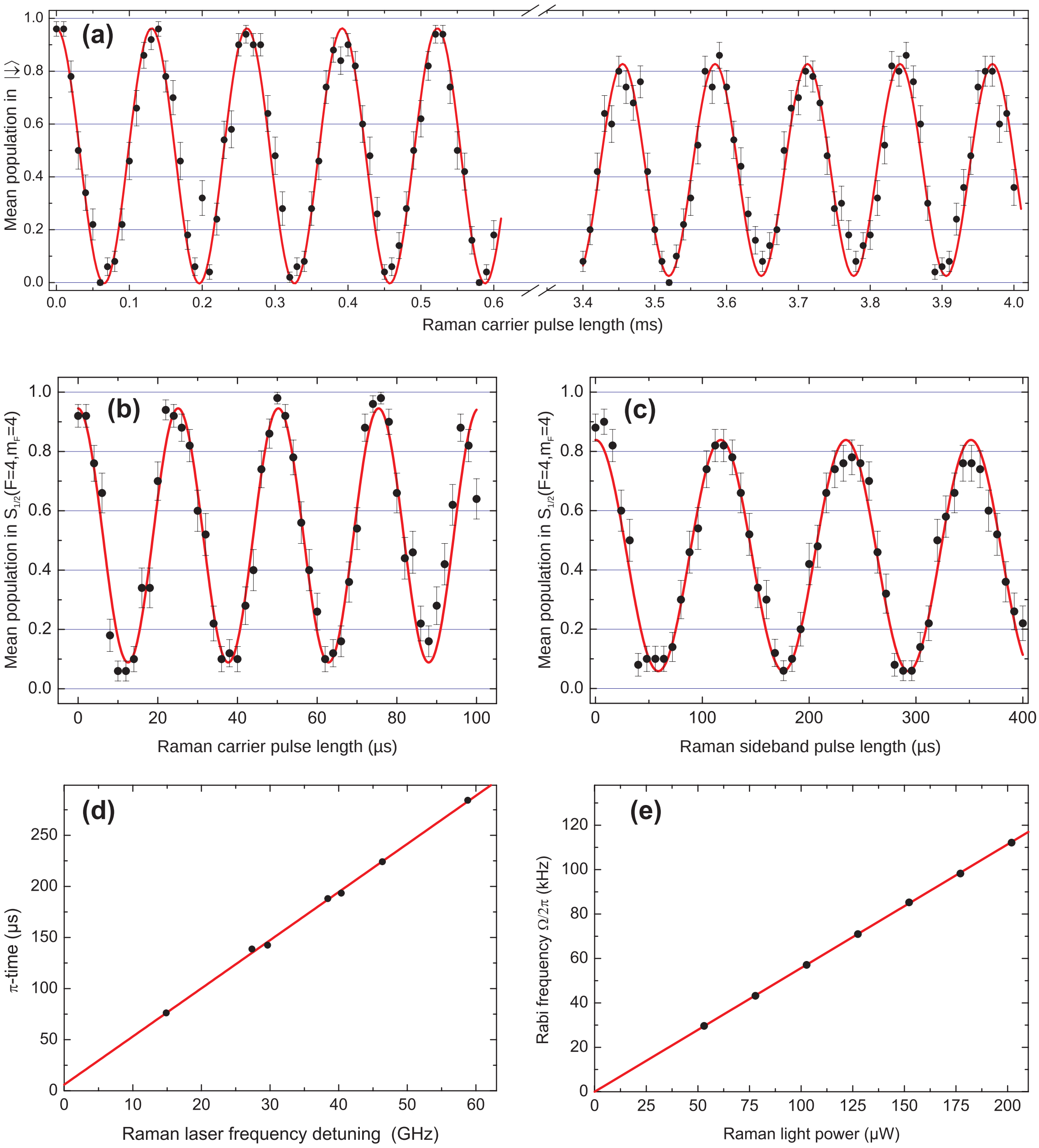

Figure 6.6: **(a)** Rabi oscillations on the ^{43}Ca$^+$ hyperfine qubit induced by a collinear Raman light field. Each data point represents 50 individual measurements. As for the microwave excitation, we fitted a sinusoidal function to the data set from 0 to 600 μs which yields a fringe amplitude $A = 0.97(1)$, a π-time of $\tau_\pi = 65.3(1)\,\mu$s and a fringe center at $y_0 = 0.479(5)$. Fitting to the data points beyond 3.4 ms a small offset phase had to be introduced and τ_π adjusted to 63.8(2) μs indicating a slow increase of the Raman light power during the measurement. The amplitude reduces to $A = 0.80(2)$ and the fringe center dropped to $y_0 = 0.428(7)$. A comparison with microwave excitation reveals imperfections caused by spontaneous scattering and laser amplitude fluctuations. **(b)+(c)** Direct comparison of Rabi oscillations on the carrier and on the blue axial sideband. From the ratio of the times τ_π we find a Lamb-Dicke parameter $\eta = 0.216(2)$. **(d)** The pulse duration to achieve a π-pulse is linearly dependent on the detuning of the laser to the $P_{1/2}$ energy level. **(e)** The Rabi frequency is linearly dependent on the light power/intensity of the Raman light fields. For this measurement the Raman detuning was set to 58 GHz.

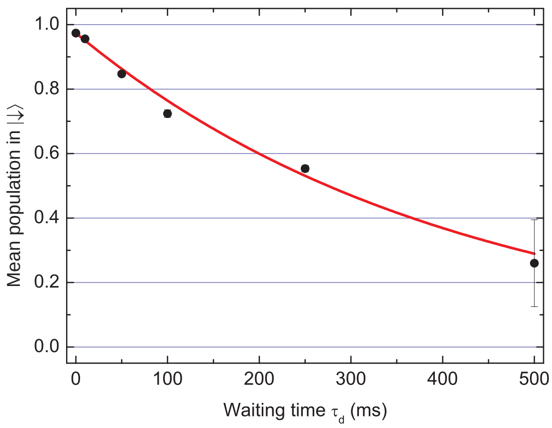

Figure 6.7: Measurement of the $|\downarrow\rangle$-state population probability after a variable waiting time τ_d. Single photon scattering events induced by residual light at 397 nm lead to a transfer of population from the $|\downarrow\rangle$-state to other Zeeman states in the ground-state manifold. The solid line is an exponential fit with a decay time constant of 410 ms.

practical purposes. Scattering can be induced though by imperfectly switched off laser beams. To judge the importance of this effect, we prepared a single ^{43}Ca$^+$ ion in the state $|\downarrow\rangle$. After waiting for a time τ_d, we transferred the population with two subsequent π-pulses to $D_{5/2}(F=6, m_F=0)$ and $D_{5/2}(F=4, m_F=2)$. Ideally no fluorescence should be observed. Figure 6.7 shows the decrease of an initial $|\downarrow\rangle$-population probability of 0.97 with increasing waiting time τ_d. An exponential decay fit yields a time constant of 410 ms. This observation can be explained by imperfect switching off the cooling laser at a wavelength of 397 nm by one single-pass AOM only. For every blue photon that is scattered the ion will be lost from the state $|\downarrow\rangle$ with a high probability by decaying to one of the other $S_{1/2}$ Zeeman states. This complication was avoided by using a mechanical shutter completely switching off the Doppler-cooling laser in all Rabi and Ramsey experiments lasting for 50 ms and longer similarly as we have done for the measurement of the isotope shift (see section 5.2).

Decoherence due to phase errors does not alter the state occupation probabilities. Instead, the phase information between driving field and the qubit gets lost. A powerful method to characterize this effect consists in measuring fringe amplitudes in Ramsey phase experiments. Here, a superposition of the two qubit states is created by a $\pi/2$-pulse. After a waiting time τ_R, during which the qubit evolves freely, a second $(\pi/2)_\phi$-pulse is applied. By scanning the Ramsey phase ϕ of the second pulse, a sinusoidal fringe pattern is observed whose fringe amplitude is a measure of the maintained coherence.

For the Raman light field, the relevant phase is not only determined by the radiofrequency devices supplying the AOM's creating the 3.2 GHz splitting but also by the relative optical path length of the red and the blue beamlines. In general, the absolute phase is not of interest as long as it does not change during the experiment. The experimental setup (see subsection 3.2.3) can be considered as an interferometer whose sensitivity is also dependent

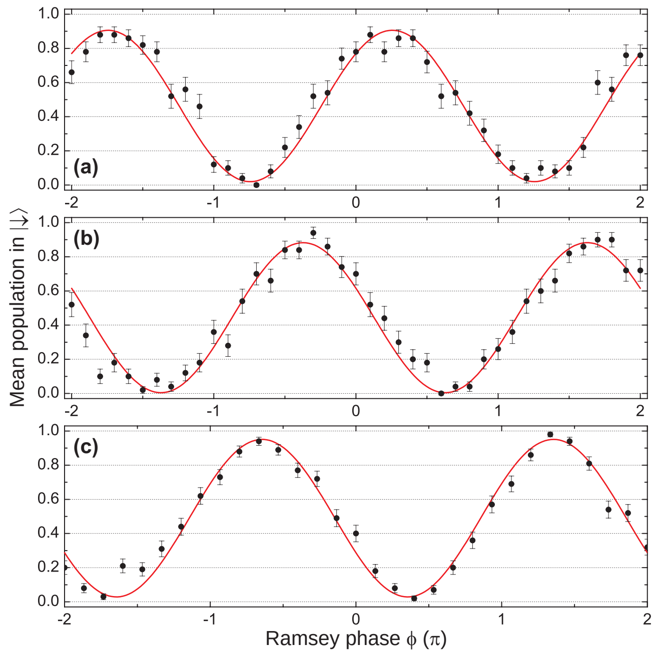

Figure 6.8: Ramsey phase experiments on the $^{43}Ca^+$ hyperfine qubit at a magnetic field of 3.4 G with a Ramsey waiting time τ_R set to 100 ms. The data were taken with three different driving fields. **(a)** Microwave drive with $\tau_\pi = 19\,\mu$s, **(b)** copropagating Raman light field with $\tau_\pi = 20\,\mu$s and **(c)** non-copropagating Raman light field where $\tau_\pi = 23\,\mu$s. The fringe amplitudes are determined by weighted least square fits with Eq. (6.2) (solid lines). This yields values of $A = 0.886(17)$, $0.879(16)$ and $0.922(13)$ respectively. Dephasing by interferometric instabilities is not limiting the experiments on these timescales. For Ramsey times beyond 100 ms we observed a further decay of the fringe amplitude.

on its size. For non-copropagating Raman beams, the enclosed area is about four times larger than for the copropagating beams. In order to see whether the experiment would be limited by this effect, we investigated three different configurations.

Figure 6.8 shows the resulting Ramsey fringe patterns when driving the hyperfine qubit with (a) a microwave, (b) a copropagating Raman field and (c) a non-copropagating Raman field. The Ramsey waiting time τ_R was set to 100 ms, the $\pi/2$-pulses had a duration of about 20 μs. Each data point represents either 50 or 100 measurements. The error bars indicate the statistical errors (1σ) and are used as weights when fitting the function

$$g(\phi) = \frac{A}{2}\sin(\phi + \phi_0) + y_0 \tag{6.2}$$

to the data in order to determine the fringe amplitude A. The parameters y_0 and ϕ_0 are also free fit parameters but not further considered. For the different excitation schemes, we find fringe amplitudes of 0.886(17), 0.879(16) and 0.922(13) respectively. From this we conclude that errors introduced by interferometric instabilities in generating the Raman beams do not limit our experiment on time scales up to 100 ms. For longer Ramsey times, we observed a further decay of the fringe amplitude which we attribute to dephasing.

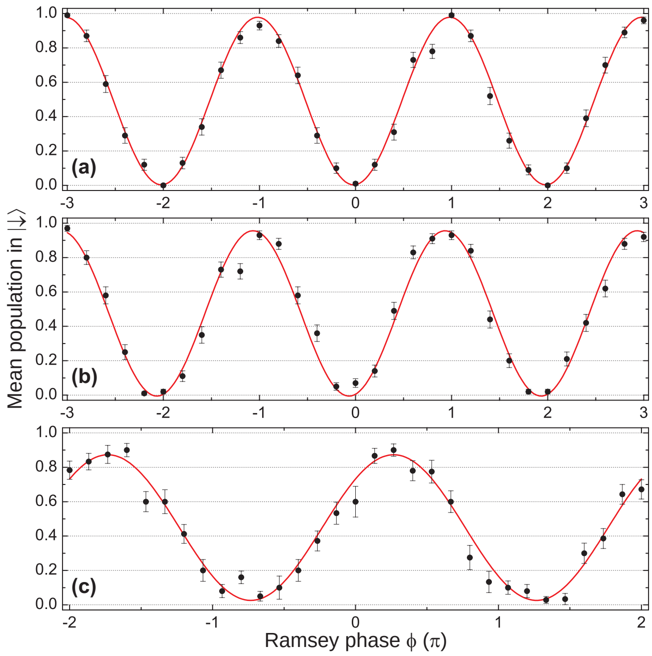

Figure 6.9: Ramsey phase experiments on the $^{43}Ca^+$ hyperfine qubit with microwave excitation at a magnetic field of 0.5 G. The fringe amplitudes are determined by weighted least square fits based on Eq. (6.2) (solid lines) with a amplitude A and offset phase free. **(a)** A scan with $\tau_R = 50\,\mu$s results in an amplitude of 0.976(4) and demonstrates the ability of state initialization, manipulation and readout at low magnetic fields. **(b)** For a Ramsey time $\tau_R = 200$ ms the amplitude is 0.962(11). **(c)** For a Ramsey time of $\tau_R = 1$ s a fringe amplitude of 0.847(21) was measured. Here the measurement time was about 90 min. The reduction of the amplitude is attributed to the residual sensitivity of 1.2 kHz/G to ambient magnetic field fluctuations.

These measurements were performed at a magnetic field of 3.4 G. For small magnetic fields, the residual qubit sensitivity to magnetic field fluctuations increases linearly with a slope of 2.4 kHz/G^2. Therefore, we reduced the magnetic field to 0.5 G and repeated the measurement with the microwave field. The resulting fringe patterns for three different Ramsey times τ_R are depicted in Fig. 6.9. A short waiting time of $\tau_R = 50\,\mu$s (a) results in a fringe pattern amplitude of 0.976(4). This demonstrates the ability of reliable state initialization, readout and single-qubit gate operation for the $^{43}Ca^+$ hyperfine qubit also for low magnetic fields. For a Ramsey time of $\tau_R = 200$ ms (b) we still obtain a fringe amplitude of 0.962(11). A drop in amplitude to 0.847(21) is observed only after increasing the Ramsey waiting time to $\tau_R = 1$ s (c). For the last measurement data points were taken in a random order over an interval of about 90 min.

Comparing the measurements at 3.4 G and 0.5 G, we conclude that the main limitation to the coherence time comes from the residual sensitivity of the qubit at finite fields. Further improvements can be made by means of active magnetic field stabilization and passive shielding. In addition, rephasing can be achieved by an intermediate spin-echo pulse that exchanges the populations of the two qubit levels. Typically, the coherence time is defined as the Ramsey time for which the fringe amplitude A has dropped to a value of $1/e$. Extrapolation of our measurements would lead to a coherence time on the order of 6.0 s when assuming an exponential decay and 2.5 s for Gaussian decay.

It is experimentally demanding though to develop and confirm a particular noise model. Moreover, in practice we are mostly interested in keeping the fringe amplitude close to one for as long as possible rather than in the exact behavior of the fringe amplitude decay between 0.9 and $1/e$. The numbers stated above as coherence times certainly do not give a good guess for the number of operations possible when comparing them with the gate times for instance. Since we are now entering a regime where all basic building blocks can be performed with errors below 1% it makes sense to quote a relevant coherence time $T^{i}_{t_g}$ which relates to the time it takes to lose 10^{-i} in fringe amplitude and where t_g corresponds to time needed to perform the slowest basic gate operation in this particular system. This number enables an easy comparison between different systems and does not require measurements in a regime which is not of interest nor requires a sophisticated noise model. In our case this relevant coherence time is estimated to be

$$T^{2}_{0.1\,\mathrm{ms}} \approx 100\,\mathrm{ms},$$

if we assume the two-qubit entangling operation described in the next chapter operating on the $^{43}Ca^{+}$ optical qubit and a mapping between the hyperfine qubits and the optical qubits[1]. Therefore, in theory the quantum memory time becomes limiting after about 1000 basic operations only. However, in reality there are a few other hindrances to make use of these long storage times. One major limitation will come from the concatenation of two-qubit operations. Even when using the two-qubit gate producing entangled state with the lowest errors so far (see chapter 7), we acquire an error of 20% of the produced entangled states after 21 repetitions. Moreover, it will be interesting to investigate the scaling of this coherence time with the number of ions involved. On the one hand a significant shortening can be expected for instance when N-ion Greenberger-Horne-Zeilinger-states of the form $(|{\downarrow\downarrow\downarrow}\ \ldots\rangle + |{\uparrow\uparrow\uparrow}\ \ldots\rangle)/\sqrt{N}$ are involved since for these states the susceptibility to relative frequency fluctuations scales with N [138]. On the other hand, with a high fidelity entangling gate quantum information can be stored in a *decoherence-free subspace* given by a pair of entangled ions $(|{\downarrow\uparrow}\rangle + |{\uparrow\downarrow}\rangle)/\sqrt{2}$ as demonstrated in reference [67, 139]. This can help to suppress sensitivity to external magnetic field fluctuations by several orders of magnitude. In summary the quantum information storage times will certainly not limit our system in the near future.

[1] We already have experimental evidence that this is indeed a good assumption!

7 Entangled states with high fidelity

One of the most difficult operations in ion trap based QIP is to perform a universal multi-qubit gate operation. At present only very few of these operations can be applied in series without compromising the error rate of the computation too much. Their quality is the major restriction for scaling ion trap QIP systems up to more complex algorithms. This chapter quickly reviews the different gate operations that have been used for creating entangled states and the progress that has been made here over the last decade. Then a theoretical description of the Mølmer-Sørensen gate applied to optical qubits is given. Furthermore, the experimental realization of such a gate on two $^{40}Ca^{+}$ ions is described which is a major result of this thesis. Finally, possible error sources are discussed and the creation of highly entangled ions in thermal motion is demonstrated for the first time. The main findings of this chapter were also published in reference [73].

7.1 Review of entanglement creation in ion traps

When it comes to scaling ion traps to large systems a set of universal gates is needed that operates with low errors to realize large quantum computations. It has been shown [140] that the combination of arbitrary single-qubit rotations and a single entangling two-qubit gate fulfills this demand. As in classical models of computation, quantum error correction techniques enable rectification of small imperfections in gate operations, thus enabling perfect computation in the presence of noise. For fault-tolerant computation [11], it is believed that error thresholds ranging between 10^{-4} and 10^{-2} [12, 13, 14] will be required - depending on the noise model and the computational overhead for realizing the quantum gates - but so far all experimental implementations have fallen short of these requirements.

In contrast to single-qubit gates, which have been realized now for many years with such low errors, the best two-qubit gate so far had an error as high as $3(\pm 2)\%$ [53]. One reason is that the typical length scale of state-dependant interactions between neighboring ions in ground or low-lying excited states is small compared to the inter-ion distances caused by the repulsive Coulomb force. In the experiments that have created entangled ions [53, 51, 54, 141, 55] the state dependent interaction was mediated by one or more laser light fields and a vibrational degree of freedom of the ion string. These gate operations fall into two categories [142]:

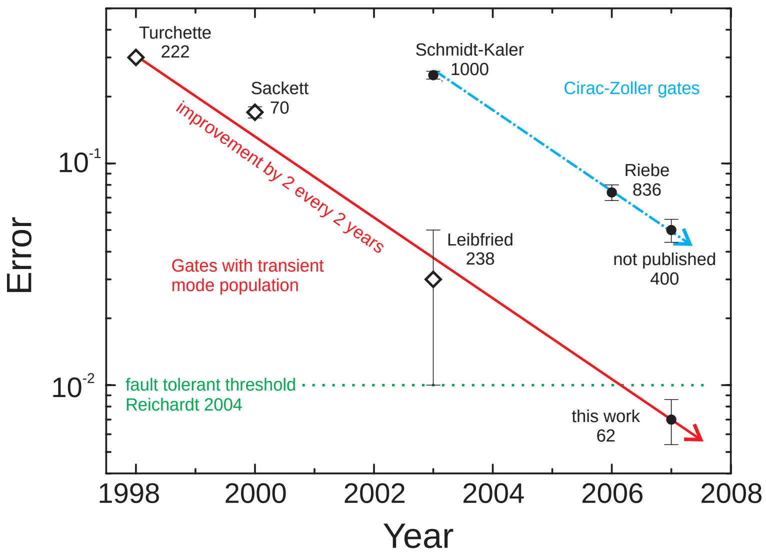

Figure 7.1: The graph shows some of the results of entangling state production in ion traps over the last decade with different multi-qubit gates [143, 49, 53, 51, 70, 144]. The duration of the entangling operations are given as the number of trap oscillations of the mediating mode. In 1998 two ions were entangled for the first time by using a geometric phase gate on hyperfine qubits (◇). The Cirac-Zoller gate has been used so far only on optical qubits (•) where it is comparatively slow. Furthermore, it is experimentally more demanding and hence the obtained fidelities are lower compared to the bichromatic gates. The solid and the dash-dotted arrow indicate for each type of gate operation a reduction of errors of about a factor of two every two years, similar to the trend found by Gordon E. Moore in 1965 for the history of classical computer's hardware [145]. Assuming that the measured Bell state infidelity is a good estimate for our gate infidelity we find our gate to be the first below a threshold required for fault-tolerant quantum computing [14].

1. Quantum gates induced by a laser beam that interacts with a single ion at a time as originally proposed in the seminal paper by I. Cirac and P. Zoller [46] and later realized by the Innsbruck ion trapping group [51]. In these gates, a single ion is entangled with a vibrational mode [47] of the ion string and the entanglement is subsequently transferred from the vibrational mode to the internal state of a second ion. This concept brings the advantage that it can act on any two ions in a string that share a motional mode leaving the other ions unaffected. The downside is that it relies on a pure quantum state in the mediating motional mode which is difficult to achieve with low errors. Also individual ion addressing is needed and so far all implementations were rather slow.

2. Quantum gates induced by a bichromatic laser that collectively interacts with two or more ions. Here, a vibrational mode becomes transiently entangled with the qubits before getting disentangled at the end of the gate operation, resulting in an effective interaction between the qubits capable of entangling them. Gates of this type were first proposed by G. Milburn [146, 147], A. Sørensen, K. Mølmer [148, 79] and E. Solano [149], and subsequently realized by ion trapping groups in Boulder,

Ann Arbor and Oxford [53, 54, 55]. Here the demands concerning the purity of the mediating motional mode are far more relaxed. Furthermore, these schemes can be applied to many ions at the time and can be much faster compared to the Cirac-Zoller-gates. But in order to address a particular set of ions these schemes require techniques of hiding the other ions into unaffected internal states or trap areas.

Even though both classes of gates are applicable to hyperfine qubits as well as optical qubits, current experiments with optical qubits have used the former and experiments with hyperfine qubits have used the latter type of interaction. This is illustrated in Fig. 7.1 which shows the results of entanglement creation in ion traps over the last decade on beryllium and calcium ions. Entanglement was created deterministically for the first time in 1998 by Q. A. Turchette *et al.* [143] with hyperfine qubits in ion traps. For both classes of gates we see a rapid progress towards lower errors with an improvement rate of about a factor of two every two years. Up to now bichromatic gates on hyperfine qubits performed significantly better compared to Cirac-Zoller-gates on optical qubits regarding error and speed. Today, the two major goals are to further improve on the fidelity and to speed up the process. Here, a natural limitation to the gate speed is given by the periodicity of the mediating vibrational degree of freedom. To make a comparison between different implementations easier the gate durations indicated in Fig. 7.1 are given as the number of trap oscillations of the mediating motional mode.

For the sake of completeness, we would like to mention that there exist other ideas for entangling gates of which some have been realized [150, 50]. With strong laser pulses as outlined in reference [151] it might be possible to overcome the speed limit set by the trap periodicity. And two ions can also be entangled without any laser-ion interactions at all but with resonant magnetic fields in the presence of strong static magnetic field gradients [94]. However, the latter two proposals have not been experimentally implemented so far.

7.2 The Mølmer-Sørensen interaction on the optical qubit

A detailed theoretical description of the Mølmer-Sørensen gate operation on optical qubits is given in reference [142]. Here, only the facts relevant for understanding the performed experiments shall be recapitulated briefly.

7.2.1 Laser-ion-interaction

A Mølmer-Sørensen gate inducing collective spin flips is achieved by the use of a bichromatic laser field with frequencies $\nu_\pm = \nu_0 \pm \delta$, with ν_0 the qubit transition frequency and δ close to the vibrational mode frequency ω (see Fig. 7.2 (a)). For optical qubits,

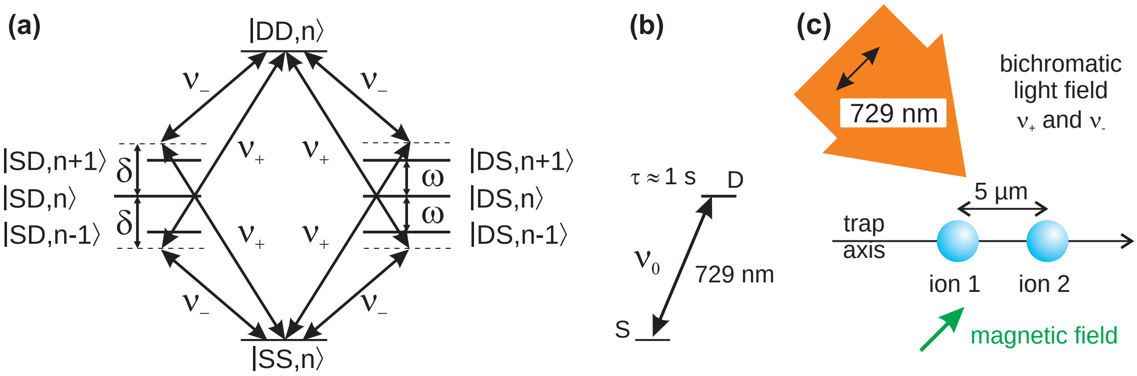

Figure 7.2: **(a)** A bichromatic laser field with frequencies ν_+, ν_- satisfying $2\nu_0 = \nu_+ + \nu_-$ is tuned close to the upper and lower motional sideband of the qubit transition. The field couples the qubit states $|SS\rangle \leftrightarrow |DD\rangle$ via the four interfering paths shown in the figure, n denoting the vibrational quantum number of the axial COM mode. Similar processes couple the states $|SD\rangle \leftrightarrow |DS\rangle$. **(b)** For the experiments described in this chapter, the qubits are encoded in the ground state $S_{1/2}(m = 1/2)$ and the metastable state $D_{5/2}(m = 3/2)$ of $^{40}\mathrm{Ca}^+$ ions and manipulated by a narrow bandwidth laser emitting at a wavelength of 729 nm (see also Fig. 2.2). **(c)** The amplitude modulated laser beam, the trap axis and the magnetic field are all aligned in the same plane with 45° degree angles in between as depicted.

the bichromatic field can be a pair of copropagating lasers which is equivalent to a single laser beam resonant with the qubit transition and amplitude-modulated with frequency δ. For a gate mediated by the axial COM mode, the Hamiltonian describing the laser-qubit interaction is given by

$$H = \hbar\Omega e^{-i\phi} S_+ (e^{-i(\delta t+\zeta)} + e^{i(\delta t+\zeta)}) e^{i\eta(ae^{-i\omega t}+a^\dagger e^{i\omega t})} + \text{h.c.} \tag{7.1}$$

Here, $S_j = \sigma_j^{(1)} + \sigma_j^{(2)}, j \in \{+,-,x,y,z\}$, denotes a collective atomic operator constructed from Pauli spin operators $\sigma_j^{(i)}$ acting on ion i, and $\sigma_+^{(i)}|S\rangle_i = |D\rangle_i$. The operators a, $a^\dagger$ annihilate and create phonons of the COM mode with Lamb-Dicke factor η. The optical phase of the laser field (with coupling strength Ω) is labeled ϕ, and the phase ζ accounts for a time difference between the start of the gate operation and the maximum of the amplitude modulation of the laser beam. In the Lamb-Dicke regime, and for $\phi = 0$, the gate operation is very well described by the propagator [142]

$$U(t) = e^{-iF(t)S_x} \hat{D}(\alpha(t)S_{y,\psi}) \exp(-i(\lambda t + \chi \sin(\omega-\delta)t) S_{y,\psi}^2). \tag{7.2}$$

Here, the operator to the right describes collective spin flips induced by the operator $S_{y,\psi} = S_y \cos\psi + S_z \sin\psi$, $\psi = \frac{4\Omega}{\delta}\cos\zeta$, and $\lambda \approx \eta^2\Omega^2/(\omega-\delta)$, $\chi \approx \eta^2\Omega^2/(\omega-\delta)^2$. With $\alpha(t) = \alpha_0(e^{i(\omega-\delta)t} - 1)$, the displacement operator $\hat{D}(\beta) = e^{\beta a^\dagger - \beta^* a}$ accounting for the transient entanglement between the qubits and the harmonic oscillator becomes equal to the identity after the gate time $\tau_{\text{gate}} = \frac{2\pi}{|\omega-\delta|}$. In order to realize an entangling gate of duration τ_{gate} described by the unitary operator $U_{gate} = \exp(-i\frac{\pi}{8}S_y^2)$ (matrix representation see Eq. (2.7)), the laser intensity needs to be set such that $\eta\Omega \approx |\delta - \omega|/4$.

7.2.2 Amplitude-shaped laser pulses

Our experiments are performed in the limit of short gate operations, where $\Omega \ll \delta$ no longer strictly holds. Here, the Hamiltonian (7.1) becomes sensitive to the phase ζ and the operator $e^{-iF(t)S_x}$ with $F(t) = (2\Omega/\delta)(\sin(\delta t + \phi) - \sin\phi)$ describes fast non-resonant excitations of the carrier transition. Non-resonant excitations are suppressed by intensity-shaping the laser pulse such that the Rabi frequency $\Omega(t)$ is switched on and off smoothly. Moreover, adiabatic switching makes the collective spin flip operator independent of ζ as $S_{y,\psi} \to S_y$ for $\Omega \to 0$. To achieve adiabatic following, it turns out to be sufficient to switch on the laser within 2.5 oscillation periods of the ions' axial COM mode. When the laser is switched on adiabatically, Eq. (7.2) can be simplified by dropping the factor $e^{-iF(t)S_x}$ and replacing $S_{y,\psi}$ by S_y.

7.3 Measurement results

Two $^{40}Ca^+$ ions are loaded into the trap at a magnetic field of 4 G. The qubit is encoded in the levels $|S\rangle \equiv S_{1/2}(m = 1/2)$ and $|D\rangle \equiv D_{5/2}(m = 3/2)$, and the mediating laser (linear polarized) targets the ions orthogonal to the magnetic field (see Fig. 7.2 (b)+(c) and Fig. 2.2 for a detailed level scheme). For these settings we measured a qubit coherence time of 3 ms. The COM mode secular trapping frequencies are set to $\omega_{\mathrm{ax}}/(2\pi) = 1.23$ MHz and $\omega_{\mathrm{r}}/(2\pi) = 4$ MHz. After Doppler-cooling and frequency-resolved optical pumping [129] the two axial modes are cooled close to the motional ground-state ($\bar{\mathrm{n}}_{\mathrm{com}}$, $\bar{\mathrm{n}}_{\mathrm{stretch}} < 0.05(5)$). Both ions are now initialized to $|SS\rangle$ with a probability of higher than 99.8%. Then the subsequent gate operation is carried out, followed by an optional carrier pulse on both ions for analysis. Finally, we measure the probability p_k of finding k ions in the $|S\rangle$-state by detecting light scattered on the $S_{1/2} \leftrightarrow P_{1/2}$ dipole transition with a photo-multiplier for 3 ms. The error in state detection due to spontaneous decay from the D-state is estimated to be less than 0.15%. Each experimental cycle is synchronized with the frequency of the AC power line and repeated 50 to 200 times.

The laser beam performing the entangling operation is controlled by a double-pass AOM which allows setting the frequency ν_L and phase ϕ of the beam (AO4 in Fig. 3.4). By means of a variable-gain amplifier, we control the radiofrequency input power and hence the intensity profile of each laser pulse. To generate a bichromatic light field, the beam is passed through another AOM (AO7 in Fig. 3.4) in single-pass configuration that is driven simultaneously by two radiofrequency signals with difference frequency δ/π. Phase coherence of the laser frequencies is maintained by phase-locking all radiofrequency sources to an ultra-stable quartz oscillator. We use 1.8 mW average light power focused down to a spot size of 14 μm Gaussian beam waist illuminating both ions from an angle of 45° with

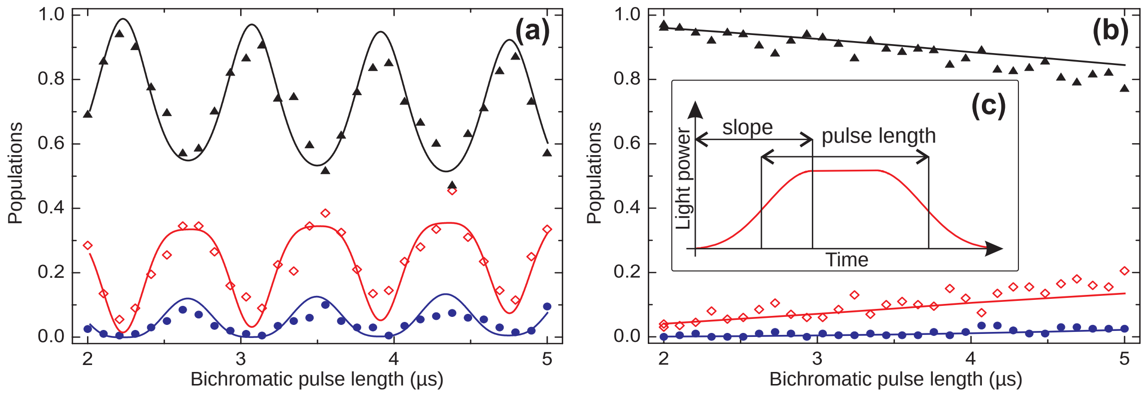

Figure 7.3: Dynamics induced by the bichromatic laser light field at short time scales. The probabilities p_0 ($\bullet$), p_1 ($\diamond$), and p_2 ($\blacktriangle$) for observing 0,1,2 ions in the $|S\rangle$-state are displayed as a function of the duration a bichromatic pulse was applied. For both plots the trap frequency was set to $\omega_{\mathrm{ax}}/(2\pi) = 1.233\,\mathrm{MHz}$ and $(\omega_{\mathrm{ax}} - \delta)/(2\pi) = 40\,\mathrm{kHz}$. Each data point represents the average over 200 individual measurements. The phase ζ was not controlled and is assumed to be random for each measurement. **(a)** In the case of instantly switching the laser on we observe fast dynamical processes on the carrier transition with a periodicity given by $\tau = 2\pi/\delta$. **(b)** Pulse shaping of the laser intensity of $2.5\,\mu\mathrm{s}$ with a Blackman-shape suppresses these oscillations almost completely and so the sensitivity to ζ is also strongly reduced. The solid lines are predictions calculated with the propagator (7.2) averaged over different values of ζ. The inset **(c)** shows the definitions of the pulse and the slope length.

equal intensity to achieve the Rabi frequencies $\Omega/(2\pi) \approx 110\,\mathrm{kHz}$ required for performing a gate operation with $(\omega - \delta)/(2\pi) = 20\,\mathrm{kHz}$ and $\eta = 0.044$.

7.3.1 Amplitude-shaping and the compensation for AC-Stark shifts

Figure 7.3 illustrates the use of amplitude-shaping in order to make the Mølmer-Sørensen gate operation robust against fluctuations in the phase ζ between the blue- and the red-detuned laser beam component. At the time when these experiments were carried out we were not able to control ζ and it took random values for each experiment. To see pronounced non-resonant carrier oscillations, we set the detuning to $(\omega - \delta)/(2\pi) = 40\,\mathrm{kHz}$ corresponding to a gate time of $\tau_{\mathrm{gate}} = 25\,\mu\mathrm{s}$. With an axial COM mode frequency of $\omega_{\mathrm{ax}}/(2\pi) = 1.233\,\mathrm{MHz}$, a complete gate operation is carried out within $N_t = 31$ trap oscillations and a product $N_t\eta = 1.36$ close to 1 indicates a non-resonant coupling to the carrier of the same order as to the sidebands relevant for the gate interaction. The dynamics of the populations p_k is depicted in Fig. 7.3 at short time scales when the bichromatic beam is turned on. Switching the laser pulse on instantly leads to fast dynamical processes on the carrier transition with a periodicity given by $\tau = 2\pi/\delta$. To make the bichromatic laser pulses independent of the phase ζ, the pulse is switched on and off by the use of Blackman-shaped pulse slopes of duration $\tau_r = 2.5\,\mu\mathrm{s}$ (defined in Fig. 7.3 (c)). As illustrated in Fig. 7.3 (b) the laser intensity pulse shaping suppresses non-resonant carrier oscillations almost completely and with them the sensitivity to the phase ζ. For

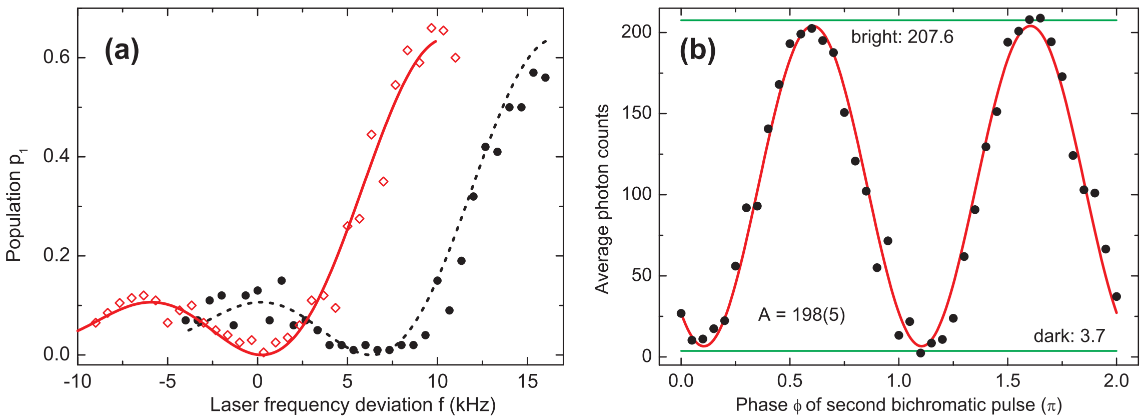

Figure 7.4: **(a)** Measurement of the AC-Stark shift induced by the bichromatic light field by recording the population p_1 as a fuction of the laser detuning f. For equal coupling strengths (●) of the blue and the red beam component $\Omega_+/\Omega_- = 1$ the expected dip of the population p_1 is shifted by about 7 kHz. This shift was compensated (◇) by slightly unbalancing the Rabi frequencies $\Omega_+/\Omega_- = 1.094$. The solid line is a numerical evaluation of the propagator (7.2). The dashed line is equivalent to the solid line shifted by 7 kHz. **(b)** Measurement of the Bell state coherence by applying a second bichromatic pulse where the global laser phase ϕ is scanned. Here, the fringe amplitude can be obtained from the bare average photon counts without setting discrimination thresholds. The average photon counts for the states $|SS\rangle$ (bright) and $|DD\rangle$ (dark) were independently measured and are indicated as horizontal lines as a reference.

the experiments carried out with $(\omega - \delta)/(2\pi) = 20\,\text{kHz}$ a pulse shaping time $\tau_r = 2.0\,\mu\text{s}$ turned out to be sufficient.

The red- and the blue-detuned frequency components $\nu_\pm$ of the bichromatic light field cause AC-Stark shifts by non-resonant excitation on the carrier and the first-order sidebands that exactly cancel each other if the corresponding laser intensities $I_\pm$ are equal. The remaining AC-Stark shift due to other Zeeman transitions and far-detuned dipole transitions were mapped out by measuring the qubit transition frequency first with a Ramsey type experiment. Then a bichromatic pulse was applied where the global frequency was changed for each data point. Figure 7.4 shows the population p_1 after a pulse length of $\tau_{\text{gate}} = 50\,\mu\text{s}$ as a function of the global laser frequency detuning $f \equiv (\nu_L - \nu_0)/(2\pi)$. For equal intensities I_+ and I_- the measured pattern is shifted by about 7 kHz from the qubit frequency from what a numerical evaluation of the propagator (7.2) for gates with $(\omega-\delta)/(2\pi) = 20\,\text{kHz}$ predicts. This shift could be compensated by using an additional far-detuned light field [152] or by properly setting the intensity ratio I_+/I_-. We utilize the latter technique which makes the coupling strengths $\Omega_{SS\leftrightarrow DD} \propto 2\sqrt{I_+I_-}$, $\Omega_{SD\leftrightarrow DS} \propto I_+ + I_-$ slightly unequal. However, the error is insignificant as $\Omega_{SD\leftrightarrow DS}/\Omega_{SS\leftrightarrow DD} - 1 = 4 \times 10^{-3}$ in our experiments.

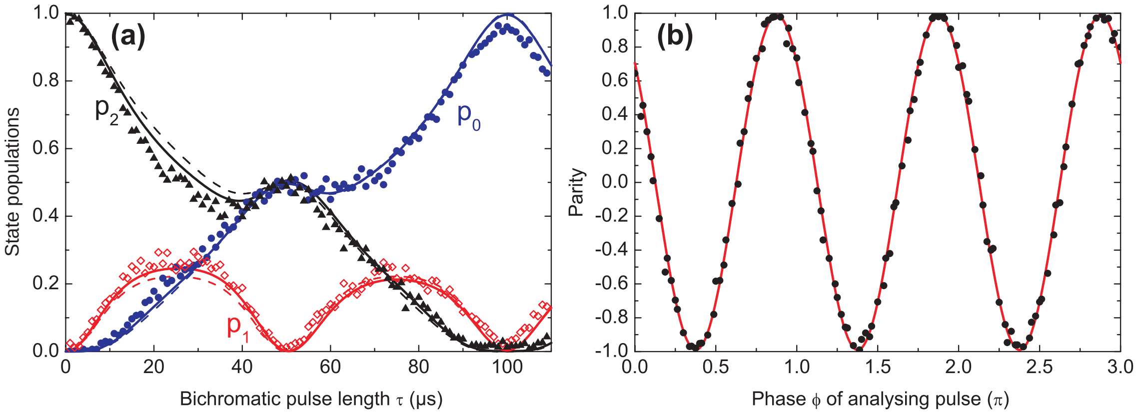

Figure 7.5: **(a)** Evolution of the populations p_0 (•), p_1 (◇), and p_2 (▲) induced by a Mølmer-Sørensen bichromatic pulse of duration τ. The Rabi frequency $\Omega(t)$ is smoothly switched on and off within $2\,\mu$s and adjusted such that a maximally entangled state is created at $\tau_{\text{gate}} = 50\ \mu s$. The dashed lines are calculated for $\bar{\text{n}}_{\text{com}} = 0.05$ from the propagator (7.2), neglecting pulse shaping and non-resonant carrier excitation. The solid lines are obtained from numerically solving the Schrödinger equation for time-dependent $\Omega(t)$ and imbalanced Rabi frequencies $\Omega_+/\Omega_- = 1.094$. **(b)** A $(\frac{\pi}{2})_\phi$ analysis pulse applied to both ions prepared in Ψ_1 gives rise to a parity oscillation $P(\phi) = \sin(2\phi)$ as a function of ϕ. A fit with a function $P_{\text{fit}} = A\sin(2\phi + \phi_0)$ yields the parity fringe amplitude $A = 0.990(1)$ and $\phi_0/\pi = -1.253(1)$. The precise value of the phase ϕ_0 is without significance. It arises from phase-locking the frequencies ν_0, ν_+, ν_- and could have been experimentally adjusted to zero.

7.3.2 Measurement of the fidelity

In order to assess the fidelity of the gate operation, we adopt the strategy first applied in references [49, 53] consisting in measuring the fidelity of Bell states created ($\Psi_1 = |SS\rangle + i|DD\rangle$, see Eq. (7.4)) by a single application of the gate to the state $|SS\rangle$ (see Fig. 7.5 (a)). The fidelity

$$F = \langle\Psi_1|\rho^{\text{exp}}|\Psi_1\rangle = (\rho^{\text{exp}}_{SS,SS} + \rho^{\text{exp}}_{DD,DD})/2 + \text{Im}\rho^{\text{exp}}_{DD,SS}, \tag{7.3}$$

with the density matrix ρ^{exp} describing the experimentally produced qubits' state, is inferred from measurements on a set of 42 400 Bell states continuously produced within a measurement time of 35 minutes. Fluorescence measurements on 13 000 Bell states reveal that $\rho^{\text{exp}}_{SS,SS} + \rho^{\text{exp}}_{DD,DD} = p_2 + p_0 = 0.9965(4)$. The off-diagonal element $\rho^{\text{exp}}_{DD,SS}$ is determined by measuring $P(\phi) = \langle\sigma_\phi^{(1)}\sigma_\phi^{(2)}\rangle$ for different values of ϕ, where $\sigma_\phi = \sigma_x\cos\phi + \sigma_y\sin\phi$, by applying $(\frac{\pi}{2})_\phi$-pulses to the remaining 29 400 states and measuring $p_0 + p_2 - p_1$ to obtain the parity $\langle\sigma_z^{(1)}\sigma_z^{(2)}\rangle$. The resulting parity oscillation $P(\phi)$ shown in Fig. 7.5 (b) is fitted with a function $P_{\text{fit}}(\phi) = A\sin(2\phi + \phi_0)$ that yields $A = 2|\rho^{\text{exp}}_{DD,SS}| = 0.990(1)$. Combining the two measurements, we obtain the fidelity $F = 99.3(1)\%$ for the Bell state Ψ_1.

In a similar set of measurements where the speed of the entangling gate operation was doubled ($(\omega - \delta)/(2\pi) = 40\,\text{kHz}$, $\tau_{\text{gate}} = 25\,\mu\text{s}$), we obtained a fidelity of the produced Bell state of $F = 98.7(8)\%$. Since the non-resonant oscillations are not suppressed completely (see Fig. 7.3 (b) recorded with the same parameters), we expect further improvements here once we are able to control the phase ζ.

Alternatively to the method described above, the coherence of the Bell state can be inferred by applying a second bichromatic pulse of length τ_{gate} to both ions and scanning its relative phase ϕ [60]. This way the Bell state is transferred back into a superposition of $\alpha|SS\rangle + \beta|DD\rangle$ where the corresponding probabilities $|\alpha|^2$ and $|\beta|^2$ are a function of ϕ. Since the average fluorescence count-rate is a direct measure of the probability of finding the ions in the $|S\rangle$-state, the photon counts can be used to infer the amplitude of the oscillation instead of setting thresholds and determining the probabilities p_i first. An example is given in Fig. 7.4 (b) where the number of average photon counts for the states $|SS\rangle$ (bright) and $|DD\rangle$ (dark) were independently measured to serve as a reference.

Instead of varying the phase ϕ of the second pulse, we can also scan the waiting time between the two pulses. This is a sensitive method to detect the frequency detuning f between the laser and the atomic transition frequency [153]. We make use of this scheme in order to determine residual AC-Stark shifts and compensate for them.

7.3.3 Multiple gate operations and errors and sources for gate infidelities

Multiple application of the bichromatic pulse of duration τ_{gate} ideally maps the state $|SS\rangle$ to

$$|SS\rangle \xrightarrow{\tau_{\text{gate}}} \underbrace{|SS\rangle + i|DD\rangle}_{\Psi_1} \xrightarrow{\tau_{\text{gate}}} |DD\rangle \xrightarrow{\tau_{\text{gate}}} |DD\rangle + i|SS\rangle \xrightarrow{\tau_{\text{gate}}} |SS\rangle \xrightarrow{\tau_{\text{gate}}} \ldots \qquad (7.4)$$

up to global phases. Maximally entangled states appear at instances $\tau_m = m \times \tau_{\text{gate}}$ $(m = 1, 3, \ldots)$. A similar mapping of product states onto Bell states and vice versa also occurs when starting from state $|SD\rangle$.

A wealth of further information is obtained by studying the state dynamics under the action of the gate Hamiltonian. Starting from state $|SS\rangle$, Fig. 7.6 depicts the time evolution of the state populations for pulse lengths equivalent to up to 17 gate times. The ions are entangled and disentangled consecutively up to nine times, the populations closely following the predicted unitary evolution of the propagator (7.2) for $\zeta = 0$ shown in Fig. 7.6 as solid lines.

To study sources of gate imperfections we measured the fidelity of Bell states obtained after a pulse length τ_m for up to $m = 21$ gate operations. The sum of the populations $p_0(t)+p_2(t)$ does not return perfectly to one at times τ_m as shown in Fig. 7.7 but decreases by about 0.0022(1) per gate. This linear decrease could be explained by resonant spin flip processes caused by spectral components of the qubit laser that are far outside the laser's

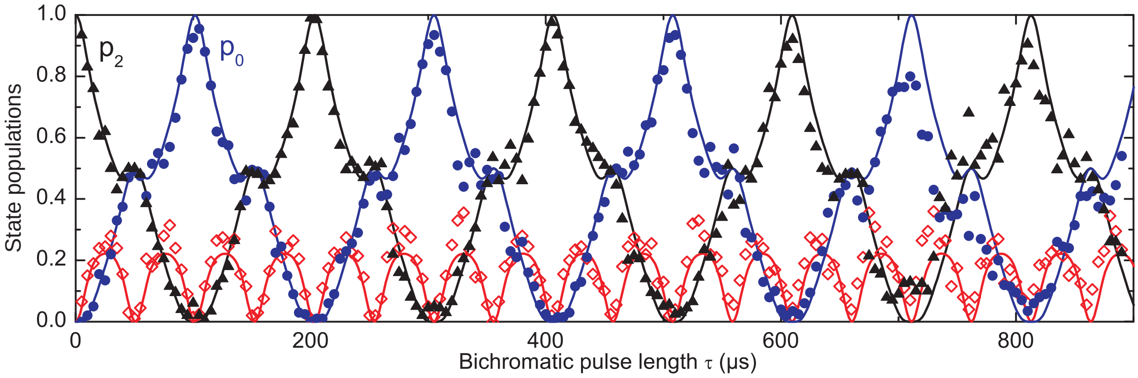

Figure 7.6: Observation of the entanglement and disentanglement dynamics of the Mølmer-Sørensen interaction. Starting from state $|SS\rangle$ for a detuning of the bichromatic laser from the sidebands set to $(\omega - \delta)/(2\pi) = 20\,\text{kHz}$, the figure shows the time evolution of the populations p_0, p_1, and p_2 denoted by the symbols (•), (◇), and (▲), respectively. The length of the pulse is equivalent to the application of up to 17 gate operations. Maximally entangled states are created whenever $p_0(\tau)$ and $p_2(\tau)$ coincide and $p_1(\tau)$ vanishes. The solid lines represent the predicted unitary evolution of the propagator (7.2) for $\zeta = 0$.

line width of about 20 Hz (see Fig. 5.7 (c)). A beat frequency measurement between the gate laser and a similar independent laser system that was spectrally filtered indicates that a fraction γ of about 2×10^{-7} of the total laser power is contained in a 20 kHz bandwidth B around the carrier transition when the laser is tuned close to a motional sideband. A simple model (see Appendix C) predicts spin flips to cause a gate error with probability $p_{\text{flip}} = \gamma\pi^2/\eta^2$. This would correspond to a probability $p_{\text{flip}} = 10^{-3}$ whereas the measured state populations shown in Fig. 7.7 would be consistent with $p_{\text{flip}} = 2 \times 10^{-3}$. Spin flip errors could be further reduced by two orders of magnitude by spectrally filtering the laser light and increasing the trap frequency $\omega/(2\pi)$ to above 2 MHz where noise caused by the laser frequency stabilization is much reduced.

A bichromatic force with time-dependent $\Omega(t)$ acting on ions prepared in an eigenstate of S_y creates coherent states $\alpha(t)$ following trajectories in phase space that generally do not close [154, 142]. For the short rise times used in our experiments, this effect can be made negligibly ($< 10^{-4}$) small by slightly increasing the gate time.

Imperfections due to low frequency noise randomly shifting the laser frequency ν_L with respect to the atomic transition frequency ν_0 were estimated from Ramsey measurements on a single ion showing that an average frequency deviation $\sigma_{(\nu_L - \nu_0)}/(2\pi) = 160\,\text{Hz}$ occurred. From numerical simulations, we infer that for a single gate operation this frequency uncertainty gives rise to a fidelity loss of 0.25% (an infidelity of 10^{-4} would require $\sigma_{(\nu_L - \nu_0)}/(2\pi) = 30\,\text{Hz}$). In our parity oscillation experiments shown in Fig. 7.5 (b) and Fig. 7.7, however, this loss is not directly observable since a small error in the frequency of the bichromatic laser beam carrying out the gate operation is correlated with a similar frequency error of the carrier $(\frac{\pi}{2})_\phi$-pulse probing the entanglement produced by the gate

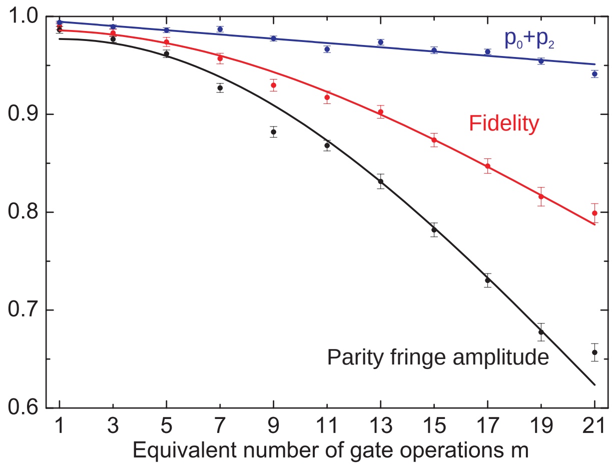

Figure 7.7: Gate imperfections as a function of the bichromatic pulse length $\tau_m = m\,\tau_{\text{gate}}$ given by the equivalent number of gate operations m. The upper curve shows a linear decrease of the state populations $p_0 + p_2$ with a slope of 0.0022(1). All errors given are 1σ statistical errors. The lower curve represents the magnitude of the coherence $2\rho_{DD,SS}$ measured by detecting parity oscillations and fitted by a Gaussian decay function that accounts for low-frequency noise of the laser-ion coupling strength Ω. Combining both measurements yields the Bell state fidelity F_m shown as the middle trace. For $m = 21$, the fidelity is still $F_{21} = 80(1)\%$. Similar results are achieved when replacing the entangling pulse of length τ_m by m amplitude-shaped pulses each of which realizes an entangling gate operation.

so that the phase ϕ of the analyzing pulse with respect to the qubit state remains well defined.

In an experimental approach to measure the frequency sensitivity we determined the fidelity of the produced Bell states as a function of laser frequency deviation f. The result is illustrated in Fig. 7.8. In a second order approximation with a weighted least square fit of the function $g(f) = F_0 + a\,(f - f_{\text{off}})^2$ to the data points we obtained for the free fit parameters: $F_0 = 0.992(2)$, an offset frequency $f_{\text{off}} = 106(94)\,\text{Hz}$ and a slope $a = -7.8(5) \times 10^{-9}\,\text{Hz}^{-2}$. For an average frequency deviation of $\sigma_{(\nu_L - \nu_0)}/(2\pi) = 160\,\text{Hz}$ this leads to an error of 2×10^{-4} of our Bell state fidelity measurement.

Figure 7.7 also shows the amplitude of parity fringe pattern scans at odd integer multiples of τ_{gate} similar to the one in Fig. 7.5 (b). The Gaussian shape of the amplitude decay is consistent with variations in the coupling strength Ω that occur from one experiment to the next. These variations in the coupling strength $\delta\Omega$ induced by low-frequency laser intensity noise and thermally occupied radial modes were inferred from an independent measurement by recording the amplitude decay of carrier oscillations. Assuming a Gaussian decay, we find a relative variation of $\delta\Omega/\Omega = 1.4(1) \times 10^{-2}$. For m entangling gate operations, the loss of fidelity is approximately given by $1 - F = (\frac{\pi m}{2})^2(\delta\Omega/\Omega)^2$ and contributes with 5×10^{-4} to the error of a single gate operation. For the multiple gate operations shown in Fig. 7.7, this source of noise explains the Gaussian decay of the parity fringe amplitude whereas laser frequency noise reduces the fringe amplitude by less than

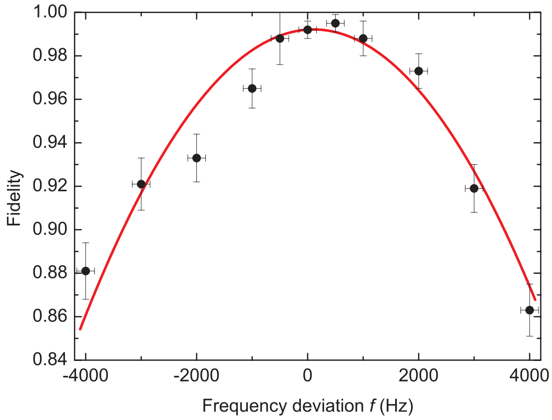

Figure 7.8: The fidelity of the produced Bell states were measured as a function of the laser-qubit frequency deviation f. From a weighted least square fit with a parabola $g(f)$ we obtain for the free fitting parameters a maximum fidelity of $F_0 = 0.992(2)$, an offset frequency $f_{\text{off}} = 106(94)\,\text{Hz}$ and a parabola slope of $a = -7.8(5) \times 10^{-9}\,\text{Hz}^{-2}$.

1% even for 21 gate operations. In combination with error estimates for state preparation, detection and laser noise, the analysis of multiple gates provides us with a good understanding of the most important sources of gate infidelity.

7.3.4 Entangled ions in thermal motion

According to the original proposal by Mølmer and Sørensen the amount of control needed over the ions' motion is largely relaxed. Up to now nobody has observed this in an experiment. On the contrary, most experiments performed ground-state cooling of all axial motional modes as we have done for the results shown earlier in this chapter.

Here, we demonstrate for the first time the application of a Mølmer-Sørensen gate to ions in thermal motion. Experimentally this was done by simply omitting sideband cooling and by the application of the bichromatic pulse directly after Doppler-cooling and optical pumping. At first we mapped out the evolution of the population as illustrated in Fig. 7.9 (a). Since the coupling terms increase with the square root of the mediating mode population (see subsection 2.3.2) we observe a different pattern of the population evolution. For the ions in thermal motion the intermediate states $|SD, n \pm 1\rangle$ and $|DS, n \pm 1\rangle$ get much faster populated and only shortly before the end of the gate time $\tau_{\text{gate}} = 50\,\mu\text{s}$ the population probability p_1 returns to a value close to zero again.

We assume a thermal state, where the mode population probabilities are given by

$$\widetilde{p}_n = \frac{1}{\bar{n}+1}\left(\frac{\bar{n}}{\bar{n}+1}\right)^n .$$

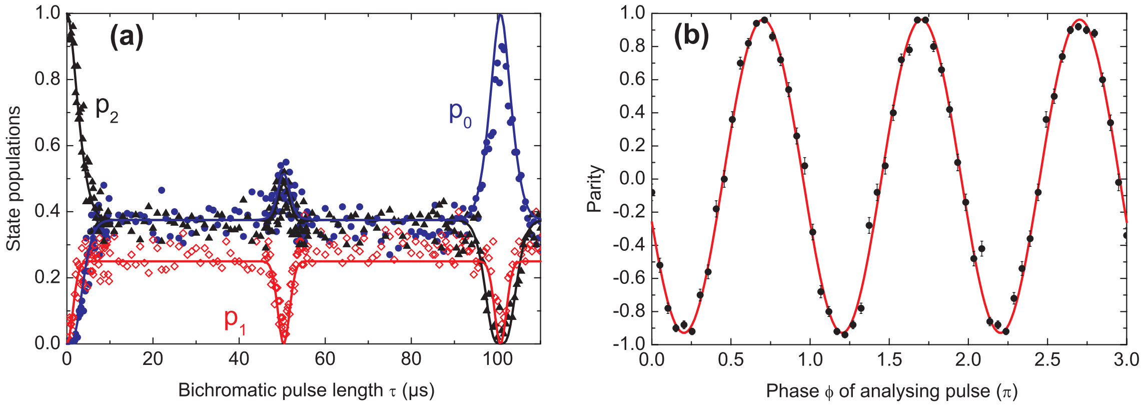

Figure 7.9: Measurement results for the same experimental parameters as for the plot given in Fig. 7.5 but without sideband cooling. **(a)** Evolution of the populations p_0 (●), p_1 (◇), and p_2 (▲) induced by a Mølmer-Sørensen bichromatic pulse of duration τ on two ions in thermal motion. The Rabi frequency $\Omega(t)$ is smoothly switched on and off within $2\,\mu$s and adjusted such that a maximally entangled state is created after $\tau_{\text{gate}} = 50\,\mu$s. The solid lines are least square fits based on the Eq. (7.5) resulting in a mean occupation of the axial COM mode of $\bar{\text{n}}_{\text{com}} = 16.7(1.5)$. **(b)** A $(\frac{\pi}{2})_\phi$ analysis pulse applied to both ions prepared in Ψ_1 gives rise to a parity oscillation $P(\phi) = \sin(2\phi)$ as a function of ϕ. A weighted least square fit with a function $P_{\text{fit}} = A\sin(2\phi + \phi_0)$ yields a parity fringe amplitude of $A = 0.949(4)$.

Disregarding the non-resonant carrier oscillations, one finds the following expressions for the qubit state populations [155]:

$$\begin{aligned}
p_{SS}(t) = p_2(t) &= \frac{1}{8}\left(3 + e^{-16|\alpha|^2(\bar{n}+\frac{1}{2})} + 4\cos(4\gamma)e^{-4|\alpha|^2(\bar{n}+\frac{1}{2})}\right) \\
p_{SD}(t) + p_{DS}(t) = p_1(t) &= \frac{1}{4}\left(1 - e^{-16|\alpha|^2(\bar{n}+\frac{1}{2})}\right) \\
p_{DD}(t) = p_0(t) &= \frac{1}{8}\left(3 + e^{-16|\alpha|^2(\bar{n}+\frac{1}{2})} - 4\cos(4\gamma)e^{-4|\alpha|^2(\bar{n}+\frac{1}{2})}\right)
\end{aligned} \tag{7.5}$$

with $\alpha(t)$ and $\gamma(t) = \lambda t - \chi\sin(\epsilon t)$ containing the time dependent terms.

From a least square fit based on this set of equations we obtained a mean population of the axial mode of $\bar{\text{n}}_{\text{com}} = 16.7(1.5)$. The fit data are given as solid lines in Fig. 7.9 (a). Similar to the analysis above we also measured the fidelity of the created Bell states after a single gate operation. Now, about 2.5% of the population are left in the undesired states $|SD\rangle$ and $|DS\rangle$, leaving a state population $p_0 + p_2$ of 0.975(3). The fringe amplitude was determined from the parity oscillations illustrated in Fig. 7.9 (b) to be $A = 0.949(4)$ resulting in a Bell state fidelity of $F_{\text{hot}} = 96.2(4)\%$.

This result is particularly encouraging for the work towards quantum error correction. Some of the proposed schemes distribute the quantum information of a certain qubit over a set of ancilla qubits that are measured at a certain stage [75]. The measurement outcome is then used to eventually rectify errors on the qubit by the application of conditional multi-qubit gates. However, in ion trap quantum information experiments, state detection typically requires many photon scattering events on a dipole transition that would leave the ions' motion in some thermal state. This makes a subsequent multi-qubit gate operation challenging. One solution to this problem is to introduce a sympathetic cooling step after the state detection. However, this comes at the additional overhead of at least one additional ion (typically a different species) and hence the need of further laser light fields and their control. Our results could help to reduce these technical demands and the control complexity significantly. From the experience with the different types of two-qubit gate operations we have already learned that the technical simplicity of a scheme strongly correlates with the achieved fidelity.

7.3.5 Conclusion

The observed Bell state infidelity of 7×10^{-3} indicates that the gate operation has an error below the threshold required by some models of fault-tolerant quantum computation [12, 13, 14] (an indication to be confirmed by full quantum gate tomography [70] in future experiments). However, further experimental advances will be needed before fault-tolerant computation will become a reality as the overhead implied by these models is considerable. Nevertheless, in addition to making the implementation of quantum algorithms with tens of entangling operations look realistic, the gate presented here also opens interesting perspectives for generating multi-particle entanglement [78] by a single laser interacting with more than two qubits at once. For the generation of N-qubit Greenberger-Horne-Zeilinger-states, there exist no constraints on the positioning of ions in the bichromatic beam that otherwise made generation of these multi-qubit entangled states beyond $N = 6$ so difficult in the experiment with hyperfine qubits described in reference [60]. While the bichromatic force lacks a strong spatial modulation that would enable tailoring of the gate interaction by choosing particular ion spacings [58, 62], more complex multi-qubit interactions could be engineered by interleaving entangling laser pulses addressing all qubits with a focussed laser inducing phase shifts in single qubits. Akin to nuclear magnetic resonance techniques, this method should allow for refocussing of unwanted qubit-qubit interactions [25] and open the door to a wide variety of entangling multi-qubit interactions.

8 Summary and outlook

In this thesis, the construction of an experiment was reported that enabled us to investigate the isotope $^{43}\mathrm{Ca}^+$ as a new qubit candidate. Our scheme makes intensive use of the laser driving the quadrupole transition at 729 nm. Therefore, a precise study of the hyperfine structure splitting in an external magnetic field was required at first. The hyperfine structure of the $D_{5/2}$ level in $^{43}\mathrm{Ca}^+$ was precisely measured by observing frequency intervals of the $S_{1/2}(F=4) \leftrightarrow D_{5/2}(F=2\ldots6, m_F)$ transitions at a non-zero magnetic field. These measurements yielded values for the hyperfine constants $A_{D_{5/2}}$, $B_{D_{5/2}}$ as well as a determination of the isotope shift of the quadrupole transition with respect to $^{40}\mathrm{Ca}^+$. With the apparatus available, the accuracy of both measurements could be further improved by a more detailed investigation of possible error sources. For the purpose of quantum computation though the measurement results obtained are ample.

Different experimental schemes were discussed in order to use the hyperfine clock states of $^{43}\mathrm{Ca}^+$ as quantum information carrier. With a single $^{43}\mathrm{Ca}^+$, we demonstrated sideband cooling close to the motional ground-state by driving a motional sideband of the quadrupole transition. Initialization of the electronic state was achieved by optical pumping and two state transfers on the quadrupole transition. A microwave field and a Raman light field were used to drive qubit transitions on the hyperfine clock states, and the coherence times for both fields were compared. Phase errors due to interferometric instabilities in the Raman field generation were not limiting the experiments on a time scale of 100 ms. We found a quantum information storage time of many seconds for the hyperfine qubit. With the possibility of shelving different hyperfine ground states to the metastable $D_{5/2}$-states we have demonstrated a versatile tool to discriminate between the different Zeeman states in the $S_{1/2}$ and $D_{5/2}$ manifolds. Here, theoretical simulations could help to find the cause for the smaller fluorescence rate of $^{43}\mathrm{Ca}^+$ relative to $^{40}\mathrm{Ca}^+$ ions which could reveal means to improve. Moreover, a time resolved fluorescence detection would allow a significant speed up and a reduction of state discrimination errors [156]. As the setup gets more mature we expect to improve on all experimental steps and target error probabilities for each operation of 10^{-4} in the long run. For this purpose it is desirable to find efficient ways to quantify such small errors quickly in order to be able to adjust experimental techniques and parameters accordingly. Developments in this direction are already underway [157]. In parallel, we need to learn how to deal with strings of multiple $^{43}\mathrm{Ca}^+$ ions and to demonstrate that the schemes proposed in this thesis really work robustly when applied to many ions at the same time. Since the quantum computer is an analog device, we need to have control over the input parameters with sufficient precision. For some of the parameters (e.g. pulse timing) this can be achieved already whereas for other parameters (e.g. laser intensity) this seems challenging even for the future. It is therefore important to develop methods to achieve the basic operations with a much lower sensitivity to certain input parameters. The pulse amplitude-shaping and frequency chirp used in chapter 6 for the state transfer serve as a simple example for such methods.

Finally, we implemented a Mølmer-Sørensen type gate operation entangling ions with a fidelity of 99.3(1)% on the optical qubit encoded in two $^{40}Ca^{+}$ ions. We analyze the performance of a single gate and concatenations of up to 21 gate operations. The result marks the best on-demand entanglement production of all physical realizations today. Assuming that the measured Bell state infidelity is a good estimate for our gate infidelity we find our gate to be the first undercutting one of the harsh thresholds for fault-tolerant quantum computing. Compared to previous implementations it exhibits nearly half an order of magnitude lower errors and it is the fastest in terms of the number of trap oscillations. Meanwhile, the Mølmer-Sørensen interaction has also been applied on the optical qubit of two $^{43}Ca^{+}$ ions and the entanglement was mapped to the hyperfine clock states with a high success rate. In the future we want to apply the operation to multiple ions and generate different Greenberger-Horne-Zeilinger states to investigate the scaling of the fidelity with the number of ions.

Once we are able to use the Mølmer-Sørensen interaction with multiple ions, we need to address the question how a more complex algorithm can be implemented. It turns out that two laser beams, one addressing all ions simultaneously and the other one addressing individual ions, are sufficient to perform arbitrary operations on multiple qubits (see Fig. 8.1 (a)). It is important to note that phase stability between both laser fields is not required. The concept is very similar to NMR quantum computing where spin-spin interactions happen all the time and unwanted interactions need to be canceled out by complicated pulse sequences. A major difference though is that in our case the global interaction is only switched on when needed whereas in NMR quantum computing a considerable effort is spent on the cancelation of unwanted interactions. These ideas were investigated in Volckmar Nebendahl's Diplomarbeit [158]. One of his results is a scheme depicted in Fig. 8.1 (b) consisting of 11 laser pulses which implements a quantum Toffoli gate with three ions. Assuming single qubit rotations with Rabi frequencies of a few MHz and an entangling operation time of $50\,\mu$s the whole scheme would take no more than $150\,\mu$s. The Toffoli gate is particularly interesting since it is a major building block of some quantum error correction schemes.

So far, most ideas of future developments in ion trap QIP assume hyperfine qubits that are manipulated by laser fields containing multiple frequencies detuned from an optical dipole

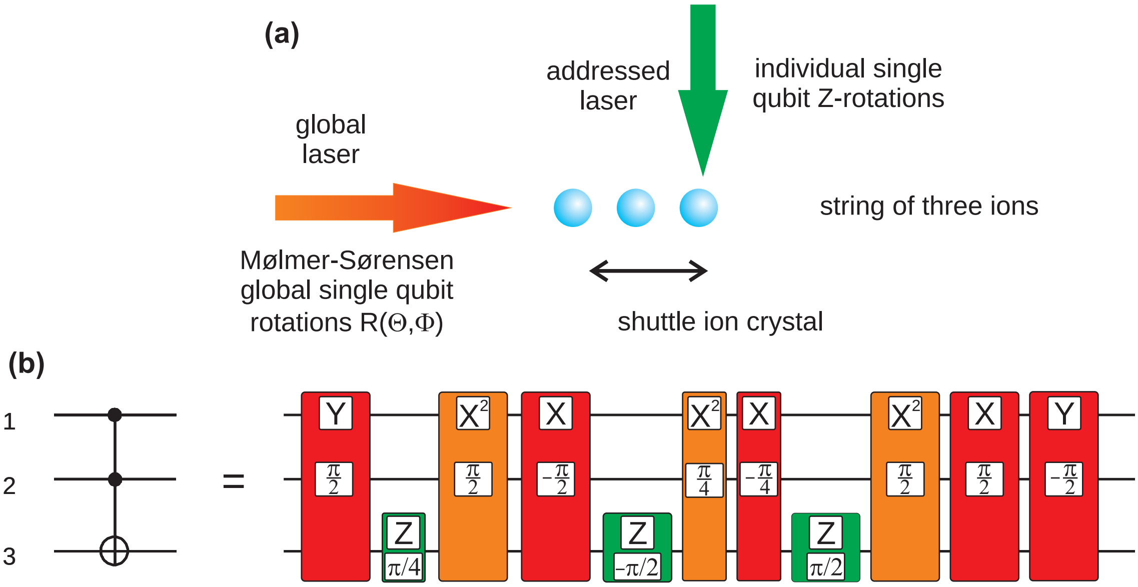

Figure 8.1: **(a)** Three ions aligned in a string can be subject to interactions with two different laser beams. One is used on all ions simultaneously inducing single-qubit rotations and Mølmer-Sørensen interactions. The other beamline serves to make the ions distinguishable by applying slightly detuned laser pulses to effectively achieve rotations around the z-axis in the Bloch sphere picture. Phase stability between both beams is not required. **(b)** With a series of the indicated 11 laser pulses, a quantum Toffoli gate can be implemented. For typical experimental parameters this would take about 150 μs.

transition. These schemes are currently limited by spontaneous scattering due to a lack of laser power allowing for larger detunings. Moreover, the most successful entangling gate schemes are not applicable to the qubits that are magnetic field insensitive. Our results give rise to think towards a new direction where the external field for single qubit rotation could consist of a bichromatic Raman laser field slightly detuned from a quadrupole transition. Reasonably high Rabi frequencies for the laser powers available at the place of the ion today can be expected. One proposal for the realization of a universal gate in this scheme is to directly apply multiple frequencies of light at 729 nm to the hyperfine clock states as suggested in reference [137]. Alternatively, we can map the hyperfine qubit of the target ions to the optical qubit (this could also be a field insensitive transition) and use the Mølmer-Sørensen interaction as universal multi-qubit entangling gate operation. After this global laser pulse the ions are mapped back to the hyperfine structure where the quantum information is stored for a long time.

A Calcium physical and optical properties and hyperfine measurement data

speed of light	c	2.99792458 × 108 m/s (exact)
permeability of vacuum	μ_0	$4\pi \times 10^7 N/A^2$ (exact)
permittivity of vacuum	ϵ_0	$1/(\mu_0 c^2)$ (exact) $= 8.854\,187\,817\,...10^{-12}\,\mathrm{F/m}$
Planck's constant	$h = 2\pi\hbar$	$6.626\,0693(11)\times\,10^{-34}\,\mathrm{J\,s}$
elementary charge	e	$1.602\,176\,53(14) \times 10^{-19}$ C
Bohr magneton	μ_B	$927.400\,949(80) \times 10^{-24}$ J/T
atomic mass unit	u	$1.660\,538\,86(28) \times 10^{-27}$ kg
electron mass	m_e	$5.485\,799\,094\,5(24) \times 10^{-4}$ u
fine structure constant	α	$7.297\,352\,568(24) \times 10^{-3}$
Bohr radius	a_0	$0.529\,177\,2108(18) \times 10^{-10}$ m
Boltzmann constant	k_B	$1.380\,650\,5(24) \times 10^{-23}$ J/K

Table A.1: Fundamental physical constants relevant to the experiment (2002 CODATA recommended values [159]).

isotope	decay mode	half life time	nuclear spin, I
^{41}Ca	electron capture	103, 000 a	7/2
^{43}Ca	stable	-	7/2
^{45}Ca	β^- emitter	162.7 d	7/2
^{47}Ca	β^- emitter	4.536 d	7/2
^{49}Ca	β^- emitter	8.72 min	3/2
^{51}Ca	β^- emitter	10 s	3/2

Table A.2: Calcium isotopes with non-zero nuclear spin and half-lives greater than 1 s [160].

atomic weight	40.078
atomic number	20
melting point	839 °C
boiling point	1484 °C
specific gravity	1.55 g/cm^3 at 20 °C
specific heat	0.63 J/g K
thermal conductivity	2.00 W/cm K

Table A.3: Calcium physical properties.

transition	λ_{air} (nm)	IS (MHz)	reference
$S_{1/2} \leftrightarrow P_{3/2}$	393.366	713(31)	[124]
$S_{1/2} \leftrightarrow P_{1/2}$	396.847	706(42)	[124]
$S_{1/2} \leftrightarrow D_{5/2}$	729.147	4134.711 720(390)	section 5.2
$S_{1/2} \leftrightarrow D_{3/2}$	732.389	4145(43)	[124]
$P_{3/2} \leftrightarrow D_{3/2}$	849.802	−3462.4(2.6)	[85]
$P_{3/2} \leftrightarrow D_{5/2}$	854.209	−3465.4(3.7)	[85]
$P_{1/2} \leftrightarrow D_{3/2}$	866.214	−3464.3(3.0)	[85]

Table A.4: $^{40}Ca^+$ wavelengths in air (λ_{air}) (taken from the NIST database [161]) and the corresponding isotope shifts (IS) between $^{40}Ca^+$ and $^{43}Ca^+$.

isotope	quantity	value	reference
$^{40}Ca^+$	$4S_{1/2} \leftrightarrow 3D_{5/2}$ transition frequency	411 042 129 776 393.2(1.0) Hz	[128]
$^{40}Ca^+$	P-state fine structure splitting	6682.22 GHz	wavelengths
$^{40}Ca^+$	D-state fine structure splitting	1 819.599 021 504(37) GHz	[162]
$^{40}Ca^+$	life time ($3D_{3/2}$)	1.20(1) s	[81]
$^{40}Ca^+$	life time ($3D_{5/2}$)	1.168(7) s	[81]
$^{40}Ca^+$	life time ($4P_{1/2}$)	7.098(20) ns	[82]
$^{40}Ca^+$	life time ($4P_{3/2}$)	6.924(19) ns	[82]
$^{40}Ca^+$	$g_J(4S_{1/2})$	2.002 256 64(9)	[86]
$^{40}Ca^+$	$g_J(3D_{5/2})$	1.200 334 0(3)	[128]
$^{40}Ca^+$	quadrupole moment $Q(3D_{5/2})$	$1.83(1)ea_0^2$	[129]
$^{43}Ca^+$	hyperfine constant $A(4S_{1/2})$	−806.402 071 60(8) MHz	[84]
$^{43}Ca^+$	hyperfine constant $A(4P_{1/2})$	−145.4(0.1) MHz	[85]
$^{43}Ca^+$	hyperfine constant $A(4P_{3/2})$	−31.0(0.2) MHz	[85]
$^{43}Ca^+$	hyperfine constant $B(4P_{3/2})$	−6.9(1.7) MHz	[85]
$^{43}Ca^+$	hyperfine constant $A(3D_{3/2})$	−47.3(0.2) MHz	[85]
$^{43}Ca^+$	hyperfine constant $B(3D_{3/2})$	−3.7(1.9) MHz	[85]
$^{43}Ca^+$	hyperfine constant $A(3D_{5/2})$	−3.893 12(3)) MHz	section 5.1
$^{43}Ca^+$	hyperfine constant $B(3D_{5/2})$	−4.239(1) MHz	section 5.1
$^{43}Ca^+$	nuclear quadrupole moment Q	−40.8(8) mb	[163]
$^{43}Ca^+$	nuclear g-factor g_I	$2.050\,32(1) \times 10^{-4}$	[87]

Table A.5: Calcium atomic properties.

$3^2D_{5/2}$

F´	Δm	m´ = -6	-5	-4	-3	-2	-1	0	1	2	3	4	5	6
F´= 2	Δm = -2					0.03	0.06	0.11	0.17	0.24				
	Δm = -1					0.06	0.11	0.15	0.18	0.17				
	Δm = 0					0.11	0.15	0.17	0.15	0.11				
	Δm = 1					0.17	0.18	0.15	0.11	0.06				
	Δm = 2					0.24	0.17	0.11	0.06	0.03				
F´= 3	Δm = -2				0.09	0.17	0.24	0.29	0.31	0.28				
	Δm = -1				0.19	0.26	0.26	0.20	0.08	0.10	0.34			
	Δm = 0				0.30	0.26	0.14	0.00	0.14	0.26	0.30			
	Δm = 1				0.34	0.10	0.08	0.20	0.26	0.26	0.19			
	Δm = 2					0.28	0.31	0.29	0.24	0.17	0.09			
F´= 4	Δm = -2			0.22	0.33	0.40	0.42	0.40	0.33	0.22				
	Δm = -1			0.41	0.39	0.27	0.09	0.09	0.27	0.39	0.41			
	Δm = 0			0.48	0.12	0.14	0.29	0.34	0.29	0.14	0.12	0.48		
	Δm = 1				0.41	0.39	0.27	0.09	0.09	0.27	0.39	0.41		
	Δm = 2					0.22	0.33	0.40	0.42	0.40	0.33	0.22		
F´= 5	Δm = -2		0.48	0.57	0.57	0.52	0.44	0.34	0.23	0.12				
	Δm = -1		0.68	0.31	0.00	0.23	0.39	0.48	0.50	0.44	0.31			
	Δm = 0			0.53	0.53	0.40	0.22	0.00	0.22	0.40	0.53	0.53		
	Δm = 1				0.31	0.44	0.50	0.48	0.39	0.23	0.00	0.31	0.68	
	Δm = 2					0.12	0.23	0.34	0.44	0.52	0.57	0.57	0.48	
F´= 6	Δm = -2	1.00	0.82	0.65	0.50	0.38	0.27	0.17	0.10	0.04				
	Δm = -1		0.58	0.70	0.71	0.67	0.59	0.49	0.38	0.25	0.13			
	Δm = 0			0.30	0.47	0.58	0.65	0.67	0.65	0.58	0.47	0.30		
	Δm = 1				0.13	0.25	0.38	0.49	0.59	0.67	0.71	0.70	0.58	
	Δm = 2					0.04	0.10	0.17	0.27	0.38	0.50	0.65	0.82	1.00

Figure A.1: Coupling strength $\tilde{g}$ (see Eq. (2.19)) for the $^{43}Ca^+$ quadrupole transitions $S_{1/2}(F=4, m) \leftrightarrow D_{5/2}(F', m')$ with $\Delta m = m' - m$ neglecting the geometry and polarization dependence by omitting the factor $c_{ij}^{(q)} \varepsilon_i n_j$.

F	m	F'	m'_F	sensitivity (MHz/G)	correction (Hz)	measured (MHz)	model (MHz)	delta (Hz)
4	0	2	2	1.9851	169	37.682177	37.682425	247.5
4	0	2	1	-0.6073	-50	32.245023	32.245066	42.7
4	0	2	0	0.3668	15	34.456625	34.456012	-613.7
4	-4	2	-2	2.9556	-44	38.116136	38.116636	500.8
4	-3	2	-1	2.0780	15	36.372196	36.372168	-27.4
4	0	3	2	0.3185	40	25.991071	25.990850	-221.1
4	0	3	1	-1.3596	-98	23.276546	23.276575	28.9
4	0	3	-1	-0.7849	-29	22.493793	22.493612	-181.0
4	2	3	0	-1.7937	470	22.636769	22.636754	-15.2
4	4	3	3	0.7253	-362	29.474775	29.474820	45.6
4	-4	3	-3	1.1409	74	22.752164	22.752472	308.9
4	-4	3	-2	0.8923	22	22.566618	22.566615	-2.4
4	0	4	2	0.3333	110	12.228975	12.228201	-774.7
4	0	4	1	-0.5001	-138	10.153826	10.153631	-195.3
4	0	4	0	-1.0184	-213	8.460164	8.460244	80.1
4	0	4	-1	-1.3374	-273	7.067254	7.067394	139.6
4	0	4	-2	-1.5418	-305	5.898093	5.898417	323.8
4	4	4	4	1.2625	-643	17.411124	17.410458	-665.5
4	4	4	3	0.0130	-8	14.666808	14.666456	-352.0
4	-4	4	-4	-0.3780	-21	4.022361	4.023172	811.7
4	-4	4	-3	-0.2807	-23	4.896428	4.896924	496.0
4	0	5	2	0.6649	230	-6.602169	-6.602450	-281.0
4	0	5	1	-0.0784	-21	-8.717575	-8.717884	-309.6
4	0	5	-2	-1.8305	-544	-14.366945	-14.368385	-1440.1
4	2	5	0	-1.4390	479	-10.712478	-10.712596	-117.8
4	4	5	5	1.9874	-948	0.478488	0.478325	-162.4
4	4	5	4	1.0008	-436	-2.001504	-2.001663	-158.7
4	4	5	3	0.0886	-32	-4.362923	-4.363359	-436.1
4	-4	5	-5	-1.6657	-260	-19.154682	-19.156556	-1874.0
4	-4	5	-4	-1.2965	-237	-17.639476	-17.640944	-1467.8
4	-4	5	-3	-0.8880	-73	-16.046653	-16.047827	-1173.3
4	-3	5	-1	-0.2679	-6	-12.599459	-12.593171	6288.9
4	0	6	2	0.9190	312	-31.593282	-31.593820	-537.8
4	0	6	1	0.1774	48	-33.790214	-33.790629	-414.9
4	0	6	0	-0.5327	-118	-35.940081	-35.940603	-522.2
4	0	6	-2	-1.8622	-575	-40.104837	-40.103771	1065.8
4	4	6	6	2.7988	-579	-22.329680	-22.330245	-565.1
4	4	6	5	1.9300	-625	-24.716975	-24.717668	-692.9
4	4	6	4	1.0924	-352	-27.056890	-27.057522	-631.5
4	4	6	3	0.2866	-116	-29.348315	-29.349560	-1244.4
4	-4	6	-6	-2.7988	-599	-47.919541	-47.918950	591.7
4	-4	6	-5	-2.2516	-356	-46.026198	-46.025413	785.2
4	-4	6	-4	-1.6811	-240	-44.093296	-44.092722	574.4
4	-4	6	-3	-1.0857	-127	-42.119985	-42.119338	647.0
4	-3	6	-1	-0.1626	-3	-38.037507	-38.044619	-7111.3

Table A.6: In order to determine the hyperfine constants of the $^{43}Ca^{+}$ $D_{5/2}$-state we probed all 45 available levels (F',m'_F) from the $S_{1/2}(F=4, m_F)$ manifold (corresponding quantum numbers are given in columns 1-4). The fifth column contains the magnetic field sensitivity of the probed transitions. With the knowledge of the magnetic field for each transition measurement we applied small corrections (column 6) to our measurement such that all results (column 7) are consistent with a magnetic field of 3.045 524 G. The expected values and the difference between these and the measurement are given in the right most columns.

B Method of separated oscillatory fields

In order to probe an atomic transition frequency with a laser there exist a variety of different methods. One option is to use a single laser pulse of fixed duration and power, and sweep the frequency to record an excitation spectrum. It has been shown though that in many applications it is favorable to split the single pulse into two with a waiting time in between. It was Norman F. Ramsey who invented this method of spatially separated oscillatory fields in 1949 [164] for which he received the Nobel prize in physics only 40 years later. Since its invention the method was applied in many precision experiments and has been further developed. In the experiments described in this thesis we use a variation of the method termed time-separated oscillatory fields for instance to reference the laser at a wavelength of 729 nm to calcium ions, and to measure the hyperfine structure of $^{43}Ca^+$ and the isotope shift, and to investigate the phase coherence of our qubits.

B.1 Errors in frequency determination

As an example we consider two levels as sketched in Fig. B.1 (a). With a laser pulse of frequency ν_L and a duration of $\tau_\pi/2$ we create a superposition of the two atomic levels labeled S and D. In case the laser is detuned from the atomic transition by $\delta = \nu_L - \nu_0$, the relative phase of the superposition state changes by $\phi_0 = \delta\,\tau_\mathrm{R}$ during a Ramsey waiting time τ_R. The phase ϕ_0 is then probed by a second pulse of equal length but variable phase ϕ (Fig. B.1 (b)).

This model is correct in the limit where $\tau_\mathrm{R} \gg \tau_\pi$. In case the two laser pulses have a finite length we see that also during these pulses a small phase is acquired. Omitting $\hbar$ the Hamiltonian describing the laser ion interaction on the Bloch sphere is given by

$$H = \frac{1}{2}\left(\delta\sigma_z + \tilde{\Omega}\sigma_x\right)$$

with a coupling strength[1] $\tilde{\Omega}$ and the Pauli operators σ_x and σ_z (see section 2.1). This interaction leads to a time evolution that can be described by the general rotation

$$\tilde{R}(\theta) = \exp(iH\tau) = \exp(i\frac{\theta}{2}(n_x\sigma_x + n_z\sigma_z)) = \cos\frac{\theta}{2} + i\sin\frac{\theta}{2}(n_x\sigma_x + n_z\sigma_z)$$

[1]Here it is convenient to use the Rabi frequency defined such that $\tilde{\Omega} = \pi/\tau_\pi$.

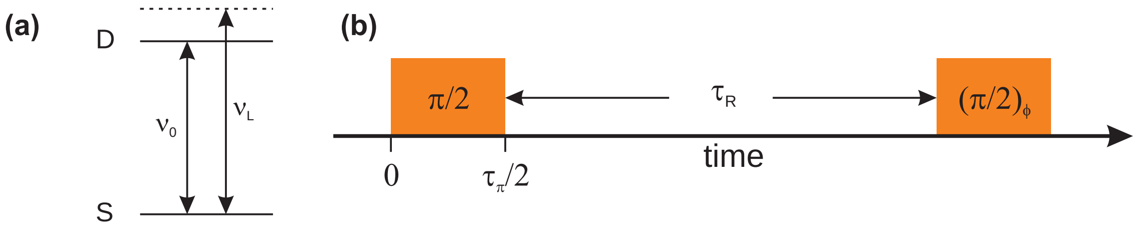

Figure B.1: **(a)** An atomic system comprised of the levels S and D with an energy splitting of $\hbar\nu_0$ is probed with a laser (frequency ν_L) **(b)** Pulse sequence of a Ramsey type experiment using time-separated oscillatory fields.

where we set the pulse length to $\tau = \theta_0/\tilde{\Omega}$ and used the the replacements

$$\theta = \theta_0 \frac{\sqrt{\tilde{\Omega}^2 + \delta^2}}{\tilde{\Omega}}, \quad n_x = \frac{\tilde{\Omega}}{\sqrt{\tilde{\Omega}^2 + \delta^2}}, \quad n_z = \frac{\delta}{\sqrt{\tilde{\Omega}^2 + \delta^2}}.$$

If we split the overall rotation in three different parts

$$\tilde{R}(\theta) \equiv R_z(\alpha) R_x(\beta) R_z(\alpha),$$

where

$$\begin{aligned} R_z(\alpha) &= \cos\left(\frac{\alpha}{2}\right) + i \sin\left(\frac{\alpha}{2}\right) \sigma_z \\ R_x(\beta) &= \cos\left(\frac{\beta}{2}\right) + i \sin\left(\frac{\beta}{2}\right) \sigma_x, \end{aligned}$$

we can show that

$$\begin{aligned} \alpha &= \arg\tan\left(n_z \tan\left(\frac{\theta}{2}\right)\right) \\ \beta &= 2 \arg\tan\left(n_x \tan\left(\frac{\theta}{2}\right)\right). \end{aligned}$$

For $\delta \ll \tilde{\Omega}$ and $\theta_0 = \pi/2$ we find $n_z = \delta/\tilde{\Omega}$, $n_z = 1$ and $\theta \approx \theta_0$, so that we obtain as a good approximation

$$\alpha \approx n_z \tan\frac{\theta}{2} \approx \frac{\delta}{\tilde{\Omega}}.$$

With that the acquired phase is given by

$$\phi' = \phi_0 + 2\alpha = \delta\left(\tau_{\mathrm{R}} + \tau_\pi \frac{2}{\pi}\right),$$

where the last term in brackets can be considered as the effective Ramsey time.

Driving the two $\pi/2$-pulses in the Ramsey scheme can also lead to AC-Stark shifts of the levels probed by coupling of the laser to other levels in the system. These shifts δ_{ac} cause an additional phase shift

$$\phi_{ac} = \delta_{ac}\,\tau_\pi\,\frac{2}{\pi} = 2\,\frac{\delta_{ac}}{\tilde{\Omega}}.$$

The total acquired phase adds then to

$$\phi_{\mathrm{tot}} = \delta\left(\tau_{\mathrm{R}} + \tau_\pi\,\frac{2}{\pi}\right) + \phi_{ac}.$$

If not considered, these AC-Stark shifts δ_{ac} lead to an error in the estimation of the transition frequency

$$\Delta\nu = \frac{\phi_{ac}}{\left(\tau_{\mathrm{R}} + \tau_\pi\,\frac{4}{\pi}\right)}.$$

Considering the $S_{1/2} \leftrightarrow D_{5/2}$ quadrupole transition of calcium ions the major contributions arise from the dipole transitions and transitions on other Zeeman levels. For the experiment located at the university these shifts were precisely determined [152]. For our experiment we expect to have the same contribution for the coupling to far detuned dipole transitions which is given by

$$\delta^d_{ac} = b\,\frac{\tilde{\Omega}^2}{2}$$

with a constant $b = 0.112(5)/(2\pi)(\mathrm{MHz})^{-1}$. For typical values of excitation times this leads to shift of a couple of Hz. The contributions of the neighboring Zeeman transitions strongly depend on the frequency differences between the levels and hence the magnetic field and also on the laser geometry and polarization. These effects have not yet been investigated in this experiment and are certainly a major contribution to the error budget of the measurements described in chapter 5.

B.2 Ramsey contrast and phase coherence

Apart from the precise determination of a transitions frequency we make use of Ramsey experiments to explore the phase coherence between an external field (e.g. microwave or a laser) and an atomic two-level system. A perfect operation of the $\pi/2$-pulses in the Ramsey sequence is assumed, which is the case when the relative frequency deviations are small in comparison with the inverse of the duration of these pulses. Averaging over many experiments where we measure the probability P_D denotes the qubit being in the D-state, we expect a fringe pattern described by

$$P_D = \frac{1}{2}\left(A\,\cos(\phi + \phi_0) + 1\right)$$

with an amplitude A and an offset phase ϕ_0. Perfect phase coherence corresponds to $A = 1$. In a simple noise model we assume that every single experiment is carried out at a fixed frequency detuning $\delta = \nu_L - \nu_0$ of driving field and atomic resonance. Therefore, in a single Ramsey experiment we will accumulate an extra phase $\delta\,\tau_{\mathrm{R}}$ during the waiting time τ_{R}. For simplicity we further assume that the detuning δ is a fluctuating parameter with a Gaussian distribution

$$P(\delta) = \frac{1}{\sigma\sqrt{2\pi}} \exp\left[-\frac{\delta^2}{2\sigma^2}\right].$$

where the FWHM $\Delta\nu_{\mathrm{FWHM}}$ of the frequency fluctuations is linked to the standard deviation σ by

$$\sigma = \frac{\Delta\nu_{\mathrm{FWHM}}}{2\sqrt{2\ln 2}}.$$

The fringe pattern observed in an experiment will be given by the average over an ensemble of single experiments with fluctuating δ. Thus A is obtained by calculating the average over the phase factors:

$$A(\tau_{\mathrm{R}}) = |\langle \exp(i\delta\tau_{\mathrm{R}})\rangle| = \left|\int_{-\infty}^{+\infty} d\delta\ P(\delta)\ \cos(\delta\tau_{\mathrm{R}})\right| = \exp\left[-\frac{\sigma^2\tau_{\mathrm{R}}^2}{2}\right].$$

In case we measure the fringe amplitude A^* for a certain Ramsey time τ_{R}^*, we obtain an effective transition line width

$$\Delta\nu_{\mathrm{FWHM}} = \frac{4}{\tau_{\mathrm{R}}^*}\sqrt{-\ln A^*\ \ln 2}.$$

In general the coherence time T_2 is defined as Ramsey waiting time where the fringe amplitude has decreased to $1/e$. This noise model predicts for a particular measurement

$$T_2 = \frac{4\sqrt{\ln 2}}{\Delta\nu_{\mathrm{FWHM}}^*} = \frac{\tau_{\mathrm{R}}^*}{\sqrt{-\ln A^*}}.$$

In case an exponential decay is expected for the fringe amplitude we calculate for the same data a coherence time of

$$T_2 = \frac{\tau_{\mathrm{R}}^*}{-\ln A^*}.$$

C Spin flip errors during the Mølmer-Sørensen interaction

The implementation of a Mølmer-Sørensen gate operation described in chapter 7 is carried out with a laser of high spectral purity. Nevertheless will residual spectral components separated by $\pm\delta$ from the laser frequency ν_L lead to an excitation on the carrier transition. The following calculations estimate the contribution of this effect to the infidelity of the produced Bell states.

As an example we consider two levels as sketched in Fig. B.1 (a). The Schrödinger equation for the problem reads then

$$\begin{aligned} i\,\dot{c}_D &= \Omega^* f(t) e^{-i\nu_0\,t} c_S \\ i\,\dot{c}_S &= \Omega f(t) e^{i\nu_0\,t} c_D, \end{aligned}$$

with state amplitudes c_S, c_D, coupling strength Ω and a function $f(t)$ describing the time evolution of the laser-ion coupling. The solution to this problem is given by the integration

$$\begin{aligned} c_D &= -i\Omega \int_0^t dt'\, f(t') e^{-i\nu_0\,t'} c_S \\ &\simeq -i\Omega \int_0^t dt'\, f(t') e^{-i\nu_0\,t'}, \end{aligned} \tag{C.1}$$

where the approximation holds for short times t with $c_S \simeq 1$.

The electric field of the laser is now considered in a bandwidth B as a decomposition of discrete frequency components given by

$$f(t) = \frac{1}{\sqrt{N}} \sum_{k=1}^{N} \cos(\tilde{\nu}_k\,t + \varphi_k) \tag{C.2}$$

with a random phase φ_k and $\tilde{\nu}_k = \nu_0 + \nu_k$, where $\nu_k = -\frac{B}{2} + B\frac{k}{N}$. Plugging Eq. (C.2) into Eq. (C.1) and evaluating the integral we obtain

$$c_D = \frac{\Omega}{2\sqrt{N}} \sum_{k=1}^{N} \frac{e^{-i\nu_k\,t} - 1}{\nu_k}\, e^{-i\varphi_k}$$

such that the excitation of the upper state p_D evolves as

$$p_D(t) = |c_D(t)|^2 = \frac{\Omega^2}{4N} \sum_{k=1}^{N} \frac{\left|e^{-i\nu_k\, t/2} - e^{i\nu_k\, t/2}\right|}{\nu_k^2} = \frac{\Omega^2}{4N} \sum_{k=1}^{N} \frac{\sin^2(\nu_k\, t/2)}{\nu_k^2}. \tag{C.3}$$

For a continuous spectrum ($N \to \infty$) the sum in Eq. (C.3) turns into an integral as

$$\begin{aligned} p_D(t) &= \frac{\Omega^2 t}{B} \int_{-B/2}^{B/2} d\nu \frac{\sin^2(\nu\, t/2)}{\nu^2} \\ &= \frac{\Omega^2 t}{2B} \int_{-Bt/4}^{Bt/4} dx \frac{\sin^2 x}{x^2} \\ &\simeq \frac{\pi}{2} \frac{\Omega^2\, t}{B}, \end{aligned} \tag{C.4}$$

where we set $x = \nu t/2$ and the approximation holds for large Bt. Equation C.4 describes the spin flip probability for a light source spectrally spread over an interval B and centered on the atomic transition frequency. An equivalent amount of light power provided as monochromatic resonant light source would give rise to a Rabi frequency Ω.

In case of the Mølmer-Sørensen interaction, the Rabi frequency is given by $\Omega = (\omega_{\mathrm{ax}} - \delta)/2\eta$. During the gate operation only the part of the spectrum contained in a bandwidth $B = (\omega_{\mathrm{ax}} - \delta)$ centered on $\nu_L \pm \delta$ gives rise to carrier excitations. The coupling strength of this part of the spectrum is assumed to be by a factor γ less as for ν_L. Moreover, for the Mølmer-Sørensen interaction we have to take into account the red and the blue detuned frequency component and both ions can experience a spin flip. The spin flip error probability for a single gate operation is then given by

$$p_{\mathrm{flip}} = p_D(\tau_{\mathrm{gate}}) = \gamma \left(\frac{\pi}{\eta}\right)^2.$$

From the measurement displayed in Fig. 3.5 (b) we see that at a frequency $\delta/(2\pi) \simeq 1.2\,\mathrm{MHz}$ the emitted laser intensity is reduced by a factor 3×10^{-9} with respect to the carrier for a resolution bandwidth of $\tilde{B}/(2\pi) = 1\,\mathrm{kHz}$. At this particular part of the spectrum our laser exhibits a "servo bump" from the fast feedback branch. Thus, the actual ratio is strongly dependent on the parameters of the laser frequency stabilization. We take $\gamma = 2 \times 10^{-7}$ as a conservative estimate for the ratio in the relevant bandwidth of $B/(2\pi) = 20\,\mathrm{kHz}$ and calculate a spin flip probability of $p_{\mathrm{flip}} = 10^{-3}$ per gate operation.

D Journal publications

The work described in this thesis has given rise to a number of journal publications which are attached in the following order:

1. "Towards fault-tolerant quantum computing with trapped ions"
   J. Benhelm, G. Kirchmair, C. F. Roos, & R. Blatt
   Nature Physics **4**, 463 (2008)
2. "Experimental quantum-information processing with $^{43}Ca^{+}$"
   J. Benhelm, G. Kirchmair, C. F. Roos, & R. Blatt
   Phys. Rev. A **77**, 062306 (2008)
3. "Measurement of the hyperfine structure of the $S_{1/2}$-$D_{5/2}$ transition in $^{43}Ca^{+}$"
   J. Benhelm, G. Kirchmair, U. Rapol, T. Körber, C. F. Roos, & R. Blatt
   Phys. Rev. A **75**, 032506 (2007)

Articles in preparation:

4. "High fidelity Mølmer-Sørensen gate with hot and cold ions"
   G. Kirchmair, **J. Benhelm**, F. Zähringer, R. Gerritsma, C. F. Roos, & R. Blatt
5. "Absolute frequency measurement of the $^{40}Ca^{+}$ $4s\,^2S_{1/2} - 3d\,^2D_{5/2}$ clock transition"
   M. Chwalla, **J. Benhelm**, K. Kim, G. Kirchmair, T. Monz, M. Riebe, P. Schindler, A. Villar, W. Hänsel, C. F. Roos, R. Blatt, M. Abgrall, G. Santarelli, G. D. Rovera, & P. Laurent
   arXiv:0806.1414v1 [quant-ph]

Further articles that have been published in the framework of this thesis:
(available online at http://quantumoptics.at)

6. "Teleportation with atoms: quantum process tomography"
   M. Riebe, M. Chwalla, **J. Benhelm**, H. Häffner, W. Hänsel, C. F. Roos, & R. Blatt
   New J. Phys. **9**, 211 (2007)
7. "High-fidelity ion-trap quantum computing with hyperfine clock states"
   L. Aolita, K. Kim, **J. Benhelm**, C. F. Roos, & H. Häffner
   Phys. Rev. A **76**, 040303 (2007)

8. "Robust entanglement"
   H. Häffner, F. Schmidt-Kaler, W. Hänsel, C. Roos, T. Körber, M. Chwalla, M. Riebe, **J. Benhelm**, U. D. Rapol, C. Becher, & R. Blatt
   Appl. Phys. B **81**, 151 (2005)
9. "Scalable multiparticle entanglement of trapped ions"
   H. Häffner, W. Hänsel, C. F. Roos, **J. Benhelm**, D. C. al Kar, M. Chwalla, T. Körber, U. D. Rapol, M. Riebe, P. O. Schmidt, C. Becher, O. Gühne, W. Dür, & R. Blatt
   Nature **438**, 643 (2005)
10. "Deterministic quantum teleportation with atoms"
   M. Riebe, H. Häffner, C. F. Roos, W. Hänsel, **J. Benhelm**, G. P. T. Lancaster, T. Körber, C. Becher, F. Schmidt-Kaler, D. F. V. James, & R. Blatt
   Nature **429**, 734 (2004)
11. "Control and measurement of three-qubit entangled states"
   C. F. Roos, M. Riebe, H. Häffner, W. Hänsel, **J. Benhelm**, G. P. T. Lancaster, C. Becher, F. Schmidt-Kaler, & R. Blatt
   Science **304**, 1478 (2004)

Towards fault-tolerant quantum computing with trapped ions

JAN BENHELM, GERHARD KIRCHMAIR, CHRISTIAN F. ROOS* AND RAINER BLATT
Institut für Experimentalphysik, Universität Innsbruck, Technikerstr. 25, A-6020 Innsbruck, Austria
Institut für Quantenoptik und Quanteninformation, Österreichische Akademie der Wissenschaften, Otto-Hittmair-Platz 1, A-6020 Innsbruck, Austria
*e-mail: Christian.Roos@uibk.ac.at

Published online: 27 April 2008; doi:10.1038/nphys961

Today, ion traps are among the most promising physical systems for constructing a quantum device harnessing the computing power inherent in the laws of quantum physics[1,2]. For the implementation of arbitrary operations, a quantum computer requires a universal set of quantum logic gates. As in classical models of computation, quantum error correction techniques[3,4] enable rectification of small imperfections in gate operations, thus enabling perfect computation in the presence of noise. For fault-tolerant computation[5], it is believed that error thresholds ranging between 10^{-4} and 10^{-2} will be required—depending on the noise model and the computational overhead for realizing the quantum gates[6–8]—but so far all experimental implementations have fallen short of these requirements. Here, we report on a Mølmer–Sørensen-type gate operation[9,10] entangling ions with a fidelity of 99.3(1)%. The gate is carried out on a pair of qubits encoded in two trapped calcium ions using an amplitude-modulated laser beam interacting with both ions at the same time. A robust gate operation, mapping separable states onto maximally entangled states is achieved by adiabatically switching the laser–ion coupling on and off. We analyse the performance of a single gate and concatenations of up to 21 gate operations.

For ion traps, all building blocks necessary for the construction of a universal quantum computer[1] have been demonstrated over the past decade. Currently, the most important challenges consist of scaling up the present systems to a higher number of qubits and raising the fidelity of gate operations up to the point where quantum error correction techniques can be successfully applied. Although single-qubit gates are easily carried out with high quality, the realization of high-fidelity entangling two-qubit gates[11–16] is much more demanding because the inter-ion distance is orders of magnitude bigger than the characteristic length scale of any state-dependent ion–ion interaction. Apart from quantum gates of the Cirac–Zoller type[2,12], where a laser couples a single qubit with a vibrational mode of the ion string at a time, most other gate realizations entangling ions have relied on collective interactions of the qubits with the laser control fields[11,13–15]. These gate operations entangle transiently the collective pseudospin of the qubits with the vibrational mode and produce either a conditional phase shift[17] or a collective spin flip[9,10,18] of the qubits. Whereas the highest fidelity $F = 97\%$ reported until now[13] has been achieved with a conditional phase gate acting on a pair of hyperfine qubits in $^9Be^+$, spin-flip gates have been limited so far to $F \approx 85\%$ (refs 11,14). All of these experiments have used qubits encoded in hyperfine or Zeeman ground states and a Raman transition mediated by an electric-dipole transition for coupling the qubits.

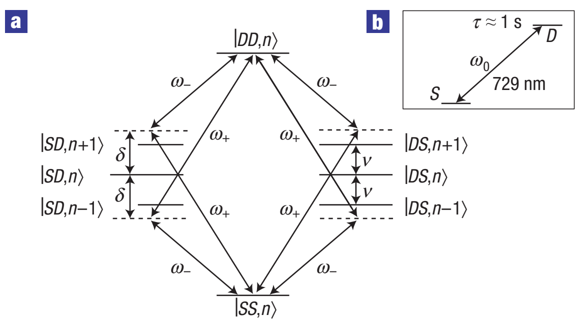

Figure 1 Gate mechanism. a, A bichromatic laser field with frequencies ω_+, ω_- satisfying $2\omega_0 = \omega_+ + \omega_-$ is tuned close to the upper and lower motional sideband of the qubit transition. The field couples the qubit states $|SS\rangle \leftrightarrow |DD\rangle$ through the four interfering paths shown in the figure, n denoting the vibrational quantum number of the axial COM mode. Similar processes couple the states $|SD\rangle \leftrightarrow |DS\rangle$. **b**, The qubits are encoded in the ground state $S_{1/2}(m = 1/2)$ and the metastable state $D_{5/2}(m = 3/2)$ of $^{40}Ca^+$ ions and are manipulated by a narrow bandwidth laser emitting at a wavelength of 729 nm.

Whereas spontaneous scattering from the mediating short-lived levels degrades the gate fidelity owing to the limited amount of laser power available in current experiments[19], this source of decoherence does not occur for optical qubits, that is, qubits encoded in a ground state and a metastable electronic state of an ion. In the experiment presented here, where the qubit comprises the states $|S\rangle \equiv S_{1/2}(m = 1/2)$ and $|D\rangle \equiv D_{5/2}(m = 3/2)$ of the isotope $^{40}Ca^+$, spontaneous decay of the metastable state reduces the gate fidelity by less than 5×10^{-5}.

A Mølmer–Sørensen gate inducing collective spin flips is achieved with a bichromatic laser field with frequencies $\omega_\pm = \omega_0 \pm \delta$, with ω_0 being the qubit transition frequency and δ close to the vibrational mode frequency ν (Fig. 1). For optical qubits, the bichromatic field can be a pair of co-propagating lasers, which is equivalent to a single laser beam resonant with the qubit transition and amplitude-modulated with frequency δ. For a gate mediated by the axial centre-of-mass (COM) mode, the hamiltonian describing the laser–qubit interaction is given by $H = \hbar\Omega e^{-i\phi} S_+ (e^{-i(\delta t+\zeta)} + e^{i(\delta t+\zeta)}) e^{i\eta(a e^{-i\nu t} + a^\dagger e^{i\nu t})} + \mathrm{h.c.}$ Here, $S_j = \sigma_j^{(1)} + \sigma_j^{(2)}, j \in \{+, -, x, y, z\}$, denotes a collective atomic operator constructed from Pauli spin operators $\sigma_j^{(i)}$ acting on ion

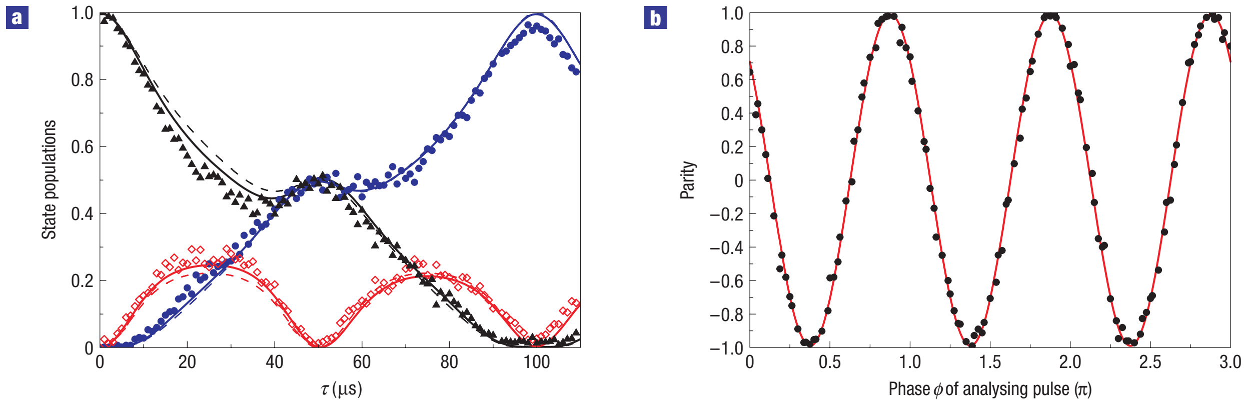

Figure 2 High-fidelity gate operation. a, Evolution of the populations p_0 (filled circle), p_1 (open diamond) and p_2 (filled triangle) induced by a Mølmer–Sørensen bichromatic pulse of duration τ. The Rabi frequency $\Omega(t)$ is smoothly switched on and off within 2 μs and adjusted such that a maximally entangled state is created at $\tau_{\rm gate} = 50$ μs. The dashed lines are calculated for $\bar{n}_{\rm COM} = 0.05$ from the propagator (1), neglecting pulse shaping and non-resonant carrier excitation. The solid lines are obtained by numerically solving the Schrödinger equation for time-dependent $\Omega(t)$ and imbalanced Rabi frequencies $\Omega_+/\Omega_- = 1.094$ (see the Methods section). **b**, A $(\pi/2)_\phi$ analysis pulse applied to both ions prepared in Ψ_1 gives rise to a parity oscillation $P(\phi) = \sin(2\phi)$ as a function of ϕ. A fit with a function $P_{\rm fit} = A\sin(2\phi + \phi_0)$ yields the parity fringe amplitude $A = 0.990(1)$ and $\phi_0/\pi = -1.253(1)$. The precise value of the phase ϕ_0 is without significance. It arises from phase-locking the frequencies $\omega_0, \omega_+, \omega_-$ and could have been experimentally adjusted to zero.

i, and $\sigma_+^{(i)}|S\rangle_i = |D\rangle_i$. The operators a, $a^\dagger$ annihilate and create phonons of the COM mode with Lamb–Dicke factor η. The optical phase of the laser field (with coupling strength Ω) is labelled ϕ, and the phase ζ accounts for a time difference between the start of the gate operation and the maximum of the amplitude modulation of the laser beam. In the Lamb–Dicke regime, and for $\phi = 0$, the gate operation is very well described by the propagator[20]

$$U(t) = \mathrm{e}^{-iF(t)S_x}\hat{D}(\alpha(t)S_{y,\psi})\exp(-i(\lambda t + \chi\sin(\nu-\delta)t)S_{y,\psi}^2). \quad (1)$$

Here, the operator to the right describes collective spin flips induced by the operator $S_{y,\psi} = S_y\cos\psi + S_z\sin\psi$, $\psi = (4\Omega/\delta)\cos\zeta$, and $\lambda \approx \eta^2\Omega^2/(\nu-\delta)$, $\chi \approx \eta^2\Omega^2/(\nu-\delta)^2$. With $\alpha(t) = \alpha_0(\mathrm{e}^{i(\nu-\delta)t} - 1)$, the displacement operator $\hat{D}(\beta) = \mathrm{e}^{\beta a^\dagger - \beta^* a}$ accounting for the transient entanglement between the qubits and the harmonic oscillator becomes equal to the identity after the gate time $\tau_{\rm gate} = 2\pi/|\nu-\delta|$. The operator $\mathrm{e}^{-iF(t)S_x}$ with $F(t) = (2\Omega/\delta)(\sin(\delta t + \phi) - \sin\phi)$ describes fast non-resonant excitations of the carrier transition that occur in the limit of short gates when $\Omega \ll \delta$ no longer strictly holds. Non-resonant excitations are suppressed by intensity-shaping the laser pulse so that the Rabi frequency $\Omega(t)$ is switched on and off smoothly. Moreover, adiabatic switching makes the collective spin-flip operator independent of ζ as $S_{y,\psi} \to S_y$ for $\Omega \to 0$. To achieve adiabatic following, it turns out to be sufficient to switch on the laser within 2.5 oscillation periods of the ions' axial COM mode. When the laser is switched on adiabatically, equation (1) can be simplified by dropping the factor $\mathrm{e}^{-iF(t)S_x}$ and replacing $S_{y,\psi}$ by S_y. To realize an entangling gate of duration $\tau_{\rm gate}$ described by the unitary operator $U_{\rm gate} = \exp(-i(\pi/8)S_y^2)$, the laser intensity needs to be set such that $\eta\Omega \approx |\delta - \nu|/4$.

Two $^{40}Ca^+$ ions are confined in a linear trap[21] with axial and radial COM mode frequencies of $\nu_{\rm axial}/2\pi = 1.23$ MHz and $\nu_{\rm radial}/2\pi = 4$ MHz, respectively. After Doppler cooling and frequency-resolved optical pumping[22] in a magnetic field of 4 G, the two axial modes are cooled close to the motional ground state ($\bar{n}_{\rm COM}$, $\bar{n}_{\rm stretch} < 0.05(5)$). Both ions are now initialized to $|SS\rangle$ with a probability of more than 99.8%. Then, the gate operation is carried out, followed by an optional carrier pulse for analysis. Finally, we measure the probability p_k of finding k ions in the $|S\rangle$ state by detecting light scattered on the $S_{1/2} \leftrightarrow P_{1/2}$ dipole transition with a photomultiplier for 3 ms. The error in state detection due to spontaneous decay from the D state is estimated to be less than 0.15%. Each experimental cycle is synchronized with the frequency of the a.c.-power line and repeated 50–200 times. The laser beam carrying out the entangling operation is controlled by a double-pass acousto-optic modulator, which enables setting the frequency $\omega_{\rm L}$ and phase ϕ of the beam. By means of a variable gain amplifier, we control the radiofrequency input power and hence the intensity profile of each laser pulse. To generate a bichromatic light field, the beam is passed through another acousto-optic modulator in single-pass configuration that is driven simultaneously by two radiofrequency signals with difference frequency δ/π (see the first paragraph of the Methods section). Phase coherence of the laser frequencies is maintained by phase-locking all radiofrequency sources to an ultrastable quartz oscillator. We use 1.8 mW average light power focused down to a spot size of 14 μm gaussian beam waist illuminating both ions from an angle of 45° with equal intensity to achieve the Rabi frequencies $\Omega/(2\pi) \approx 110$ kHz required for carrying out a gate operation with $(\nu-\delta)/(2\pi) = 20$ kHz and $\eta = 0.044$. To make the bichromatic laser pulses independent of the phase ζ, the pulse is switched on and off by using Blackman-shaped pulse slopes of duration $\tau_r = 2$ μs.

Multiple application of the bichromatic pulse of duration $\tau_{\rm gate}$ ideally maps the state $|SS\rangle$ to

$$|SS\rangle \xrightarrow{\tau_{\rm gate}} \underbrace{|SS\rangle + i|DD\rangle}_{\Psi_1} \xrightarrow{\tau_{\rm gate}} |DD\rangle \xrightarrow{\tau_{\rm gate}} |DD\rangle$$
$$+\, i|SS\rangle \xrightarrow{\tau_{\rm gate}} |SS\rangle \xrightarrow{\tau_{\rm gate}} \cdots \quad (2)$$

up to global phases. Maximally entangled states occur at instances $\tau_m = m \cdot \tau_{\rm gate}$ $(m = 1, 3, \ldots)$. A similar mapping of product states onto Bell states and vice versa also occurs when starting from state $|SD\rangle$. To assess the fidelity of the gate operation, we adapt the strategy first applied in refs 11,13 consisting of measuring the fidelity of Bell states created by a single application of the gate to the state $|SS\rangle$ (Fig. 2a). The fidelity

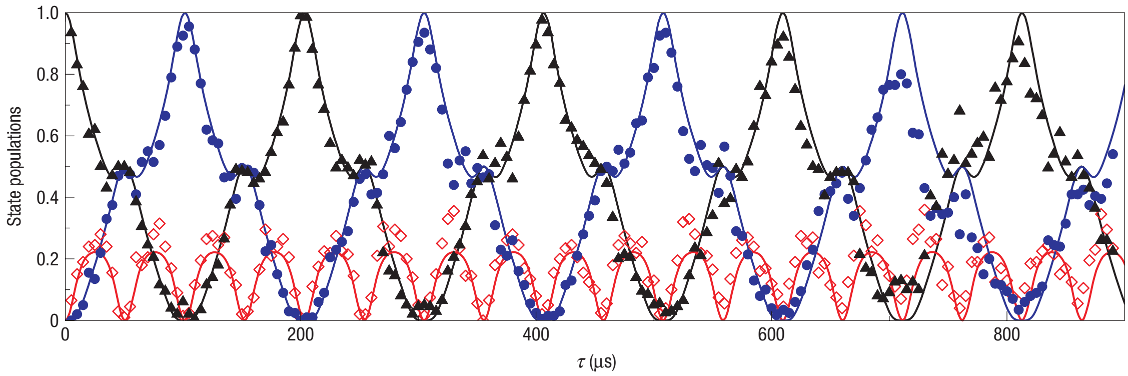

Figure 3 Entanglement and disentanglement dynamics of the Mølmer–Sørensen interaction. Starting from state $|SS\rangle$ for a detuning of the bichromatic laser from the sidebands set to $\delta - \nu = -20$ kHz, the figure shows the time evolution of the populations p_0, p_1 and p_2 denoted by the filled circles, open diamonds and filled triangles respectively. The length of the pulse is equivalent to the application of up to 17 gate operations. Maximally entangled states are created whenever $p_0(\tau)$ and $p_2(\tau)$ coincide and $p_1(\tau)$ vanishes.

$F = \langle \Psi_1|\rho^{\exp}|\Psi_1\rangle = (\rho^{\exp}_{SS,SS} + \rho^{\exp}_{DD,DD})/2 + \mathrm{Im}\rho^{\exp}_{DD,SS}$, with the density matrix $\rho^{\exp}$ describing the experimentally produced qubits' state, is inferred from measurements on a set of 42,400 Bell states continuously produced within a measurement time of 35 min. Fluorescence measurements on 13,000 Bell states reveal that $\rho^{\exp}_{SS,SS} + \rho^{\exp}_{DD,DD} = p_2 + p_0 = 0.9965(4)$. The off-diagonal element $\rho^{\exp}_{DD,SS}$ is determined by measuring $P(\phi) = \langle \sigma^{(1)}_\phi \sigma^{(2)}_\phi \rangle$ for different values of ϕ, where $\sigma_\phi = \sigma_x \cos\phi + \sigma_y \sin\phi$, by applying $(\pi/2)_\phi$ pulses to the remaining 29,400 states and measuring $p_0 + p_2 - p_1$ to obtain the parity $\langle \sigma^{(1)}_z \sigma^{(2)}_z \rangle$. The resulting parity oscillation $P(\phi)$ shown in Fig. 2b is fitted with a function $P_{\mathrm{fit}}(\phi) = A\sin(2\phi + \phi_0)$ that yields $A = 2|\rho^{\exp}_{DD,SS}| = 0.990(1)$. Combining the two measurements, we obtain the fidelity $F = 99.3(1)\%$ for the Bell state Ψ_1.

A wealth of further information is obtained by studying the state dynamics under the action of the gate hamiltonian (see equation (2)). Starting from state $|SS\rangle$, Fig. 3 shows the time evolution of the state populations for pulse lengths equivalent to up to 17 gate times. The ions are entangled and disentangled consecutively up to nine times, the populations closely following the predicted unitary evolution of the propagator (1) for $\zeta = 0$ shown in Fig. 3 as solid lines.

To study sources of gate imperfections we measured the fidelity of Bell states obtained after a pulse length τ_m for up to $m = 21$ gate operations. The sum of the populations $p_0(t) + p_2(t)$ does not return perfectly to one at times τ_m as shown in Fig. 4 but decreases by about 0.0022(1) per gate. This linear decrease could be explained by resonant spin-flip processes caused by spectral components of the qubit laser that are far outside the laser's linewidth of 20 Hz (ref. 21) (see the Methods section). The figure also shows the amplitude of parity fringe pattern scans at odd integer multiples of τ_{gate} similar to the one in Fig. 2b. The gaussian shape of the amplitude decay is consistent with variations in the coupling strength Ω that occur from one experiment to the next (see the Methods section).

The observed Bell-state infidelity of 7×10^{-3} indicates that the gate operation has an infidelity below the error threshold required by some models of fault-tolerant quantum computation[6–8] (an indication to be confirmed by full quantum gate tomography[16] in future experiments). However, further experimental advances will be needed before fault-tolerant computation will become a reality as the overhead implied by these models is considerable. Nevertheless, in addition to making the implementation of

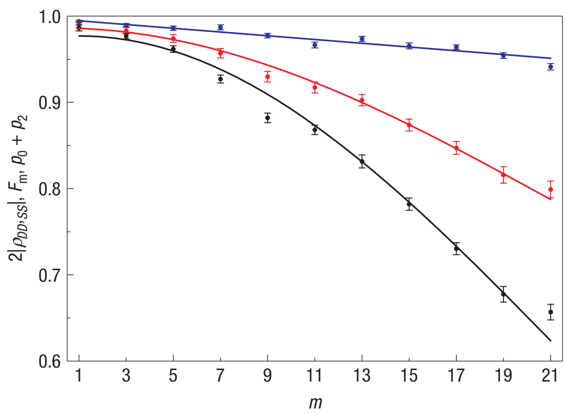

Figure 4 Multiple gate operations. Gate imperfections as a function of the bichromatic pulse length $\tau_m = m \cdot \tau_{\mathrm{gate}}$ given in equivalent number of gate operations m. The upper curve shows a linear decrease of the state populations $p_0 + p_2$ with a slope of 0.0022(1). All errors given are 1σ statistical errors. The lower curve represents the magnitude of the coherence $2\rho_{DD,SS}$ measured by detecting parity oscillations and fitted by a gaussian decay function that accounts for low-frequency noise of the laser–ion coupling strength Ω (see the Methods section). Combining both measurements yields the Bell-state fidelity F_m shown as the middle trace. For $m = 21$, the fidelity is still $F_{21} = 80(1)\%$. Similar results are achieved when replacing the entangling pulse of length τ_m by m amplitude-shaped pulses each of which is realizing an entangling gate operation.

quantum algorithms with tens of entangling operations look realistic, the gate presented here also opens interesting perspectives for generating multiparticle entanglement[23] by a single laser interacting with more than two qubits at once. For the generation of N-qubit Greenberger–Horne–Zeilinger states, there exist no constraints on the positioning of ions in the bichromatic beam that otherwise made generation of Greenberger–Horne–Zeilinger states beyond $N = 6$ difficult in the experiment with hyperfine qubits described in ref. 24. Although the bichromatic force lacks a strong spatial modulation that would enable tailoring of the gate interaction by choosing particular ion spacings[25,26], more complex multiqubit interactions could be engineered by interleaving entangling laser pulses addressing all qubits with a focused laser inducing phase shifts in single qubits. Akin to nuclear magnetic resonance techniques, this method should enable refocusing of unwanted qubit–qubit interactions[27] and open the door to a wide variety of entangling multiqubit interactions.

METHODS

A.C.-STARK-SHIFT COMPENSATION

The red- and the blue-detuned frequency components $\omega_\pm$ of the bichromatic light field cause dynamic (a.c.-) Stark shifts by non-resonant excitation on the carrier and the first-order sidebands that exactly cancel each other if the corresponding laser intensities $I_\pm$ are equal. The remaining a.c.-Stark shift due to other Zeeman transitions and far-detuned dipole transitions amounts to 7 kHz for a gate time $\tau_{\rm gate} = 50\,\mu$s. These shifts could be compensated by using an extra far-detuned light field[28] or by properly setting the intensity ratio I_+/I_-. We use the latter technique, which makes the coupling strengths $\Omega_{SS\leftrightarrow DD} \propto 2\sqrt{I_+ I_-}$, $\Omega_{SD\leftrightarrow DS} \propto I_+ + I_-$ slightly unequal. However, the error is insignificant as $\Omega_{SD\leftrightarrow DS}/\Omega_{SS\leftrightarrow DD} - 1 = 4\times10^{-3}$ in our experiments.

SOURCES OF GATE INFIDELITY

A bichromatic force with time-dependent $\Omega(t)$ acting on ions prepared in an eigenstate of S_y creates coherent states $\alpha(t)$ following trajectories in phase space that generally do not close[20,29]. For the short rise times used in our experiments, this effect can be made negligibly ($<10^{-4}$) small by slightly increasing the gate time.

Spin flips induced by incoherent off-resonant light of the bichromatic laser field reduce the gate fidelity. A beat frequency measurement between the gate laser and a similar independent laser system that was spectrally filtered indicates that a fraction γ of about 2×10^{-7} of the total laser power is contained in a 20 kHz bandwidth B around the carrier transition when the laser is tuned close to a motional sideband. A simple model predicts spin flips to cause a gate error with probability $p_{\rm flip} = (\pi\gamma|\nu-\delta|)/(2\eta^2 B)$. This would correspond to a probability $p_{\rm flip} = 8\times10^{-4}$, whereas the measured state populations shown in Fig. 4 would be consistent with $p_{\rm flip} = 2\times10^{-3}$. Spin-flip errors could be further reduced by two orders of magnitude by spectrally filtering the laser light and increasing the trap frequency $\nu/(2\pi)$ to above 2 MHz where noise caused by the laser frequency stabilization is much reduced.

Imperfections due to low-frequency noise randomly shifting the laser frequency $\omega_{\rm L}$ with respect to the atomic transition frequency ω_0 were estimated from Ramsey measurements on a single ion showing that an average frequency deviation $\sigma_{(\omega_{\rm L}-\omega_0)}/(2\pi) = 160$ Hz occurred. From numerical simulations, we infer that for a single gate operation this frequency uncertainty gives rise to a fidelity loss of 0.25% (an infidelity of 10^{-4} would require $\sigma_{(\omega_{\rm L}-\omega_0)}/(2\pi) = 30$ Hz). In our parity oscillation experiments shown in Figs 2b and 4, however, this loss is not directly observable because a small error in the frequency of the bichromatic laser beam carrying out the gate operation is correlated with a similar frequency error of the carrier $(\frac{\pi}{2})_\phi$ pulse probing the entanglement produced by the gate so that the phase ϕ of the analysing pulse with respect to the qubit state remains well defined.

Variations in the coupling strength $\delta\Omega$ induced by low-frequency laser intensity noise and thermally occupied radial modes were inferred from an independent measurement by recording the amplitude decay of carrier oscillations. Assuming a gaussian decay, we find a relative variation of $\delta\Omega/\Omega = 1.4(1)\times10^{-2}$. For m entangling gate operations, the loss of fidelity is approximately given by $1-F = (\pi m/2)^2(\delta\Omega/\Omega)^2$ and contributes with 5×10^{-4} to the error of a single gate operation. For the multiple gate operations shown in Fig. 4, this source of noise explains the gaussian decay of the parity fringe amplitude, whereas laser frequency noise reduces the fringe amplitude by less than 1% even for 21 gate operations. In combination with error estimates for state preparation, detection and laser noise, the analysis of multiple gates provides us with a good understanding of the most important sources of gate infidelity.

Received 19 December 2007; accepted 25 March 2008; published 27 April 2008.

References

1. Nielsen, M. A. & Chuang, I. L. *Quantum Computation and Quantum Information* (Cambridge Univ. Press, Cambridge, 2000).
2. Cirac, J. I. & Zoller, P. Quantum computations with cold trapped ions. *Phys. Rev. Lett.* **74**, 4091–4094 (1995).
3. Shor, P. W. Scheme for reducing decoherence in quantum computer memory. *Phys. Rev. A* **52**, R2493–R2496 (1995).
4. Steane, A. M. Error correcting codes in quantum theory. *Phys. Rev. Lett.* **77**, 793–797 (1996).
5. Shor, P. W. *37th Symposium on Foundations of Computing* 56–65 (IEEE Computer Society Press, Washington DC, 1996).
6. Knill, E. Quantum computing with realistically noisy devices. *Nature* **434**, 39–44 (2005).
7. Raussendorf, R. & Harrington, J. Fault-tolerant quantum computation with high threshold in two dimensions. *Phys. Rev. Lett.* **98**, 190504 (2007).
8. Reichardt, B. W. Improved ancilla preparation scheme increases fault-tolerant threshold. Preprint at <http://arxiv.org/abs/quant-ph/0406025v1> (2004).
9. Sørensen, A. & Mølmer, K. Quantum computation with ions in thermal motion. *Phys. Rev. Lett.* **82**, 1971–1974 (1999).
10. Sørensen, A. & Mølmer, K. Entanglement and quantum computation with ions in thermal motion. *Phys. Rev. A* **62**, 022311 (2000).
11. Sackett, C. A. *et al*. Experimental entanglement of four particles. *Nature* **404**, 256–259 (2000).
12. Schmidt-Kaler, F. *et al*. Realization of the Cirac–Zoller controlled-NOT quantum gate. *Nature* **422**, 408–411 (2003).
13. Leibfried, D. *et al*. Experimental demonstration of a robust, high-fidelity geometric two ion-qubit phase gate. *Nature* **422**, 412–415 (2003).
14. Haljan, P. C. *et al*. Entanglement of trapped-ion clock states. *Phys. Rev. A* **72**, 062316 (2005).
15. Home, J. P. *et al*. Deterministic entanglement and tomography of ion spin qubits. *New J. Phys.* **8**, 188 (2006).
16. Riebe, M. *et al*. Process tomography of ion trap quantum gates. *Phys. Rev. Lett.* **97**, 220407 (2006).
17. Milburn, G. J., Schneider, S. & James, D. F. V. Ion trap quantum computing with warm ions. *Fortschr. Phys.* **48**, 801–810 (2000).
18. Solano, E., de Matos Filho, R. L. & Zagury, N. Deterministic Bell states and measurement of the motional state of two trapped ions. *Phys. Rev. A* **59**, R2539–R2543 (1999).
19. Ozeri, R. *et al*. Errors in trapped-ion quantum gates due to spontaneous photon scattering. *Phys. Rev. A* **75**, 042329 (2007).
20. Roos, C. F. Ion trap quantum gates with amplitude-modulated laser beams. *New J. Phys.* **10**, 013002 (2008).
21. Benhelm, J. *et al*. Measurement of the hyperfine structure of the $S_{1/2}$–$D_{5/2}$ transition in $^{43}Ca^+$. *Phys. Rev. A* **75**, 032506 (2007).
22. Roos, C. F., Chwalla, M., Kim, K., Riebe, M. & Blatt, R. 'Designer atoms' for quantum metrology. *Nature* **443**, 316–319 (2006).
23. Mølmer, K. & Sørensen, A. Multiparticle entanglement of hot trapped ions. *Phys. Rev. Lett.* **82**, 1835–1838 (1999).
24. Leibfried, D. *et al*. Creation of a six-atom 'Schrödinger cat' state. *Nature* **438**, 639–642 (2005).
25. Chiaverini, J. *et al*. Realization of quantum error correction. *Nature* **432**, 602–605 (2004).
26. Reichle, R. *et al*. Experimental purification of two-atom entanglement. *Nature* **443**, 838–841 (2006).
27. Vandersypen, L. M. K. & Chuang, I. L. NMR techniques for quantum control and computation. *Rev. Mod. Phys.* **76**, 1037–1069 (2004).
28. Häffner, H. *et al*. Precision measurement and compensation of optical Stark shifts for an ion-trap quantum processor. *Phys. Rev. Lett.* **90**, 143602 (2003).
29. Leibfried, D., Knill, E., Ospelkaus, C. & Wineland, D. J. Transport quantum logic gates for trapped ions. *Phys. Rev. A* **76**, 032324 (2007).

Acknowledgements

We gratefully acknowledge the support of the European network SCALA and the Disruptive Technology Office and the Institut für Quanteninformation GmbH. We thank R. Gerritsma and F. Zähringer for help with the experiments.

Author information

Reprints and permission information is available online at http://npg.nature.com/reprintsandpermissions. Correspondence and requests for materials should be addressed to C.F.R.

Experimental quantum-information processing with $^{43}Ca^{+}$ ions

J. Benhelm,[1,2] G. Kirchmair,[1,2] C. F. Roos,[1,2] and R. Blatt[1,2]
[1]*Institut für Experimentalphysik, Universität Innsbruck, Technikerstrasse 25, A-6020 Innsbruck, Austria*
[2]*Institut für Quantenoptik und Quanteninformation, Österreichische Akademie der Wissenschaften, Otto-Hittmair-Platz 1, A-6020 Innsbruck, Austria*

(Received 8 April 2008; published 4 June 2008)

For quantum-information processing (QIP) with trapped ions, the isotope $^{43}Ca^{+}$ offers the combined advantages of a quantum memory with long coherence time, a high-fidelity readout, and the possibility of performing two-qubit gates on a quadrupole transition with a narrow-band laser. Compared to other ions used for quantum computing, $^{43}Ca^{+}$ has a relatively complicated level structure. We discuss how to meet the basic requirements for QIP and demonstrate ground-state cooling, robust state initialization, and efficient readout for the hyperfine qubit with a single $^{43}Ca^{+}$ ion. A microwave field and a Raman light field are used to drive qubit transitions, and the coherence times for both fields are compared. Phase errors due to interferometric instabilities in the Raman field generation do not limit the experiments on a time scale of 100 ms. We find a quantum-information storage time of many seconds for the hyperfine qubit.

DOI: 10.1103/PhysRevA.77.062306 PACS number(s): 03.67.Lx, 32.80.Qk, 37.10.Ty, 42.50.Dv

I. INTRODUCTION

Quantum-information processing (QIP) with trapped ions has made huge progress since it was first proposed more than a decade ago [1]. The question of which ion species is best suited for QIP is still undecided. So far, qubits encoded in trapped ions come in two flavors. On the one hand, two energy levels of the hyperfine (or Zeeman) ground-state manifold of an ion can serve as a qubit commonly termed a *hyperfine qubit*. The energy splitting is typically several GHz. Many successful experiments have been performed on hyperfine qubits with cadmium and beryllium ions, illustrating the capabilities for QIP [2–5]. On the other hand, quantum information can be encoded in the ground state and a metastable energy state of an ion. Here the energy splitting lies in the optical domain and the qubit is therefore referred to as an *optical qubit*. This concept has been pursued so far mainly with calcium ions, where all major building blocks for QIP have been demonstrated [6–8].

When it comes to judging the suitability of a particular ion for QIP, the fidelities and speed of the basic gate operations and the quantum-information storage time are important criteria. Concerning the latter the hyperfine qubit has been the clearly better choice. For the optical qubit, it is technically challenging to achieve quantum-information storage times much longer than a few milliseconds since this requires a laser with a linewidth of less than a few Hz. Yet optical qubits have excellent initialization and readout properties. Moreover, the metastable states can be used as intermediate levels when driving the hyperfine qubits with a Raman light field as suggested in Ref. [9]. Errors induced by spontaneous scattering, which are a major limitation in present experiments with Raman light fields detuned from an optical dipole transition, are then largely suppressed.

From today's perspective, it seems necessary to integrate the building blocks that have been acquired over the years into a single system. By using hyperfine qubits in combination with metastable states, it is possible to exploit the best of both concepts. Only a few ion species offer this possibility, one of them being $^{43}Ca^{+}$. It is the only calcium isotope with nonzero nuclear spin, and it offers the advantage that all necessary laser wavelengths lying within the range from 375 nm to 866 nm can be produced by commercially available solid-state lasers. For QIP, only a small number of electronic levels are of interest (Fig. 1). The $S_{1/2}$ ground state is split into the states $F=4$ and $F=3$ with a hyperfine splitting of 3.2

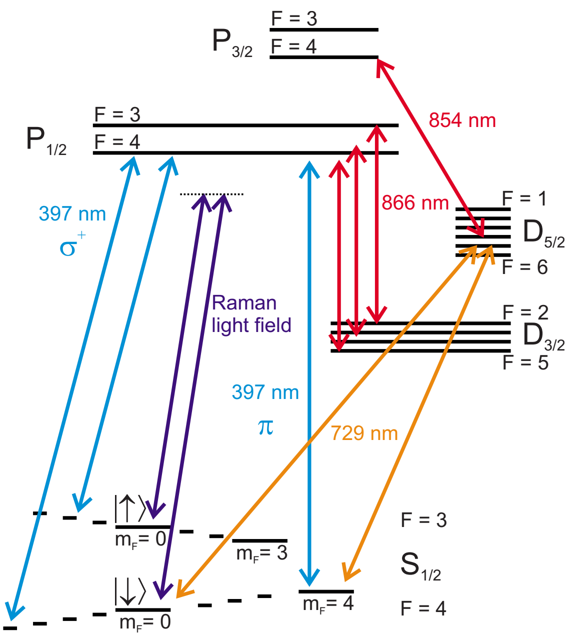

FIG. 1. (Color online) Energy level diagram of the valence electron of $^{43}Ca^{+}$ showing the hyperfine splitting of the lowest energy levels. Laser light at 397 nm is used for Doppler cooling and detection; the lasers at 866 nm and 854 nm pump out the metastable D states. A laser at 729 nm excites the ions on the transition from the $S_{1/2}(F=4)$ states to the $D_{5/2}(F=2,\ldots,6)$ states. It is used for ground-state cooling, state initialization, and state discrimination. Microwave radiation applied to an electrode close to the ions as well as a Raman light field at 397 nm can drive transitions between different levels in the hyperfine structure of the $S_{1/2}$-state manifold.

GHz [10]. It is connected by electric-dipole transitions to the short-lived levels $P_{1/2}$ and $P_{3/2}$ and by electric-quadrupole transitions to the metastable states $D_{3/2}$ and $D_{5/2}$ with a lifetime of ~ 1 s. Because of the fairly large nuclear spin of $I = 7/2$, these levels split into a total of 144 Zeeman states. This results in a very rich spectrum for the $S_{1/2} \leftrightarrow D_{5/2}$ transition, which has been investigated to a high precision recently [11].

II. EXPERIMENTAL SETUP

$^{43}Ca^+$ ions are loaded from an enriched source into a linear Paul trap by a two-step photoionization process (423 nm and 375 nm) [11–13]. Radial confinement is provided by a quadrupole field created by the application of a radio frequency voltage to two out of four blade electrodes and connecting the other two blade electrodes to ground [14]. Axial confinement is achieved by setting two tip electrodes to dc voltages of 500–500 V, resulting in center-of-mass (c.m.) mode secular trapping frequencies of $\omega_{ax}/2\pi = 0.8 - 1.5$ MHz. Applying slightly unequal voltages to the tips leads to an axial shift in the ions' equilibrium position. The closest distance between the ions and the tip (blade) electrodes is 2.5 mm (0.8 mm). Two additional electrodes compensate for external electric stray fields in the radial directions. One of them, located at a distance of 7.3 mm to the trap center, can also be used to guide microwave signals to the ions. The trap is housed in a vacuum environment with a pressure below 2×10^{-11} mbar. When no laser light is present, ion storage times as long as 2 weeks have been observed.[1]

For most experimental steps, we use a titanium-sapphire laser at 729 nm for coupling the energy levels of the $S_{1/2}(F=4)$ and $D_{5/2}(F=2,\ldots,6)$ manifolds via their electric-quadrupole transition (Fig. 1). The laser's frequency is stabilized to an ultrastable Fabry-Perot cavity [15] with a linewidth of 4.7 kHz. A Lorentzian fit to a beat note measurement with another similar laser reveals a width of the beat note's power spectral density of 1.8 Hz (4 s data acquisition time). This is indicative of a linewidth for each laser below 1 Hz. In a measurement where a single $^{43}Ca^+$ ion served as a frequency reference [11], we obtained a linewidth of 16 Hz with an integration time of 60 s.

In order to stabilize the laser's frequency to the atomic transition frequency, we use a feedback loop based on spectroscopic measurements typically taken every 1–2 min. Since Ramsey phase experiments are used to probe the frequencies of two different Zeeman transitions, these measurements serve also to infer the strength of the magnetic field at the ion's position. The result is automatically analyzed and fed back to an acousto-optic modulator (AOM) located between the laser and its reference cavity. By this means the laser's output frequency remains constant with respect to the ion's quadrupole transition frequency. The mean frequency deviation between laser and ion depends on the Ramsey probe time, the measurement interval, and the actual frequency drift of the reference cavity and is typically smaller than 200 Hz. With the knowledge of the laser frequency and the magnetic field, the transition frequency of all required Zeeman transitions are calculated to an accuracy of ± 500 Hz. The optical frequency and phase of the laser are controlled with a double-pass AOM (270 MHz) between laser and ion. Slow drifts of the magnetic field ($\lesssim 200\ \mu$G/h) are taken into account by properly adjusting the radio frequency feeding the AOM. Deteriorating effects due to magnetic field noise components at 50 Hz, typically on the order of 1 mG, are largely suppressed by triggering all experiments to the ac-line frequency.

The hyperfine qubit can be driven with a Raman light field comprising two phase stable frequency components. It is derived from a commercial diode laser system, consisting of a tapered amplifier and a frequency-doubling stage emitting at a wavelength of 397 nm. To achieve the frequency difference of 3.2 GHz required for bridging the ground-state hyperfine splitting in $^{43}Ca^+$, the light is first sent through an AOM (1 GHz) that splits the laser beam into a blue beam line (+1st order of diffraction) and a red beam line (0th order). The latter passes another AOM operated at 1 GHz (−1st order of diffraction). The remaining frequency shift is achieved by two more AOMs (~ 300 MHz) in each beamline. For noncopropagating Raman light fields, the two beam lines are separately guided to the ions through the viewports labeled NW and NE in Fig. 2(a).

Frequency, phase, and amplitude control of these lasers is synonymous to controlling the radio frequency signals applied to the AOMs. We use a homemade versatile frequency source (VFS) based on direct digital synthesis that can phase-coherently provide 16 different radio frequencies up to 305 MHz. Amplitude shaping is achieved with a variable-gain amplifier controlled by a field-programmable gate array. The VFS and all other radio frequency sources providing the input signals of the AOMs mentioned above are referenced to an ultrastable quartz oscillator with a long-term stabilization provided by the global positioning system. For direct microwave driving the hyperfine qubit, the output of the VFS is mixed with a signal of 1.35 GHz, then filtered, frequency doubled, filtered, and amplified. In this way, full amplitude, frequency, and phase control of the VFS is up-converted to 3.2 GHz.

The laser sources at 866 nm, 854 nm, and 397 nm are commercially available diode lasers whose frequencies are referenced to Fabry-Perot cavities. The Doppler cooling laser at 397 nm is produced by frequency-doubling light of a near-infrared laser diode. Except for the Raman light fields, all other light sources are linked to the experiment with single-mode fibers. As sketched in Fig. 2, the vacuum vessel provides optical access for illuminating the ion by laser beams mostly arriving in a plane containing also the symmetry axis of the trap. In addition, two beams used for laser cooling (729 nm and 866 nm) are sent in from below with a 60° angle to the trap axis.

Fluorescence light is collected with a custom-designed lens (with a numerical aperture of 0.3), correcting for aberrations induced by the vacuum window. The light is sent to a photomultiplier (PMT) or a sensitive camera with a magni-

[1]With two $^{40}Ca^+$ ions trapped, we repeatedly observe that one of the ions forms a $CaOH^+$ molecule by measuring the change of the axial sideband frequencies. These events occur every few hours.

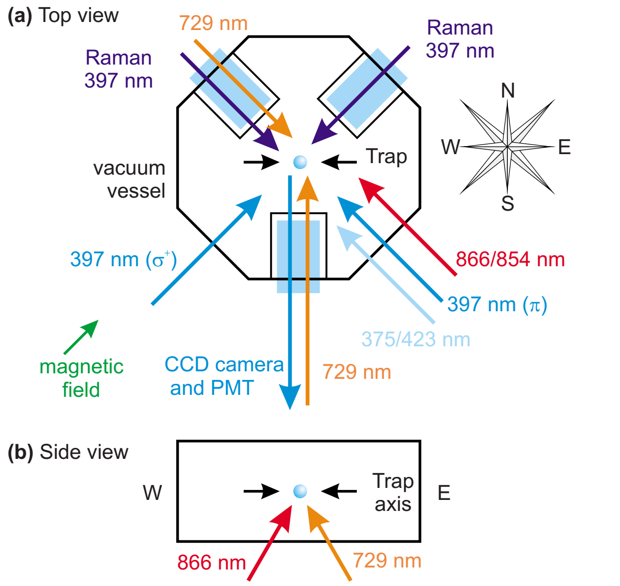

FIG. 2. (Color online) (a) Most laser beams are sent to the ion from a plane containing also the symmetry axis of the trap (top view). With three custom-made lenses in the inverted viewports S, NE, and NW, we can tightly focus light at wavelengths 729 nm and 397 nm. The lens in S is also used to collect fluorescence light which is sent to a PMT or a camera. The quantization axis is defined by a magnetic field along SW-NE. (b) Two beams (729 nm and 866 nm) are sent in from below in a 60° angle to the trap axis (side view). The axial trapping potential is provided by two tips indicated by arrows along the z axis. Unbalancing the tip voltages results in a shift of the ion crystal along the trap axis (E-W).

fication of 25 and a resolution of 2.2 μm. For a single $^{43}Ca^+$ ion, the signal-to-noise ratio at the PMT is typically around 50. The same type of lens is also used to focus light at 729 nm and 397 nm from the S, NE, and NW viewports.

III. INITIALIZING THE $^{43}Ca^+$ HYPERFINE QUBIT

There are many ways to encode quantum information in the $^{43}Ca^+$ level structure. An optical qubit with vanishing first-order dependence on magnetic field fluctuations has been proposed in Ref. [11]. Here, we consider the hyperfine ground-state manifold depicted in Fig. 1 where the energy splitting between the $F=3$ and $F=4$ manifold is about 3.2 GHz. For low magnetic fields, the two states $|\downarrow\rangle \equiv S_{1/2}(F=4, m_F=0)$ and $|\uparrow\rangle \equiv S_{1/2}(F=3, m_F=0)$ exhibit no linear Zeeman effect and are therefore attractive as a robust quantum-information carrier [16]. As in classical computing, QIP devices also need to be initialized. In our experiment, the initialization step comprises Doppler cooling, optical pumping, cooling to the motional ground state, and state transfer to $|\downarrow\rangle$.

A. Doppler cooling and optical pumping

For Doppler cooling and fluorescence detection, the ion is excited on the $S_{1/2} \leftrightarrow P_{1/2}$ dipole transition with two laser beams. The beam entering from SE is π polarized and is slightly red detuned from the transition $S_{1/2}(F=4) \leftrightarrow P_{1/2}(F=4)$. The second beam is σ^+ polarized. It is sent through an electro-optic phase modulator (3.2 GHz) to excite the ions from the $S_{1/2}(F=3)$ and $S_{1/2}(F=4)$ to $P_{1/2}(F=4)$ manifold. Coherent population trapping is avoided by lifting the degeneracy of the Zeeman sublevels with a magnetic field. To avoid population trapping in the $D_{3/2}$ manifold, repumping laser light at 866 nm is applied. The repumping efficiency was improved by tuning the laser close to the $D_{3/2}(F=3) \leftrightarrow P_{1/2}(F=3)$ transition frequency and providing two additional frequencies shifted by −150 MHz and −395 MHz such that all hyperfine $D_{3/2}$ levels are resonantly coupled to one of the $P_{1/2}(F=3,4)$-levels. We observed a maximum fluorescence count rate of 24000 counts per second and per $^{43}Ca^+$ ion on a PMT for magnetic fields ranging from 0.2 to 5 G. This is about 45% of the count rate we observe for $^{40}Ca^+$ ions. The count rate difference, possibly caused by coherent population trapping, is still under investigation.

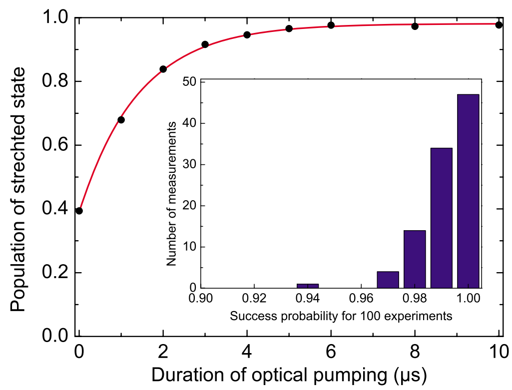

FIG. 3. (Color online) The population in the stretched state $S_{1/2}(F=4, m_F=4)$ is plotted as a function of the duration of optical pumping. An exponential fit (solid line) reveals a time constant of 1.4 μs. After 10 μs the population is in the desired state in 98% of the measurements. The inset shows a histogram of the success rate of 100 measurements each containing 100 experiments when two π pulses on the quadrupole transition are applied and an additional intermediated optical pumping interval is used. This enhances the fidelity of the process to above 99.2%.

After switching off the π-polarized laser beam, the ion is optically pumped into the state $S_{1/2}(F=4, m_F=4)$. The state's population was measured with two consecutive π pulses exciting the population to the $D_{5/2}$ state and subsequent fluorescence detection (Sec. IV). Figure 3 shows the dynamics of optical pumping and illustrates that the stretched Zeeman states of the ground-state manifold are already strongly populated during Doppler cooling. An exponential fit to the data points yields a time constant of the process of 1.4 μs. After 10 μs, the desired state is populated in 98% of the cases.

The pumping efficiency can be improved by transferring the population after this first step with a π pulse to the $D_{5/2}(F=6, m_F=6)$ state and repeating the optical pumping. By applying another π pulse on the same transition, the populations in $S_{1/2}(F=4, m_F=4)$ and $D_{5/2}(F=6, m_F=6)$ are exchanged. On average, 98% should now be in $S_{1/2}(F=4, m_F=4)$ and the rest in the $D_{5/2}$ state. Finally the two populations are combined by switching on the 854-nm laser

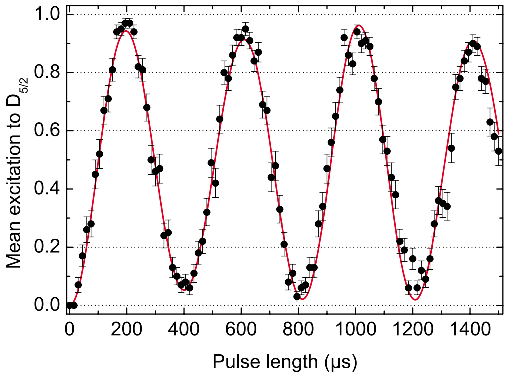

FIG. 4. (Color online) Rabi oscillations on the blue axial sideband of the transition $S_{1/2}(F=4,\ m_F=4)\leftrightarrow D_{5/2}(F=6,\ m_F=6)$ after ground-state cooling. The solid line is a fit assuming a thermal state. It yields a mean occupation of the axial mode of $\bar{n}_{ax}=0.06$.

for a short time to clear out the $D_{5/2}$ state via the $P_{3/2}(F=5,\ m_F=5)$ state from where it can decay only into the desired stretched state. The inset of Fig. 3 shows a histogram built from 100 measurements, each comprising 100 experiments, indicating a lower bound of the pumping efficiency of 99.2%.

After Doppler cooling and optical pumping, an average population $\bar{n}_{ax}=10(5)$ of the axial mode is inferred from measuring the decay of Rabi oscillations on the blue axial sideband. The average number of quanta is heavily dependent on the different laser detunings and powers.

B. Ground-state cooling, heating rate, and ion shuttling

Cooling the ions to the motional ground state is mandatory in order to maximize quantum gate fidelities. In our experiment, it has been implemented with a scheme analogous to what has been demonstrated with $^{40}Ca^+$ ions [17]. In order to obtain a closed cooling cycle, the frequency of the laser at 729 nm is tuned to the red sideband ($\omega_{ax}/2\pi=1.18$ MHz) of the transition $S_{1/2}(F=4,\ m_F=4)\leftrightarrow D_{5/2}(F=6,\ m_F=6)$. An additional quenching laser at 854 nm is required to increase the spontaneous decay rate to the energy level $S_{1/2}$ by coupling the $D_{5/2}(F=6,\ m_F=6)$ to the $P_{3/2}(F=5,\ m_F=5)$ state. Spontaneous decay to the stretched state takes the entropy away from the ion. In each cycle, one motional quantum can be removed. The residual occupation of the motional mode is measured by comparison of the red and blue sideband excitations. Alternatively, Rabi oscillations on a blue motional sideband can be observed in order to infer the average population of the axial mode (see Fig. 4). The solid line is a fitted model function with $\bar{n}_{ax}$ as a free parameter. From both methods, we consistently obtain $\bar{n}_{ax}=0.06$.

By introducing and varying a delay time between ground-state cooling and the temperature measurement, we determined a heating rate on the axial com-mode of 1 motional quantum per 370 ms. The coherence of a motional superposition state $|0\rangle+|1\rangle$ was investigated by performing Ramsey experiments that mapped the motional superposition states after a variable waiting time to the $S_{1/2}$ and $D_{5/2}$ electronic states. These measurements showed that the motional coherence was preserved for more than 320(10) ms, in good agreement with the measured heating rate.

When it comes to scaling the system up to strings of many ions, it is important that single-qubit gates can be applied to each individual ion. Individual addressing can be achieved by using an electro-optical deflector to rapidly steer a strongly focused laser beam to different ions in the string with high precision [14]. Driving Raman transitions in $^{43}Ca^+$ requires more than a single laser beam that would have to be steered this way. To avoid this complication, we prefer to shuttle the ion string along the axis of the trap instead of moving the laser beams. For an axial trapping frequency of $\omega_{ax}/(2\pi)=1.18$ MHz we are able to shuttle the ions over a distance of up to 10 μm by changing the right (left) tip voltage from 990 V (1010 V) to 1010 V (990 V). The switching speed is currently limited by a low-pass filter with a cutoff at 125 kHz, which prevents external electrical noise from coupling to the trap electrodes. Shuttling over the full distance in order to individually address single ions works for transport durations as low as 40 μs. In a test run with a single $^{40}Ca^+$ ion, quantum information encoded into the motional states $|n=0\rangle$ and $|n=1\rangle$ was fully preserved during the shuttling.

C. Transfer to the hyperfine clock states

Ground-state cooling on quadrupole transitions requires a closed cooling cycle which can only be achieved efficiently when working with the stretched hyperfine ground states $(F=4,\ m_F=\pm 4)$. For this reason, methods are needed that allow for a transfer from these states to the qubit state $|\downarrow\rangle$. Four different techniques were under consideration.

1. Optical pumping on the $S_{1/2}$ to $P_{1/2}$ transition

The state $|\downarrow\rangle$ could be populated by optical pumping with π-polarized light fields exciting the transitions $S_{1/2}(F=4)\leftrightarrow P_{1/2}(F=4)$ and $S_{1/2}(F=3)\leftrightarrow P_{1/2}(F=4)$ within a few microseconds. However, many scattering events would be required to pump the population to the desired state that are likely to heat up the ion from the motional ground state. Moreover, the efficiency of the optical pumping would probably be fairly poor as small polarization imperfections of the beams and repumping via the $S_{1/2}(F=4)\leftrightarrow P_{1/2}(F=3)$ are likely to occur.

2. Raman light field

Transferring the population can also be achieved with a Raman light field detuned from the $S_{1/2}\leftrightarrow P_{1/2}$ dipole transition at 397 nm. In the simplest scenario, a sequence of four π pulses would be used to populate the state $|\downarrow\rangle$ starting from $S_{1/2}(F=4,\ m_F=\pm 4)$ by changing the magnetic quantum number in units of $\Delta m=\pm 1$. Use of copropagating beams suppresses unwanted excitations of motional sidebands.

3. Microwave

Instead of a Raman light field, also a microwave field can be used to transfer the ions in a four-step process to $|\downarrow\rangle$. An additional advantage here is that the field's wavelength is

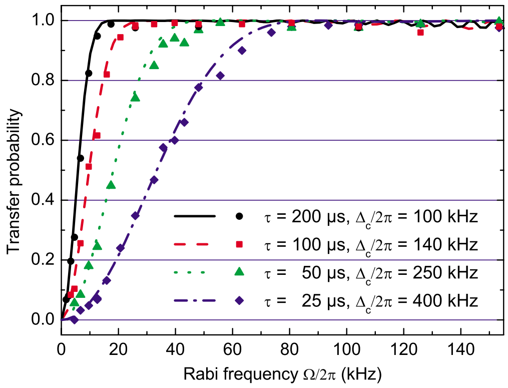

FIG. 5. (Color online) Transfer probability measurement of an amplitude shaped laser pulse on the transition $S_{1/2}(m_F=1/2) \leftrightarrow D_{5/2}(m_F=3/2)$ of a single $^{40}Ca^+$ ion as a function of the Rabi frequency. Data were taken for four different pulse lengths τ and frequency chirp spans Δ_c as given in the plot legend. The lines indicate what is theoretically expected. With enough laser power available, the transfer probability hardly changes over a wide range of Rabi frequencies.

huge compared to the distance of the ions and therefore an equal coupling of all ions to the field is guaranteed.

A limitation for both methods—Raman light field and microwave—is the small coupling strength on the transitions $(F=3,\ m_F=\pm 3) \leftrightarrow (F=4,\ m_F=\pm 2)$. That makes the whole process either slow or necessitates a larger frequency separation of the Zeeman levels in order to suppress nonresonant excitation of neighboring transitions.

4. Transfer via quadrupole transitions

State transfer based on a laser operating on the quadrupole transition $S_{1/2} \leftrightarrow D_{5/2}$ reduces the transfer process to two steps since the selection rules allow for $\Delta m = \pm 2$. The duration of a π pulse can be as short as a few microseconds, and only a single laser beam is needed that can be either focused to a small region or illuminate the whole trap volume. If the $D_{5/2}(F=4)$ is chosen as intermediate state, a good compromise is achieved between the quadrupole coupling strength of the involved transitions and the frequency separation of the neighboring D-state Zeeman levels. The latter is by a factor 1.6 larger as for the ground states. In particular, for low magnetic fields this method is expected to work better than a transfer with Raman or microwave fields.

With the precision laser for the quadrupole transition acting on a single $^{43}Ca^+$ ion, the implementation of state transfer is straightforward. With two consecutive π pulses, we achieved a transfer success probability of more than 99%. Assuming Gaussian beam waists, such high probabilities cannot be expected for larger ions crystals though, unless one is willing to waste most of the laser power by making the beam size very large. As variations of the coupling strengths may also arise from other technical imperfections, a more robust scheme seems to be desirable. Inspired by Ref. [18], we introduce amplitude shaping and a linear frequency sweep of the transfer pulses to demonstrate a transfer technique less sensitive to changes in the laser intensity. Figure 5 shows the transfer probability for a single $^{40}Ca^+$ ion and the transition $S_{1/2}(m=1/2) \leftrightarrow D_{5/2}(m=3/2)$ as a function of the Rabi frequency for four different pulse durations τ. The amplitude of the laser pulse had a $\cos^2$ shape over the pulse length. The frequency of the laser was linearly swept over a range Δ_c centered on the transition frequency. The data show clearly that the transfer probability is hardly affected over a broad range of Rabi frequencies Ω for the different parameters.

IV. STATE DETECTION

For $^{43}Ca^+$ ions, the electron shelving technique first introduced by Dehmelt [21] allows for an efficient state discrimination between the $|\downarrow\rangle$ and $|\uparrow\rangle$ hyperfine qubit states by scattering light on the $S_{1/2}$ to $P_{1/2}$ transition after having shelved the $|\downarrow\rangle$ state in the $D_{5/2}$ metastable state with a π pulse. In our experiment, the same light fields as for Doppler cooling are used, but with slightly more power. With this method, not only $|\uparrow\rangle$ and $|\downarrow\rangle$ can be discriminated, but the other Zeeman levels in the $S_{1/2}$-state and $D_{5/2}$-state manifolds, too. The quality of the transfer pulses sets a limitation on the state discrimination. Again, pulse shaping and frequency sweeping can help to increase the robustness with respect to intensity variations of the shelving laser. In addition, instead of using a single π-pulse excitation to a certain Zeeman state in the $D_{5/2}$-state manifold, the first π pulse can be followed by a second one, exciting any population still remaining in $|\downarrow\rangle$ to a different Zeeman state. Assuming a transfer probability of 0.99 for each of the pulses, one expects a transfer error probability of less then 10^{-4}. The final detection fidelity will then be limited by spontaneous decay from the $D_{5/2}$ state during the detection whose duration depends on the signal-to-noise ratio and signal strength. For the experiments reported here, the detection time was set to 5 ms. The error due to spontaneous decay is estimated to be 0.5%.

V. SINGLE-QUBIT GATES ON THE $^{43}Ca^+$ HYPERFINE QUBIT

Once external and internal degrees of freedom are initialized, quantum information needs to be encoded into the ions, stored, and manipulated. This is achieved with a driving field tuned to the qubits' transition frequency. Two different driving fields were investigated.

A. Microwave drive

From an experimental point of view, quantum-state manipulation by microwave radiation is simple and robust. There is no alignment required, and stable frequency sources are readily available with computer-controlled power, frequency, and phase.

To characterize the microwave properties on a single $^{43}Ca^+$ ion, Rabi oscillations were recorded on the hyperfine qubit $|\downarrow\rangle \leftrightarrow |\uparrow\rangle$ at a magnetic field of 3.4 G. After initializing the ion into $|\downarrow\rangle$, a microwave signal of 3.226 GHz is turned on for a variable amount of time followed by state detection. Figure 6 shows the resulting Rabi oscillations at instances of

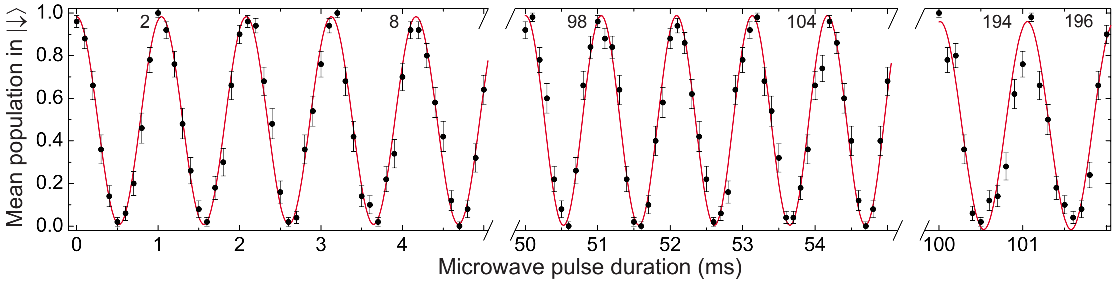

FIG. 6. (Color online) Rabi oscillations on the $^{43}Ca^+$ hyperfine qubit mediated by a microwave field after 0, 50, and 100 ms. Each data point represent 50 individual measurements. The solid line is a weighted least-squares fit with the function $\frac{A}{2}\cos(\pi t/\tau_\pi)+y_0$, resulting in $y_0=0.490(3)$, $\tau_\pi=520.83(3)$ μs, and $A=0.974(11)$. The number of state transfers is indicated. Since the amplitude of the Rabi oscillation is still close to unity even after 200 state transfers, the microwave can serve as a reference to the Raman light field regarding power and phase stability.

0, 50, and 100 ms. The solid line represents a weighted least-squares fit to the function $f(t)=\frac{A}{2}\cos(\pi t/\tau_\pi)+y_0$, resulting in $y_0=0.490(3)$, $\tau_\pi=520.83(3)$ μs, and $A=0.974(11)$. About 200 state transfers are observed over a time of 100 ms with hardly any decrease in fringe amplitude. Also, for measurements with $\tau_\pi=34.3$ μs, a fringe amplitude A close to unity has been observed for more than 150 state transfers. In both cases, the subsequent decay of the fringe amplitude for more oscillations indicates a limitation due to small fluctuations of the microwave power.

Unfortunately, microwave excitation does not couple motional and electronic states unless strong magnetic field gradients are applied [19] and it cannot be focused to a single qubit location. Nevertheless, microwave excitation turns out to be a useful reference for investigating the phase stability of Raman excitation schemes to be discussed in the next subsection.

B. Raman light field

In contrast to the microwave drive, the interaction region of the Raman field detuned from the dipole transition $S_{1/2}\leftrightarrow P_{1/2}$ is as small as the diameter of the involved laser beams. When a single ion is illuminated, the coupling to the center-of-mass mode along the trap axis (unit vector $\boldsymbol{e}_z$) is described by the Lamb-Dicke parameter $\eta=(\boldsymbol{k}_+ -\boldsymbol{k}_-)\cdot\boldsymbol{e}_z\sqrt{\frac{\hbar}{2M\omega}}$. Here, $\boldsymbol{k}_\pm$ is the wave vector of the blue and red Raman light fields, respectively, M is the mass of all ions in the string, and ω denotes the trap frequency. For copropagating lasers the Lamb-Dicke factor is negligible, whereas it is maximized for lasers counterpropagating along the motional mode axis.

We characterize the Raman interaction on a single ion by driving Rabi oscillations on the hyperfine qubit with copropagating beams from NW that are detuned from the $S_{1/2}$ to $P_{1/2}$ transition frequency by -10 GHz. Figure 7 shows Rabi oscillations for excitation times of up to 4 ms with a duration of a π pulse of $\tau_\pi=65.3(1)$ μs. The first few oscillations have a fringe amplitude of $A=0.97(1)$, which is reduced to 0.80(2) after more than 50 state transfers. Shot-to-shot variations in Raman light intensity contribute to a loss symmetrically to the average excitation. In addition, the fringe center, ideally at $y_0=0.5$, has dropped to $y_0=0.428(7)$ due to nonresonant scattering introduced by the Raman light field.

The ability to couple electronic and motional states by the Raman excitation was tested by comparing Rabi frequencies on the carrier and on the first blue sideband with noncopropagating beams (from NW and NE) illuminating an ion initially prepared in the motional ground state. The two Raman beams enclose a 90° angle such that the residual momentum transfer is optimized for the axial direction. From the ratio of the Rabi frequencies, we directly infer the Lamb-Dicke parameter to be $\eta=0.216(2)$, in good agreement with the theory.

VI. COHERENCE PROPERTIES OF THE $^{43}Ca^+$ HYPERFINE QUBIT

Applying the methods described before, we investigated quantum-information storage capabilities of the $^{43}Ca^+$ hyper-

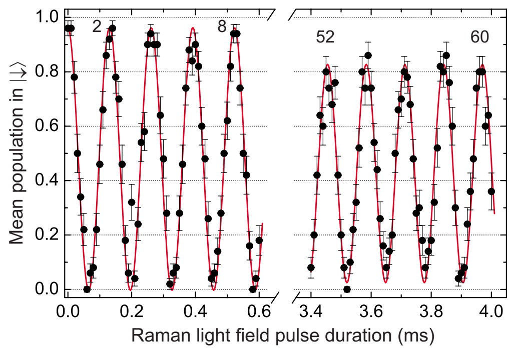

FIG. 7. (Color online) Rabi oscillations on the $^{43}Ca^+$ hyperfine qubit induced by a colinear Raman light field. Each data point represents 50 individual measurements. As for the microwave excitation, we fitted a sinusoidal function to the data set from 0 to 600 μs, which yields a fringe amplitude $A=0.97(1)$, a π time of $\tau_\pi=65.3(1)$ μs, and a fringe center at $y_0=0.479(5)$. Fitting to the data points beyond 3.4 ms, a small offset phase had to be introduced and τ_π adjusted to 63.8(2) μs, indicating a small increase of the Raman light power during the measurement. The amplitude reduced to $A=0.80(2)$, and the fringe center dropped to $y_0=0.428(7)$. A comparison with microwave excitation reveals imperfections caused by spontaneous scattering and laser amplitude fluctuations.

fine qubit. Limitations on the coherence time arise from both spontaneous scattering events and dephasing [16]. For the hyperfine qubit, spontaneous decay is negligible since the lifetime of the involved states can be considered as infinite for all practical purposes. Scattering can be induced though by imperfectly switched off laser beams. To judge the importance of this effect, we prepared the ion in the $|\downarrow\rangle$ state. After waiting for a time τ_d, we transferred the population with two subsequent π pulses to $D_{5/2}(F=6, m_F=0)$ and $D_{5/2}(F=4, m_F=2)$. Ideally no fluorescence should be observed. Figure 8 shows how an initial $|\downarrow\rangle$ population of 0.97 decreases with increasing waiting time τ_d. An exponential decay fit yields a time constant of 410 ms. This observation can be explained by imperfectly switching off the cooling laser at a wavelength of 397 nm by one single-pass AOM only. For every blue photon that is scattered, the ion will be lost from the state $|\downarrow\rangle$ with a high probability by decaying to one of the other $S_{1/2}$ Zeeman states. This complication was avoided by using a mechanical shutter completely switching off the Doppler cooling laser in all Rabi and Ramsey experiments lasting for 50 ms and longer.

Decoherence due to dephasing does not alter the state occupation probabilities. Instead, the phase information between driving field and the qubit gets lost. A powerful method to characterize this effect consists in measuring fringe amplitude in Ramsey phase experiments. Here a superposition of the two qubit states is created by a $\pi/2$ pulse. After a waiting time τ_R, during which the qubit evolves freely, a second $\pi/2$ pulse is applied. By scanning the Ramsey phase ϕ of the second pulse, a sinusoidal fringe pattern is observed whose fringe amplitude is a measure of the coherence.

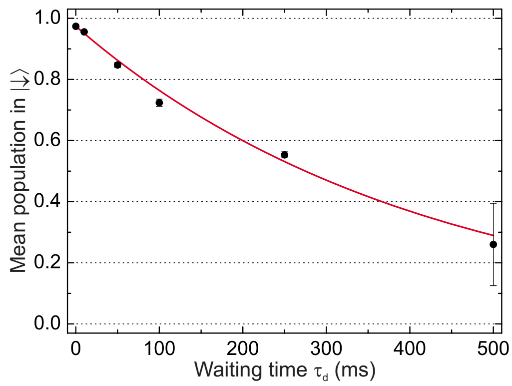

FIG. 8. (Color online) Measurement of the qubit state $|\downarrow\rangle$-population probability after a waiting time τ_d. Single-photon scattering events induced by residual light at 397 nm lead to a transfer of population from the $|\downarrow\rangle$ state to other Zeeman states in the ground-state manifold. The solid line is an exponential fit with a decay time constant of 410 ms.

For the Raman light field, the relevant phase is not only determined by the radio frequency devices supplying the AOMs creating the 3.2 GHz splitting, but also by the relative optical path length of the red and blue beamlines. In general, the absolute phase is not of interest as long as it does not change during the experiment. The setup can be considered as an interferometer whose sensitivity is also dependent on its size. In case of a copropagating Raman light field, the two beamlines are recombined on a polarizing beam splitter directly after the relative frequency generation. Here the interferometer encloses an area of about 0.04 m^2, whereas the

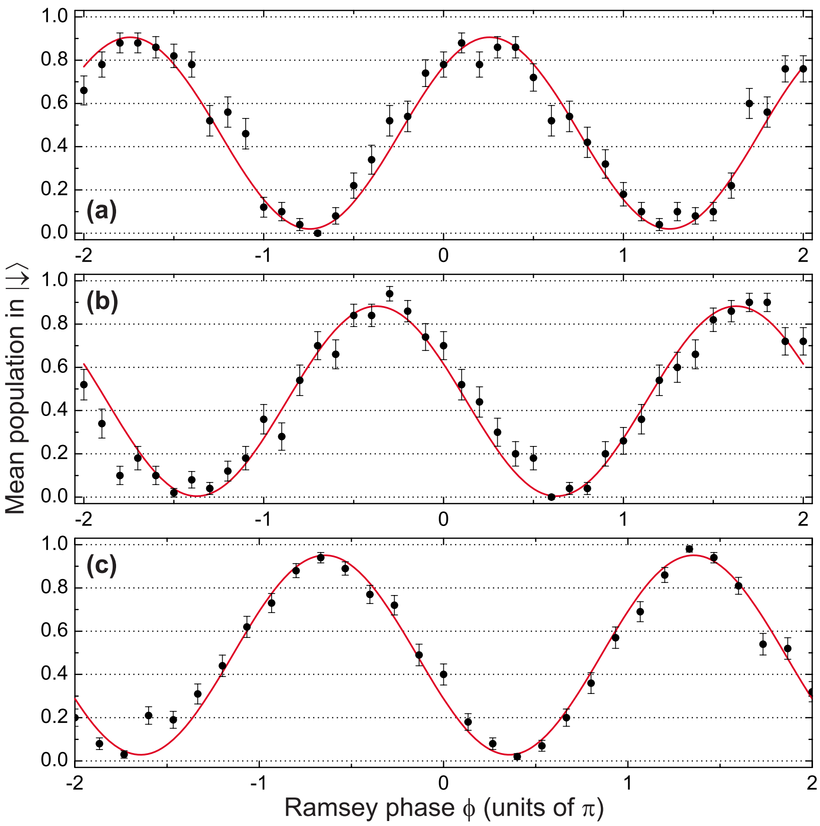

FIG. 9. (Color online) Ramsey phase experiments on the $^{43}Ca^+$ hyperfine qubit at a magnetic field of 3.4 G with a Ramsey waiting time τ_R set to 100 ms. The data were taken with three different driving fields. (a) Microwave drive with $\tau_\pi=19$ μs, (b) copropagating Raman light field with $\tau_\pi=20$ μs, and (c) noncopropagating Raman light field where $\tau_\pi=23$ μs. The fringe amplitudes are determined by weighted least-squares sinusoidal fits with amplitude A, offset phase Φ_0, and fringe center y_0 as free parameters. This yields fringe amplitudes of 0.886(17), 0.879(16), and 0.922(13), respectively. Dephasing by interferometric instabilities does not limit the experiments on these time scales. For Ramsey times beyond 100 ms, we observed a further decay of the fringe amplitude.

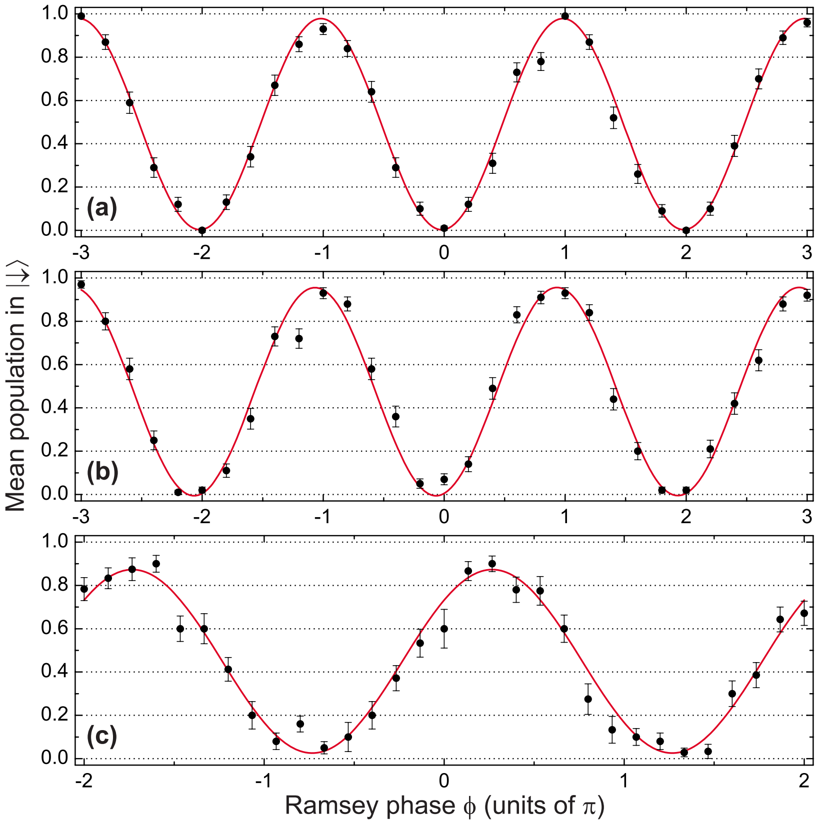

FIG. 10. (Color online) Ramsey phase experiments on the $^{43}Ca^+$ hyperfine qubit with microwave excitation at a magnetic field of 0.5 G. (a) A scan with $\tau_R = 50\ \mu s$ results an amplitude of 0.976(4) and demonstrates the ability of state initialization, manipulation, and readout. (b) For a Ramsey time $\tau_R = 200$ ms, the amplitude is 0.962(11). (c) For a Ramsey time of $\tau_R = 1$ s, a fringe amplitude of 0.847(21) was measured. Here the measurement time was about 90 min. The reduction of the amplitude is attributed to the residual sensitivity of 1.2 Hz/mG to ambient magnetic field fluctuations.

noncopropagating beams enclosing an area of about 0.15 m^2. In order to see whether the experiment would be limited by this effect, we investigated three different configurations.

Figure 9 shows the resulting Ramsey fringe patterns when driving the hyperfine qubit with (a) a microwave, (b) a copropagating Raman field, and (c) a noncopropagating Raman field. The Ramsey waiting time τ_R was set to 100 ms, the $\pi/2$ pulses having a duration of about 20 μs. Each data point represents either 50 or 100 measurements. The error bars indicate statistical errors and are used as weights when fitting the function $f(\phi) = \frac{A}{2}\sin(\phi + \phi_0) + y_0$ to the data in order to determine the fringe amplitude A. The parameters y_0 and ϕ_0 are also free fit parameters, but are not further considered. For the different excitation schemes, we find fringe amplitudes of 0.886(17), 0.879(16), and 0.922(13), respectively. From this we conclude that errors introduced by interferometric instabilities in generating the Raman beams do not limit our experiment on time scales up to 100 ms. For longer Ramsey times, we observed a further decay of fringe amplitude, which we attribute to dephasing. These measurements were performed at a magnetic field of 3.4 G. For small magnetic fields, the residual qubit sensitivity to magnetic field fluctuations increases linearly with a slope of 2.4 kHz/G^2. Therefore we reduced the magnetic field to 0.5 G and repeated the measurement with the microwave field. The resulting fringe patterns for three different Ramsey times τ_R are depicted in Fig. 10. A short waiting time of $\tau_R = 50\ \mu s$ results in a fringe pattern amplitude of (a) 0.976(4). This demonstrates the ability of reliable state initialization, readout, and single-qubit gate operation for the $^{43}Ca^+$ hyperfine qubit at low magnetic fields. For a Ramsey time of $\tau_R = 200$ ms we still obtain a fringe amplitude of (b) 0.962(11). A drop in amplitude to (c) 0.847(21) is observed only after increasing the Ramsey waiting time to $\tau_R = 1$ s.

Typically, the coherence time is defined as the Ramsey time for which the fringe amplitude A has dropped to a value of $1/e$. Extrapolation of our measurements would lead to a coherence time on the order of about 6.0 s assuming an exponential decay and 2.5 s for Gaussian decay. Comparing the measurements at 3.4 G and 0.5 G, we conclude that the main limitation to the coherence time comes from the residual sensitivity of the qubit at finite fields. Further improvements can be made by means of active magnetic field stabilization and passive shielding. In addition, rephasing can be achieved by an intermediate spin-echo pulse that exchanges the populations of the two qubit levels.

VII. SUMMARY AND DISCUSSION

In conclusion, we have discussed and demonstrated various experimental techniques for high-fidelity QIP with $^{43}Ca^+$ ions. These techniques were applied for measuring the quantum-information storage capabilities of the hyperfine qubit in a noisy environment to be many seconds. Furthermore, we demonstrated that interferometric instabilities due to Raman frequency creation do not limit the phase coherence on time scales up to 100 ms. For most experimental steps, use of the quadrupole transition laser is crucial for our scheme. It seems straightforward to apply these techniques to strings of ions without compromising the error rate. From other experiments with $^{40}Ca^+$ ions, we already have experimental evidence that high-fidelity two-qubit operations are possible for the optical qubits [20]. It will be interesting to explore how these can be combined with the long storage times found here by swapping quantum information between hyperfine and optical qubits.

ACKNOWLEDGMENTS

We gratefully acknowledge the support of the European network SCALA, the Institut für Quanteninformation GmbH, DTO, and IARPA.

[1] J. I. Cirac and P. Zoller, Phys. Rev. Lett. **74**, 4091 (1995).
[2] D. Leibfried, R. Blatt, C. Monroe, and D. Wineland, Rev. Mod. Phys. **75**, 281 (2003).
[3] D. Leibfried, E. Knill, S. Seidelin, J. Britton, R. B. Blakestad, J. Chiaverini, D. B. Hume, W. M. Itano, J. D. Jost, C. Langer *et al.*, Nature (London) **438**, 639 (2005).
[4] K.-A. Brickman, P. C. Haljan, P. J. Lee, M. Acton, L. Deslauriers, and C. Monroe, Phys. Rev. A **72**, 050306(R) (2005).
[5] P. C. Haljan, P. J. Lee, K.-A. Brickman, M. Acton, L. Deslauriers, and C. Monroe, Phys. Rev. A **72**, 062316 (2005).
[6] F. Schmidt-Kaler, H. Häffner, M. Riebe, S. Gulde, G. P. T. Lancaster, T. Deuschle, C. Becher, C. F. Roos, J. Eschner, and R. Blatt, Nature (London) **422**, 408 (2003).
[7] M. Riebe, H. Häffner, C. F. Roos, W. Hänsel, J. Benhelm, G. P. T. Lancaster, T. W. Körber, C. Becher, F. Schmidt-Kaler, D. F. V. James *et al.*, Nature (London) **429**, 734 (2004).
[8] H. Häffner, W. Hänsel, C. F. Roos, J. Benhelm, D. C. al Kar, M. Chwalla, T. Körber, U. D. Rapol, M. Riebe, P. O. Schmidt *et al.*, Nature (London) **438**, 643 (2005).
[9] L. Aolita, K. Kim, J. Benhelm, C. F. Roos, and H. Häffner, Phys. Rev. A **76**, 040303(R) (2007).
[10] F. Arbes, M. Benzing, T. Gudjons, F. Kurth, and G. Werth, Z. Phys. D: At., Mol. Clusters **31**, 27 (1994).
[11] J. Benhelm, G. Kirchmair, U. Rapol, T. Körber, C. F. Roos, and R. Blatt, Phys. Rev. A **75**, 032506 (2007).
[12] S. Gulde, D. Rotter, P. Barton, F. Schmidt-Kaler, R. Blatt, and W. Hogervorst, Appl. Phys. B: Lasers Opt. **73**, 861 (2001).
[13] D. M. Lucas, A. Ramos, J. P. Home, M. J. McDonnell, S. Nakayama, J. P. Stacey, S. C. Webster, D. N. Stacey, and A. M. Steane, Phys. Rev. A **69**, 012711 (2004).
[14] F. Schmidt-Kaler, H. Häffner, S. Gulde, M. Riebe, G. P. T. Lancaster, T. Deuschle, C. Becher, W. Hänsel, J. Eschner, C. F. Roos *et al.*, Appl. Phys. B: Lasers Opt. **77**, 789 (2003).
[15] M. Notcutt, L.-S. Ma, J. Ye, and J. L. Hall, Opt. Lett. **30**, 1815 (2005).
[16] D. M. Lucas, B. C. Keitch, J. P. Home, G. Imreh, M. J. McDonnell, D. N. Stacey, D. J. Szwer, and A. M. Steane, e-print arXiv:0710.4421.
[17] C. Roos, T. Zeiger, H. Rohde, H. C. Nägerl, J. Eschner, D. Leibfried, F. Schmidt-Kaler, and R. Blatt, Phys. Rev. Lett. **83**, 4713 (1999).
[18] T. Lu, X. Miao, and H. Metcalf, Phys. Rev. A **71**, 061405(R) (2005).
[19] F. Mintert and C. Wunderlich, Phys. Rev. Lett. **87**, 257904 (2001).
[20] J. Benhelm, G. Kirchmair, C. F. Roos, and R. Blatt, Nat. Phys. **4**, 463 (2008).
[21] H.G. Dehmelt, Bull. Am. Phys. Soc. **20**, 60 (1975).

Measurement of the hyperfine structure of the $S_{1/2}$-$D_{5/2}$ transition in $^{43}Ca^+$

J. Benhelm,[1,*] G. Kirchmair,[1] U. Rapol,[1,†] T. Körber,[1] C. F. Roos,[1,2] and R. Blatt[1,2,‡]
[1]*Institut für Experimentalphysik, Universität Innsbruck, Technikerstr. 25, A-6020 Innsbruck, Austria*
[2]*Institut für Quantenoptik und Quanteninformation, Österreichische Akademie der Wissenschaften, Otto-Hittmair-Platz 1, A-6020 Innsbruck, Austria*

(Received 14 November 2006; published 15 March 2007)

The hyperfine structure of the $4s\ ^2S_{1/2}$-$3d\ ^2S_{5/2}$ quadrupole transition at 729 nm in $^{43}Ca^+$ has been investigated by laser spectroscopy using a single trapped $^{43}Ca^+$ ion. We determine the hyperfine structure constants of the metastable level as $A_{D_{5/2}}=3.8931(2)$ MHz and $B_{D_{5/2}}=4.241(4)$ MHz. The isotope shift of the transition with respect to $^{40}Ca^+$ was measured to be $\Delta_{\mathrm{iso}}^{43,40}=4134.713(5)$ MHz. We demonstrate the existence of transitions that become independent of the first-order Zeeman shift at nonzero low magnetic fields. These transitions might be better suited for building a frequency standard than the well-known "clock transitions" between $m=0$ levels at zero magnetic field.

DOI: 10.1103/PhysRevA.75.032506 PACS number(s): 31.30.Gs, 32.80.Pj, 42.62.Fi, 32.60.+i

I. INTRODUCTION

In recent years, optical frequency standards based on single trapped ions and neutral atoms held in optical lattices have made remarkable progress [1,2] towards achieving the elusive goal [3] of a fractional frequency stability of 10^{-18}. In $^{199}Hg^+$, $^{27}Al^+$, $^{171}Yb^+$, $^{115}In^+$, and $^{88}Sr^+$, optical frequencies of dipole-forbidden transitions have been measured [1,4–7]. Among the singly charged alkali-earth ions, the odd isotope $^{43}Ca^+$ has been discussed as a possible optical frequency standard [8,9] because of its nuclear spin $I=7/2$ giving rise to transitions $4s\ ^2S_{1/2}(F,m_F=0)\leftrightarrow 3d\ ^2D_{5/2}(F',m_{F'}=0)$ that are independent of the first-order Zeeman effect. While the hyperfine splitting of the $S_{1/2}$ ground state has been precisely measured [10], the hyperfine splitting of the metastable $D_{5/2}$ has been determined with a precision of only a few MHz so far [11]. A precise knowledge of the $S_{1/2}\leftrightarrow D_{5/2}$ transition is also of importance for quantum information processing based on $^{43}Ca^+$ [12]. In these experiments where quantum information is encoded in hyperfine ground states, the quadrupole transition can be used for initialization of the quantum processor and for quantum state detection by electron shelving.

This paper describes the measurement of the hyperfine constants of the $D_{5/2}$ level by probing the quadrupole transition of a single trapped ion with a narrow-band laser. Our results confirm previous measurements and reduce the error bars on $A_{D_{5/2}}$ and $B_{D_{5/2}}$ by more than three orders of magnitude. In addition, we precisely measure the isotope shift of the transition with respect to $^{40}Ca^+$.

With a precise knowledge of the hyperfine structure constants at hand, the magnetic field dependence of the $D_{5/2}$ Zeeman states is calculated by diagonalizing the Breit-Rabi Hamiltonian. It turns out that several transitions starting from one of the stretched states $S_{1/2}(F=4,m_F=\pm 4)$ become independent of the first-order Zeeman shift at field values of a few gauss. Transitions with vanishing differential Zeeman shifts at nonzero fields have been investigated in experiments with cold atomic gases [14] to achieve long coherence times and with trapped ions [15] for the purpose of quantum information processing. These transitions are also potentially interesting for building an optical frequency standard and have several advantages over $m_F=0\leftrightarrow m_{F'}=0$ transitions. We experimentally confirm our calculations by mapping the field dependence of one of these transitions.

II. EXPERIMENTAL SETUP

Our experiments are performed with a single $^{43}Ca^+$ ion confined in a linear Paul trap consisting of two tips and four blade-shaped electrodes [16]. A radio frequency voltage ($\nu_{\mathrm{rf}}=25.642$ MHz; $P_{\mathrm{rf}}=7$ W) is fed to a helical resonator and the up-converted signal is applied to one pair of blade electrodes while the other blade pair is held at ground. In such a way, a two-dimensional electric quadrupole field is generated which provides radial confinement for a charged particle if the radio frequency and amplitude are chosen properly. Two stainless steel tips are placed 5 mm mm apart in the trap's symmetry axis and are held at a positive voltage $U_{\mathrm{tips}}=1000$ V providing axial confinement. The electrodes are electrically isolated by Macor ceramic spacers which assure a 20 μm tolerance in the positioning of the four blades and the tip electrodes. For the parameters given above, the ion trap confines a $^{43}Ca^+$ ion in a harmonic potential with oscillation frequencies $\nu_{\mathrm{axial}}=1.2$ MHz and $\nu_{\mathrm{radial}}=4.2$ MHz in the axial and radial directions. Micromotion due to stray electric fields is compensated by applying voltages to two compensation electrodes. The correct compensation voltages are found by minimizing the Rabi frequency of the first micromotional sideband of the quadrupole transition for two different laser beam directions. The trap is housed in a vacuum chamber with a pressure of about 10^{-10} mbar.

Single $^{43}Ca^+$ ions are loaded from an isotope-enriched source (Oak Ridge National Laboratory; 81.1% $^{43}Ca^+$, 12.8% $^{40}Ca^+$, and 5.4% $^{44}Ca^+$) into the trap by isotope-selective two-step photoionization [17,18]. The first transition from the $4s\ ^1S_0$ ground state to the $4p\ ^1P_1$ excited state in neutral

*Electronic address: jan.benhelm@uibk.ac.at
†Present address: GE India Technology Center, Bangalore, India.
‡URL: http://www.quantumoptics.at

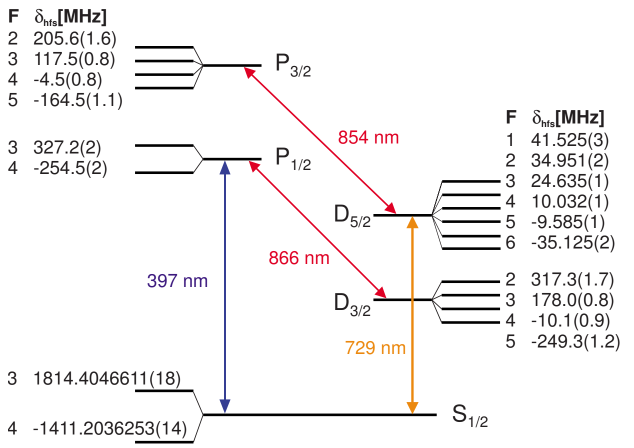

FIG. 1. (Color online) $^{43}\mathrm{Ca}^{+}$ level scheme showing the hyperfine splitting of the lowest energy levels. Hyperfine shifts δ_{hfs} of the levels are quoted in MHz (the splittings are taken from [10,11] and our own measurement). Laser light at 397 nm is used for Doppler cooling and detection; the lasers at 866 and 854 nm pump out the D states. An ultrastable laser at 729 nm is used for spectroscopy on the quadrupole transition.

calcium is driven by an external cavity diode laser in Littrow configuration at 423 nm. Its frequency is monitored by saturation spectroscopy on a calcium vapor cell held at a temperature of 300 °C and by a wavelength meter with a relative accuracy of 10 MHz. The second excitation step connecting the $4p\ ^1P_1$ state to continuum states requires light with a wavelength below 390 nm. In our experiment, it is driven by a free-running laser diode at 375 nm.

For laser cooling, a grating-stabilized diode laser is frequency-doubled to produce light at 397 nm for exciting the $S_{1/2} \leftrightarrow P_{1/2}$ transition (see Fig. 1). By means of polarization optics and an electro-optical modulator operated at 3.2 GHz, laser beams exciting the following transitions are provided:

Beam no.	Polarization	Transition
1, 2	π, σ^+	$S_{1/2}(F=4) \leftrightarrow P_{1/2}(F'=4)$
3	σ^+	$S_{1/2}(F=3) \leftrightarrow P_{1/2}(F'=4)$

Laser beams no. 1–3 are all switched on for Doppler cooling and fluorescence detection. We avoid coherent population trapping by lifting the degeneracy of the Zeeman sublevels with a magnetic field. To avoid optical pumping into the $D_{3/2}$ manifold repumping laser the light at 866 nm has to be applied. The repumping efficiency was improved by tuning the laser close to the $D_{3/2}(F=3) \leftrightarrow P_{1/2}(F'=3)$ transition frequency and redshifting part of the light by $-f_1$, $-f_1 - f_2$ with two acousto-optical modulators (AOMs) operating at frequencies $f_1 = 150$ MHz and $f_2 = 245$ MHz. In this manner, all hyperfine $D_{3/2}$ levels are resonantly coupled to one of the $P_{1/2}(F'=3,4)$ levels. Since the electronic g factor of the $D_{3/2}(F=3)$ level vanishes, coherent population trapping in this level needs to be avoided by either polarization-modulating the laser beam or by coupling the level to both $P_{1/2}(F'=3,4)$ levels. In our experiment, nonresonant light ($\delta \approx 190$ MHz) exciting the $D_{3/2}(F=3) \leftrightarrow P_{1/2}(F'=4)$ seems to be sufficient for preventing coherences from building up. After switching off laser beam no. 1, the ion is optically pumped into the state $S_{1/2}(F=4, m_F=4)$. The pumping efficiency is better than 95%.

All diode lasers are stabilized to Fabry-Pérot cavities. The cavity spacer is a block of Zerodur suspended in a temperature stabilized vacuum housing. For frequency tuning, one of the reference cavity mirrors is mounted using two concentric piezo transducers that are compensated for thermal drift. This allows frequency tuning of the lasers over several GHz while achieving low drift rates (typically <100 Hz/s) once the piezos have settled.

To set the magnitude and orientation of the magnetic field, a single $^{40}\mathrm{Ca}^{+}$ ion was loaded into the trap. The ambient magnetic B field was nulled by applying currents to magnetic field compensation coils so as to minimize the ion's fluorescence. After that, the magnetic field can be set to the desired value by sending a current through a pair of coils defining the quantization axis. All coils are powered by homemade current drivers having a relative drift of less than 2×10^{-5} in 24 h.

Light for the spectroscopy on the $S_{1/2} \leftrightarrow D_{5/2}$ quadrupole transition is generated by a Ti:sapphire laser stabilized to an ultrastable high finesse reference cavity (finesse $\mathcal{F} = 410\,000$) [13]. The free spectral range of the cavity was measured to be $\Delta_{\mathrm{FSR}} = 1933.07309(20)$ MHz by using a second independently stabilized laser and observing the beat note for the Ti:Sa laser locked to several different modes. From this measurement, also an upper limit of less than 50 Hz could be determined for the laser linewidth. The frequency drift of the 729 nm laser stabilized to the reference cavity is typically less than 0.5 Hz/s. By locking the laser to different modes of the reference cavity and by changing its frequency with AOMs we are able to tune the laser frequency in resonance with any transition between levels of $S_{1/2}$ and $D_{5/2}$ in $^{40}\mathrm{Ca}^{+}$ and $^{43}\mathrm{Ca}^{+}$. The radio frequencies applied to the AOMs are generated by a versatile frequency source based on direct digital synthesis.

Spectroscopy on the quadrupole transition is implemented using a pulsed scheme. In a first step, the ion is Doppler cooled and prepared in the $S_{1/2}(F=4, m_F=\pm 4)$ level by optical pumping. Then the ion is probed on the quadrupole transition by light at 729 nm. At the end of the experimental cycle, the ion's quantum state is detected by a quantum jump technique. For this, the cooling laser and the repumper at 866 nm are turned back on for a duration of 5 ms, projecting the ion onto either the fluorescing $S_{1/2}$ or the dark $D_{5/2}$ state. The light emitted by the ion is collected with a customized lens system ($NA = 0.27$, transmission $>95\%$) and observed on a photomultiplier tube and a CCD camera simultaneously. A threshold set for the number of photomultiplier counts discriminates between the two possibilities with high efficiency. Finally, the $D_{5/2}$ state population is pumped back to $S_{1/2}$ by means of another grating-stabilized diode laser operating at 854 nm. This measurement cycle is repeated a hundred times before setting the probe laser to a different frequency and repeating the experiments all over again.

In order to set the magnetic field precisely, we use a single $^{40}\mathrm{Ca}^{+}$ ion to determine the field strength by measuring the frequency splitting of the two transitions

$S_{1/2}(m=+1/2) \leftrightarrow D_{5/2}(m'=+5/2)$ and $S_{1/2}(m=+1/2) \leftrightarrow D_{5/2}(m'=-3/2)$. Stray magnetic fields oscillating at multiples of 50 Hz change the magnitude of the field by less than 2 mG over one period of the power line frequency. By synchronizing the experiments with the phase of the power line, ac-field fluctuations at multiples of 50 Hz are eliminated as a source of decoherence. As the duration of a single experiment typically is on the order of 20 ms, this procedure does not significantly slow down the repetition rate of the experiments.

III. RESULTS

A. Hyperfine coefficients for the $D_{5/2}$ state

The hyperfine structure splitting of the $S_{1/2}$ and $D_{5/2}$ states is determined by effective Hamiltonians [19] $H_{\rm hfs}^{(S_{1/2})} = hA_{S_{1/2}}\mathbf{I}\cdot\mathbf{J}$ and, assuming that J is a good quantum number,

$$H_{\rm hfs}^{(D_{5/2})} = hA_{D_{5/2}}\mathbf{I}\cdot\mathbf{J} + hB_{D_{5/2}}\frac{3(\mathbf{I}\cdot\mathbf{J})^2 + \frac{3}{2}(\mathbf{I}\cdot\mathbf{J}) - I(I+1)J(J+1)}{2I(2I-1)J(2J-1)} \tag{1}$$

operating on the hyperfine level manifolds of the ground and metastable state. Here h is Planck's constant and $A_{D_{5/2}}(A_{S_{1/2}})$ and $B_{D_{5/2}}$ are the hyperfine constants describing the magnetic dipole and electric quadrupole interactions in the $D_{5/2}$ ($S_{1/2}$) state; higher-order multipoles [20] are not taken into account. Terms arising from second-order perturbation theory [20] are expected to shift the levels by only negligible amounts as $(A_{D_{5/2}}\cdot A_{D_{3/2}})/\Delta_{\rm FS} \approx 100$ Hz where $\Delta_{\rm FS}$ denotes the fine-structure splitting of the D states.

In a nonzero magnetic field, the Hamiltonian (1) is replaced by

$$H^{(D_{5/2})} = H_{\rm hfs}^{(D_{5/2})} + g_{D_{5/2}}\mu_B\mathbf{J}\cdot\mathbf{B} + g_I'\mu_B\mathbf{I}\cdot\mathbf{B}, \tag{2}$$

where $g_{D_{5/2}}$ is the electronic g factor of the $D_{5/2}$ state and g_I' denotes the nuclear g factor. Figure 2 shows the resulting energy shifts of the Zeeman level caused by hyperfine and Zeeman interactions. The energies of the $S_{1/2}(F=4, m_F=\pm 4)$ levels used in our spectroscopic measurements are linearly shifted by $h\delta_\pm = \pm[g_{S_{1/2}}S + g_I'I]\mu_B B$ with $S=1/2$.

From earlier measurements and calculations of the isotope shift [21] and the hyperfine splitting of the $S_{1/2}$ [10] and the $D_{5/2}$ [11,22,23] states, the transition frequencies on the quadrupole transition in $^{43}Ca^+$ are known to within 20 MHz with respect to the transition in $^{40}Ca^+$. This enabled us to unambiguously identify the lines observed in spectra of the $S_{1/2}\leftrightarrow D_{5/2}$ transition. In a first series of measurements the ion was prepared in the state $S_{1/2}(F=4, m_F=+4)$ by optical pumping with σ_+-polarized light. There are fifteen transitions to the $D_{5/2}$ levels allowed by the selection rules for quadrupole transitions. Spectra were recorded on all of them with an excitation time of 500 μs in a magnetic field of about 3.40 G. In a second measurement series, after pumping the ion into $S_{1/2}(F=4, m_F=-4)$ another fifteen transitions were measured. To obtain the hyperfine constants of the $D_{5/2}$ state, we fitted the set of 30 transition frequencies by diagonalizing the Hamiltonian taking the hyperfine constants $A_{D_{5/2}}$, $B_{D_{5/2}}$, the magnetic field B, and a frequency offset as free parameters. The hyperfine constant $A_{S_{1/2}} = -806.402\,071\,6$ MHz was measured in [10]. The g factors $g_I' = 2.0503\times 10^{-4}$ and $g_{S_{1/2}} = 2.00225664$ were taken from [24,25]; $g_{D_{5/2}} = 1.2003(1)$ was measured by us in an experiment with a single $^{40}Ca^+$ ion. The fit yields

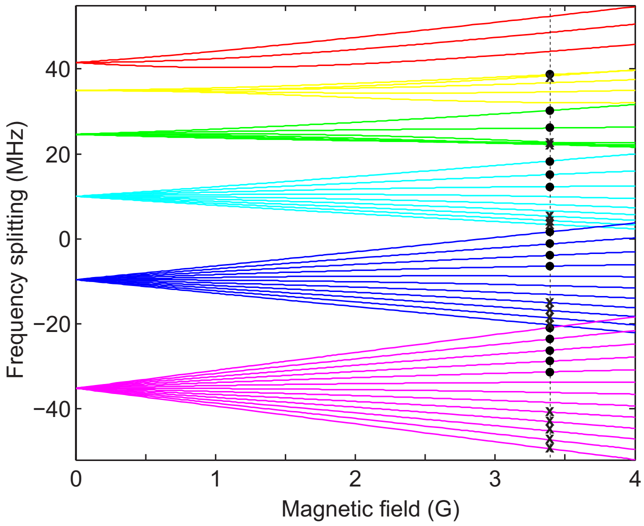

FIG. 2. (Color online) Hyperfine and Zeeman splitting of the $D_{5/2}$ state manifold calculated for hyperfine constants measured in our experiment. Filled circles (●) and crosses (×) mark states that can be excited starting from the $S_{1/2}(F=4)$ state with magnetic quantum number $m_F=+4$ ($m_F=-4$), respectively. The vertical dashed line indicates the magnetic field used for measuring the frequency shifts in the experiment.

$$A_{D_{5/2}} = 3.8931(2)\ \text{MHz},$$

$$B_{D_{5/2}} = 4.241(4)\ \text{MHz},$$

where the standard uncertainty of the determination is added in parentheses. The average deviation between the measured and the fitted frequencies is about 1 kHz. If $g_{D_{5/2}}$ is used as a free parameter, we obtain $g_{D_{5/2}} = 1.2002(2)$ and the fitted values of the hyperfine constants do not change. Also, adding a magnetic octupole interaction [20] to the hyperfine Hamiltonian does not change the fit values of the hyperfine constants.

B. Isotope shift

After having determined the values of $A_{D_{5/2}}$ and $B_{D_{5/2}}$, the line center of the $^{43}Ca^+$ $S_{1/2}\leftrightarrow D_{5/2}$ transition can be found. By comparing the transition frequencies in $^{43}Ca^+$ and in $^{40}Ca^+$, the isotope shift $\Delta_{\rm iso}^{43,40} = \nu_{43} - \nu_{40}$ is determined. Switching the laser from ν_{40} to ν_{43} is achieved by locking the laser to a TEM_{00} cavity mode three modes higher

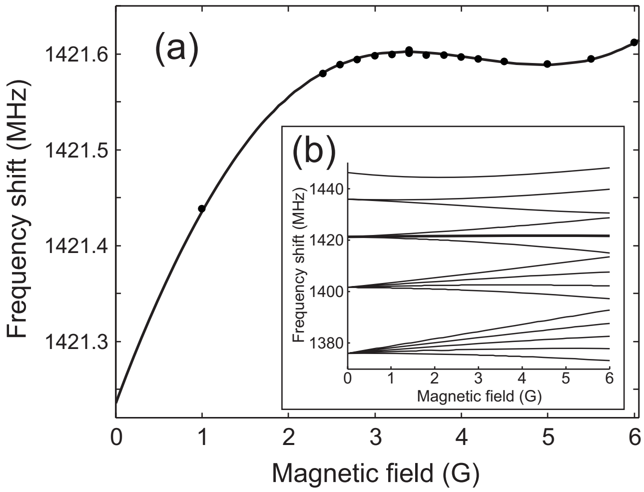

FIG. 3. (a) Frequency dependence of the $S_{1/2}(F=4,m_F=4) \leftrightarrow D_{5/2}(F=4,m_F=3)$ transition frequency for low magnetic fields. The transition frequency becomes field-independent at $B=3.38$ G and $B=4.96$ G with a second-order Zeeman shift of ± 16 kHz/G^2. The measured data are not corrected for the drift of the reference cavity which may lead to errors in the shift of about 1–2 kHz. To match the data with the theoretical curve based on the previously measured values of $A_{D_{5/2}}$ and $B_{D_{5/2}}$, an overall frequency offset was adjusted. (b) Calculated shift of the fifteen allowed transitions starting from $S_{1/2}(F=4,m_F=4)$. The thick line shows the transition to the state $D_{5/2}(F'=4,m_{F'}=3)$.

$(\nu_{n+3}=\nu_n+3\Delta_{\mathrm{FSR}})$ than for ^{40}Ca$^+$ and adjusting its frequency with an AOM. For the isotope shift, we obtain

$$\Delta_{\mathrm{iso}}^{43,40}=4134.713(5)\ \mathrm{MHz}.$$

This value is in good agreement with a previous measurement [$\Delta_{\mathrm{iso}}^{43,40}$=4129(18) MHz [10]]. Frequency drift between the measurements, accuracy of the reference cavity's free spectral range Δ_{FSR}, and the uncertainty in the determination of the exact line centers limit the accuracy of our measurement.

C. Magnetic field independent transitions

Given the measured values of the hyperfine coefficients $A_{D_{5/2}}$ and $B_{D_{5/2}}$, we calculate that there are seven transitions starting from the stretched states $S_{1/2}(F=4,m_F=\pm 4)$ that have no first order Zeeman effect for suitably chosen magnetic fields in the range of 0–6 G. These transitions are useful as they offer the possibility of measuring the linewidth of the spectroscopy laser in the presence of magnetic field noise. To demonstrate this property, we chose the transition $S_{1/2}(F=4,m_F=4) \leftrightarrow D_{5/2}(F'=4,m_{F'}=3)$ which has the lowest second-order dependence on changes in the magnetic field. We measured the change in transition frequency for magnetic fields ranging from one to six gauss as shown in Fig. 3. The black curve is a theoretical calculation based on the measurement of the hyperfine constants. For the data, the frequency offset is the only parameter that was adjusted to match the calculated curve. Both the experimental data and the model show that the transition frequency changes by less than 400 kHz when the field is varied from 0 to 6 G. The transition frequency becomes field-independent at about $B=3.38$ G with a second order B-field dependency of -16 kHz/G^2, which is six times less than the smallest coefficient for a clock transition based on $m_F=0 \leftrightarrow m_{F'}=0$ transitions at zero field. At $B=4.96$ G the linear Zeeman shift vanishes again.

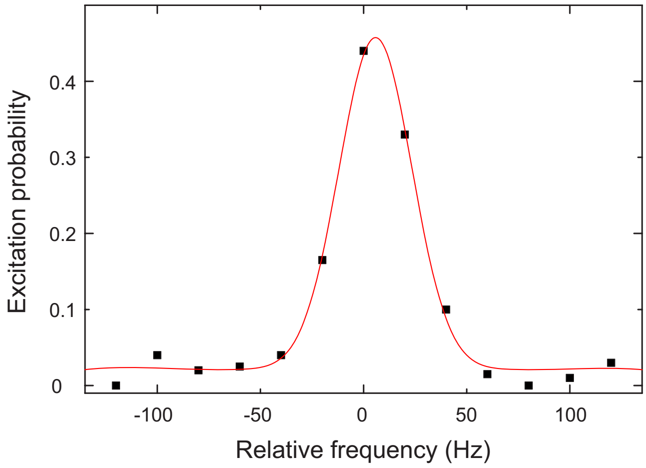

FIG. 4. (Color online) Frequency scan over the transition $S_{1/2}(F=4,m_F=4) \leftrightarrow D_{5/2}(F'=4,m_{F'}=3)$ with an interrogation time of 100 ms. A Gaussian fit (solid line) determines a width of 42 Hz which is dominated by the linewidth of the spectroscopy laser at 729 nm.

We used the field independence of this transition for investigating the phase coherence of our spectroscopy laser. For this, we set the magnetic field to 3.39 G and recorded an excitation spectrum of the transition by scanning the laser over the line with an interrogation time of 100 ms. The result is depicted in Fig. 4. A Gaussian fit gives a linewidth of 42 Hz. The observed linewidth is not yet limited by the lifetime τ of the $D_{5/2}$ state (τ=1.17 s) or by the chosen interrogation time. Line broadening caused by magnetic field fluctuations can be excluded on this transition. Also, ac-Stark shifts are expected to play only a minor role. Therefore, we believe that the observed linewidth is mostly related to the linewidth of the exciting laser.

IV. SUMMARY AND DISCUSSION

The hyperfine structure of the $D_{5/2}$ level in ^{43}Ca$^+$ has been observed and precisely measured by observing frequency intervals of the $S_{1/2}(F=4,m_F=\pm 4) \leftrightarrow D_{5/2}(F'=2\ldots 6,m_{F'})$ transitions at nonzero field. These measurements yielded values for the hyperfine constants $A_{D_{5/2}}$ and $B_{D_{5/2}}$ as well as a determination of the isotope shift of the quadrupole transition with respect to ^{40}Ca$^+$. A diagonalization of the $D_{5/2}$ state's Hamiltonian showed that several transitions exist which become magnetic-field independent at small but nonzero values of B. These transitions are of practical importance for probing the laser linewidth of the spectroscopy laser and for monitoring the drift rate of its reference cavity. For the purpose of building an optical frequency standard based on $^{43}Ca^{+}$ [8,9], they might be superior to the transitions $S_{1/2}(F, m_F=0) \leftrightarrow D_{5/2}(F', m_{F'}=0)$ for the following reasons: (i) The initialization step requires only optical pumping to the stretched state $S_{1/2}(F=4, m_F=\pm 4)$ which can be conveniently combined with resolved sideband cooling to the motional ground state of the external potential. (ii) The magnetic field can be exactly set to the value where the transition becomes field-independent while still maintaining a well-defined quantization axis. (iii) The second-order Zeeman effect can be reduced to a value that is six times smaller than what can be achieved for the best $m_F=0 \leftrightarrow m_{F'}=0$ "clock transition." Still, we are somewhat cautious about the usefulness of $^{43}Ca^{+}$ as an optical frequency standard as compared to other candidate ions. While the rather small hyperfine splitting of the metastable state has the nice property of providing field-independent transitions at low magnetic fields, it risks also being troublesome as the induced level splitting is about the same size as typical trap drive frequencies. Improperly balanced oscillating currents in the trap electrodes might give rise to rather large ac-magnetic level shifts.

ACKNOWLEDGMENTS

We wish to acknowledge support by the Institut für Quanteninformation GmbH and by the U.S. Army Research Office. We acknowledge P. Pham's contribution to the development of a versatile source of shaped rf pulses.

[1] W. H. Oskay *et al.*, Phys. Rev. Lett. **97**, 020801 (2006).
[2] M. M. Boyd *et al.*, e-print physics/0611067.
[3] H. G. Dehmelt, IEEE Trans. Instrum. Meas. **31**, 83 (1982).
[4] J. C. Bergquist (private communication).
[5] T. Schneider, E. Peik, and Chr. Tamm, Phys. Rev. Lett. **94**, 230801 (2005).
[6] J. v. Zanthier *et al.*, Opt. Lett. **25**, 1729 (2000).
[7] H. S. Margolis *et al.*, Science **306**, 1355 (2004).
[8] C. Champenois *et al.*, Phys. Lett. A **331**, 298 (2004).
[9] M. Kajita, Y. Li, K. Matsubara, K. Hayasaka, and M. Hosokawa, Phys. Rev. A **72**, 043404 (2005).
[10] F. Arbes, M. Benzing, Th. Gudjons, F. Kurth, and G. Werth, Z. Phys. D: At., Mol. Clusters **31**, 27 (1994).
[11] W. Nörtershäuser *et al.*, Eur. Phys. J. D **2**, 33 (1998).
[12] A. Steane, Appl. Phys. B: Lasers Opt. **64**, 623 (1997).
[13] M. Notcutt, L.-S. Ma, J. Ye, and J. L. Hall, Opt. Lett. **30**, 1815 (2005).
[14] D. M. Harber, H. J. Lewandowski, J. M. McGuirk, and E. A. Cornell, Phys. Rev. A **66**, 053616 (2002).
[15] C. Langer *et al.*, Phys. Rev. Lett. **95**, 060502 (2005).
[16] F. Schmidt-Kaler *et al.*, Appl. Phys. B: Lasers Opt. **77**, 789 (2003).
[17] D. M. Lucas, A. Ramos, J. P. Home, M. J. McDonnell, S. Nakayama, J. P. Stacey, S. C. Webster, D. N. Stacey, and A. M. Steane, Phys. Rev. A **69**, 012711 (2004).
[18] S. Gulde, D. Rotter, P. Barton, F. Schmidt-Kaler, R. Blatt, and W. Hogervorst, Appl. Phys. B: Lasers Opt. **73**, 861 (2001).
[19] L. Armstrong, *Theory of the Hyperfine Structure of Free Atoms* (John Wiley & Sons, New York, 1971).
[20] C. Schwartz, Phys. Rev. **97**, 380 (1955).
[21] F. Kurth, T. Gudjons, B. Hilbert, T. Reisinger, G. Werth, and A.-M. Mårtensson-Pendrill, Z. Phys. D: At., Mol. Clusters **34**, 227 (1995).
[22] B. K. Sahoo *et al.*, J. Phys. B **36**, 1899 (2003).
[23] K. Z. Yu, L. J. Wu, B. C. Gou, and T. Y. Shi, Phys. Rev. A **70**, 012506 (2004).
[24] N. J. Stone, At. Data Nucl. Data Tables **90**, 75 (2005).
[25] G. Tommaseo, T. Pfeil, G. Revalde, G. Werth, P. Indelicato, and J. P. Desclaux, Eur. Phys. J. D **25**, 113 (2003).

Erratum: Measurement of the hyperfine structure of the $S_{1/2}$-$D_{5/2}$ transition in $^{43}Ca^{+}$ [Phys. Rev. A 75, 032506 (2007)]

J. Benhelm, G. Kirchmair, U. Rapol, T. Körber, C. F. Roos, and R. Blatt

(Received 4 April 2007; published 18 April 2007)

DOI: 10.1103/PhysRevA.75.049901 PACS number(s): 31.30.Gs, 32.80.Pj, 42.62.Fi, 32.60.+i, 99.10.Cd

By mistake, the correct sign factors appearing in front of the measured hyperfine constants $A_{D_{5/2}}$ and $B_{D_{5/2}}$ were omitted. The correct values are

$$A_{D_{5/2}} = -3.8931(2)\ \text{MHz},$$

$$B_{D_{5/2}} = -4.241(4)\ \text{MHz}.$$

This correction does not affect the analysis of the measured spectral lines that the hyperfine structure determination is based on.

Bibliography

[1] P. Benioff: The computer as a physical system: A microscopic quantum mechanical Hamiltonian model of computers as represented by Turing machines. *J. Stat. Phys.* **22**, 563 (1980)

[2] P. Benioff: Quantum mechanical models of Turing machines that dissipate no energy. *Phys. Rev. Lett.* **48**, 1581 (1982)

[3] R. Feynman: Simulating physics with computers. *Int. J. Theoret. Phys.* **21:467** (1982)

[4] R. Feynman: Quantum mechanical computers. *Opt. News* **11**, 11 (1985)

[5] P. W. Shor: Algorithms for quantum computation: discrete logarithms and factoring. In *Proceedings of the 35th Annual Symposium on Foundations of Computer Science, Santa Fe, NM, Nov. 20-22, IEEE Computer Society Press, pp. 124–134* (1994)

[6] C. H. Bennett, G. Brassard, & N. D. Mermin: Quantum cryptography without Bell's theorem. *Phys. Rev. Lett.* **68**, 557 (1992)

[7] A. K. Ekert: Quantum cryptography based on Bell's theorem. *Phys. Rev. Lett.* **67**, 661 (1991)

[8] L. K. Grover: A fast quantum mechanical algorithm for database search. In *Proceedings, 28th Annual ACM Symposium on the Theory of Computing (STOC)*, pages 212–219 (1996)

[9] P. W. Shor: Scheme for reducing decoherence in quantum computer memory. *Phys. Rev. A* **52**, R2493 (1995)

[10] A. M. Steane: Error correcting codes in quantum theory. *Phys. Rev. Lett.* **77**, 793 (1996)

[11] P. Shor: Fault-tolerant quantum computation. *37th Annual Symposium on Foundations of Computer Science (FOCS '96) and arXiv:quant-ph/9605011v2* (1996)

[12] E. Knill: Quantum computing with realistically noisy devices. *Nature* **434**, 39 (2005)

[13] R. Raussendorf & J. Harrington: Fault-tolerant quantum computation with high threshold in two dimensions. *Phys. Rev. Lett.* **98**, 190504 (2007)

[14] B. W. Reichardt: Improved ancilla preparation scheme increases fault-tolerant threshold. *arXiv:quant-ph/0406025v1* (2004)

[15] D. P. DiVincenzo: The physical implementation of quantum computation. *Fortschr. Phys.* **48**, 771 (2000)

[16] N. A. Gershenfeld & I. L. Chuang: Bulk spin-resonance quantum computation. *Science* **275**, 350 (1997)

[17] B. E. Kane: A silicon-based nuclear spin quantum computer. *Nature* **393**, 133 (1998)

[18] D. Loss & D. P. DiVincenzo: Quantum computation with quantum dots. *Phys. Rev. A* **57**, 120 (1998)

[19] R. Hanson, L. P. Kouwenhoven, J. R. Petta, S. Tarucha, & L. M. K. Vandersypen: Spins in few-electron quantum dots. *Rev. Mod. Phys.* **79**, 1217 (2007)

[20] Y. Makhlin, G. Schön, & A. Shnirman: Quantum-state engineering with Josephson-junction devices. *Rev. Mod. Phys.* **73**, 357 (2001)

[21] E. Knill, R. Laflamme, & G. J. Milburn: A scheme for efficient quantum computation with linear optics. *Nature* **409**, 46 (2001)

[22] T. Pellizzari, S. A. Gardiner, J. I. Cirac, & P. Zoller: Decoherence, continuous observation, and quantum computing: A Cavity QED Model. *Phys. Rev. Lett.* **75**, 3788 (1995)

[23] H. J. Briegel, T. Calarco, D. Jaksch, J. Cirac, & P. Zoller: Quantum computing with neutral atoms. *J. of Mod. Opt.* **47**, 415 (2000)

[24] I. H. Deutsch, G. K. Brennen, & P. S. Jessen: Quantum computing with neutral atoms in an optical lattice. *Fortschr. Phys.* **48**, 925 (2000)

[25] L. M. K. Vandersypen & I. L. Chuang: NMR techniques for quantum control and computation. *Rev. Mod. Phys.* **76**, 1037 (2004)

[26] M. Steffen, M. Ansmann, R. C. Bialczak, N. Katz, E. Lucero, R. McDermott, M. Neeley, E. M. Weig, A. N. Cleland, & J. M. Martinis: Measurement of the entanglement of two superconducting qubits via state tomography. *Science* **313**, 1423 (2006)

[27] J. H. Plantenberg, P. C. de Groot, C. J. P. M. Harmans, & J. E. Mooij: Demonstration of controlled-NOT quantum gates on a pair of superconducting quantum bits. *Nature* **447**, 836 (2007)

[28] R. J. Schoelkopf & S. M. Girvin: Wiring up quantum systems. *Nature* **451**, 664 (2008)

[29] K. H. Kingdon: A method for the neutralization of electron space charge by positive ionization at very low gas pressures. *Phys. Rev.* **21**, 408 (1923)

[30] F. M. Penning: Glow discharge between coaxial cylinders at low pressures in an axial magnetic field. *Physica* **3**, 873 (1936)

[31] W. Paul, O. Osberghaus, & E. Fischer: Ein Ionenkäfig. *Forschungsberichte des Wirtschafts- und Verkehrsministerium Nordrhein-Westfalen* **415** (1958)

[32] W. Paul & H. Steinwedel: Ein neues Massenspektrometer ohne Magnetfeld. *Z. Naturforschung* **8a**, 448 (1953)

[33] W. Neuhauser, M. Hohenstatt, P. E. Toschek, & H. Dehmelt: Localized visible Ba^+ mono-ion oscillator. *Phys. Rev. A* **22**, 1137 (1980)

[34] D. J. Wineland & W. M. Itano: Laser cooling of atoms. *Phys. Rev. A* **21**, 1521 (1979)

[35] H. G. Dehmelt: Mono-ion oscillator as potential ultimate laser frequency standard. *IEEE Trans. Instr. Meas.* **31**, 83 (1982)

[36] K. Blaum: High-accuracy mass spectrometry with stored ions. *Phys. Rep.* **425**, 1 (2006)

[37] D. Wineland, J. Bergquist, W. Itano, & R. Drullinger: Double-resonance and optical-pumping experiments on electromagnetically confined, laser-cooled ions. *Opt. Lett.* **5**, 254 (1980)

[38] W. Nagourney, J. Sandberg, & H. Dehmelt: Shelved optical electron amplifier: Observation of quantum jumps. *Phys. Rev. Lett.* **56**, 2797 (1986)

[39] T. Sauter, W. Neuhauser, R. Blatt, & P. E. Toschek: Observation of quantum jumps. *Phys. Rev. Lett.* **57**, 1696 (1986)

[40] J. C. Bergquist, R. G. Hulet, W. M. Itano, & D. J. Wineland: Observation of quantum jumps in a single atom. *Phys. Rev. Lett.* **57**, 1699 (1986)

[41] J. J. Bollinger, D. J. Heinzen, W. M. Itano, S. L. Gilbert, & D. J. Wineland: A 303 MHz frequency standard based on trapped Be^+ ions. *IEEE Trans. Instr. Meas.* **40**, 126 (1991)

[42] F. Diedrich, E. Peik, J. M. Chen, W. Quint, & H. Walther: Observation of a phase transition of stored laser-cooled ions. *Phys. Rev. Lett.* **59**, 2931 (1987)

[43] D. J. Wineland, J. C. Bergquist, W. M. Itano, J. J. Bollinger, & C. H. Manney: Atomic ion Coulomb clusters in an ion trap. *Phys. Rev. Lett.* **59**, 2935 (1987)

[44] M. C. Raizen, J. C. Bergquist, J. M. Gilligan, W. M. Itano, & D. J. Wineland: Linear trap for high-accuracy spectroscopy of stored ions. *J. of Mod. Opt.* **39**, 233 (1992)

[45] M. G. Raizen, J. M. Gilligan, J. C. Bergquist, W. M. Itano, & D. J. Wineland: Ionic crystals in a linear Paul trap. *Phys. Rev. A* **45**, 6493 (1992)

[46] J. I. Cirac & P. Zoller: Quantum computations with cold trapped ions. *Phys. Rev. Lett.* **74**, 4091 (1995)

[47] C. Monroe, D. M. Meekhof, B. E. King, W. M. Itano, & D. J. Wineland: Demonstration of a fundamental quantum logic gate. *Phys. Rev. Lett.* **75**, 4714 (1995)

[48] Army Research Office: ARDA quantum computation roadmap. *http://qist.lanl.gov* (2004)

[49] C. A. Sackett, D. Kielpinski, B. E. King, C. Langer, V. Meyer, C. J. Myatt, M. Rowe, Q. A. Turchette, W. M. Itano, D. J. Wineland, & C. Monroe: Experimental entanglement of four particles. *Nature* **404**, 256 (2000)

[50] B. DeMarco, A. Ben-Kish, D. Leibfried, V. Meyer, M. Rowe, B. M. Jelenković, W. M. Itano, J. Britton, C. Langer, T. Rosenband, & D. J. Wineland: Experimental demonstration of a controlled-NOT wave-packet gate. *Phys. Rev. Lett.* **89**, 267901 (2002)

[51] F. Schmidt-Kaler, H. Häffner, M. Riebe, S. Gulde, G. P. T. Lancaster, T. Deuschle, C. Becher, C. F. Roos, J. Eschner, & R. Blatt: Realization of the Cirac-Zoller controlled-NOT quantum gate. *Nature* **422**, 408 (2003)

[52] F. Schmidt-Kaler, H. Häffner, S. Gulde, M. Riebe, G. P. T. Lancaster, T. Deuschle, C. Becher, W. H., J. Eschner, C. F. Roos, & R. Blatt: How to realize a universal quantum gate with trapped ions. *Appl. Phys. B* **77**, 789 (2003)

[53] D. Leibfried, B. DeMarco, V. Meyer, D. Lucas, M. Barrett, J. Britton, W. M. Itano, B. Jelenković, C. Langer, T. Rosenband, & D. J. Wineland: Experimental demonstration of a robust, high-fidelity geometric two ion-qubit phase gate. *Nature* **422**, 412 (2003)

[54] P. C. Haljan, K.-A. Brickman, L. Deslauriers, P. J. Lee, & C. Monroe: Spin-dependent forces on trapped ions for phase-stable quantum gates and entangled states of spin and motion. *Phys. Rev. Lett.* **94**, 153602 (2005)

[55] J. P. Home, M. J. McDonnell, D. M. Lucas, G. Imreh, B. C. Keitch, D. J. Szwer, N. R. Thomas, S. C. Webster, D. N. Stacey, & A. M. Steane: Deterministic entanglement and tomography of ion spin qubits. *New J. Phys.* **8**, 188 (2006)

[56] M. Riebe, H. Häffner, C. F. Roos, W. Hänsel, J. Benhelm, G. P. T. Lancaster, T. Körber, C. Becher, F. Schmidt-Kaler, D. F. V. James, & R. Blatt: Deterministic quantum teleportation with atoms. *Nature* **429**, 734 (2004)

[57] M. D. Barrett, J. Chiaverini, T. Schaetz, J. Britton, W. M. Itano, J. D. Jost, E. Knill, C. Langer, D. Leibfried, R. Ozeri, & D. J. Wineland: Deterministic quantum teleportation of atomic qubits. *Nature* **429**, 737 (2004)

[58] J. Chiaverini, D. Leibfried, T. Schaetz, M. D. Barrett, R. B. Blakestad, J. Britton,

W. M. Itano, J. D. Jost, E. Knill, C. Langer, R. Ozeri, & D. J. Wineland: Realization of quantum error correction. *Nature* **432**, 602 (2004)

[59] C. F. Roos, M. Riebe, H. Häffner, W. Hänsel, J. Benhelm, G. P. T. Lancaster, C. Becher, F. Schmidt-Kaler, & R. Blatt: Control and measurement of three-qubit entangled states. *Science* **304**, 1478 (2004)

[60] D. Leibfried, E. Knill, S. Seidelin, J. Britton, R. B. Blakestad, J. Chiaverini, D. B. Hume, W. M. Itano, J. D. Jost, C. Langer, R. Ozeri, R. Reichle, & D. J. Wineland: Creation of a six–atom 'Schrödinger cat' state. *Nature* **438**, 639 (2005)

[61] H. Häffner, W. Hänsel, C. F. Roos, J. Benhelm, D. C. al Kar, M. Chwalla, T. Körber, U. D. Rapol, M. Riebe, P. O. Schmidt, C. Becher, O. Gühne, W. Dür, & R. Blatt: Scalable multiparticle entanglement of trapped ions. *Nature* **438**, 643 (2005)

[62] R. Reichle, D. Leibfried, E. Knill, J. Britton, R. B. Blakestad, J. D. Jost, C. Langer, R. Ozeri, S. Seidelin, & D. J. Wineland: Experimental purification of two-atom entanglement. *Nature* **443**, 838 (2006)

[63] S. Gulde, M. Riebe, G. P. T. Lancaster, C. Becher, J. Eschner, H. Häffner, F. Schmidt-Kaler, I. L. Chuang, & R. Blatt: Implementation of the Deutsch-Jozsa algorithm on an ion-trap quantum computer. *Nature* **421**, 48 (2003)

[64] K.-A. Brickman, P. C. Haljan, P. J. Lee, M. Acton, L. Deslauriers, & C. Monroe: Implementation of Grover's quantum search algorithm in a scalable system. *Phys. Rev. A* **72**, 050306(R) (2005)

[65] B. B. Blinov, D. L. Moehring, L.-M. Duan, & C. Monroe: Observation of entanglement between a single trapped atom and a single photon. *Nature* **428**, 153 (2004)

[66] D. L. Moehring, P. Maunz, S. Olmschenk, K. C. Younge, D. N. Matsukevich, L.-M. Duan, & C. Monroe: Entanglement of single-atom quantum bits at a distance. *Nature* **449**, 68 (2007)

[67] D. Kielpinski, V. Meyer, M. A. Rowe, C. A. Sackett, W. M. Itano, C. Monroe, & D. J. Wineland: A decoherence-free quantum memory using trapped ions. *Science* **291**, 1013 (2001)

[68] D. Leibfried, B. DeMarco, V. Meyer, M. Rowe, A. Ben-Kish, J. Britton, W. M. Itano, B. Jelenković, C. Langer, T. Rosenband, & D. J. Wineland: Trapped-ion quantum simulator: experimental application to nonlinear interferometers. *Phys. Rev. Lett.* **89**, 247901 (2002)

[69] C. F. Roos, G. P. T. Lancaster, M. Riebe, H. Häffner, W. Hänsel, S. Gulde, C. Becher, J. Eschner, F. Schmidt-Kaler, & R. Blatt: Bell states of atoms with ultralong lifetimes and their tomographic state analysis. *Phys. Rev. Lett.* **92**, 220402 (2004)

[70] M. Riebe, K. Kim, P. Schindler, T. Monz, P. O. Schmidt, T. Körber, W. Hänsel, H. Häffner, C. F. Roos, & R. Blatt: Process tomography of ion trap quantum gates. *Phys. Rev. Lett.* **97**, 220407 (2006)

[71] M. Riebe, M. Chwalla, J. Benhelm, H. Häffner, W. Hänsel, C. F. Roos, & R. Blatt: Teleportation with atoms: quantum process tomography. *New J. Phys.* **9**, 211 (2007)

[72] J. Benhelm, G. Kirchmair, U. Rapol, T. Körber, C. F. Roos, & R. Blatt: Measurement of the hyperfine structure of the $S_{1/2}$-$D_{5/2}$ transition in $^{43}Ca^{+}$. *Phys. Rev. A* **75**, 032506 (2007)

[73] J. Benhelm, G. Kirchmair, C. F. Roos, & R. Blatt: Towards fault-tolerant quantum computing with trapped ions. *Nature Physics* **4**, 463 (2008)

[74] J. Benhelm, G. Kirchmair, C. F. Roos, & R. Blatt: Experimental quantum information processing with $^{43}Ca^{+}$. *Phys. Rev. A* **77**, 053806 (2008)

[75] M. A. Nielsen & I. L. Chuang: *Quantum Computation and Quantum Information*. Cambridge Univ. Press, Cambridge (2000)

[76] A. Einstein, B. Podolsky, & N. Rosen: Can quantum-mechanical description of physical reality be considered complete? *Phys. Rev.* **47**, 777 (1935)

[77] N. D. Mermin: Bringing home the atomic world: Quantum mysteries for anybody. *American Journal of Physics* **49**, 940 (1981)

[78] K. Mølmer & A. Sørensen: Multiparticle entanglement of hot trapped ions. *Phys. Rev. Lett.* **82**, 1835 (1999)

[79] A. Sørensen & K. Mølmer: Entanglement and quantum computation with ions in thermal motion. *Phys. Rev. A* **62**, 022311 (2000)

[80] D. A. Steck: Cesium D line data. *http://steck.us/alkalidata* (2003)

[81] P. A. Barton, C. J. S. Donald, D. M. Lucas, D. A. Stevens, A. M. Steane, & D. N. Stacey: Measurement of the lifetime of the 3d $^2D_{5/2}$ state in $^{40}Ca^{+}$. *Phys. Rev. A* **62**, 032503 (2000)

[82] J. Jian & D. A. Church: Precision lifetimes for the Ca^{+} 4p 2P levels: Experiment challenges theory at the 1% level. *Phys. Rev. Lett.* **70**, 3213 (1993)

[83] D. F. V. James: Quantum dynamics of cold trapped ions with application to quantum computation. *Appl. Phys. B* **66**, 181 (1998)

[84] F. Arbes, M. Benzing, T. Gudjons, F. Kurth, & G. Werth: Precise determination of the ground-state hyperfine-structure splitting of Ca-43-II. *Z. Phys. D* **31**, 27 (1994)

[85] W. Nörtershäuser, K. Blaum, K. Icker, P. Müller, A. Schmitt, K. Wendt, & B. Wiche: Isotope shifts and hyperfine structure in the 3d $^2D_J \rightarrow$ 4p ^2P_J transitions in calcium II. *Eur. Phys. J. D* **2**, 33 (1998)

[86] G. Tommaseo, T. Pfeil, G. Revalde, G. Werth, P. Indelicato, & J. Desclaux: The g_J-factor in the ground state of Ca^+. *Eur. Phys. J. D* **25**, 113 (2003)

[87] N. J. Stone: Table of nuclear magnetic dipole and electric quadrupole moments. *Atomic Data and Nuclear Data Tables* **90**, 75 (2005)

[88] G. Breit & I. I. Rabi: Measurement of nuclear spin. *Phys. Rev.* **38**, 2082 (1931)

[89] C. F. Roos: Controlling the quantum state of trapped ions. Dissertation, Universität Innsbruck (2000)

[90] D. J. Wineland, M. Barrett, J. Britton, J. Chiaverini, B. DeMarco, W. M. Itano, B. Jelenković, C. Langer, D. Leibfried, V. Meyer, T. Rosenband, & T. Schätz: Quantum information processing with trapped ions. *Phil. Trans. Royal Soc. London A* **361**, 1349 (2003)

[91] R. Ozeri, W. M. Itano, R. B. Blakestad, J. Britton, J. Chiaverini, J. D. Jost, C. Langer, D. Leibfried, R. Reichle, S. Seidelin, J. H. Wesenberg, & D. J. Wineland: Errors in trapped-ion quantum gates due to spontaneous photon scattering. *Phys. Rev. A* **75**, 042329 (2007)

[92] T. Körber: Atom-light interactions for the $^{43}Ca^+$ experiment. private communication (2004)

[93] R. Ozeri, C. Langer, J. D. Jost, B. DeMarco, A. Ben-Kish, B. R. Blakestad, J. Britton, J. Chiaverini, W. M. Itano, D. B. Hume, D. Leibfried, T. Rosenband, P. O. Schmidt, & D. J. Wineland: Hyperfine coherence in the presence of spontaneous photon scattering. *Phys. Rev. Lett.* **95**, 030403 (2005)

[94] F. Mintert & C. Wunderlich: Ion-trap quantum logic using long-wavelength radiation. *Phys. Rev. Lett.* **87**, 257904 (2001)

[95] S. Gulde, D. Rotter, P. Barton, F. Schmidt-Kaler, R. Blatt, & W. Hogervorst: Simple and efficient photo-ionization loading of ions for precision ion-trapping experiments. *Appl. Phys. B* **73**, 861 (2001)

[96] S. Gulde: Experimental realization of quantum gates and the Deutsch-Josza algorithm with trapped $^{40}Ca^+$–ions. Dissertation, Universität Innsbruck (2003)

[97] D. J. Berkeland, J. D. Miller, J. C. Bergquist, W. M. Itano, & D. J. Wineland: Minimization of ion micromotion in a Paul trap. *J. App. Phys.* **83**, 5025 (1998)

[98] P. K. Gosh: *Ion traps.* Clarendon Press (1995)

[99] R. W. P. Drever, J. L. Hall, & F. V. Kowalski: Laser phase and frequency stabilization using an optical resonator. *Appl. Phys. B* **31**, 97 (1983)

[100] G. Kirchmair: Frequency stabilization of a Titanium-Sapphire laser for precision spectroscopy on calcium ions. Diplomarbeit, Universität Innsbruck (2007)

[101] M. Notcutt, L.-S. Ma, J. Ye, & J. L. Hall: Simple and compact 1-Hz laser system via an improved mounting configuration of a reference cavity. *Opt. Lett.* **30**, 1815 (2005)

[102] J. Alnis, A. Matveev, N. Kolachevsky, T. Wilken, T. Udem, & T. W. Hänsch: Sub-Hz line width diode lasers by stabilization to vibrationally and thermally compensated ULE Fabry-Perot cavities. *arXiv:quant-ph/0801.4199v1* (2008)

[103] L.-S. Ma, P. Jungner, J. Ye, & J. L. Hall: Delivering the same optical frequency at two places: accurate cancellation of phase noise introduced by optical fiber or other time-varying path. *Opt. Lett.* **19**, 1777 (1994)

[104] P. T. Pham: *A general-purpose pulse sequencer for quantum computing*. Master's thesis, Massachusetts Institute of Technology (2005)

[105] P. Schindler: Frequency synthesis and pulse shaping for quantum information processing with trapped ions. Diplomarbeit, Universität Innsbruck (2008)

[106] D. M. Lucas, A. Ramos, J. P. Home, M. J. McDonnell, S. Nakayama, J. P. Stacey, S. C. Webster, D. N. Stacey, & A. M. Steane: Isotope-selective photoionization for calcium ion trapping. *Phys. Rev. A* **69**, 012711 (2004)

[107] W. Nörtershäuser, N. Trautmann, K. Wendt, & B. A. Bushaw: Isotope shifts and hyperfine structure in the $4s^2\ ^1S_0 \rightarrow 4s4p\ ^1P_1 \rightarrow 4s4d\ ^1D_2$ transitions of stable calcium isotopes and calcium-41. *Spectrochimica Acta Part B: Atomic Spectroscopy* **53**, 709 (1998)

[108] U. Tanaka, H. Matsunishi, I. Morita, & S. Urabe: Isotope-selective trapping of rare calcium ions using high-power incoherent light sources for the second step of photo-ionization. *Appl. Phys. B* **81**, 795 (2005)

[109] Q. A. Turchette, Kielpinski, B. E. King, D. Leibfried, D. M. Meekhof, C. J. Myatt, M. A. Rowe, C. A. Sackett, C. S. Wood, W. M. Itano, C. Monroe, & D. J. Wineland: Heating of trapped ions from the quantum ground state. *Phys. Rev. A* **61**, 0634318 (2000)

[110] D. Kielpinski, C. Monroe, & D. J. Wineland: Architecture for a large-scale ion-trap quantum computer. *Nature* **417**, 709 (2002)

[111] M. A. Rowe, A. Ben-Kish, B. DeMarco, D. Leibfried, V. Meyer, J. Beall, J. Britton, J. Hughes, W. M. Itano, B. Jelenković, C. Langer, T. Rosenband, & D. J. Wineland: Transport of quantum states and separation of ions in a dual rf ion trap. *Quant. Inf. Comp.* **2**, 257 (2002)

[112] W. K. Hensinger, S. Olmschenk, D. Stick, D. Hucul, M. Yeo, M. Acton, L. Deslauriers, & C. Monroe: T-junction ion trap array for two-dimensional ion shuttling storage, and manipulation. *Appl. Phys. Lett.* **88**, 034101 (2006)

[113] J. Home & A. Steane: Electrode configurations for fast separation of trapped ions. *Quantum Inf. Comput.* **6**, 289 (2006)

[114] L. Deslauriers, P. C. Haljan, P. J. Lee, K.-A. Brickman, B. B. Blinov, M. J. Madsen, & C. Monroe: Zero-point cooling and low heating of trapped $^{111}Cd^+$ ions. *Phys. Rev. A* **70**, 043408 (2004)

[115] W. H. Oskay, S. A. Diddams, E. A. Donley, T. M. Fortier, T. P. Heavner, L. Hollberg, W. M. Itano, S. R. Jefferts, M. J. Delaney, K. Kim, F. Levi, T. E. Parker, & J. C. Bergquist: Single-atom optical clock with high accuracy. *Phys. Rev. Lett.* **97**, 020801 (2006)

[116] A. D. Ludlow, T. Zelevinsky, G. K. Campbell, S. Blatt, M. M. Boyd, M. H. G. de Miranda, M. J. Martin, J. W. Thomsen, S. M. Foreman, J. Ye, T. M. Fortier, J. E. Stalnaker, S. A. Diddams, Y. Le Coq, Z. W. Barber, N. Poli, N. D. Lemke, K. M. Beck, & C. W. Oates: Sr Lattice Clock at 1×10^{-16} Fractional Uncertainty by Remote Optical Evaluation with a Ca Clock. *Science* **319**, 1805 (2008)

[117] T. Rosenband, D. B. Hume, P. O. Schmidt, C. W. Chou, A. Brusch, L. Lorini, W. H. Oskay, R. E. Drullinger, T. M. Fortier, J. E. Stalnaker, S. A. Diddams, W. C. Swann, N. R. Newbury, W. M. Itano, D. J. Wineland, & J. C. Bergquist: Frequency ratio of Al+ and Hg+ single-ion optical clocks; metrology at the 17th decimal place. *Science* **319**, 1808 (2008)

[118] P. O. Schmidt, T. Rosenband, C. Langer, W. M. Itano, J. C. Bergquist, & D. J. Wineland: Spectroscopy using quantum logic. *Science* **309**, 749 (2005)

[119] T. Schneider, E. Peik, & C. Tamm: Sub-Hertz optical frequency comparisons between two trapped $^{171}Yb^+$ ions. *Phys. Rev. Lett.* **94**, 230801 (2005)

[120] J. von Zanthier, T. Becker, M. Eichenseer, A. Y. Nevsky, C. Schwedes, E. Peik, H. Walther, R. Holzwarth, J. Reichert, T. Udem, T. W. Hänsch, P. V. Pokasov, M. N. Skvortsov, & S. N. Bagayev: Absolute frequency measurement of the In^+ clock transition with a mode-locked laser. *Opt. Lett.* **25**, 1729 (2000)

[121] H. S. Margolis, G. P. Barwood, G. Huang, H. A. Klein, S. N. Lea, K. Szymaniec, & P. Gill: Hertz-Level Measurement of the Optical Clock Frequency in a Single $^{88}Sr^+$ Ion. *Science* **306**, 1355 (2004)

[122] C. Champenois, M. Houssin, C. Lisowski, A. Knoop, G. Hagel, A. Vedel, & F. Vedel: Evaluation of the ultimate performances of a Ca^+ single-ion frequency standard. *Phys. Lett. A* **331**, 298 (2004)

[123] M. Kajita, Y. Li, K. Matsubara, K. Hayasaka, & M. Hosokawa: Prospect of optical frequency standard based on a $^{43}Ca^+$ ion. *Phys. Rev. A* **72**, 043404 (2005)

[124] F. Kurth, T. Gudjons, B. Hilbert, T. Reisinger, G. Werth, & A. M. Mårtensson-Pendrill: Doppler-free dark resonances for hyperfine measurements and isotope shifts in Ca^+ isotopes in a Paul trap. *Z. Phys. D* **34**, 227 (1995)

[125] B. K. Sahoo, R. K. Chaudhuri, B. P. Das, S. Majumder, H. Merlitz, U. S. Mahapatra, & D. Mukherjee: Influence of correlation effects on the magnetic dipole hyperfine interaction in the low-lying states of Ca^+. *J. Phys. B: At. Mol. Opt. Phys.* **36**, 1899 (2003)

[126] Kai-zhi Yu, Li-jin Wu, Bing-cong Gou, & Ting-yun Shi: Calculation of the hyperfine structure constants in $^{43}Ca^+$ and $^{87}Sr^+$. *Phys. Rev. A* **70**, 012506 (2004)

[127] C. Schwartz: Theory of hyperfine structure. *Phys. Rev.* **97**, 380 (1955)

[128] M. Chwalla, J. Benhelm, K. Kim, G. Kirchmair, T. Monz, M. Riebe, P. Schindler, A. Villar, W. Hänsel, C. F. Roos, R. Blatt, M. Abgrall, G. Santarelli, G. D. Rovera, & P. Laurent: Absolute frequency measurement of the $^{40}Ca^+$ $4s\,^2S_{1/2} - 3d\,^2D_{5/2}$ clock transition. *in preparation* (2008)

[129] C. F. Roos, M. Chwalla, K. Kim, M. Riebe, & R. Blatt: 'Designer atoms' for quantum metrology. *Nature* **443**, 316 (2006)

[130] M. Chwalla: Precision spectroscopy on $^{40}Ca^+$ ions in a Paul trap. Dissertation, Universität Innsbruck (2008)

[131] D. M. Harber, H. J. Lewandowski, J. M. McGuirk, & E. A. Cornell: Effect of cold collisions on spin coherence and resonance shifts in a magnetically trapped ultracold gas. *Phys. Rev. A* **66**, 053616 (2002)

[132] C. Langer, R. Ozeri, J. D. Jost, J. Chiaverini, B. Demarco, A. Ben-Kish, R. B. Blakestad, J. Britton, D. B. Hume, W. M. Itano, D. Leibfried, R. Reichle, T. Rosenband, T. Schaetz, P. O. Schmidt, & D. J. Wineland: Long-lived qubit memory using atomic ions. *Phys. Rev. Lett.* **95**, 060502 (2005)

[133] C. F. Roos, T. Zeiger, H. Rohde, H. Nägerl, J. Eschner, D. Leibfried, F. Schmidt-Kaler, & R. Blatt: Quantum state engineering on an optical transition and decoherence in a Paul trap. *Phys. Rev. Lett.* **83**, 4713 (1999)

[134] C. Monroe, D. M. Meekhof, B. E. King, S. R. Jefferts, W. M. Itano, D. J. Wineland, & P. L. Gould: Resolved-sideband Raman cooling of a bound atom to the 3D zero-point energy. *Phys. Rev. Lett.* **75**, 4011 (1995)

[135] T. Lu, X. Miao, & H. Metcalf: Bloch theorem on the Bloch sphere. *Phys. Rev. A* **71**, 061405(R) (2005)

[136] H. G. Dehmelt: Proposed $10^{14}\delta\nu < \nu$ laser fluorescence spectroscopy on Tl^+ mono–ion oscillator II (spontaneous quantum jumps). *Bull. Am. Phys. Soc.* **20**, 60 (1975)

[137] L. Aolita, K. Kim, J. Benhelm, C. F. Roos, & H. Häffner: High-fidelity ion-trap quantum computing with hyperfine clock states. *Phys. Rev. A* **76**, 040303 (2007)

[138] J. J. Bollinger, W. M. Itano, D. J. Wineland, & D. J. Heinzen: Optimal frequency measurements with maximally correlated states. *Phys. Rev. A* **54**, R4649 (1996)

[139] H. Häffner, F. Schmidt-Kaler, W. Hänsel, C. Roos, T. Körber, M. Chwalla, M. Riebe, J. Benhelm, U. D. Rapol, C. Becher, & R. Blatt: Robust entanglement. *Appl. Phys. B* **81**, 151 (2005)

[140] A. Barenco, C. H. Bennett, R. Cleve, D. P. DiVincenzo, N. Margolus, P. Shor, T. Sleator, J. A. Smolin, & H. Weinfurter: Elementary gates for quantum computation. *Phys. Rev. A* **52**, 3457 (1995)

[141] P. C. Haljan, P. J. Lee, K.-A. Brickman, M. Acton, L. Deslauriers, & C. Monroe: Entanglement of trapped-ion clock states. *Phys. Rev. A* **72**, 062316 (2005)

[142] C. F. Roos: Ion trap quantum gates with amplitude-modulated laser beams. *New J. Phys.* **10**, 013002 (2008)

[143] Q. Turchette, C. Wood, B. King, C. Myatt, D. Leibfried, W. Itano, C. Monroe, & D. Wineland: Deterministic entanglement of two ions. *Phys. Rev. Lett.* **81**, 3631 (1998)

[144] M. Riebe: private communication (2007)

[145] G. E. Moore: Cramming more components onto integrated circuits. *Electronics Magazine* **38** (1965)

[146] G. J. Milburn: Simulating nonlinear spin models in an ion trap. *arXiv:quant-ph/9908037v1* (1999)

[147] G. J. Milburn, S. Schneider, & D. F. James: Ion trap quantum computing with warm ions. *Fortschr. Phys.* **48**, 801 (2000)

[148] A. Sørensen & K. Mølmer: Quantum computation with ions in thermal motion. *Phys. Rev. Lett.* **82**, 1971 (1999)

[149] E. Solano, R. L. de Matos Filho, & N. Zagury: Deterministic Bell states and measurement of the motional state of two trapped ions. *Phys. Rev. A* **59**, R2539 (1999)

[150] F. Schmidt-Kaler, H. Häffner, S. Gulde, M. Riebe, G. Lancaster, J. Eschner, C. Becher, & R. Blatt: Quantized AC-Stark shifts and their use for multiparticle entanglement and quantum gates. *Europhys. Lett.* **65**, 587 (2004)

[151] J. J. Garcia-Ripoll, P. Zoller, & J. I. Cirac: Speed optimized two-qubit gates with laser coherent control techniques for ion trap quantum computing. *Phys. Rev. Lett.* **91**, 157901 (2003)

[152] H. Häffner, S. Gulde, M. Riebe, G. Lancaster, C. Becher, J. Eschner, F. Schmidt-Kaler, & R. Blatt: Precision measurement and compensation of optical Stark shifts for an ion-trap quantum processor. *Phys. Rev. Lett.* **90**, 143602 (2003)

[153] D. Leibfried, M. D. Barrett, T. Schaetz, J. Britton, J. Chiaverini, W. M. Itano, J. D. Jost, C. Langer, & D. J. Wineland: Toward Heisenberg-limited spectroscopy with multiparticle entangled states. *Science* **304**, 1476 (2004)

[154] D. Leibfried, E. Knill, C. Ospelkaus, & D. J. Wineland: Transport quantum logic gates for trapped ions. *Phys. Rev. A* **76**, 032324 (2007)

[155] G. Kirchmair, J. Benhelm, F. Zähringer, R. Gerritsma, C. F. Roos, & R. Blatt: High fidelity Mølmer-Sørensen gate with hot and cold ions. *in preparation* (2008)

[156] A. H. Myerson, D. J. Szwer, S. C. Webster, D. T. C. Allcock, M. J. Curtis, G. Imreh, J. A. Sherman, D. N. Stacey, A. M. Steane, & D. M. Lucas: High-fidelity readout of trapped-ion qubits. *Phys. Rev. Lett.* **100**, 200502 (2008)

[157] E. Knill, D. Leibfried, R. Reichle, J. Britton, R. B. Blakestad, J. D. Jost, C. Langer, R. Ozeri, S. Seidelin, & D. J. Wineland: Randomized benchmarking of quantum gates. *Phys. Rev. A* **77**, 012307 (2008)

[158] V. Nebendahl: Optimierung verschränkender Quantengatter für Experimente mit Ionenfallen. Diplomarbeit, Universität Innsbruck (2008)

[159] P. J. Mohr & B. N. Taylor: Codata recommended values of the fundamental physical constants: 2002. *Rev. Mod. Phys.* **77**, 1 (2005)

[160] M. S. Gulley, A. G. White, & D. F. V. James: A Raman approach to quantum logic in calcium-like ions. *arXiv:quant-ph/0112117v1* (2001)

[161] Y. Ralchenko, A. E. Kramida, J. Reader, & NIST ASD Team (2008): NIST Atomic Spectra Database (version 3.1.5). http://physics.nist.gov/asd3. National Institute of Standards and Technology, Gaithersburg, MD.

[162] R. Yamazaki, H. Sawamura, K. Toyoda, & S. Urabe: Stimulated Raman spectroscopy and the determination of the D-fine-structure level separation in $^{40}\mathrm{Ca}^+$. *Phys. Rev. A* **77**, 012508 (2008)

[163] D. Sundholm & J. Olsen: Finite element multiconfiguration Hartree–Fock determination of the nuclear quadrupole moments of chlorine, potassium, and calcium isotopes. *J. Chem. Phys.* **98**, 7152 (1993)

[164] N. F. Ramsey: A new molecular beam resonance method. *Phys. Rev.* **76**, 996 (1949)